

学位論文

Measurement of the
Forward-Backward Asymmetries for
b and c Quarks in e^+e^- Collisions at
 \sqrt{s} between 130 GeV and 209 GeV

重心系エネルギー 130GeV から 209GeV の電子陽電子
衝突に於ける b、c クォーク前後方非対称性の測定

平成 17 年 1 月博士 (理学) 申請

東京大学大学院理学系研究科
物理学専攻

南條 創

Abstract

A measurement of forward-backward asymmetries for $b\bar{b}$ and $c\bar{c}$ production (A_{FB}^b and A_{FB}^c) in e^+e^- annihilation is presented. The data were collected by the OPAL detector at the LEP e^+e^- collider, at center-of-mass energies (\sqrt{s}) ranging from 130 GeV to 209 GeV. Two methods are used to evaluate the production angle of the primary quark and to identify the $b\bar{b}$ or $c\bar{c}$ events. One utilizes the hemisphere charge with a powerful b-tagging algorithm based on lifetime, lepton and event-shape information. The other uses the information of the leptons from semileptonic decays of heavy hadrons both to evaluate the primary-quark direction and to enhance events with primary b or c quarks. Finally, the two independent methods are combined with a single likelihood function with which the A_{FB}^b and A_{FB}^c are measured simultaneously by fitting the distribution of the evaluated primary-quark direction. Results are presented at 11 different center-of-mass energies between 130 and 209 GeV, which are in good agreements with the standard model predictions. The same analysis is performed for the combined data with \sqrt{s} from 183 GeV to 209 GeV where the $A_{\text{FB}}^{b,c}$ is stable against \sqrt{s} . The results of

$$\begin{aligned} A_{\text{FB}}^b &= 0.52 \pm 0.09(\text{stat.}) \pm 0.09(\text{syst.}) \\ A_{\text{FB}}^c &= 0.59 \pm 0.12(\text{stat.}) \pm 0.09(\text{syst.}) \end{aligned}$$

are obtained, where the luminosity weighted center-of-mass energy is 197 GeV. These values are also in good agreements with the standard model predictions. For the data with \sqrt{s} above 189 GeV, this is the first measurement of the A_{FB}^b and A_{FB}^c . With the results, new limits on the contact interaction and leptoquarks are obtained.

Contents

1	Introduction	1
2	Theoretical Framework	5
2.1	Electroweak Theory	5
2.2	Calculation of the A_{FB}	8
2.2.1	Massless Tree-Level Calculation	8
2.2.2	Corrections	10
	Fermions' Mass Corrections	10
	One-Loop Electroweak Corrections	10
	Photonic Corrections	12
	Final State QCD Corrections	13
2.3	Fragmentation	13
2.3.1	Perturbative QCD Phase	15
2.3.2	Hadronization Phase	15
	String Fragmentation	15
2.4	Neutral B meson mixing	17
3	Experimental Apparatus	19
3.1	The LEP Collider	19
3.1.1	Injector chain	22
3.1.2	LEP Accelerator	22
3.2	The OPAL detector	23
3.2.1	Central Tracking System	26
	Silicon Microvertex Detector(SI)	26
	Vertex Chamber (CV)	27
	Jet Chamber (CJ)	28
	Z chambers (CZ)	29
	Solenoid Coil	29
3.2.2	Time-of-Flight System (TOF)	30
	Barrel Time-of-Flight detector (TB)	30

	Tile Endcap Detector (TE)	30
3.2.3	Electromagnetic Calorimeters	30
	Barrel and Endcap Electromagnetic Presamplers (PB & PE)	31
	Barrel and Endcap Electromagnetic Calorimeters (EB & EE)	31
	Gamma Catcher (FE)	31
	Minimum ionizing particle (MIP) plug	32
3.2.4	Hadron Calorimeters	32
	Barrel and Endcap Hadron Calorimeters (HB & HE)	33
	Pole-tip Hadron Calorimeters (HP)	33
3.2.5	Muon Detectors (MU)	33
	Barrel Muon Detector (MB)	33
	Endcap Muon Detector (ME)	34
3.2.6	Luminometers	34
	Forward Detectors (FD)	34
	Silicon Tungsten Detector (SW)	34
3.2.7	Trigger	35
4	Measurements of the $A_{\text{FB}}^{\text{b,c}}$	37
4.1	Overview of the Quark-Antiquark Pair Production at LEP2	37
4.2	Definition of the A_{FB} at LEP2	41
4.3	Procedure of the A_{FB} Measurement	42
4.4	Data and Monte Carlo Samples	44
	4.4.1 Luminosity Measurement	45
	4.4.2 Data	45
	4.4.3 Monte Carlo Samples	46
4.5	Event Preselections	47
	4.5.1 LEP2 Multi-Hadronic Event Selection	47
	4.5.2 s' Determination and Non-Radiative Event Selection	50
	4.5.3 4-fermion event rejection	52
	$W^+W^- \rightarrow q\bar{q}\ell\bar{\nu}_\ell$ selection	52
	$W^+W^- \rightarrow q\bar{q}q\bar{q}$ selection	53
	Preselection	54
	Likelihood based selection	54
	4-fermion event rejection with $W^+W^- \rightarrow q\bar{q}\ell\bar{\nu}_\ell$ and $W^+W^- \rightarrow$ $q\bar{q}q\bar{q}$ selection	55
	4.5.4 Acceptance Cut	56
	4.5.5 Effect of the Event Preselection	57
4.6	Inclusive Analysis	57

4.6.1	Determination of the Quark-Hemisphere	57
4.6.2	Inclusive B and C Tagging	62
	Overview	62
	Jet Clustering	63
	Secondary Vertex Reconstruction	63
	Lifetime Tag	64
	Lepton Tag	66
	Kinematics Tag	66
	Combined Likelihood Tag	67
	Event Classification with b-tagging variables	71
4.6.3	Unbinned Likelihood Fit	73
	Probability Density Function	75
	Probability Density Function with Subsamples	76
	Fitting	77
4.6.4	Corrections Applied to the Fitted Values of A_{FB}	79
4.7	Lepton Analysis	80
4.7.1	Prompt Leptons	80
4.7.2	Lepton Identification	81
	Electron Identification	81
	Muon Identification	84
4.7.3	b and c Tagging and Flavor Separation	86
	Construction of Artificial Neural Networks	86
4.7.4	Event Selection	91
4.7.5	Unbinned Likelihood Fit	91
	Making Subsamples	91
	Probability Density Function	92
4.8	Combined Analysis	95
4.9	Systematic Uncertainties	97
4.9.1	Bottom and Charm Physics Modeling	98
4.9.2	Effect of the ISR-FSR Interference	100
4.9.3	Final State QCD Corrections	100
4.9.4	The Rates of Gluon Splitting to $b\bar{b}$ or $c\bar{c}$	101
4.9.5	Total K^0 and Λ Rate	101
4.9.6	Four-fermion Background	101
4.9.7	Track Reconstruction	101
4.9.8	Event Pre-Selection	102
4.9.9	Lepton Identification	102
4.9.10	Modeling of Artificial Neural Network Inputs	102

4.9.11	Monte Carlo Statistics	102
4.9.12	Background Asymmetries	102
4.9.13	Fitting Procedure	103
4.9.14	Cross-Checks	103
4.10	Result and Discussion	104
5	Conclusion	123
A	The Standard Model	125
A.1	Elementary Particles in the Standard Model	125
A.1.1	Fermions	125
A.1.2	Bosons	126
A.1.3	Chirality and Quark Mixing	126
A.2	Interactions (Gauge Theory)	128
A.2.1	Gauge Theory	128
A.2.2	Quantum Electrodynamics(QED)	129
A.2.3	Charge	130
A.3	Electroweak Theory	132
A.3.1	Massless Electroweak Theory	132
A.3.2	Gauge Boson Masses and Higgs Mechanism	136
A.3.3	Fermion Masses	138
A.4	The Standard Model Parameters	139
B	Massless Tree-Level A_{FB} Calculation	141
C	Jet Clustering	145
C.1	Jet-Clustering Algorithm	145
C.1.1	JADE algorithm with the E0 recombination scheme	145
C.1.2	Durham algorithm	146
C.1.3	Cone algorithm	146
C.2	Evaluation of Primary-Quark Direction	147
C.3	Evaluation of Primary-Quark Charge	148
C.4	b-Tagging	151
D	Artificial Neural Network (ANN)	155
	Acknowledgment	169

Chapter 1

Introduction

At the beginning of the 20th century, only the electron and photon had been discovered among the elementary particles known today and the development of the quantum dynamics had just been started. Since then, great progress has been made in particle physics with the discoveries of elementary particles and constructions of theories to describe their interactions.

In the former part of the century, the relativistic quantum theory to describe the electromagnetic interaction, the quantum electrodynamics (QED), was constructed successfully. Then the progress in understanding the weak interaction followed. In the middle of the century, parity non-conservation in the weak interaction was discovered in beta decay [1], which is one of the most significant characteristics of the weak interaction. This made large amount of contribution to determine the structure of the weak interaction as $V - A$ type which means the Lagrangian contains only the vector coupling (v) and axial vector coupling (a) as

$$\bar{\psi}_e \gamma^\mu (v - a\gamma^5) \psi_{\nu_e}. \quad (1.1)$$

Then the possibility of the intermeduating W^\pm bosons in the charged current interaction was considered [2]. Based on the insight about the local gauge invariance [3], the electroweak theory to unify the weak and electromagnetic interactions was constructed [4–6]. The electroweak theory suggested the existence of the neutral current interaction with the intermeduating neutral Z boson. Then many experiments to test the electroweak theory were performed, finding the neutral current interactions, and the W^\pm and Z bosons. The neutral current interaction was indicated in the elastic $\bar{\nu}_\mu e^-$ scattering [7] and found in the muon-less neutrino-induced inelastic interactions [8]. At the SPS in proton and anti-proton collisions, the W^\pm [9, 10] and Z [11, 12] bosons were discovered at the masses expected in the framework of the electroweak theory with the experimental results at lower energies. The studies of the neutral current interaction with e^+e^- colliders have been performed at PEP at the center-of-mass energy (\sqrt{s}) of 29 GeV, PETRA at the \sqrt{s} from 14 to 46 GeV, TRISTAN at the \sqrt{s} from 50 to 64 GeV, SLC at the \sqrt{s} of 91.3

GeV and LEP at the \sqrt{s} from 89 GeV to 209 GeV. With the great success in the agreement between these experimental results and the theoretical predictions, the electroweak theory has been established. On the other hand, the strong interaction is described by the quantum chromodynamics (QCD). The electroweak theory and the QCD compose the standard model, which describes phenomena in particle physics successfully. Further efforts have been and will be made to construct a theory to unify the electroweak theory and QCD and to include the gravitational interaction.

In the above-mentioned e^+e^- experiments, the reaction from the electron-positron annihilation to a fermion and anti-fermion pair with intermediating γ or Z have been analyzed. The Feynman diagram of the reaction¹ is shown in Fig. 1.1.

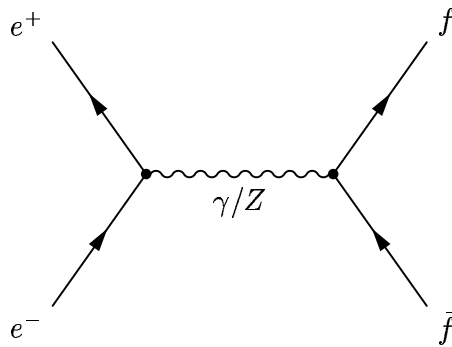


Figure 1.1: The tree-level Feynman diagram for $e^+e^- \rightarrow f\bar{f}$.

The forward-backward asymmetry (A_{FB}) is one of the most important observables of the fermion-pair processes, since it is a sensitive probe of the electroweak theory, which is mainly related to the parity-violating nature of the weak interaction and the $\gamma - Z$ interference at the propagator. The A_{FB} represents the difference between the cross-section for the fermion emitted to the electron direction and that for the fermion emitted to the positron direction defined as

$$A_{\text{FB}} = \frac{\int_0^1 \left(\frac{d\sigma}{d\cos\theta}\right) d\cos\theta - \int_{-1}^0 \left(\frac{d\sigma}{d\cos\theta}\right) d\cos\theta}{\int_0^1 \left(\frac{d\sigma}{d\cos\theta}\right) d\cos\theta + \int_{-1}^0 \left(\frac{d\sigma}{d\cos\theta}\right) d\cos\theta}, \quad (1.2)$$

where θ is angle of the fermion direction measured with respect to the electron beam direction. The A_{FB} for each lepton-pair final state can be measured. As for the quark-pair final state, the A_{FB} for b or c quark is especially important, since $b\bar{b}$ or $c\bar{c}$ events can be identified efficiently.

¹The final states of e^+e^- and $\nu_e\bar{\nu}_e$ have another t-channel diagram.

The A_{FB} for bottom quarks (A_{FB}^{b}) and for charm quarks (A_{FB}^{c}) have been measured at PEP [13–19], PETRA [20–31], TRISTAN [32–34], SLC [35] and LEP [35] as shown in Fig. 1.2. In Fig. 1.2, the standard model predictions are given by lines².

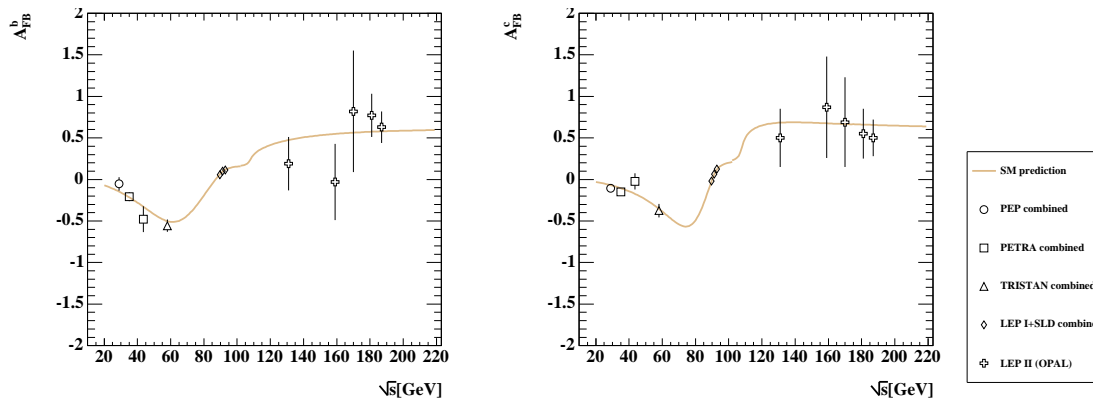


Figure 1.2: The results of the A_{FB}^{b} and A_{FB}^{c} measurements in e^+e^- collisions at the PEP, PETRA, TRISTAN, SLC and LEP are shown, where the standard model predictions are given by lines.

At \sqrt{s} below the Z resonance, the pure Z cross-section increases as the \sqrt{s} increases. It becomes comparable to the pure γ cross-section at the \sqrt{s} of approximately 60 GeV for bottom quarks and at the \sqrt{s} of approximately 70 GeV for charm quarks, where the A_{FB} is minimum due to the large γ -Z interference.

At the Z resonance, the fermion-pair production is dominated by the pure Z decays, where the A_{FB} is sensitive to the effective electroweak mixing angle³ for both the initial-state electron (θ_{eff}^e) and the final-state fermion (θ_{eff}^f). Since the dependence of the A_{FB} on the $\theta_{\text{eff}}^{\text{b}}$ or $\theta_{\text{eff}}^{\text{c}}$ is small compared to the θ_{eff}^e , the measurement of the $A_{\text{FB}}^{\text{b,c}}$ has given one of the most precise values of θ_{eff}^e [35].

Above the Z peak, the pure Z cross-section decreases and becomes comparable to the pure γ cross-section. Hence the contribution of the γ -Z interference becomes larger. The A_{FB} is sensitive to new physics beyond the standard model. Possible new physics beyond the standard model, for example, existence of the additional heavy neutral bosons (Z'), leptoquarks or R-parity violating squarks which would mediate in addition to γ/Z , could alter the standard model value of the $A_{\text{FB}}^{\text{b,c}}$ [36–39]. The $A_{\text{FB}}^{\text{b,c}}$ measurement above Z resonance is important for both testing the standard model and searching new physics

²The rapid change in the standard model prediction of A_{FB} around \sqrt{s} of 110 GeV is due to the event selection described in Section 4.5.2.

³The effective electroweak mixing angle (θ_{eff}) is related to the electroweak mixing angle (θ_{W}) through the higher order corrections as described in Section 2.2.2. The θ_{W} is one of the parameters in the electroweak theory defined in Eq. A.33.

beyond the standard model.

In this thesis, a measurement of A_{FB}^{b} and A_{FB}^{c} at \sqrt{s} above the Z resonance is presented. The data were collected by the OPAL detector at the LEP e^+e^- collider, at center-of-mass energies ranging from 130 GeV to 209 GeV, which is the highest energy for the e^+e^- collisions. In this analysis, two methods are used to evaluate the production angle of the primary quark and to identify the $b\bar{b}$ or $c\bar{c}$ events. One utilizes the hemisphere charge⁴ to evaluate the emitting direction of the primary quark together with the thrust axis⁵, where a powerful b-tagging algorithm based on lifetime, lepton and event-shape information is used to enhance events with primary b and c quarks. The other utilizes the information of the leptons from semileptonic decays of heavy hadrons together with the thrust axis, both to determine the primary-quark direction and to enrich events with primary b and c quarks. Finally, two independent methods are combined with a single likelihood function with which the A_{FB}^{b} and A_{FB}^{c} are measured simultaneously by fitting the distribution of the evaluated primary-quark direction. In order to compensate for the small statistics at \sqrt{s} above the Z resonance, powerful b or c tagging algorithms are used for the both analyses, which are more effective than these used in the $A_{\text{FB}}^{\text{b,c}}$ measurements at the Z resonance [40,41].

While the basic techniques are similar to those adopted in the previous OPAL measurement [42] at \sqrt{s} from 130 GeV to 189 GeV, more powerful b-tagging algorithm and more sophisticated fitting method are employed in this analysis. The measurement of the $A_{\text{FB}}^{\text{b,c}}$ at the \sqrt{s} beyond 189 GeV reported here is the first measurement.

This thesis is organized as follows. In Chapter 2, the theoretical background concerning this analysis is described. In Chapter 3, descriptions of the LEP accelerator and the OPAL detector are given. The A_{FB} measurement is discussed in Chapter 4, where a description about systematic errors is given and a discussion about the result is followed. The conclusion is given in Chapter 5.

⁴A description about the hemisphere charge is given in Section 4.3

⁵A description about the thrust axis is given in Section 4.3

Chapter 2

Theoretical Framework

The fermion and anti-fermion pair ($f\bar{f}$) production in e^+e^- annihilation is mainly described by the neutral current part of the electroweak theory, which is briefly described at first in this section. Then the calculation of the $A_{\text{FB}}^{b,c}$ with the electroweak theory is given, where some higher order effects and QCD effects are also described. Whereas the quark and anti-quark ($q\bar{q}$) production is described by the electroweak theory, the quarks are only detected at the detector as colorless hadrons. The process to connect the quark and particles at the detector is termed fragmentation, which is also described in this chapter. Finally, the neutral B meson mixing ($B^0 - \bar{B}^0$ mixing) is described. Since the charge of the primary quark is evaluated with the final state particles, the $B^0 - \bar{B}^0$ mixing dilutes the charge identification in the A_{FB} measurement.

2.1 Electroweak Theory

The electroweak theory is briefly described here. More detailed description is given in chapter A. The fermions (leptons and quarks) are classified as shown in Table. 2.1 with 3 independent quantum numbers, which are different between their chiral components (L or R). The quantum numbers are the electric charge¹ (Q), the third component of the weak isospin (T_3), and the color charge (C).

¹The electric charge is always measured in the unit of the electron charge magnitude ($e = 1.602176462(63) \times 10^{-19}$ C).

Table 2.1: Quantum numbers for fermions where Q is the electric charge, T_3 denotes the third component of the weak isospin, and C is the color charge.

Fermions			Quantum Numbers		
			Q	T_3	C
Leptons					
$\begin{pmatrix} \nu_e \\ e^- \end{pmatrix}_L$	$\begin{pmatrix} \nu_\mu \\ \mu^- \end{pmatrix}_L$	$\begin{pmatrix} \nu_\tau \\ \tau^- \end{pmatrix}_L$	0	$+\frac{1}{2}$	0
e_R	μ_R	τ_R	-1	$-\frac{1}{2}$	0
Quarks					
$\begin{pmatrix} u \\ d' \end{pmatrix}_L$	$\begin{pmatrix} c \\ s' \end{pmatrix}_L$	$\begin{pmatrix} t \\ b' \end{pmatrix}_L$	$+\frac{2}{3}$	$+\frac{1}{2}$	(R, G, B)
u_R	c_R	t_R	$-\frac{1}{3}$	$-\frac{1}{2}$	
d_R	s_R	b_R	$+\frac{2}{3}$	0	(R, G, B)
			$-\frac{1}{3}$	0	(R, G, B)

The interactions between the fermions are described as exchanging of a boson between them, where such bosons are called as gauge bosons. The color charge is the source of the strong interactions where the gluons act as the gauge boson, which are described by the QCD. The electric charge and the third component of the weak isospin are the sources of the electroweak force where the γ and, W and Z bosons act as the gauge bosons, which is described by the electroweak theory. In the electroweak theory, the neutral current interaction where the γ or Z boson are exchanged is described with two Lagrangians as,

$$\mathcal{L}_{\text{EM}} = e \sum_{f=d,u,s,c,b,t,e,\nu_e,\mu,\nu_\mu,\tau,\nu_\tau} [\bar{f}\gamma^\mu Q_f f] A_\mu, \quad (2.1)$$

$$\mathcal{L}_{\text{NC}}^Z = \frac{e}{2 \sin \theta_W \cos \theta_W} \sum_{f=d,u,s,c,b,t,e,\nu_e,\mu,\nu_\mu,\tau,\nu_\tau} [\bar{f}\gamma^\mu \{v_f - a_f \gamma^5\} f Z_\mu]. \quad (2.2)$$

In Eq. 2.1, 2.2, the \mathcal{L}_{EM} corresponds to the γ exchange and the $\mathcal{L}_{\text{NC}}^Z$ corresponds to the Z boson exchange where f means a fermion field, A_μ and Z_μ mean the γ and Z boson fields respectively. The θ_W is electroweak mixing angle (“Weinberg angle”) which is one of the parameters in the theory as defined in Eq. A.33. The v_f is called vector coupling and a_f

is called axial vector coupling which are defined as,

$$v_f = T_3^f(1 - 4|Q_f|\sin^2\theta_W), \quad (2.3)$$

$$a_f = T_3^f, \quad (2.4)$$

and their relations with $\sin^2\theta_W$ are shown in Table. 2.2.

Table 2.2: The fermion's vector and axial vector couplings (v and a respectively).

Fermions		v	a
neutrinos	$(\nu_e, \nu_\mu, \nu_\tau)$	$+\frac{1}{2}$	$+\frac{1}{2}$
leptons	(e, μ, τ)	$-\frac{1}{2} + 2\sin^2\theta_W$	$-\frac{1}{2}$
up-type quarks	(u, c, t)	$+\frac{1}{2} - \frac{4}{3}\sin^2\theta_W$	$+\frac{1}{2}$
down-type quarks	(d, s, b)	$-\frac{1}{2} + \frac{2}{3}\sin^2\theta_W$	$-\frac{1}{2}$

2.2 Calculation of the A_{FB}

The theoretical calculation of the A_{FB} with the electroweak theory is given in this section. At first, the tree-level calculation under massless approximation of the fermions is given. Then the description of some corrections to improve the accuracy is followed.

2.2.1 Massless Tree-Level Calculation

A schematic view of the $e^+e^- \rightarrow f\bar{f}$ reaction is shown in Fig. 2.1, where the angle θ is the angle of the fermion (f) direction measured from the e^- direction.

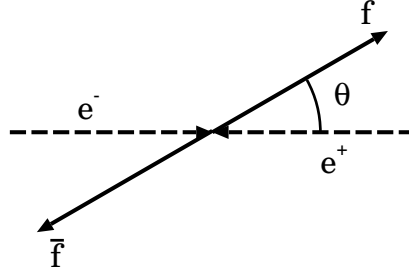


Figure 2.1: A schematic view of the $e^+e^- \rightarrow f\bar{f}$ reaction.

The differential cross section in the massless limit for the process $e^+e^- \rightarrow f\bar{f}$ except for the final states of e^+e^- and $\nu_e\bar{\nu}_e$ can be calculated with the electroweak theory [43] as

$$\frac{d\sigma}{d\Omega} = \frac{N_c\alpha^2}{4s} [G(s)(1 + \cos^2\theta) + H(s)\cos\theta], \quad (2.5)$$

where α is defined as $\alpha = \frac{e^2}{4\pi}$. The $G(s)$ and $H(s)$ are defined as

$$G(s) \equiv Q_f^2 + |\chi(s)|^2(v_e^2 + a_e^2)(v_f^2 + a_f^2) - 2Q_f v_e v_f \Re\{\chi(s)\}, \quad (2.6)$$

$$H(s) \equiv \underbrace{0}_{\gamma} + \underbrace{+8|\chi(s)|^2 v_e a_e v_f a_f}_{Z \text{ exchange}} + \underbrace{-4Q_f a_e a_f \Re\{\chi(s)\}}_{\gamma - Z \text{ interference}}, \quad (2.7)$$

where $\chi(s)$ is defined as

$$\chi(s) \equiv \left(\frac{s}{e^2}\right) \frac{g^2}{4\cos^2\theta_W} \frac{1}{s - m_Z^2 + im_Z\Gamma_Z}. \quad (2.8)$$

For both Eq. 2.6 and Eq. 2.7, the first term corresponds to the γ exchange, the second corresponds to the Z exchange and the third corresponds to the $\gamma - Z$ interference. The total cross section $\sigma(s)$ can be written as

$$\sigma(s) = \frac{4N_c\pi\alpha^2}{3s} G(s), \quad (2.9)$$

and the forward-backward asymmetry (A_{FB}) can be written as,

$$A_{\text{FB}} = \frac{3}{8} \frac{H(s)}{G(s)}, \quad (2.10)$$

and the A_{FB} is related to the angular distribution as,

$$\frac{d\sigma}{d\cos\theta} \propto 1 + \cos^2\theta + \frac{8}{3} A_{\text{FB}} \cos\theta. \quad (2.11)$$

In Eq. 2.6, 2.7, contributions of γ exchange, Z exchange and $\gamma - Z$ interference are separately written. Those for $G(s)$ are represented with $G_\gamma(s)$, $G_Z(s)$ and $G_{\gamma-Z}(s)$ and those for $H(s)$ are represented with $H_\gamma(s)$, $H_Z(s)$ and $H_{\gamma-Z}(s)$, respectively. The \sqrt{s} dependence of these functions and A_{FB} for b and c quarks are shown in Fig. 2.2.

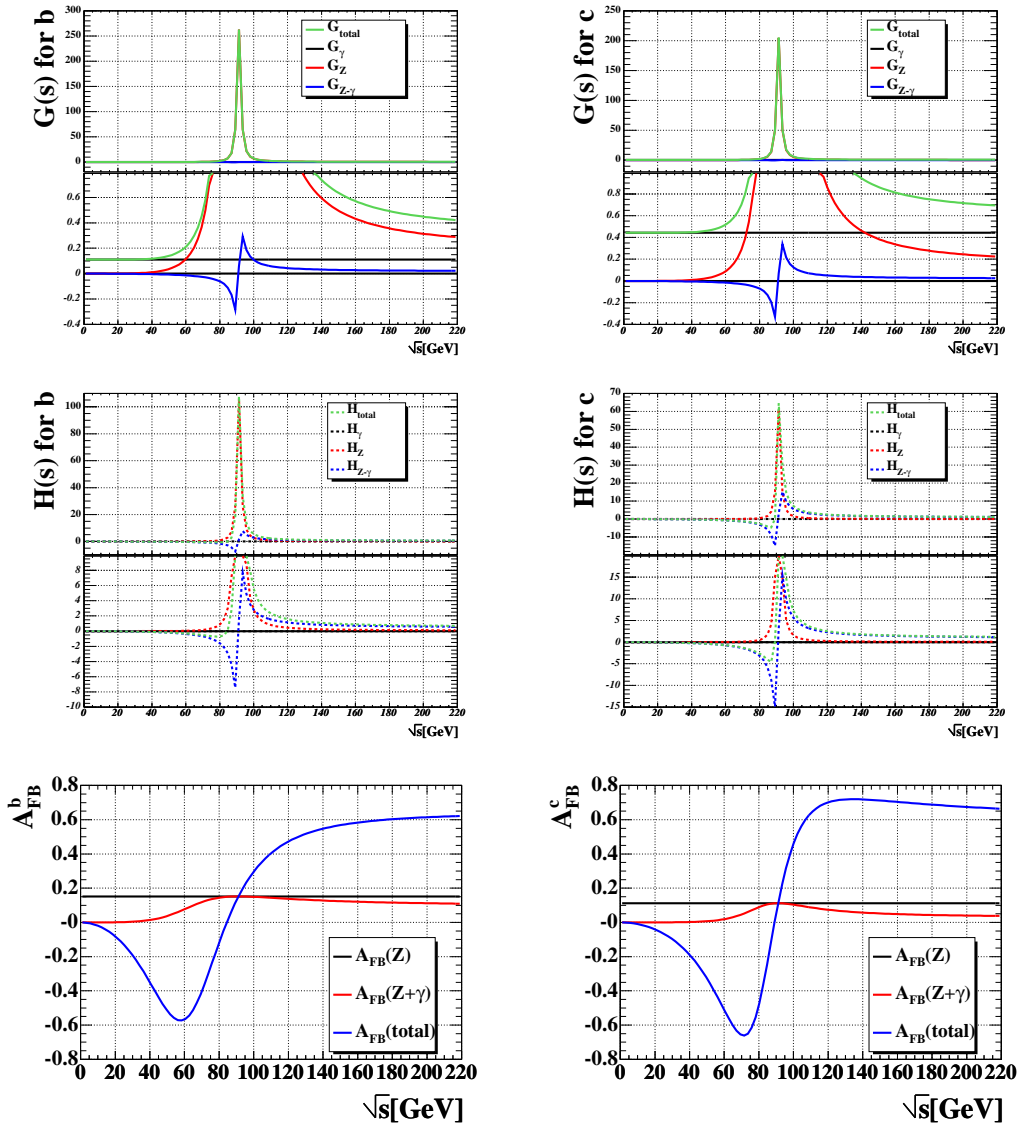


Figure 2.2: The \sqrt{s} dependence of $G(s)$ and $H(s)$ are shown for b and c quarks.

Large effect of the $\gamma - Z$ interference is appeared in the A_{FB} around \sqrt{s} where $G_\gamma(s)$ equals $G_Z(s)$. Based on the fact the cross section is proportional to $G(s)/s$ as seen in Eq. 2.9, the $\gamma - Z$ interference is naturally understood as follows. For \sqrt{s} below 40 GeV, γ makes almost all the contribution to the propagator and the interference is small. When \sqrt{s} increases, the contribution of Z increases and becomes comparable to the contribution of γ at \sqrt{s} around 60 GeV for the down-type quarks and around 70 GeV for the up-type quarks, where the interference becomes maximum. For \sqrt{s} at m_Z , the contribution of Z is maximum due to the resonance and the interference term vanishes. As the \sqrt{s} increase beyond m_Z , the contribution of Z becomes smaller and the interference appears again. As for the down-type quarks, the contribution of Z becomes close to that of γ but remain larger than that of γ . Therefore the A_{FB} increases as the \sqrt{s} increases. As to the up-type quarks, the contribution of Z becomes smaller than that of γ for \sqrt{s} beyond approximately 140 GeV. Therefore, A_{FB}^c increases while \sqrt{s} is smaller than approximately 140 GeV. For \sqrt{s} beyond 140 GeV, it decreases as \sqrt{s} increases.

2.2.2 Corrections

There are some corrections to the massless tree level calculation to improve the accuracy. Such corrections can be broken down to four categories, fermions' mass corrections, electroweak corrections, photonic corrections and QCD corrections.

Fermions' Mass Corrections

The fermions' mass can be included in the theoretical calculation as in [43]. The contribution to the A_{FB}^b is below 0.5% at \sqrt{s} more than 80 GeV and that to the A_{FB}^c is below 0.2%, which are negligible in this analysis.

One-Loop Electroweak Corrections

The one-loop electroweak corrections can be broken down into 3 types. One is the case in which a virtual particle loop is inserted in the the propagator which corresponds to the bosonic self-energy as shown in Fig. 2.3. The second is vertex correction as shown in Fig. 2.4. The third is the contribution of the box diagram of W or Z bosons as shown in Fig. 2.5. These corrections can be reflected to the tree-level cross section by introducing the running α ($\alpha(s)$), replacing the weak mixing angle by the effective weak mixing angle ($\sin \theta_{\text{eff}}^f$) and re-defining the vector and axial vector couplings. These corrections are properly treated in some programs, such as ZFITTER [44].

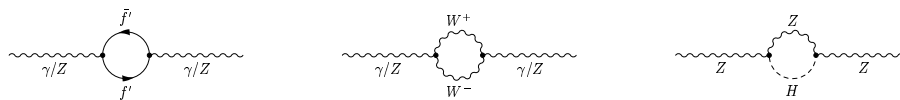


Figure 2.3: Examples of the diagrams contributing to the bosonic self-energy type electroweak corrections.

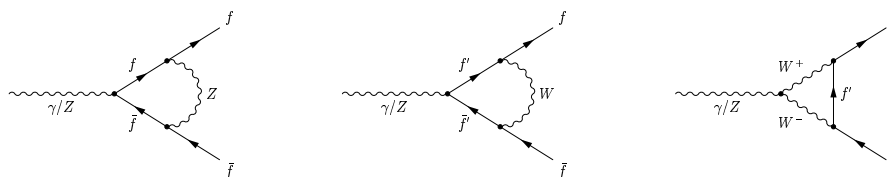


Figure 2.4: Examples of the diagrams contributing to the vertex-type electroweak corrections.

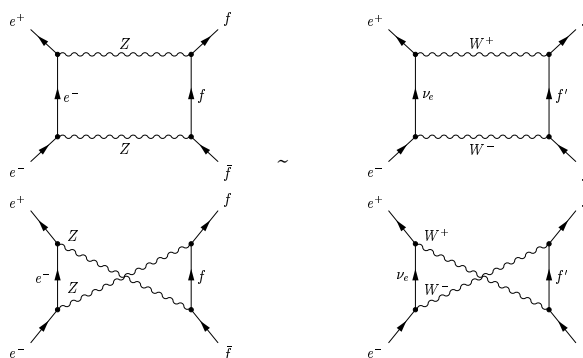


Figure 2.5: Examples of diagrams contributing to the box-type electroweak corrections.

Photonic Corrections

When the final-state fermion is a charged particle, there are both vertex-type and box-type photonic corrections as shown in Fig. 2.6.

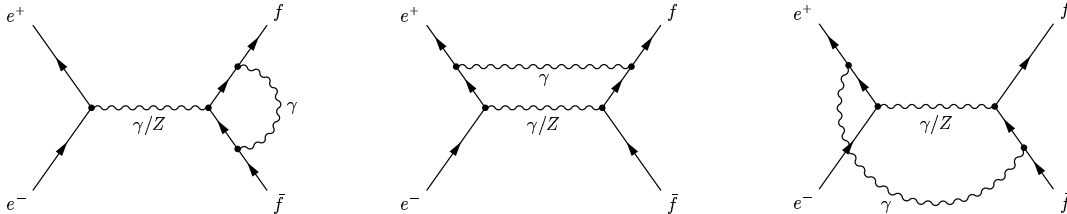


Figure 2.6: Examples of diagrams contributing to the photonic corrections.

There are also other types of photonic corrections, initial state radiation (ISR) and final state radiation (FSR), as shown in Fig. 2.7.

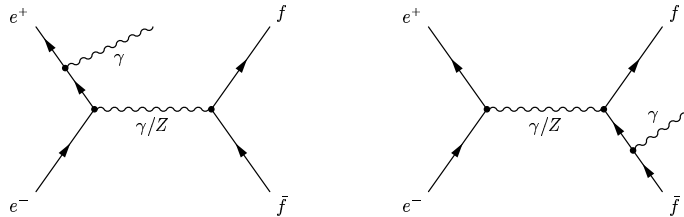


Figure 2.7: Examples of initial state radiation and final state radiation.

The effective center-of-mass energy, $\sqrt{s'}$, is defined as the invariant mass of the propagator. The ISR reduce the s' from s and boost the γ/Z against the photons corresponding to the ISR, which changes the kinematics and makes the $|A_{\text{FB}}|$ smaller.

There is another effect due to the ISR and FSR as follows. Both the ISR and FSR processes can be written as $e^+e^- \rightarrow f\bar{f} + n\gamma$ and are in principle indistinguishable in the final state. Hence the two processes interfere. Since this ISR-FSR interference (IFI) makes the definition of the s' invalid, the IFI should be neglected. The effect in neglecting the ISR-FSR interference can be evaluated with some programs such as ZFITTER or KK2f [45] and is found to be less than 2% with a cut of $\sqrt{s'/s} > 0.85$ for the \sqrt{s} above the Z resonance.

Final State QCD Corrections

Hard gluon emissions off final state quarks as shown in Fig. 2.8 distort the kinematics.

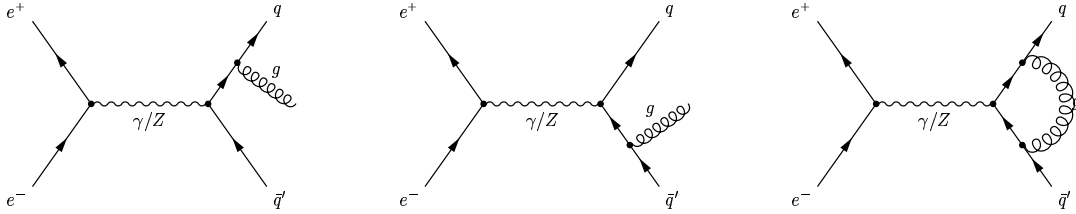


Figure 2.8: Examples of diagrams contributing to the QCD corrections.

Such QCD effect to the $A_{\text{FB}}^{b,c}$ have been calculated to second order of the strong coupling constant (α_s) in [46]. As to the first-order correction of α_s , corrected asymmetry ($A_{\text{FB}}^{\text{QCD}}$) can be written with uncorrected asymmetry ($A_{\text{FB}}^{\text{noQCD}}$) as,

$$A_{\text{FB}}^{\text{QCD}} = A_{\text{FB}}^{\text{noQCD}} \left(1 - \frac{\alpha_s}{\pi} \right), \quad (2.12)$$

where the b and c quark mass is neglected. According to [47], the second-order correction in [46] and the effect of the non-zero quark mass are considered and the decreases of the A_{FB} due to the QCD correction are evaluated as $3.30 \pm 0.37\%$ and $4.18 \pm 0.69\%$ for b and c quarks respectively. The ZFITTER can also treat the QCD correction, which gives similar results at the Z resonance and small \sqrt{s} dependence of the corrections at \sqrt{s} above the Z resonance. Such QCD corrections of about 3% for b quarks and approximately 4% for c quarks are used in this thesis.

2.3 Fragmentation

The process of quark-antiquark pair production, $e^+e^- \rightarrow q\bar{q}$, is described by the electroweak theory as seen in the previous section. A process which transforms quark-antiquark pair into colorless hadrons have to be followed due to the color-confinement nature of the QCD. This process is termed “fragmentation”. In the A_{FB} measurement, the direction of primary quarks are evaluated with the final state particles in the detector after the fragmentation process. Hence the fragmentation process is important. The fragmentation process can be broken down into 3 phases, a perturbative QCD phase, a hadronization phase and a decay phase, as shown in Fig. 2.9.

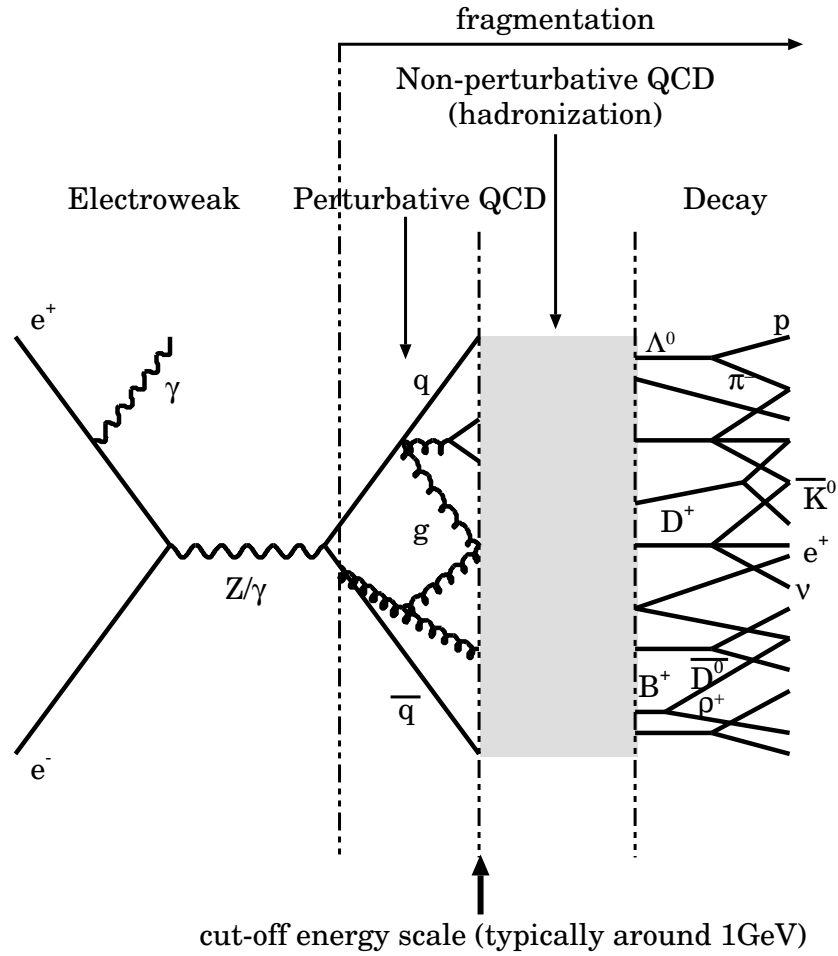


Figure 2.9: The process of quark-antiquark pair production, $e^+e^- \rightarrow q\bar{q}$ and the subsequent fragmentation process.

1. Perturbative QCD phase

The radiation of a gluon from a quark and subsequent conversion of gluon to further quark-antiquark pair or gluon pair occur. This multiplicative process is called as “parton shower”, which can be calculable with the perturbative QCD while the energy scale of such partons are high enough.

2. Hadronization phase

During the later stage of the cascade, the energy scale of the partons becomes sufficiently small (and α_s becomes sufficiently large) and the perturbative QCD calculation becomes invalid. The cut-off energy scale is typically around 1 GeV. The remaining shower evolution and subsequent formation of colorless hadrons have to be simulated with some phenomenological models. This non-perturbative process is termed “hadronization”. At LEP, due to the high center-of-mass energy, many

hadrons are produced along an orientation of the momentum vector of the initial quark, which is called a “jet”.

3. Decay phase

Unstable hadrons decay into stabler hadrons and they can be observed by detectors.

2.3.1 Perturbative QCD Phase

There are two methods to simulate the perturbative process. One is the matrix-element method, in which Feynman diagrams are calculated, order by order. Although this is a correct approach in principle, the applicability is limited by a large difficulty in higher-order calculations which are important to keep the accuracy. The second is the parton-shower method, where multi-parton processes are treated as series of a branching of one parton into two, such as $q \rightarrow qg$, $g \rightarrow gg$ and $g \rightarrow q\bar{q}$. The calculations of the probabilities of these branchings are usually performed in the leading logarithm approximation (LLA), where only the leading terms in the perturbative expansions are kept. This method is employed in the event generator, PYTHIA [48], which was used to simulate the fragmentation process of Monte-Carlo events used in this analysis.

2.3.2 Hadronization Phase

At small energy scale where perturbative calculations are not valid, phenomenological models are used to simulate the hadronization process. Among some models, the string fragmentation model is used in the PYTHIA.

String Fragmentation

The string fragmentation [49] is based on the idea that oppositely colored quark and antiquark are confined by a potential energy due to the color field between them. The potential energy linearly rises as a distance between the pair increases. When such quarks, q and \bar{q} , move apart, the color field between them can be viewed as a narrow flux tube of uniform energy density, which is stretched like a string between the partons. As the quarks move further apart, the potential energy of the string rises linearly with the distance until the string finally breaks up in a new $q'\bar{q}'$ pair. Thus, two new colorless systems $q\bar{q}'$ and $q'\bar{q}$ are formed. As long as the invariant mass of the produced strings is large enough, further splittings may occur and generate further $q''\bar{q}''$ pairs. Finally, each colorless quark-antiquark pair forms a hadron.

The mechanism of such new $q'\bar{q}'$ generation can be interpreted as quantum mechanical tunneling. Such view implies a suppression of heavy-quark production. In the PYTHIA, the ratio of the new $q'\bar{q}'$ generation rate for u, d, s and c quarks are set as $1 : 1 : 0.3 : 10^{-11}$. The tunneling mechanism can also be used to explain the production of baryons.

Furthermore, a flavor-independent Gaussian spectrum for the transverse momentum (p_t) of $q\bar{q}'$ pair is naturally introduced with the view. Since the string is assumed to have no transverse excitations, this p_t is locally compensated between the q' and \bar{q}' .

On the other hand, the sharing of the longitudinal momentum is given by some arbitrary probability distribution $f(z)$, where z is the fraction of the sum of energy (E) and longitudinal momentum (p_{\parallel}) taken by the newly generated hadron ($q\bar{q}'$) from original quark (q). For the adjacent quarks, \bar{q}'' and q'' , the same procedure is repeated in terms of the longitudinal momentum of q' . Then the z can be written as

$$(E + p_{\parallel})_{q\bar{q}'} = z \cdot (E + p_{\parallel})_q. \quad (2.13)$$

Such function, $f(z)$, is called as ‘‘fragmentation function’’. Among several fragmentation functions proposed, ‘‘Lund symmetric function’’ and ‘‘Peterson function’’ are frequently used. Further descriptions are given about the two functions, which was used in the PYTHIA to simulate the fragmentation process of the Monte-Carlo events in this thesis.

- Lund symmetric function

If the equivalence in the choice of the starting the iterative procedure from the quark end (q) or antiquark end (\bar{q}) is assumed, the shape of the fragmentation function is essentially fixed as,

$$f(z) \propto \frac{1}{z} z^{a\alpha} \left(\frac{1-z}{z} \right)^{a\beta} \exp\left(-\frac{bm_t^2}{z}\right), \quad (2.14)$$

where m_t^2 is a transverse mass ($m^2 + p_t^2$) of the quark whose mass is m . There are two kinds of parameters, a and b . The parameter a is flavor dependent, which is indicated with the index α corresponding to the ‘old’ flavor in the iteration process, and β to the ‘new’ flavor. Usually, the function is simplified by neglecting the flavor dependence of a as,

$$f(z) \propto z^{-1}(1-z)^a \exp(-bm_t^2/z). \quad (2.15)$$

- Peterson function

Charm and bottom data clearly indicate the need for a harder fragmentation function for heavy flavors. The best known of these is the Peterson/SLAC formula [50]

$$f(z) \propto \frac{1}{z \left(1 - \frac{1}{z} - \frac{\epsilon_Q}{1-z}\right)^2}, \quad (2.16)$$

where ϵ_Q is a free parameter, expected to scale between flavors like $\epsilon_Q \propto 1/m_Q^2$.

The examples of the fragmentation functions are shown in Fig. 2.10.

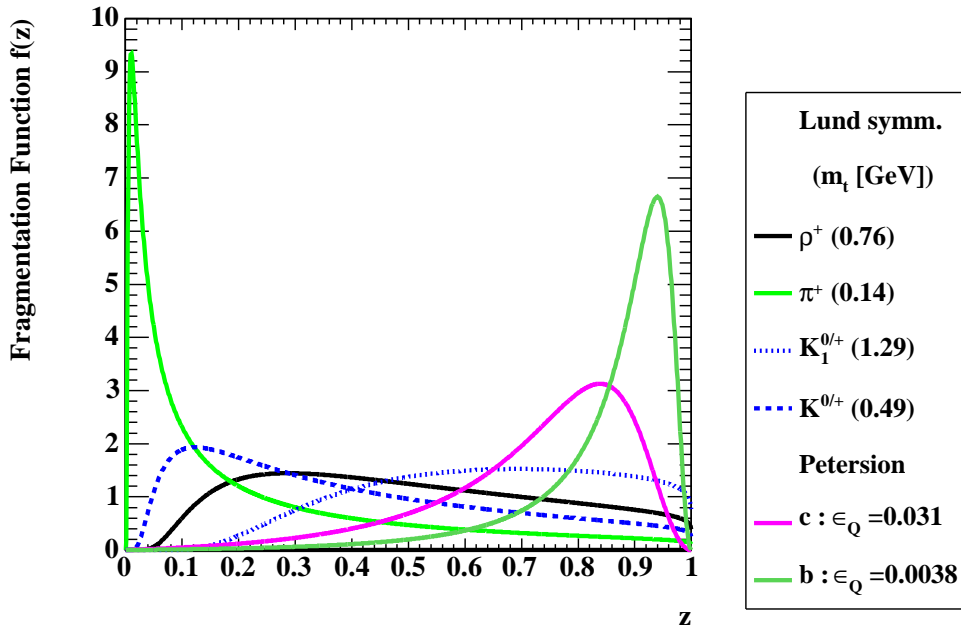


Figure 2.10: Examples of fragmentation functions. The m_t^2 in the Lund symmetric function is set to m^2 .

In another aspect of the string fragmentation, the gluon is treated as a kink on the string, carrying energy and momentum. For a $q\bar{q}g$ event, a string is stretched from the q end via the g to the \bar{q} .

2.4 Neutral B meson mixing

The neutral B meson mixing ($B^0 - \bar{B}^0$ mixing) contributes to the A_{FB} measurement diluting the charge identification, since the $B^0 - \bar{B}^0$ mixing inverts the relation between the charge of the primary quark and the charges of the final state particles. The $B^0 - \bar{B}^0$ mixing is predicted in the electroweak theory via box diagrams as shown in Fig. 2.11, where the neutral B meson is represented as B_q^0 ($q = d, s$).

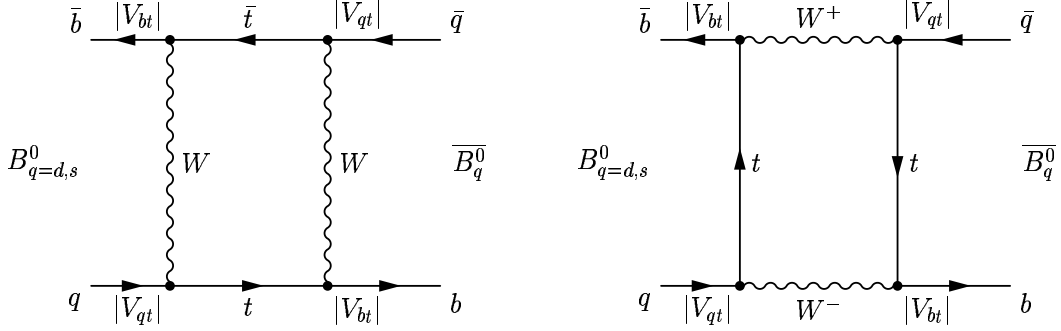


Figure 2.11: Main diagrams causing $B^0 - \bar{B}^0$ mixing.

The mass eigenstates are different from the flavor eigenstates, $|B_q^0\rangle$ and $|\bar{B}_q^0\rangle$. There are a mass difference (Δm_q) and a total decay width difference ($\Delta\Gamma_q$) between the two mass eigenstates. The time-dependent probability in which the $|B_q^0\rangle$ remains unchanged is termed $P_q^+(t)$ and the probability in which the $|B_q^0\rangle$ changes to $|\bar{B}_q^0\rangle$ is termed $P_q^-(t)$. If the CP violation is neglected, the $P_q^+(t)$ and $P_q^-(t)$ can be written with the mean of the total decay width, $\bar{\Gamma}_q$, as

$$P_q^\pm(t) = \frac{1}{2} \exp(-\bar{\Gamma}_q t) \left[\cosh\left(\frac{\Delta\Gamma_q t}{2}\right) \pm \cos(\Delta m_q t) \right]. \quad (2.17)$$

Since $\Delta\Gamma_q$ is negligible compared to $\bar{\Gamma}_q$, the above equation can be written as

$$P_q^\pm(t) \approx \frac{1}{2} \exp(-\bar{\Gamma}_q t) [1 \pm \cos(\Delta m_q t)], \quad (2.18)$$

where the contributions of both the decay and the mixing are clearly seen. The time-integrated mixing probability (mixing parameter), χ_q , is defined as,

$$\chi_q \equiv \frac{\int_0^\infty P_q^-(t) dt}{\int_0^\infty P_q^+(t) dt + \int_0^\infty P_q^-(t) dt}. \quad (2.19)$$

At LEP, since both B_d^0 and B_s^0 can be generated, the average mixing parameter, $\bar{\chi}$, is used. It is defined as,

$$\bar{\chi} \equiv f'_d \chi_d + f'_s \chi_s, \quad (2.20)$$

where f'_d and f'_s are the fractions of B_d^0 and B_s^0 respectively in a sample of semileptonic b-hadron decays. The $\bar{\chi}$ was measured to be 0.1257 ± 0.0042 [51]. The similar value is used in the Monte Carlo samples and the above-mentioned value is used to evaluate systematic uncertainty from the $B^0 - \bar{B}^0$ mixing.

Chapter 3

Experimental Apparatus

Descriptions about LEP Collider and the OPAL detector are given in this chapter. The events generated in the e^+e^- collisions in the LEP Collider were recored with the OPAL detector.

3.1 The LEP Collider

The Large Electron-Positron collider (LEP) [52, 53] at CERN (the European Laboratory for Particle Physics) was an e^+e^- storage ring with a circumference of approximately 27 km. The ring was built between 50 and 175 m below the surface. Electrons and positrons collided at four places in the ring, where large detectors, ALEPH, DELPHI, L3 and OPAL were located. The first beam at the LEP was injected in 1989 and the LEP was terminated in 2000.

The LEP was operated at $\sqrt{s} \approx m_Z \approx 91\text{GeV}$ until 1995 (LEP I phase). In the latter part of 1995, the energy was raised to 130 GeV (LEP 1.5 phase). Then the center-of-mass energy was raised beyond 130 GeV and reached to a little under 209 GeV in the year 2000 (LEP II phase). The integrated luminosities versus the number of weeks between 1991 and 2000 are shown in Fig. 3.1.

Electrons and positrons were accelerated through the injector chains and LEP ring step by step. The injector chains and the LEP accelerator are shown in Fig. 3.2.

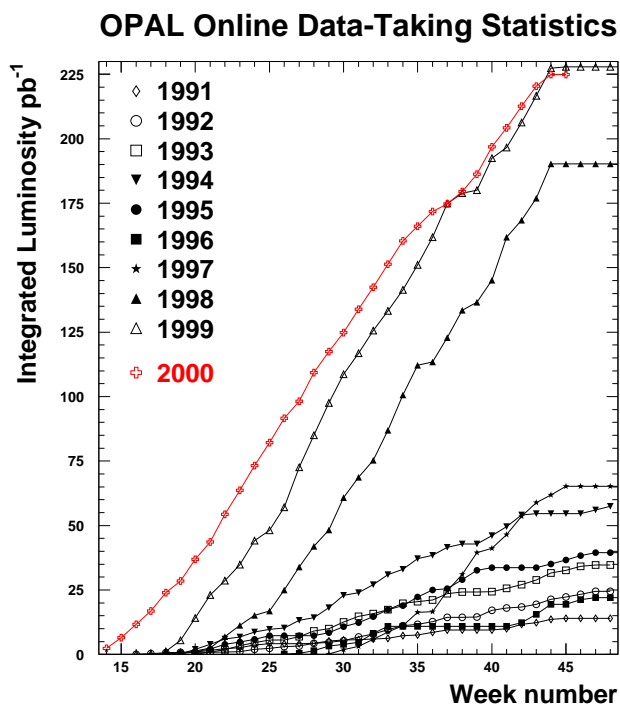


Figure 3.1: The LEP integrated luminosity

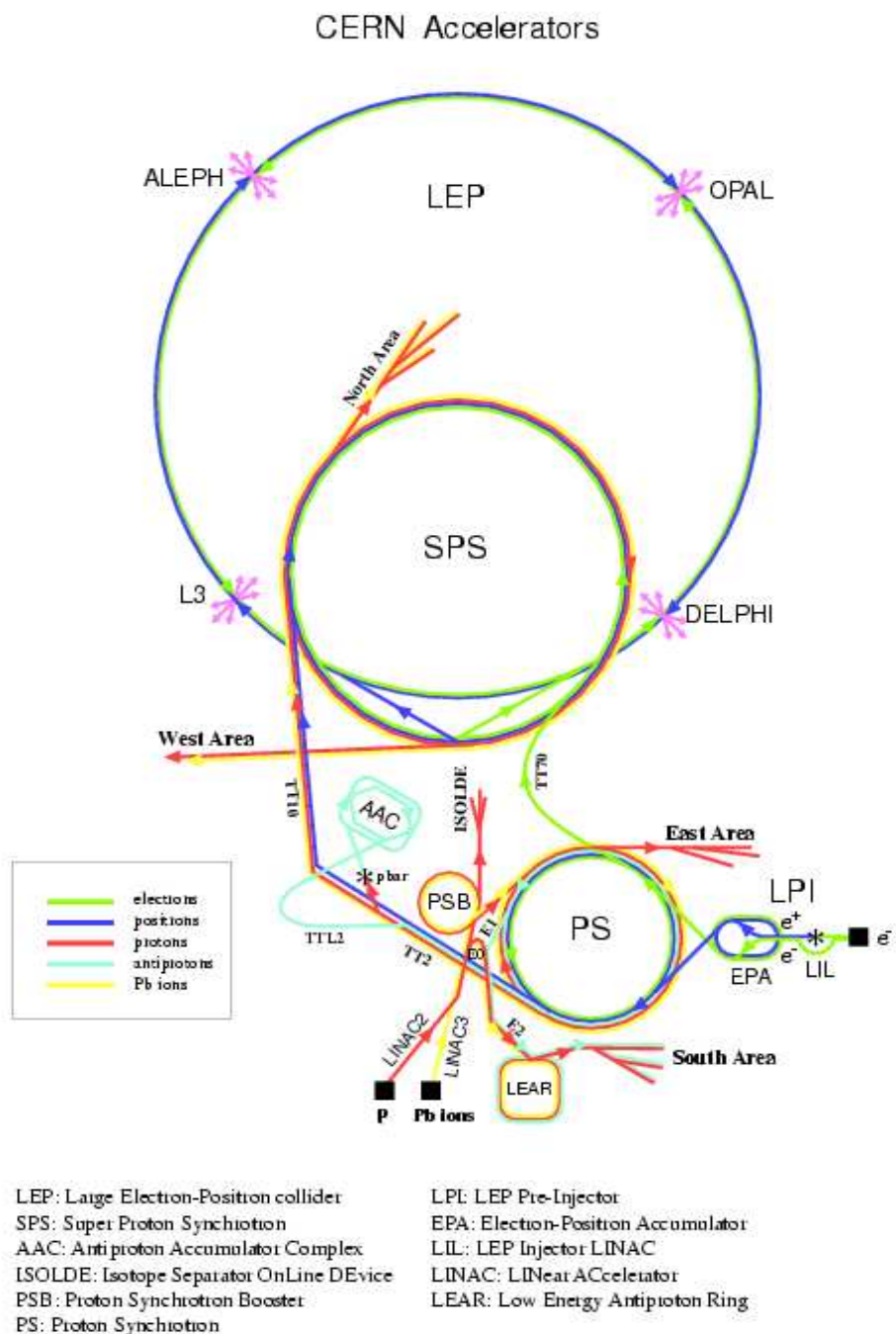


Figure 3.2: The LEP accelerator complex.

3.1.1 Injector chain

Electrons were produced by thermionic emission from a heated filament. Their energies were raised to 200 MeV in passing through the LEP Injector LINAC (LIL). Some of these electrons were directed at a tungsten target and electron-positron pair production was followed. These pairs were separated magnetically, and then accelerated further by the LIL to 600 MeV. They were transferred to the Electron-Positron Accumulator (EPA), a small storage ring, 126 m in circumference. They were accumulated in the ring and were transferred to the Proton Synchrotron (PS), 630 m in circumference. They were accelerated to 3.5 GeV there, then transferred to the Super Proton Synchrotron (SPS), 6.9 km in circumference and accelerated to about 22 GeV. At this stage, the beams were ready for injection into LEP.

3.1.2 LEP Accelerator

The LEP ring comprised eight curved sections (octants) equipped with bending magnets and eight straight sections. The acceleration of the beams was performed in the straight sections and radio-frequency (RF) cavities were used to accelerate the beams. The beams collide at interaction points situated at the center of four of these eight straight sections, where four large detector apparatus, ALEPH [52], DELPHI [54], L3 [55] and OPAL [56], were located. On either side of each experiment, strong superconducting quadrupole were employed to reduce the transverse beam dimensions at the interaction points to about $5\mu\text{m}$ and $200\mu\text{m}$ in the vertical and horizontal planes respectively.

The bending of the beams in curved sections caused energy losses of the beams due to synchrotron radiation. Additional accelerations with the RF cavities were performed in order to compensate for the energy losses. As for the beam with the energy E_b , the energy loss, δE_b , due to synchrotron radiation per each revolution is given as,

$$\delta E_b = \frac{4\pi e^2 \beta^3 \gamma^4}{3R}, \quad (3.1)$$

where β is the speed of the beams divided by the speed of light, γ is $E_b/m_e c^2$ (m_e is the electron mass) and R is the radius of the curved path.

Four bunches of electrons were made to circulate anti-clockwise, and four bunches of positrons clockwise, around the LEP ring. The collisions were occurred at each experimental site every $22 \mu\text{s}$.

3.2 The OPAL detector

The OPAL(Omni-Purpose Apparatus for LEP) detector [56] was located at the LEP at CERN. It was a multipurpose apparatus designed to study all types of events occurring in e^+e^- collisions, which enables accurate event reconstructions over an acceptance of nearly full solid angle. The OPAL detector is shown in Fig. 3.3 with its coordinate system¹.

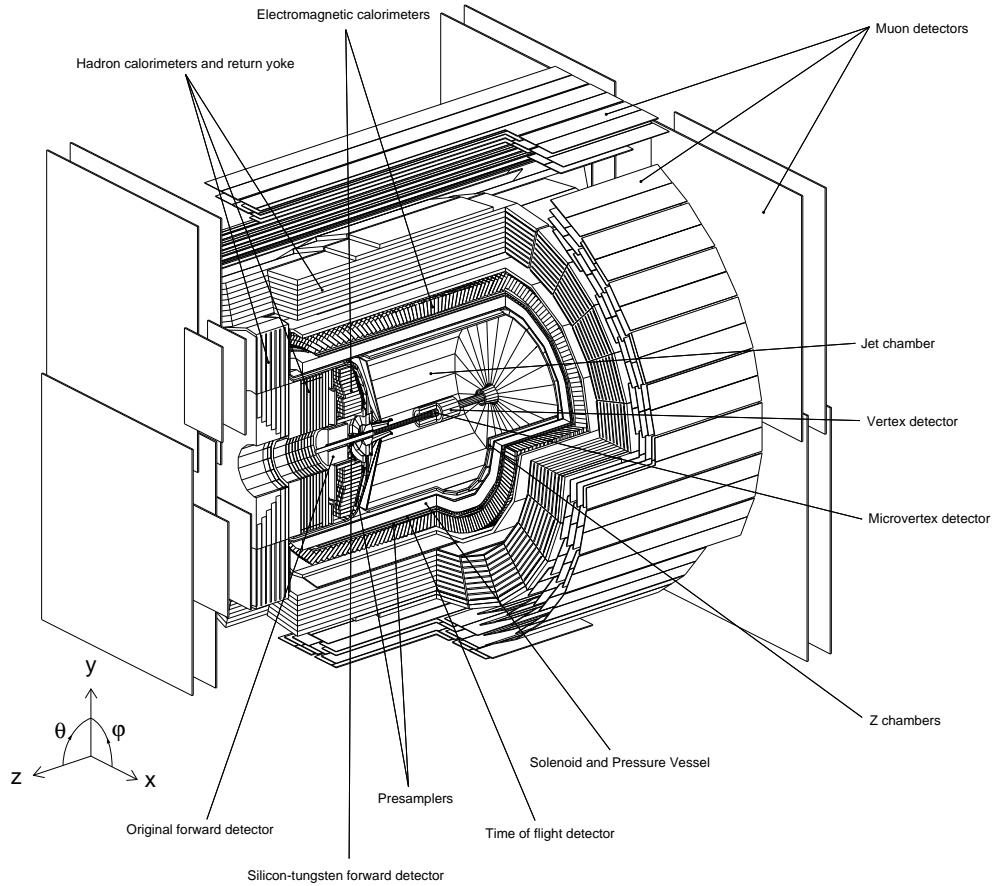


Figure 3.3: The OPAL detector.

The OPAL detector consisted of a central tracking system, a time-of-flight detector, electromagnetic calorimeters, hadron calorimeters, muon detectors and forward detectors, as shown in Fig. 3.3 and Fig. 3.4. The solid angles for these detector elements are shown in Table. 3.1. In the following sections these detector elements and their trigger system are briefly described.

¹The OPAL employs a right-handed coordinate system in which the z axis is along the electron beam direction and the x axis points toward the center of LEP. The polar angle, θ , is measured from the z axis, and the azimuthal angle, ϕ , is measured from the x axis around the z axis. The origin of the coordinate system is set at the nominal interaction point.

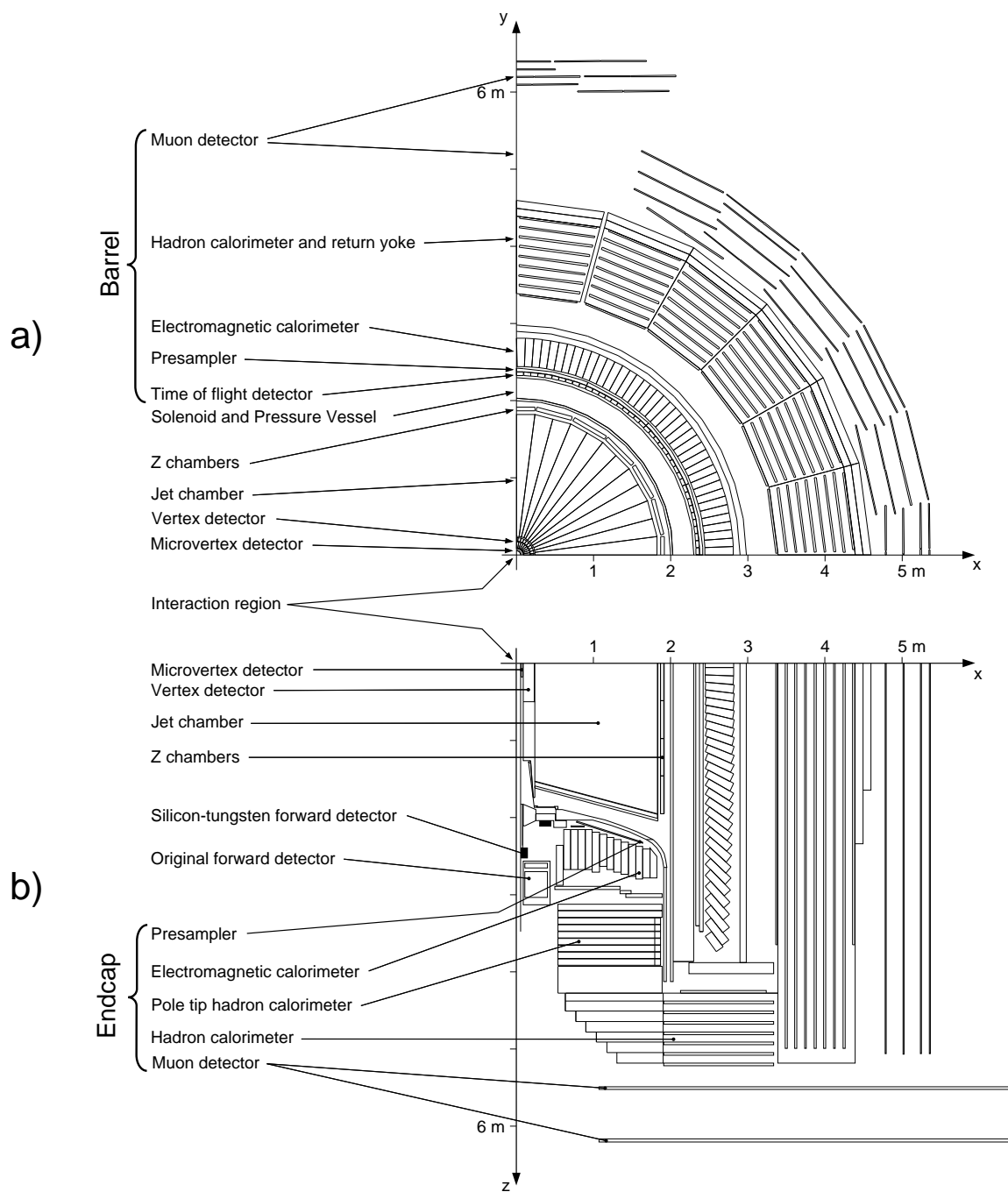


Figure 3.4: The quarter of the OPAL detector in (a) the front and (b) top views.

Table 3.1: Angular coverage of the OPAL subdetectors.

Subdetector	Coverage	
	Polar angle	Solid angle
Central tracking system		
Silicon microvertex detector	$ \cos \theta < 0.89$	86%
Vertex chamber	$ \cos \theta < 0.95$	86%
Jet chamber	$ \cos \theta < 0.98$	98%
z-chambers	$ \cos \theta < 0.72$	67%
Electromagnetic calorimeters		
Barrel electromagnetic presampler	$ \cos \theta < 0.81$	98%
Endcap electromagnetic presampler	$0.83 < \cos \theta < 0.81$	
Barrel electromagnetic calorimeter	$ \cos \theta < 0.82$	
Endcap electromagnetic calorimeter	$0.81 < \cos \theta < 0.98$	
Hadronic calorimeters		
Barrel hadron calorimeter	$ \cos \theta < 0.81$	97%
Endcap hadronic calorimeter	$0.81 < \cos \theta < 0.91$	
Pole-tip hadronic calorimeter	$0.91 < \cos \theta < 0.99$	
Muon detectors		
Barrel muon detector	$ \cos \theta < 0.72$	93%
Endcap muon detector	$0.67 < \cos \theta < 0.98$	

3.2.1 Central Tracking System

Toward outward from the beam pipe, the central tracking system consisted of the silicon microvertex detector and a series of drift chambers : the vertex chamber, the jet chamber and the z-chambers. These drift chambers were placed inside a pressure vessel whose inner pressure was kept at 4 bar by filling gas mixture of 88% argon, 9.4% methane and 2.6% iso-butane. On the outside of the pressure vessel, a solenoid was mounted, providing a uniform magnetic field of 0.435T along z axis throughout the central tracking system.

The main purpose of the tracking system was the reconstruction of the charged tracks. Since the charged particle was bended in the r - ϕ plane in the magnetic field, B , the radius of the curvature of the charged track, ρ , was connected with its momentum component perpendicular to the z axis, p_{\perp} , as

$$p_{\perp}[\text{GeV}/c] = 0.3 B[\text{T}] \rho[\text{m}]. \quad (3.2)$$

Silicon Microvertex Detector(SI)

The silicon microvertex detector (SI) [57] was positioned between the beam pipe, of outer radius 5.65 cm, and the pressure vessel, of inner radius 8.0 cm. It consisted of two layers of silicon wafer modules ('ladders'), placed at radii of 6 and 7.5 cm, respectively. An overall length of them were about 30 cm. The inner and outer layers consisted of 12 and 15 ladders respectively and ladders were tilted not to make ϕ gaps. as shown in Fig. 3.5.

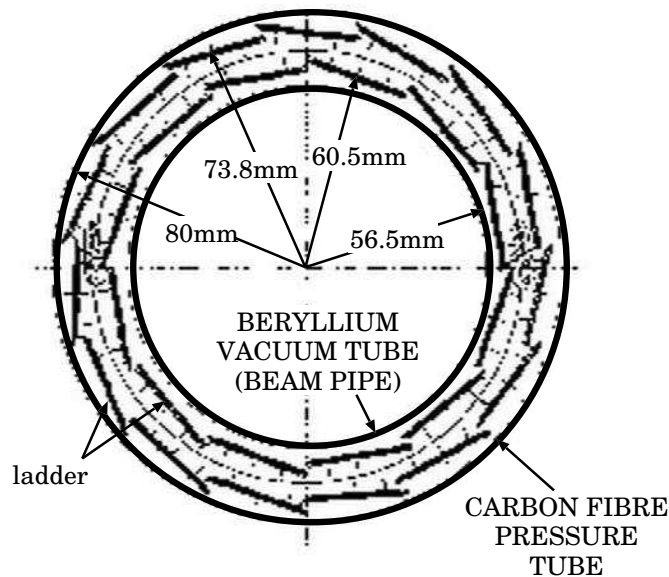


Figure 3.5: Silicon Microvertex Detector

Each layer consisted of two types of single sided silicon wafers were used. One was termed ϕ wafer with $25\ \mu$ pitch strips along the beam axis and the other was termed z wafer with $25\ \mu$ pitch strips along ϕ direction. The readout strip pitch was $50\ \mu\text{m}$ for the ϕ wafer and $100\ \mu$ for the z wafer. The two kinds of wafers were glued together.

The overall resolution of about $10\ \mu\text{m}$ in the r - ϕ plane and about $15\ \mu\text{m}$ in the z direction. The SI played a significant role in reconstructing secondary vertexes, which were distinct for the particles with long lifetime which enable them to travel several millimeters before decaying. The use of SI is essential in the b-tagging, since such long-lived particles were typically B mesons.

Vertex Chamber (CV)

The vertex detector (CV) was a high precision cylindrical jet drift chamber. It was 100 cm long with covered radii between 8.8 cm and 23.5 cm, outside the SI. The CV consisted of an inner and outer layers as shown in Fig. 3.6.

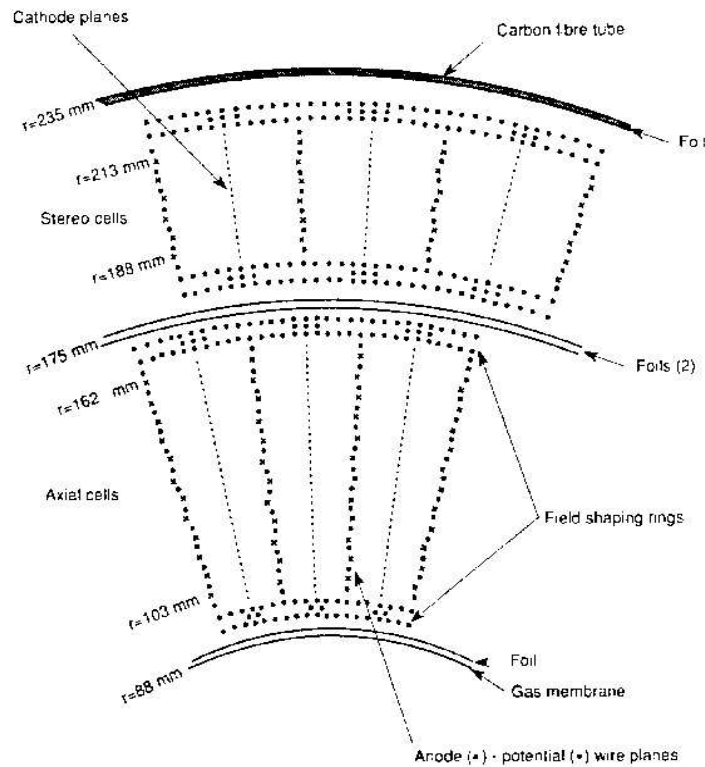


Figure 3.6: Vertex Chamber.

Each layer was divided into 36 azimuthal sectors. Each sector in the inner layer had 12 ‘axial’ sense wires running parallel to the beam direction. Each sector in the outer layer had 6 ‘stereo’ sense wires inclined at an angle of 4° to the z axis. Precise measurements of the drift times on the sense wires enabled the track positions to be determined in r - ϕ to within $50 \mu\text{m}$, and in z to within $700 \mu\text{m}$.

Tracks measured in the CV provided important links between those reconstructed in SI closest to the interaction point, and those reconstructed in the jet chamber outside the CV.

Jet Chamber (CJ)

The jet chamber (CJ) was a cylindrical jet drift chamber of length 400 cm, with an outer radius of 185cm and inner radius of 25cm, placed outside the CV. It covered 98% of the solid angle and provided good spatial and double track resolution and particle identification.

All wires used in the CJ were parallel to the beam direction. The CJ was subdivided into 24 azimuthal sectors and each sector had 159 anode sense wires equally spaced by 10 mm, alternating with potential wires. The anode wires were slightly staggered with respect to the potential plane to resolve left-right ambiguities. Cathode wire planes formed the boundaries between adjacent sectors.

The coordinates of wire hits in the r - ϕ plane were determined from a measurement of drift time. The z coordinate was measured using a charge division technique at wire ends. The resolution achieved was at the level of $135 \mu\text{m}$ in the r - ϕ plane and 6 cm in the z direction. Its good space and double track resolution were essential for the efficient recording of jet-like events. The CJ provided the most detailed information on the curvature of charged tracks, and hence their momentum and charge.

A further purpose of CJ was to provide a measurement of the ionization energy loss per unit length (referred to as “ dE/dx ”), of charged particles traversing the gaseous volume of the chamber. The measurement of dE/dx was derived from the charge collected at each hits along the track trajectory. For a given charged particle, its mass could be calculated with the information of dE/dx and the track momentum, p . Hence, the particle identification was enabled as shown in Fig. 3.7, where the hadronic tracks and muon pairs with at least 130 hits used for the dE/dx calculation. A good dE/dx resolution of 2.8% was obtained for the muon-pairs with 159 hits used for the dE/dx calculation.

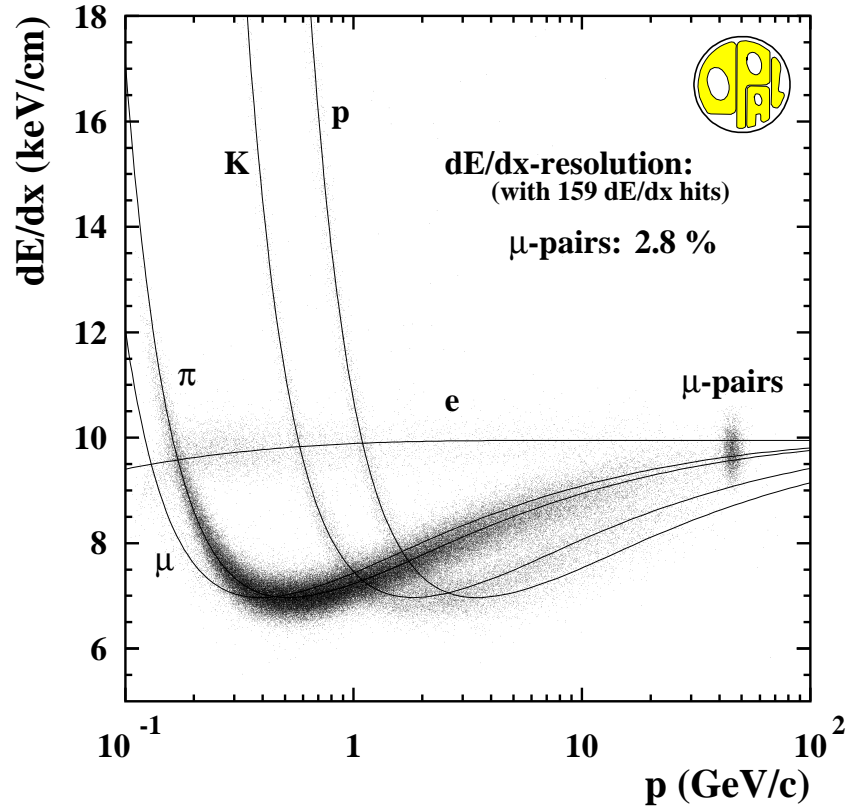


Figure 3.7: Distribution of measured and predicted dE/dx for hadronic tracks and muon pairs as a function of the momentum (p). The dE/dx resolution for the muon-pairs with 159 hits used for the dE/dx calculation was 2.8%.

Z chambers (CZ)

The z-chambers (CZ) were placed around the barrel region of CJ inside the pressure vessel which also contains CV and CJ. The CZ provided a precise measurement of the z coordinates of tracks emerging from the CJ. It was a planar drift chamber, 400 cm long, 50 cm wide and 5.9 cm thick. The CJ was surrounded by 24 z-chambers. Each of them was divided in z to 8 cells with 6 sense wires which ran perpendicular to the z axis. The time during the drift in the z direction was used to measure the z coordinates of the hits.

Solenoid Coil

The solenoid coil was self-supporting, water-cooled aluminum coil which was mounted around the pressure vessel. The solenoid coil generated the 0.435 T magnetic field, uniform to within 0.5% throughout the volume of the central tracking system. It was designed to be as thin as possible (actually about 96 mm of aluminum and 54 mm glass-epoxy), in order to minimize material in front of the calorimeters. The iron of the hadronic calorimeter served as a return yoke for the magnetic field.

3.2.2 Time-of-Flight System (TOF)

The time-of-flight system (TOF) was a scintillator array just outside the solenoid coil for the barrel region or outside the pressure vessel for the endcap region. It provided charged particle identification in the energy range from 0.6 to 2.5 GeV and fast triggering information. It also provided an effective rejection of both cosmic rays and the events from interactions between the beams and residual gas inside the beam pipe or the beam pipe itself.

Barrel Time-of-Flight detector (TB)

The barrel time-of-flight detector (TB) consisted of a cylindrical layer of 160 scintillators, 45 mm thick, 80-91 mm wide and 6.84 m long, placed as its external radius was 2.4 m, surrounding the solenoid coil. It achieved a timing resolution of about 460 ps.

Tile Endcap Detector (TE)

The tile endcap detector (TE) complemented the TB by providing timing information from the forward region. It consisted of 120 tiles containing a 10 mm thick scintillator layer and was mounted between the endcap presamplers and the endcap electromagnetic calorimeter. These were read out by wavelength-shifting fibers connected to photomultiplier tubes.

3.2.3 Electromagnetic Calorimeters

The OPAL electromagnetic calorimeter (ECAL) was designed to absorb and measure the energy of electrons, positrons and photons with energies in excess of about 100 MeV. The ECAL system consisted of main calorimeters and presampler chambers placed in front of the main calorimeters. The main calorimeters were a barrel array (EB) and endcap arrays (EE) of lead glass blocks, each with a cross-section of approximately $10 \times 10\text{cm}^2$. The EB had a depth of 24.6 radiation length (X_0) and each EE had a depth of $20 X_0$. Together with a forward lead scintillator calorimeter described in the subsection 3.2.6, ECAL covered approximately 99% of the solid angle.

Since there was about $2 X_0$ of material ahead of the main calorimeters mainly due to the pressure vessel and the solenoidal coil, the cascade shower could start before the lead glass. Presampler chambers were therefore installed in front of the main calorimeter to recover the degradation of position and energy resolution caused by the shower initiation ahead of the main calorimeters. They also gave additional γ/π^0 and electron/hadron discrimination.

Barrel and Endcap Electromagnetic Presamplers (PB & PE)

The barrel electromagnetic presampler (PB) consisted of 16 chambers forming a cylinder of radius 239 cm and length 662 cm, placed just outside the TB, covering $|\cos\theta| < 0.81$. Each chamber consisted of two layers of limited streamer tubes with the anode wires running parallel to the beam direction. On either side of the tubes were cathode strips oriented at 45° to the wire direction. Spatial positions were measured with the strips and wires. The energy deposited in front of the presampler was evaluated with hit multiplicities of the presamplers.

The endcap electromagnetic presampler (PE) was made up of 32 multiwire proportional chambers and was located between the pressure vessel and the endcap calorimeter, covering the region $0.83 < |\cos\theta| < 0.95$.

The PB and PE got spatial resolutions of about 5 mm. They assisted both in the spatial and energy resolution of the calorimetry system as a whole.

Barrel and Endcap Electromagnetic Calorimeters (EB & EE)

The barrel lead glass calorimeter consisted of a cylindrical array of 9440 lead glass blocks at a radius of 246 cm covering the range $|\cos\theta| < 0.82$. The detection efficiency was optimized by aligning the longitudinal axis of the lead glass blocks to point almost toward the interaction region. The slight offset prevented the loss of the particles through the gaps between the blocks. The Čerenkov lights produced by the relativistic charged particles passing through the lead glasses were collected by photomultipliers placed at the base of each block. The intrinsic energy resolution for the EB was

$$\frac{\delta E}{E} \approx 0.2\% + \frac{6.3\%}{\sqrt{E[\text{GeV}]}}. \quad (3.3)$$

The endcap electromagnetic calorimeter (EE) consisted of two umbrella shaped arrays, each of which had 1132 lead glass blocks aligned coaxially around the beam pipe. The Čerenkov lights were collected by vacuum photo triodes attached at the back of blocks. The intrinsic energy resolution for the EE at low energies was

$$\frac{\delta E}{E} \approx \frac{5\%}{\sqrt{E[\text{GeV}]}}. \quad (3.4)$$

Gamma Catcher (FE)

The gamma catcher was intended to complement the lead glass calorimeters by filling the gap between the inner edge of EE and the outer edge of the forward detectors described in the subsection 3.2.6. It was a ring of lead-scintillator sandwich modules with $7X_0$ thick. The signals were transported to silicon photodiodes through wavelength shifters readouts.

Minimum ionizing particle (MIP) plug

The MIP plug was designed to provide good time resolution and detection efficiency for single minimum ionizing particles, such as muons, in the forward regions of OPAL. It comprised four layers of 1 cm thick scintillator tiles, covering the $|\cos\theta|$ between 43 and 220 mrad. The first two layers were positioned behind FE, the third, behind these and at a shallower angle, and the fourth between the forward detector and the silicon-tungsten luminometer described in the subsection 3.2.6.

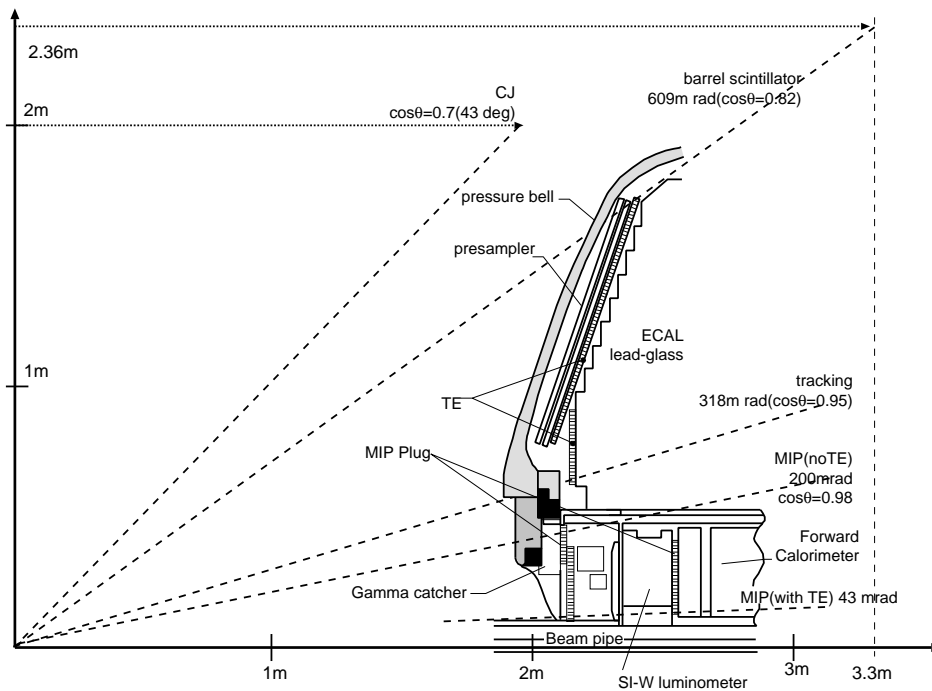


Figure 3.8: The forward region of OPAL detector..

3.2.4 Hadron Calorimeters

The hadron calorimeters (HCAL) were designed to measure the energies and positions of hadrons, which could form hadronic showers due to the cascade process of the inelastic nuclear collisions. The scale of the longitudinal development of the hadronic showers is characterized by the (λ_I) .

The hadron calorimeter was composed of three sections, the barrel (HB), the endcaps (HE) and the pole-tips (HP). They covered 97% of the solid angle. These detectors were positioned between alternate layers of the iron return yoke of the magnet, to form sampling calorimeters about 1 m thick. The total thickness of the iron yoke was about 4 ‘nuclear interaction length’ (λ_I) . Essentially all hadrons are absorbed at this stage leaving only muons to pass on into the surrounding muon chambers. Since there was a high probability

of the hadronic showers being initiated in the $2.2 \lambda_I$ of material before the HCAL, the overall hadronic energy had to be determined with the information from both the ECAL and HCAL together.

Barrel and Endcap Hadron Calorimeters (HB & HE)

The barrel (HB) and endcap (HE) hadron calorimeters had the same structure, alternating layers of iron slabs and limited streamer tubes. The barrel region (HB) contained 9 layers of 2.5 cm thick chambers alternating with 8 layers of 10 cm thick iron. The HB was placed at radii from 3.39 m to 4.39 m, covering the angular region $|\cos \theta| < 0.81$.

The HE consisted of 8 layers of chambers of 3.5 cm in thickness alternating with 7 iron slabs of 10 cm in thickness. The HE extended the angular coverage to $|\cos \theta| < 0.91$.

The limited streamer tubes had anode wires with 1 cm spacing in a gas mixture of isobutane(75%) and argon (25%). The signals were read with large pads and strips located on the surfaces of the tubes. The layers of pads were grouped together to form towers that divide up the detector volume into 48 bins in ϕ and 21 bins in θ . They provided an energy resolution as

$$\frac{\delta E}{E} \approx \frac{120\%}{\sqrt{E[\text{GeV}]}}. \quad (3.5)$$

The strips were 0.4cm wide providing the ϕ information of the hits, which were used in muon tracking.

Pole-tip Hadron Calorimeters (HP)

The pole-tip (HP) hadron calorimeter extended the angular coverage down to $|\cos \theta| < 0.99$. The HP consisted of 10 layers of thin multiwire chambers of 7 mm in thickness alternating with 9 layers of 8 cm thick iron. The chambers were operated in high gain mode with a gas mixture of CO₂ (55%) and *n*-pentane (45%). The spacing of the anode wires was 2 mm and the anode-to-cathode gap was 1.6 mm. The signals were read with pads on one side and strips on the other.

3.2.5 Muon Detectors (MU)

Muons were basically the only detectable particles capable of penetrating both the electromagnetic and hadron calorimeters. The muon detectors (MU) were therefore designed to identify these particles unambiguously from other potential background. It was divided into a barrel and two endcap regions, together covering 93% of the solid angle.

Barrel Muon Detector (MB)

The barrel muon detector (MB) covered the angular range $|\cos \theta| < 0.72$. It was composed of 110 large-area drift chambers, 1.2 m in width and 90 mm in depth. Their lengths are

6.0, 8.4 or 10.4 m. They were mounted most outer layer of the OPAL detector surrounding the HB. The MB achieved a spacial resolution of about 1.5 mm in the r - ϕ plane. Diamond-shaped cathode pads determined the z coordinate within an accuracy of about 2 mm.

Endcap Muon Detector (ME)

The endcap muon detector (ME) provided an angular coverage of $0.67 < |\cos \theta| < 0.98$ by means of 2 layers of 4 quadrant chambers and 2 layers of 2 patch chambers. The quadrant chambers were 6 m high and 6 m wide, whereas the patch chambers were 2.5 m high and 3 m wide. Each chamber contained 2 layers of limited streamer tubes. The tubes in one layer were aligned horizontally and those in the other layer were aligned vertically in the plane perpendicular to the beam direction. Each chamber was placed at about ± 5.5 m from the interaction point.

3.2.6 Luminometers

Since the cross-section for the Bhabha scattering process at small angles can be calculated theoretically to high precision, it served as a reference reaction from which the luminosity of the colliding beams was obtained. The luminometers were installed in the region between 25 and 150 mrad to measure the rate of such events.

Forward Detectors (FD)

The two modules of the forward detector (FD) were located at ± 2.6 m from the interaction point, covering angles 40 – 150 mrad from the beam pipe. Each comprised 35 sampling layers of lead-scintillator sandwich, corresponding to about 24 radiation lengths of material. In addition to providing a measurement of the luminosity to a precision of about 0.5%, this detectors also complemented the electromagnetic calorimeter, extending the angular coverage to $|\cos \theta| > 0.98$, which gave an energy resolution of

$$\frac{\delta E}{E} = \frac{17\%}{\sqrt{E[\text{GeV}]}} \quad (3.6)$$

Silicon Tungsten Detector (SW)

The two modules of the silicon-tungsten detector (SW) [58,59] were placed at ± 238.94 cm from the interaction point, covering the angular range between 25 and 58 mrad from the beam. Each had 19 layers of silicon detectors sandwiched between 18 layers of tungsten absorbers. The SW achieved good energy resolution of approximately 4% and position resolution on the radial coordinate of 130-170 μm for electrons and positrons scattered into the detector.

3.2.7 Trigger

Bunch crossing occurred every $22 \mu s$ at LEP. The OPAL trigger system [60] was designed to provide high efficiency for the various physics reactions, and good rejection of backgrounds arising from cosmic rays, from interactions of the beam particles with the gas inside the beam pipe or the wall of the beam pipe, and from the detector noise. The trigger system used fast information from the subdetectors to select crossing with a possible e^+e^- interaction, which enabled the reset of the data acquisition system with no loss of the beam crossing in case of the negative trigger decision. The trigger system reduced the 45 kHz bunch crossing rate to an event rate of about 10Hz which can be handled by the data acquisition system. The trigger system was briefly described as follows.

The trigger system used the information of subdetectors, CV, CJ, TOF, ECAL, HCAL, MU, FD, and SW. The signals from the CV and CJ were combined to form the information of “track trigger” . In addition, random trigger of the beam crossing was used. The trigger system consisted of two complementary parts, “stand-alone” and “ $\theta - \phi$ ” triggers. The stand-alone trigger utilized the information from the single subdetector, such as track multiplicity in the track trigger, total energy in the barrel ECAL. As for the $\theta - \phi$ trigger, 24 elements were made from each subdetector subdivided into 6 in θ and 24 in ϕ ($\theta - \phi$ matrix), whose information enabled to use the spacial correlations of hits within and between subdetectors. The final trigger decision was made from the combination of the stand-alone and $\theta - \phi$ trigger signals, which made the trigger system highly redundant. If an event was triggered, full data acquisition was followed which need about 15 ms.

The trigger efficiency for the multihadronic process ($e^+e^- \rightarrow$ hadrons) used as a main process in this thesis was 100% for the full acceptance. Some of the important trigger conditions for the multihadronic process were described as follows.

- At least 3 tracks were obtained in the track trigger.
- At least 2 tracks were obtained in the track trigger in the barrel region.
- Collinear hits were obtained in the $\theta - \phi$ bins in the track trigger.
- Coincident hits were obtained in the same $\theta - \phi$ bin for the track and ECAL trigger.
- Coincident hits were obtained in the same $\theta - \phi$ bin for the track and TOF trigger.
- At least 7 hits were obtained in the TOF $\theta - \phi$ bins.
- Coincident hits were obtained in the same $\theta - \phi$ bin for the TOF and ECAL trigger.
- Total energy in the barrel ECAL was at least 7 GeV.
- Total energy in one side of the endcap ECAL was at least 6 GeV.

- Total energy in one side of the endcap ECAL was at least 6 GeV.
- At least 1 $\theta - \phi$ bin with the energy of at least 2.6 GeV was obtained in the barrel ECAL.
- At least 1 $\theta - \phi$ bin with the energy of at least 3 GeV was obtained in one side of the endcap ECAL.

Chapter 4

Measurements of the $A_{\text{FB}}^{b,c}$

In this chapter, an overview of the physics processes at LEP2 is given at first. Some additional conditions to define A_{FB} is described, which is needed under such situation. Then a brief description of the procedure to measure the $A_{\text{FB}}^{b,c}$ is given. The descriptions of the data and the Monte Carlo samples used in this thesis are followed. With these materials, the analyses are performed.

4.1 Overview of the Quark-Antiquark Pair Production at LEP2

The quark-antiquark pair production ($e^+e^- \rightarrow q\bar{q}$) at LEP2 is the main process in this thesis, which contains the signal processes, $e^+e^- \rightarrow b\bar{b}$ and $e^+e^- \rightarrow c\bar{c}$. The quark and antiquark can be emitted in back-to-back direction, which form two back-to-back jets as shown in Fig. 4.2(b). (If hard gluon emissions are accompanied, it forms three or more jets.) At LEP2, large fraction of quark-antiquark pair production accompanies the initial-state radiation (ISR) ($e^+e^- \rightarrow q\bar{q} + n\gamma$). The Feynman diagram for the case of single ISR is shown in Fig. 4.1 and such a event with the ISR escaped in the beam pipe is shown in Fig. 4.2(a).

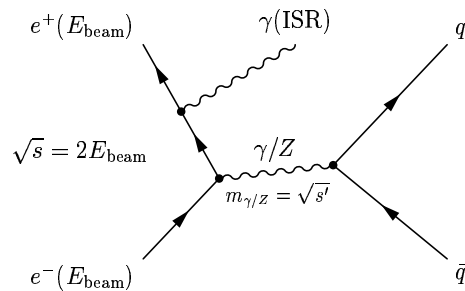


Figure 4.1: A Feynman diagram of quark-antiquark production with single ISR.

The \sqrt{s} of the quark-antiquark production is effectively decreased by the ISR to the mass of the γ/Z propagator, as which the effective center-of-mass energy ($\sqrt{s'}$) is defined. The simulated distribution of $\sqrt{s'}$ at \sqrt{s} of 189 GeV is shown in Fig. 4.2(c). Approximately 70% of events have the $\sqrt{s'}$ around the Z mass. Such phenomena is called “radiative return to Z”. An event with lower $\sqrt{s'}$ is termed “radiative event” and that with $\sqrt{s'}$ close to the \sqrt{s} is termed “non-radiative event”. Since the A_{FB} is measured for the non-radiative events in this analysis, the s' evaluation is important.

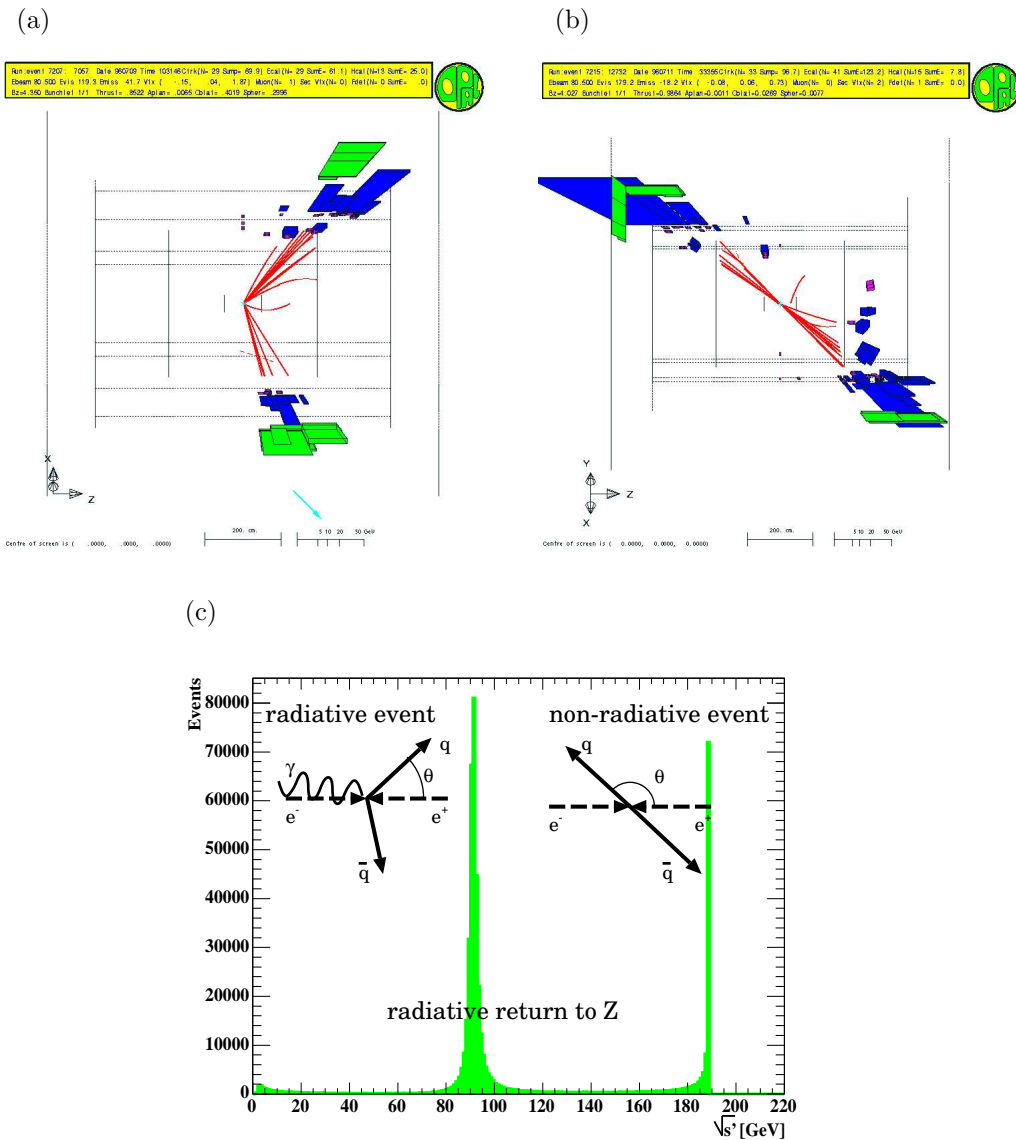


Figure 4.2: (a) A quark-antiquark pair production with ISR escaped in the beam pipe. (b) A quark-antiquark pair production without ISR. (c) The $\sqrt{s'}$ distribution of simulated quark-antiquark pair events at the \sqrt{s} of 189 GeV. A large peak of the radiative return is seen around the Z mass.

Some other physics processes than the quark-antiquark pair production exist at LEP2. The cross-sections of representative physics processes at LEP are shown as a function of the center-of-mass energy (\sqrt{s}) in Fig. 4.3.

The cross-sections of the fermion-pair production ($e^+e^- \rightarrow f\bar{f}$) in the figure are calculated with ZFITTER except for the Bhabha process ($e^+e^- \rightarrow e^+e^-$), which contains a t-channel diagram. As for the quark-antiquark pair production, contamination of large fraction of radiative events can be seen by comparing the cross-sections of $\sqrt{s'/s} > 0.85$ and $\sqrt{s'/s} > 0.1$. The s' estimation is important to distinguish the non-radiative events from the radiative events.

As for the lepton pair production, the cross-section of the muon pair production ($e^+e^- \rightarrow \mu\mu$) is a few times smaller than that of the $b\bar{b}$ or $c\bar{c}$ production. The cross-section of the τ pair production is the same as that of the muon pair production. The cross-sections of the Bhabha process is calculated with BHWIDE [61]. Both the inclusive ($|\cos\theta|$ of the electron smaller than 0.9996¹) cross-section and the large angle non-radiative ($|\cos\theta|$ of the electron smaller than 0.7 with the collinearity angle² (θ_{acoll}) smaller than 10 degree) cross-section are calculated. The large cross-section of the small angle Bhabha process can be seen by comparing the two cross-sections. Such events are used to measure the luminosity. The cross-section of the large angle Bhabha process is similar to that of $b\bar{b}$ or $c\bar{c}$ production. The lepton-pair events are distinct from the quark-antiquark pair events in the number of tracks. The events with hadronic τ decay is thought to be a background.

The cross-section of the photon pair process ($e^+e^- \rightarrow \gamma\gamma$) is calculated with QED under the condition in which the $|\cos\theta|$ of the emitted photon is smaller than 0.93. The cross-section is a few times smaller than that of $b\bar{b}$ or $c\bar{c}$ and such events are thought to be well separated from quark-antiquark pair events.

The cross-sections of W boson pair ($e^+e^- \rightarrow W^+W^-$) and Z boson pair production ($e^+e^- \rightarrow ZZ$), which are the main sources of the events with four fermion final state, are calculated with YFSWW [62] and YFSZZ [63], respectively. The cross-section of the W boson pair production is comparable to that of $b\bar{b}$ or $c\bar{c}$ production at \sqrt{s} larger than 180 GeV, while that of the Z boson pair production is smaller by one order. They are thought to be backgrounds due to their hadronic decay modes which form some jets.

The cross-section of the 2-photon process with hadronic final state ($e^+e^- \rightarrow e^+e^- \gamma\gamma \rightarrow e^+e^- + \text{hadrons}$) is calculated with PHOJET [64] under the condition in which the minimum center-of-mass energy of the 2-photon system ($W_{\gamma\gamma}$) is larger than 2 GeV. It may be a background due to the large cross-section in spite of the large missing energy or the forward activity in the detector.

¹The maximum value of $|\cos\theta|$ covered by SW.

²The collinearity angle = 180[degree] – the opening angle among the emitted e^+e^- .

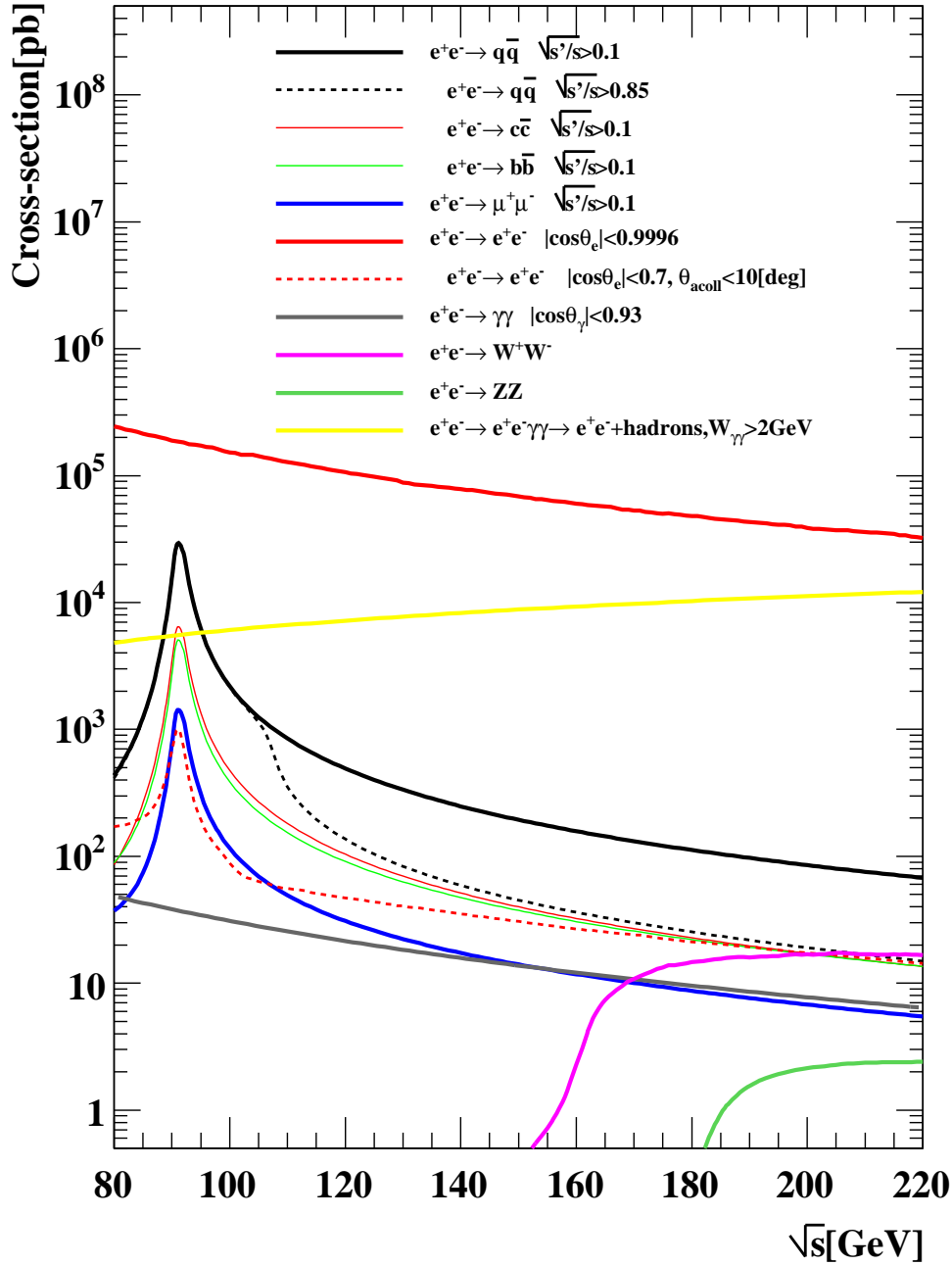


Figure 4.3: The cross-sections of main physics processes at LEP. The cross-sections of the fermion-pair production except for the Bhabha process is calculated with ZFITTER. The cross-section of the Bhabha process is calculated with BHWIDE. That of the photon-pair process is analytically calculated with pure QED. Those of the W boson pair and Z boson pair production are calculated with YFSWW and YFSZZ, respectively. That of the 2-photon process with hadronic final state is calculated with PHOJET.

4.2 Definition of the A_{FB} at LEP2

The A_{FB} is defined generally as Eq. 1.2. Since radiative events make up more than half of the events at LEP2, some additional conditions to define the A_{FB} are needed. The A_{FB} can be defined for the non-radiative events defined with the effective center-of-mass energy ($\sqrt{s'}$). It means the ISR is excluded but the FSR is included in the calculation of $\sqrt{s'}$, which is invalid for the case in which the ISR-FSR interference exists. Considering such situation at LEP2, the A_{FB} to be measured is defined as Eq. 1.2 under the conditions as follows.

- The effective center-of-mass energy ($\sqrt{s'}$) is defined as the mass of the γ/Z propagator as in the section 4.1.
- The effect of the ISR-FSR interference (IFI) is excluded, which assures the definition of $\sqrt{s'}$ mentioned above.
- Events with $\sqrt{s'/s}$ larger than 0.85 (non-radiative events) are taken.
- The A_{FB} is defined within the full angular acceptance.
- The direction of the final quark (after the hard gluon emission) is used to calculate the A_{FB} , where the QCD effect of the gluon radiation is included.

The theoretical values are calculated with ZFITTER (v6.36). It can calculate the A_{FB} corresponding to the above definition with the configuration flags as follows.

- INTF=0
The initial-final interference term is ignored.
- FINR=0
The final state QED and QCD corrections are included.
- BOXD=2
The contributions of ZZ and WW box diagrams are added.
- CONV=2
Both the running $\alpha(s)$ and the electroweak radiative correction are calculated against each s' and then convoluted.

With the definition of the A_{FB} and the configuration of the ZFITTER, the experimental result can be compared with the theoretical calculation consistently.

4.3 Procedure of the A_{FB} Measurement

The A_{FB} for the fermion pair production in e^+e^- annihilation is connected to the angular distribution according to Eq.2.11. The equation is still valid for the A_{FB} defined in the section 4.2 since the convolution of the A_{FB} for the $\sqrt{s'}$ smaller than \sqrt{s} ensure the same relation as Eq.2.11. With the relation, the procedure to measure the $A_{\text{FB}}^{\text{b,c}}$ is essentially to fit the angular distribution of b or c quark by a function of $1 + \cos^2\theta + 8/3 A_{\text{FB}} \cos\theta$. Accordingly, there are 5 points to measure the A_{FB} as follows.

1. To select quark-antiquark pair events ($e^+e^- \rightarrow q\bar{q}$).
2. To determine the axis along which the quark-antiquark pair is emitted.
3. To determine to which direction along the axis the quark is emitted.
4. To select events with $b\bar{b}$ ($b\bar{b}$ events) or $c\bar{c}$ ($c\bar{c}$ events).
5. Fitting the angular direction to which the b-quark or c-quark is emitted with a function of $1 + \cos^2\theta + 8/3 A_{\text{FB}} \cos\theta$.

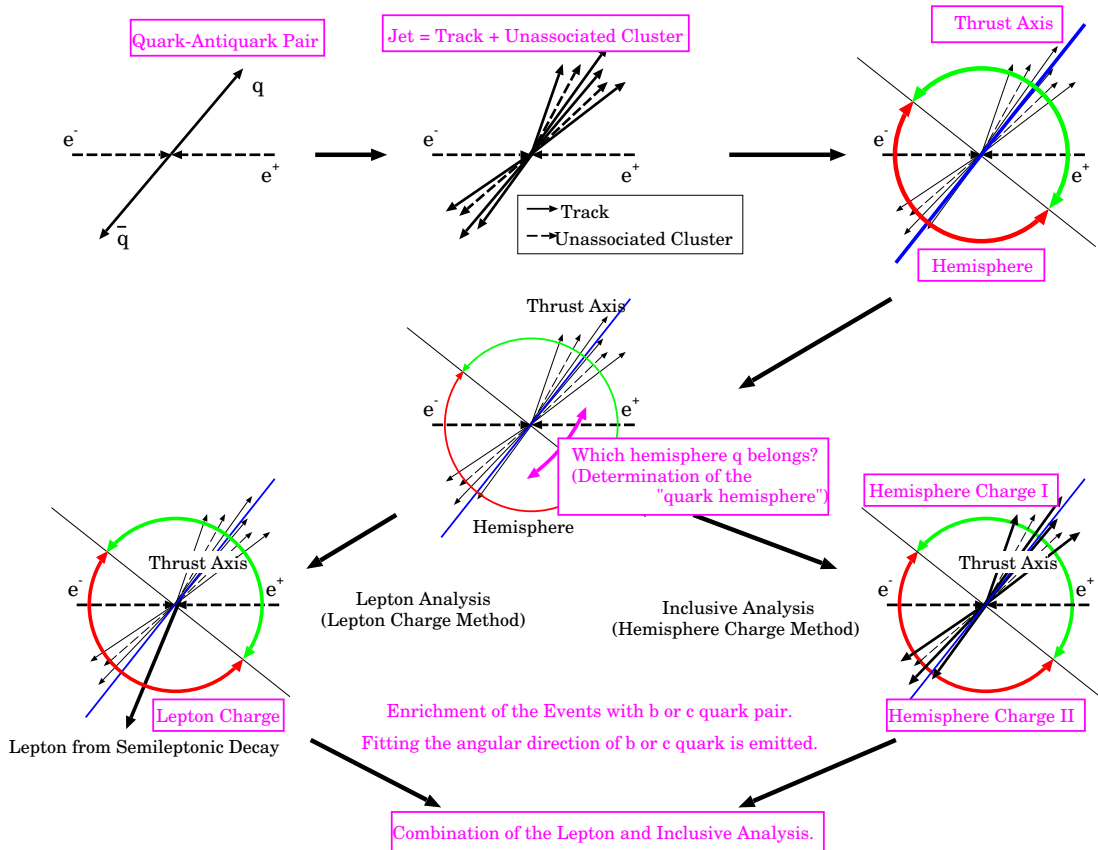


Figure 4.4: The procedure to measure the A_{FB} .

From here, the procedure to measure the $A_{\text{FB}}^{\text{b,c}}$ practically with the information from the detector is briefly described. The procedure is schematically shown in Fig. 4.4.

The events with quark-antiquark pair can be seen as two jets or more jets in the case with hard gluon emissions, where the jet is constructed from both the tracks formed in the central tracking system and ECAL clusters which have no association with the tracks (“unassociated cluster”). The quark-antiquark-pair events can be selected with that characteristics.

For such events with multi-jets, the axis along which the quark-antiquark pair is emitted can be determined with a “thrust axis” [65], which is defined in the relation with a quantity termed “thrust” as follows. The thrust (T) is defined as,

$$T = \max \left(\frac{\sum_i |\vec{p}_i \cdot \vec{n}|}{\sum_i |\vec{p}_i|} \right), \quad (4.1)$$

where the sum runs over all the particles (tracks and unassociated clusters) in a event, and where \vec{p}_i is referred to as the momentum of the i^{th} particle and \vec{n} is referred to as the unit vector to maximize the sum. The thrust axis is defined as the \vec{n} , which is a good approximation of the direction along which the primary quark-antiquark pair is emitted. The angle of the thrust axis measured from the e^- direction is termed θ_{thrust} . As regards the thrust axis, each event is divided into two hemispheres defined by a plane that is orthogonal to the thrust axis and is containing the origin of the coordinate system (the nominal e^+e^- interaction point).

If the hemisphere to which the quark is emitted is termed a “quark hemisphere”, to determine to which direction along the thrust axis the quark is emitted can be described as the determination of the quark hemisphere. As regards the quark-hemisphere determination, two methods to utilize the charge information is taken. For each method, a different method to enrich $b\bar{b}$ or $c\bar{c}$ events is used.

One termed “lepton charge method” utilizes the charge of leptons from the semileptonic decays of b- or c-hadrons. For example, if a lepton with positive charge from the semileptonic decay of a c-hadron is found, it is decided that the c-quark is emitted to the hemisphere containing the lepton. For the case of the $c\bar{c}$ events, the probability to correctly determine the quark hemisphere with the lepton charge method is expected to be approximately 100%, whereas a smaller probability is expected for the $b\bar{b}$ events due to the $B^0 - \bar{B}^0$ mixing. The analysis in which the lepton charge method is used is termed “lepton analysis”, where the information of the leptons from semileptonic decays is used to enrich $b\bar{b}$ or $c\bar{c}$ events. This analysis can be applied to the events with leptons from the semileptonic decays.

The other termed “hemisphere charge method” utilizes “hemisphere charge” [66], Q_{hemi} , which is defined as

$$Q_{\text{hemi}} = \frac{\sum_i^{\text{hemi.}} (p_{\parallel i})^\kappa q_i}{\sum_i^{\text{hemi.}} (p_{\parallel i})^\kappa}, \quad (4.2)$$

where the sum runs over all tracks in a hemisphere, and where $p_{\parallel i}$ is referred to as the longitudinal momentum component with respect to the thrust axis and q_i is referred to as the charge of track i . The value of the exponent, κ , is chosen in order to maximize the power of the quark-hemisphere identification. As regards the identification, the hemisphere with larger hemisphere charge is determined as the quark hemisphere for up-type quarks, whereas the hemisphere with smaller hemisphere charge is determined as the quark hemisphere for down-type quarks. The analysis in which the hemisphere charge method is used is termed “inclusive analysis”, since this method can be applied to all the events. In this analysis, a powerful b-tagging algorithm based on lifetime, lepton and event-shape information is used to enhance events with $b\bar{b}$ or $c\bar{c}$.

For both the analyses, the enrichment of the $b\bar{b}$ or $c\bar{c}$ event is performed so as to achieve high purity, to keep high efficiency and to minimize the biases on the A_{FB} . Accordingly, several subsamples to hold different sensitivity to A_{FB}^{b} or A_{FB}^{c} are obtained and unbinned likelihood fits are performed against the angular distributions for each subsample to get $A_{\text{FB}}^{\text{b,c}}$ simultaneously.

Finally, some corrections are applied to the fitted values of $A_{\text{FB}}^{\text{b,c}}$. Biases on A_{FB} due to the event selections has to be corrected to recover the original A_{FB} . Biases due to the use of the thrust axis to estimate the emitting direction of the primary quark-antiquark pair also has to be corrected. The IFI effect is included in the fitted values, since the effect is naturally included in the real data. The effect is removed to get the A_{FB} defined in the previous section. The QCD effect (effect due to the final state gluon radiation) in the fitted value is already reduced since the thrust axis is insensitive to the gluon radiation and tended to indicate the direction of primary quark-antiquark pair. The QCD effect has to be recovered to get the A_{FB} defined in the previous section.

As regards the combination of the two methods, each analysis is performed avoiding the event sharing between the two analyses. The two independent analyses are combined with a single likelihood function in the unbinned likelihood fit.

4.4 Data and Monte Carlo Samples

The data collected with the OPAL detector are divided into 12 coarse subsamples (18 fine subsamples) according to the center-of-mass energy. The names of the division and the E_{cm} ranges are shown in Table. 4.1. The analysis in this thesis is performed for each coarse subsample.

Table 4.1: The division of the data into 12 coarse subsamples (18 fine subsamples).

Name of the data subsamples		Range of E_{cm} [GeV]		
91 GeV		90	–	92
133 GeV	130 GeV	127	–	133
	136 GeV	133	–	141
161 GeV		158	–	165
172 GeV		169	–	175
183 GeV		180	–	186
189 GeV		188	–	190
192 GeV		191	–	192
196 GeV		195	–	197
200 GeV		199	–	201
202 GeV		201	–	202.5
205 GeV	203 GeV	202.5	–	203.5
	204 GeV	203.5	–	204.5
	205 GeV	204.5	–	205.5
207 GeV	206 GeV	205.5	–	206.5
	207 GeV	206.5	–	207.5
	208 GeV	207.5	–	208.5
	209 GeV	208.5	–	209.5

4.4.1 Luminosity Measurement

The luminosity is measured using small-angle Bhabha events, $e^+e^- \rightarrow e^+e^-$, detected in the SW. Since the small-angle Bhabha cross section is dominated by the t-channel exchange of a photon, highly accurate calculation of the cross section is possible under a framework of nearly pure QED. The measurement of the luminosity is performed essentially by counting the number of the small-angle Bhabha events and comparing it with the theoretical cross section. The statistical and systematic errors in the luminosity measurements is less than 0.5%.

4.4.2 Data

The breakdown of the integrated luminosity is shown in Table. 4.2. The data collected at \sqrt{s} above 130 GeV are used for the measurement of the $A_{\text{FB}}^{\text{b,c}}$ and the data collected at Z resonance are used to check the methods used in the analysis.

Table 4.2: A breakdown of the integrated luminosity

E_{cm} [GeV]		Integrated Luminosity							[pb ⁻¹]		mean E_{cm} [GeV]	
		[pb ⁻¹ /year]										
		1995*	1996	1997	1998	1999	2000	Sum				
	91	0.01	1.14	1.48	1.79	3.43	3.98	11.83		91.27		
133	130	2.32		2.27				4.59	7.97	130.12	133.29	
	136	0.03		3.35				3.38		135.99		
	161		9.90					9.90		161.36		
	172		9.89					9.89		172.10		
	183			42.22				42.22		182.68		
	189				163.43			163.43		188.63		
	192					18.35		18.35		191.61		
	196					60.03		60.03		195.54		
	200					56.35	0.82	57.17		199.53		
	202					30.94	0.66	31.60		201.65		
205	203						1.47	1.47	76.99	202.67	204.88	
	204						7.97	7.97		203.85		
	205						67.54	67.54		205.05		
207	206						64.09	64.09	133.87	206.31	206.56	
	207						61.96	61.96		206.63		
	208						7.74	7.74		208.00		
	209						0.08	0.08		208.64		
Sum		2.36	20.93	49.31	165.23	169.10	216.32	623.24				

*) The integrated luminosity in the year 1995 is the integrated luminosity in the last period of 1995 when the LEP energy increased beyond 91 GeV.

4.4.3 Monte Carlo Samples

The main physics process at LEP is described in section 4.1. The signal process is the quark-antiquark pair production. The 4-fermion process which has 4-fermion final states mainly from W^+W^- or ZZ decays, 2-photon and tau-pair process are the possible backgrounds. The contributions from other processes are checked and found to be negligible. For the above-mentioned signal and background processes, the final-state particles were simulated with a specialized event generator. Subsequently, the full simulation of the OPAL detector was performed.

As for the multi-hadronic events at Z, JETSET 7.4 [67] was used for the quark-antiquark pair production and their fragmentation. On the other hand, for the events at \sqrt{s} more than 130 GeV, quark-antiquark pair was generated with KK2f v4 and fragmentation of the quark and antiquark were treated with PYTHIA 6.125 or 6.158 [48]. The KK2f [45] includes first order $\mathcal{O}(\alpha)$ QED and electroweak corrections and includes almost complete $\mathcal{O}(\alpha^2)$ QED corrections especially for the ISR with CEEX (coherent exclusive exponentiation) method. The accurate treatment of the ISR process is important since the ISR is more significant at LEP2 than at LEP1. However the FSR was disabled and it was

treated in the showering process in the PYTHIA instead. The ISR-FSR interference was disabled in order to hold validity of the definition of $\sqrt{s'}$ as the mass of the γ/Z propagator. The fragmentation was performed by the PYTHIA 6.150 (string model), and heavy quark fragmentation was modeled according to the Peterson fragmentation scheme with parameters tuned according to [68].

The 4-fermion events were generated with `grc4f` v2.1 [69] or `KORALW` v1.42 [70]. Events with final states of `eeee`, `ee $\mu\mu$` or `eeqq` were generated by `grc4f` and events with final states of `qqqq`, `llqq` or `llll` were generated by `KORALW` in which matrix elements from `grc4f` were used. The fragmentation were treated by JETSET 7.4 for both cases.

The 2-photon events were generated by PYTHIA or PHOJET and the $\tau^+\tau^-$ pair events were generated by KK2f, interfaced to the tau decay package (Tauola [71]).

4.5 Event Preselections

From here, the analysis is performed with the data and the Monte Carlo (MC) described above. At first, the event preselection is described and the description of the inclusive and lepton analysis are followed.

As regards the event preselection, the multi-hadronic events are selected at first with a selection termed “LEP2 multi-hadronic event selection”, which keeps 98% of the quark-antiquark pair events and events from almost all the other processes are rejected but for 4-fermion events. Then 4-fermion events rejection are performed and non-radiative event selection, $\sqrt{s'} > 0.85\sqrt{s}$, and the acceptance cut, $|\cos \theta_{\text{thrust}}| < 0.9$ are applied.

4.5.1 LEP2 Multi-Hadronic Event Selection

The standard multi-hadronic events selection at LEP2 (L2MH) is constructed with the information of both tracks and electromagnetic clusters with good quality. The tracks were constructed with the information of CV, CJ and CZ, and the electromagnetic clusters were constructed with the information of EB and EE, where the detector statuses of these subdetectors were already required. The criteria to select good tracks are as follows.

- At least 20 hits measured in the tracking system of CV, CJ and CZ are required.
- The point of closest approach to the beam axis lies less than 2cm in the $r - \phi$ plane from the nominal interaction point.
- The point of closest approach to the beam axis lies less than 40cm along the z axis from the nominal interaction point.
- The distance between the primary vertex and the first hit associated with the track must be less than 60cm.

- The transverse momentum to the beam direction is more than $50\text{MeV}/c$.
- The $|\cos\theta|$ of the track is smaller than 0.995.

The criteria to select good electromagnetic clusters are as follows.

- For the clusters in EB, the energy deposit is larger than 0.1 GeV.
- For the clusters in EE, the energy deposit is larger than 0.2 GeV and are spread over at least 2 adjacent lead glass blocks.

The hadronic events are characterized by both the large visible energy and the high multiplicities of the tracks and clusters in the final states. In order to select them efficiently, the LEP2 multi-hadronic event selection is constructed as,

$$N_{\text{track}} \geq 5, \quad (4.3)$$

$$N_{\text{ecal}} \geq 7, \quad (4.4)$$

$$R_{\text{vis}} \equiv \frac{\sum E_{\text{ecal}}}{\sqrt{s}} \geq 0.14, \quad (4.5)$$

$$R_{\text{bal}} \equiv \frac{|\sum E_{\text{ecal}} \cos\theta_{\text{ecal}}|}{\sum E_{\text{ecal}}} \leq 0.75, \quad (4.6)$$

where N_{track} is the number of charged tracks, N_{ecal} is the number of the electromagnetic clusters, E_{ecal} is the energy of the electromagnetic cluster, and θ_{ecal} is the polar angle of the cluster. The R_{vis} means the ratio of the visible energy to \sqrt{s} and the R_{bal} means the energy unbalance in z direction.

- The cuts on N_{track} and N_{ecal} are reflected the high-multiplicity nature of the hadronic events which efficiently rejects the leptonic events.
- The cuts on R_{vis} is introduced in order to reject 2-photon background events which tends to have large missing energy due to the escape of electron or positron in the beam pipe. Some of the radiative hadronic events with large missing energy due to the escape of the ISR photons in the beam pipe are also lost by this cut.
- The cuts on R_{bal} is introduced to further reject 2-photon background events which tends to have large energy unbalance due to the escape of one of the electron or positron into the beam pipe. Some of the radiative hadronic events with large energy unbalance due to the escape of ISR photons are also lost.

The selection efficiency of these cuts for the multihadronic events with $\sqrt{s'} > 0.85\sqrt{s}$ is approximately 98% from MC, while radiative events tends to be lost. The effect of the L2MH selection on the hadronic events is shown in Fig. 4.5.

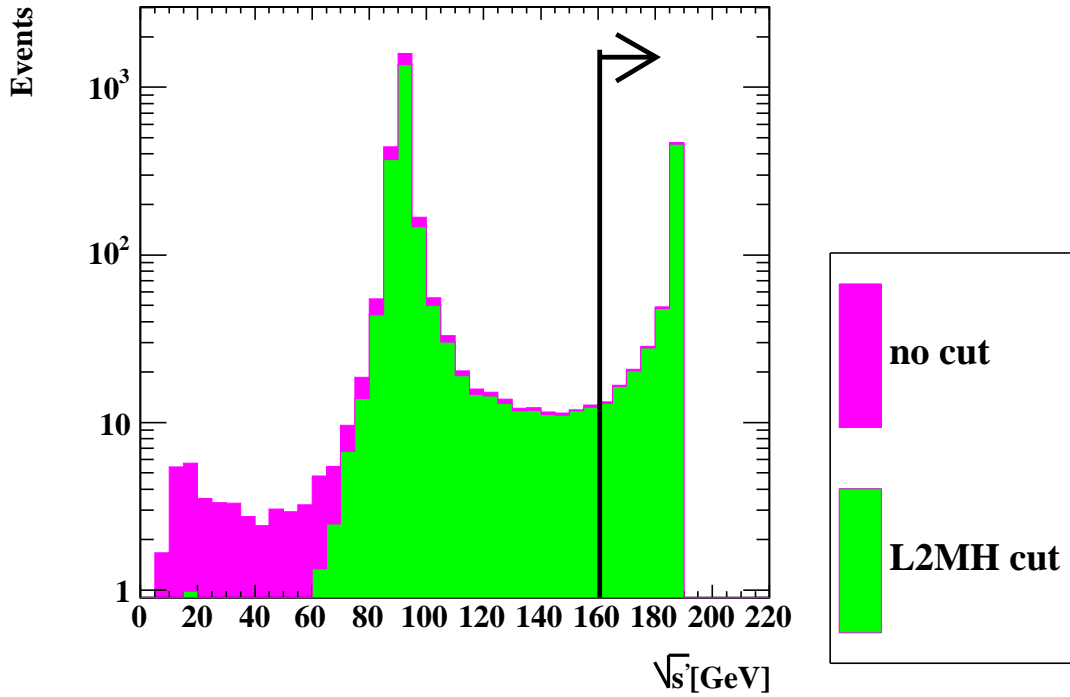


Figure 4.5: The $\sqrt{s'}$ distribution of multihadronic MC sample at $\sqrt{s} = 189$ GeV before and after LEP2 multihadronic event selection (L2MH). The arrow indicates the non-radiative events with $\sqrt{s'} > 0.85\sqrt{s}$.

The distributions of N_{track} , N_{ecal} , R_{vis} and R_{val} are shown in Fig. 4.6, where a good agreement between the data and MC is obtained. Almost all the 2-photon events and $\tau^+\tau^-$ events are rejected. The main background to the multi-hadronic events is the 4-fermion events. The fraction of the 4-fermion events is approximately 18% and that of the 2-photon events is approximately 2% and that of the $\tau^+\tau^-$ events is approximately 0.2%.

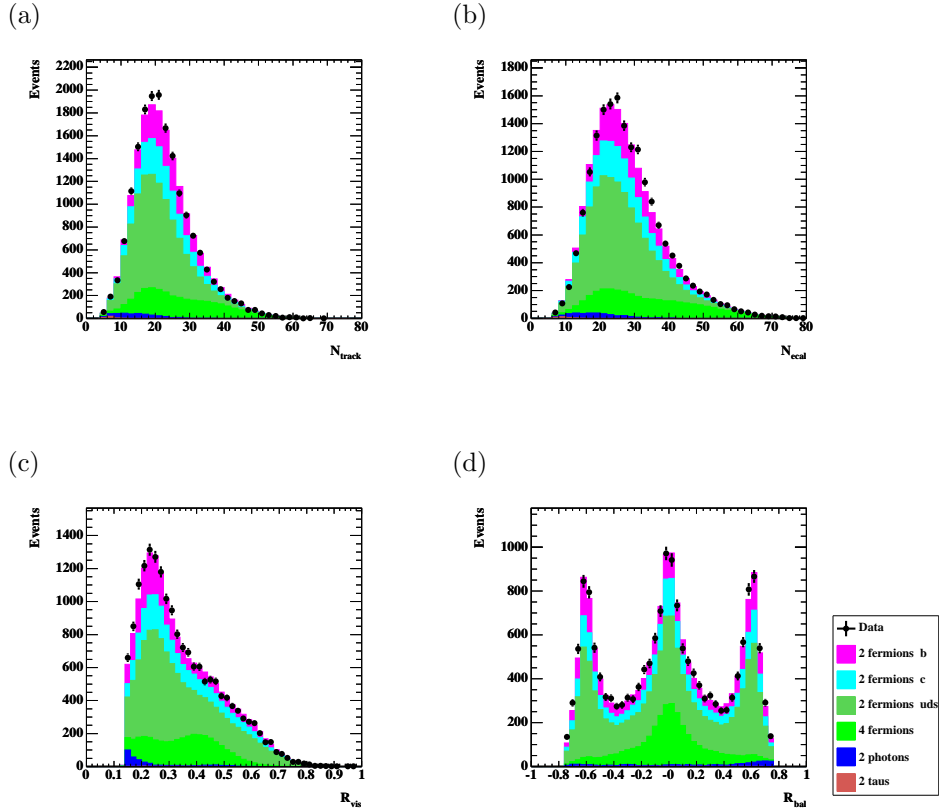


Figure 4.6: The distributions of (a) N_{track} , (b) N_{ecal} , (c) R_{vis} and (d) R_{bal} for the remaining events after the L2MH selection collected at \sqrt{s} of 189 GeV.

4.5.2 s' Determination and Non-Radiative Event Selection

The effective center-of-mass energy, $\sqrt{s'}$, is determined as in [72]. The method is described briefly as follows. The isolated photon candidates are identified with the following criteria.

- Energy of the ECAL cluster is larger than 10 GeV.
- The selection of ECAL clusters is done by assigning the upper limits to both the number of lead glass blocks and the number of blocks which includes the 90% of the cluster energy.
- The sum of ECAL cluster energy in the cone with an angle of 0.2 radian is required to be smaller than 1 GeV.
- Energy of associated HCAL cluster in the region $|\cos \theta| < 0.95$ is required to be less than 4 GeV.

The tracks and clusters except the isolated photon clusters are formed into jets using Durham algorithm [73] with a jet resolution parameter $y_{cut} = 0.02$. If more than four jets were found the number was forced to be four by adjusting the jet resolution parameter. The jets and observed photons are then subjected to a series of kinematic fits imposing the constraints of energy and momentum conservation, in which zero, one, or two additional photons emitted close to the beam direction are allowed. The fit with the lowest number of extra photons which gives an acceptable χ^2 is chosen. The value of $\sqrt{s'}$ is then computed from the fitted four-momenta of the jets. If none of the kinematic fits gives an acceptable χ^2 , $\sqrt{s'}$ is estimated directly from the angles of the jets.

A symbol of s'_{measured} is used to represent the estimated s' and a symbol of s'_{true} is used to represent the true s' , if there is some ambiguity in using s' . The distribution of the measured $\sqrt{s'}$ is shown in Fig. 4.7.

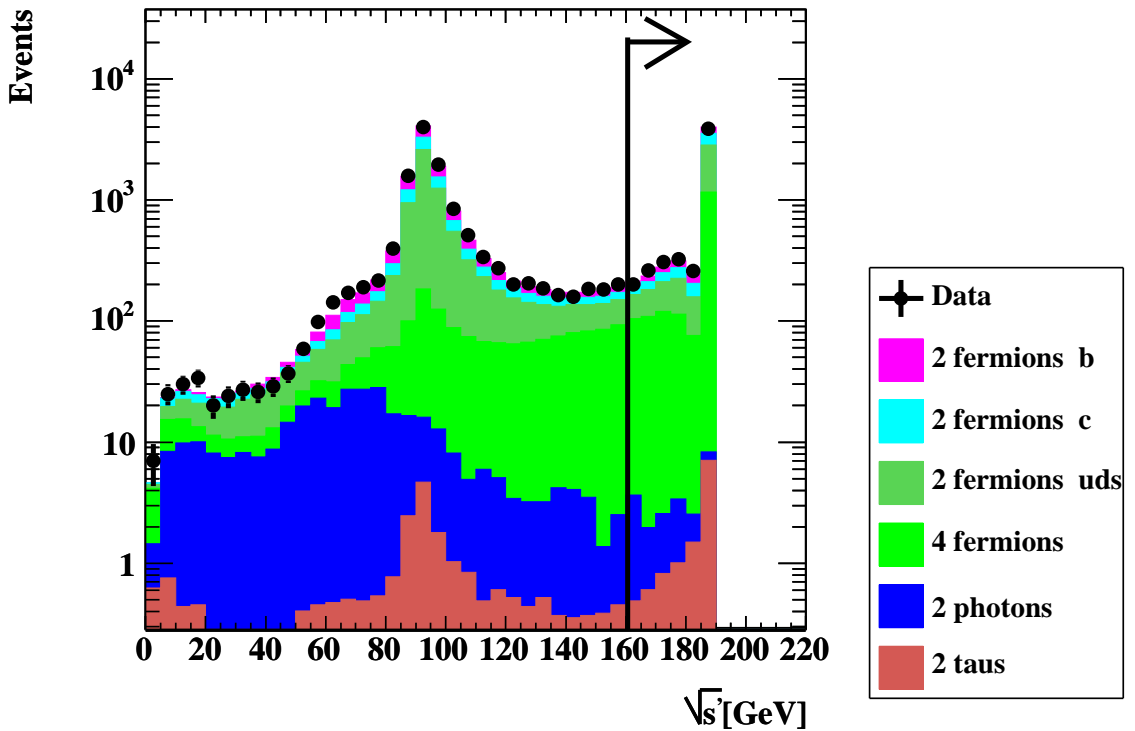


Figure 4.7: The measured $\sqrt{s'}$ distribution of multihadronic MC sample at $\sqrt{s} = 189$ GeV after LEP2 multihadronic event selection (L2MH). The arrow indicates the non-radiative events with $\sqrt{s'} > 0.85\sqrt{s}$.

The non-radiative event selection is performed by applying a cut of $\sqrt{s'} > 0.85\sqrt{s}$. This was set as a common cut among 4 experiments at LEP and this rather inclusive selection reduces the effect of the ISR-FSR interference on the A_{FB} .

The distribution of $\sqrt{s'_{\text{measured}}}$ for the 189 GeV multi-hadronic MC sample is shown in Fig. 4.8, where the distribution of events with $\sqrt{s'_{\text{true}}/s} > 0.85$ is shown with a colored positive-slope hatch and that of events with $\sqrt{s'_{\text{true}}/s} < 0.85$ is shown with a negative-slope hatch. For the selection, the loss of the true non-radiative events (with $\sqrt{s'_{\text{true}}} > 0.85\sqrt{s}$) is approximately 5% and the contamination of the true radiative events (with $\sqrt{s'_{\text{true}}} < 0.85\sqrt{s}$) is approximately 5%.

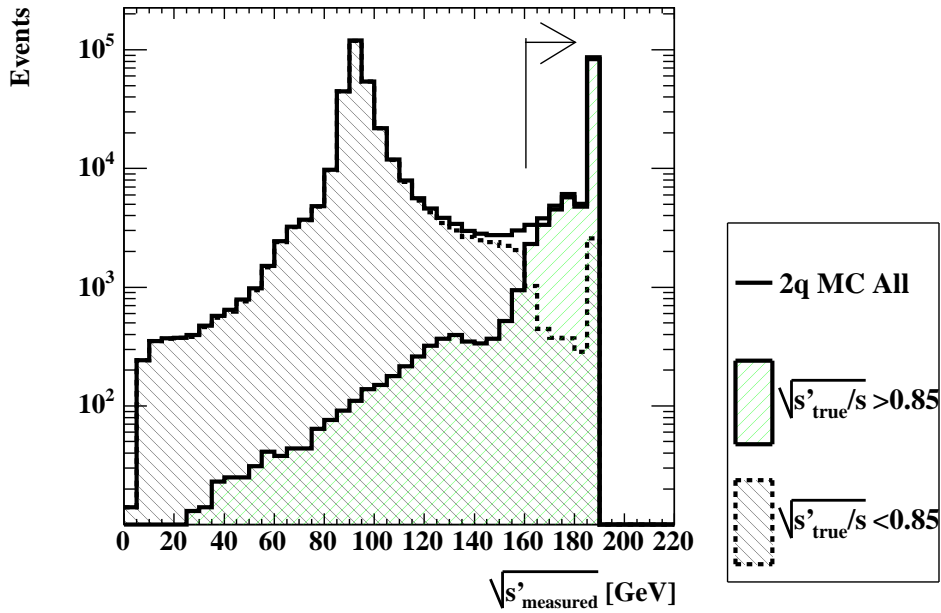


Figure 4.8: The distribution of $\sqrt{s'_{\text{measured}}}$ for the 189 GeV multi-hadronic MC sample, where the distribution of events with $\sqrt{s'_{\text{true}}/s} > 0.85$ is shown with a colored positive-slope hatch and that of events with $\sqrt{s'_{\text{true}}/s} < 0.85$ is shown with a negative-slope hatch.

4.5.3 4-fermion event rejection

The 4-fermion events are the main background after the multi-hadronic event selection. In order to reduce them, the OPAL W^+W^- event selection [74–76] is used. It is divided into two types, $W^+W^- \rightarrow q\bar{q}\ell\bar{\nu}_\ell$ selection and $W^+W^- \rightarrow q\bar{q}q\bar{q}$ selection. For both of them, likelihood based discriminants are constructed after cut based preselections.

$W^+W^- \rightarrow q\bar{q}\ell\bar{\nu}_\ell$ selection

Events with $W^+W^- \rightarrow q\bar{q}\mu\bar{\nu}_\mu$ or $W^+W^- \rightarrow q\bar{q}e\bar{\nu}_e$ are characterized by two well-separated hadronic jets, high momentum lepton, and missing momentum due to the undetected neutrino, whereas events with $W^+W^- \rightarrow q\bar{q}\tau\bar{\nu}_\tau$ are characterized by two well-separated

jets from hadronic W decay, one low multiplicity jet typically containing one or three tracks, and low visible energy due to the undetected neutrinos from W and τ decays. Such events are selected as follows.

- Preselection

Loose cuts on visible energy (R_{vis}), number of charged tracks (N_{track}) and number of ECAL clusters (N_{ecal}) are applied to reject obvious background events such as low multiplicity events or 2-photon events. ($R_{\text{vis}} > 0.2$, $N_{\text{track}} > 5$ and $N_{\text{ecal}} > 5$)

- Identification of Lepton Candidates from W

For all tracks, a track most consistent with the lepton coming from $W^+W^- \rightarrow q\bar{q}\ell\bar{\nu}_\ell$ decays is selected from information of the track isolation, the energy of the track and e , μ or τ identification (hit multiplicity in the MU and HCAL, dE/dx , etc).

- Likelihood based selections

Likelihoods ($\mathcal{L}_{q\bar{q}\ell\bar{\nu}_\ell}$) corresponding to each $W^+W^- \rightarrow q\bar{q}\ell\bar{\nu}_\ell$ decay to e , μ and τ are constructed from the information of the kinematics and e , μ or τ identification.

The $\mathcal{L}_{q\bar{q}\ell\bar{\nu}_\ell}$ distribution is shown in Fig. 4.9. Events with $\mathcal{L}_{q\bar{q}\ell\bar{\nu}_\ell}$ larger than 0.5 are selected as W^+W^- events.

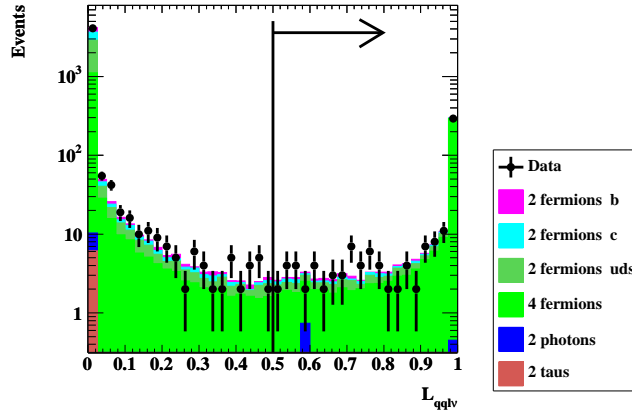


Figure 4.9: The $W^+W^- \rightarrow q\bar{q}\ell\bar{\nu}_\ell$ likelihood discriminant ($\mathcal{L}_{q\bar{q}\ell\bar{\nu}_\ell}$) distribution. The arrow indicates the W^+W^- -selection cut of $\mathcal{L}_{q\bar{q}\ell\bar{\nu}_\ell} > 0.5$.

$W^+W^- \rightarrow q\bar{q}q\bar{q}$ selection

Any event selected in the $W^+W^- \rightarrow q\bar{q}\ell\bar{\nu}_\ell$ selection is rejected from a $W^+W^- \rightarrow q\bar{q}q\bar{q}$ candidate. Events with $W^+W^- \rightarrow q\bar{q}q\bar{q}$ are characterized by 4 energetic, hadronic jets and little missing energy. Such events are selected as follows.

Preselection

- The ratio of the visible energy to the \sqrt{s} , R_{vis} , is larger than 0.7.
- The single largest electromagnetic cluster, R_{max} , is less than 30% of the \sqrt{s} to reject events from the radiative $Z/\gamma \rightarrow q\bar{q}$ process.
- The estimated invariant mass, $\sqrt{s'_{\text{measured}}}$, is greater than 75% of the \sqrt{s} .
- $\log_{10} W_{\text{QCD}}$ [77] is less than 0, where the W_{QCD} is the event weight calculated from the matrix elements for four jet production in $Z/\gamma \rightarrow q\bar{q}$ process [78].
- The charged multiplicity of the lowest multiplicity jet, $N_{\text{min}}^{\text{jet}}$, is greater than zero, where the event is forced to four jets using the Durham algorithm [73].
- The charged multiplicity of the second lowest multiplicity jet, N_2^{jet} , is greater than one, where the event is forced to four jets using the Durham algorithm.

Likelihood based selection The likelihood discriminant (\mathcal{L}_{qqqq}) for the $W^+W^- \rightarrow q\bar{q}q\bar{q}$ selection is constructed from four input variables:

- $\log_{10} W_{\text{QCD}}$.
- $\log_{10} W_{\text{EXE}}$, where W_{EXE} is the event weight for the $WW \rightarrow q\bar{q}q\bar{q}$ process calculated from the EXCALIBUR [79] matrix element.
- Sphericity [65,80] of the event, $S = 3/2 \min(\sum_i p_{it}^2 / \sum p_i^2)$, where the sum runs over all tracks in the event, p_i is the momentum of the i^{th} track, and p_{it} is the transverse momentum of the i^{th} track with respect to a vector to minimize the sum.
- $\log_{10}(y_{45})$, where the y_{45} is the value of jet resolution parameter at which the event is reclassified from a four jet to a five jet event by Durham algorithm.

The distribution of $\log_{10} W_{\text{QCD}}$ before the 4-fermion rejection is shown in Fig. 4.10(a). The $\mathcal{L}_{q\bar{q}q\bar{q}}$ likelihood distribution is shown in Figure 4.10(b). The events with $\mathcal{L}_{q\bar{q}q\bar{q}}$ larger than 0.24 are tagged as W^+W^- events.

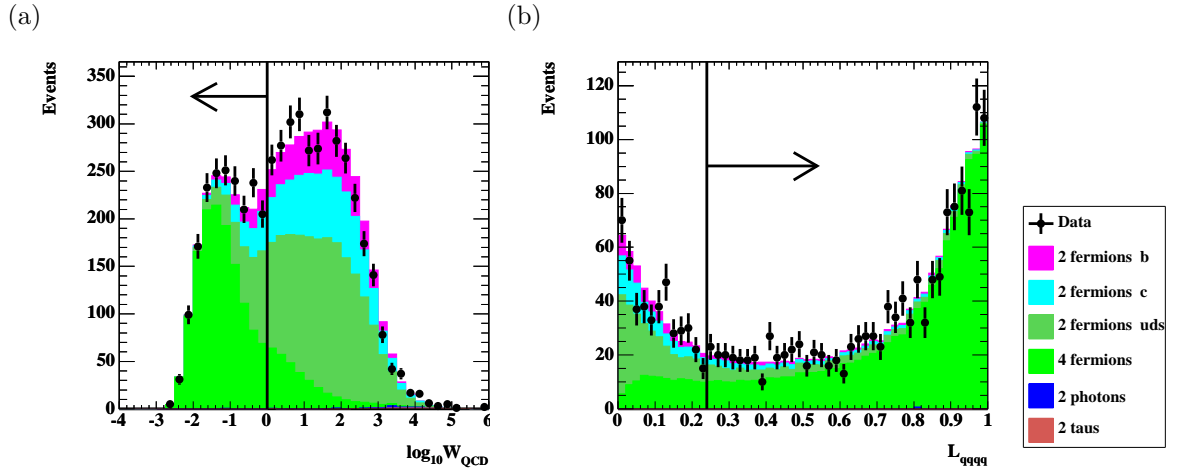


Figure 4.10: (a) the $\log_{10} W_{\text{QCD}}$ distribution and (b) the $W^+W^- \rightarrow q\bar{q}q\bar{q}$ likelihood discriminant ($\mathcal{L}_{\text{qqqq}}$) distribution after non-radiative event selection at \sqrt{s} of 189 GeV. The arrows indicate the W^+W^- selection.

4-fermion event rejection with $W^+W^- \rightarrow q\bar{q}\ell\bar{\nu}_\ell$ and $W^+W^- \rightarrow q\bar{q}q\bar{q}$ selection

The events with $\mathcal{L}_{q\bar{q}\ell\bar{\nu}_\ell}$ larger than 0.5 or $\mathcal{L}_{\text{qqqq}}$ larger than 0.24 are tagged as W^+W^- events and rejected for the $A_{\text{FB}}^{b,c}$ measurements. The distribution of $\log_{10} W_{\text{QCD}}$ after the 4-fermion rejection at $\sqrt{s} = 189$ GeV is shown in Fig. 4.11(a). The measured $\sqrt{s'}$ distribution at $\sqrt{s} = 189$ GeV after 4-fermion rejection but non-radiative event selection is shown in Fig. 4.11(b). Approximately 86% of the 4-fermion events are rejected and the contamination of the 4-fermion events is approximately 6% after the 4-fermion rejection.

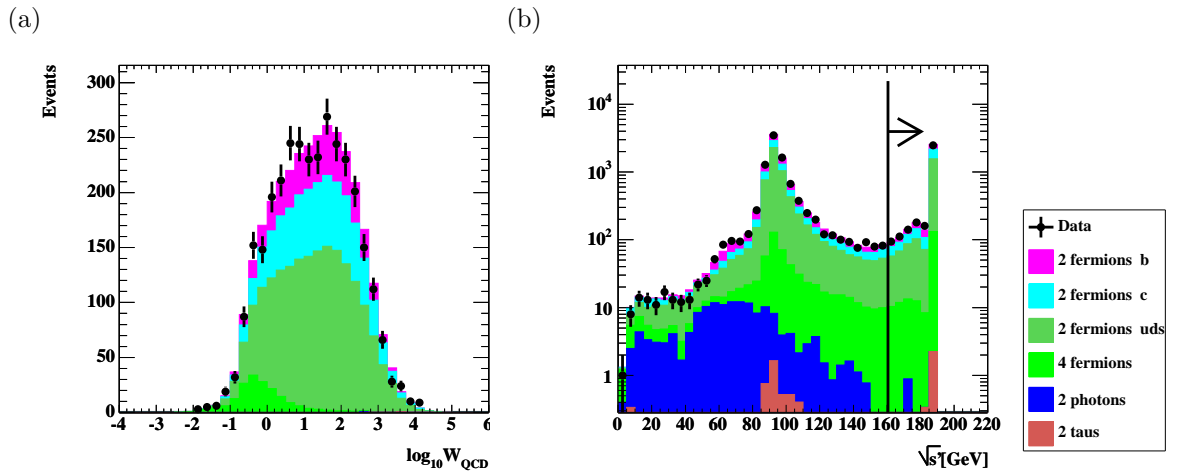


Figure 4.11: (a) The $\log_{10} W_{\text{QCD}}$ distribution and (b) The measured $\sqrt{s'}$ distribution at $\sqrt{s} = 189$ GeV after 4-fermion rejection but the non-radiative event selection. The arrow indicates the non-radiative event selection.

4.5.4 Acceptance Cut

The thrust axis is constructed from the tracks and unassociated ECAL clusters which passed the quality criteria as follows. The quality criteria for the track are as follows.

- The number of CJ hits is equal or more than 20.
- The transverse momentum is larger than 0.15 GeV/c.
- The magnitude of the cosine of the polar angle is less than 0.99995.
- The magnitude of the z co-ordinate of the point of closest approach to the beam axis in the r - ϕ plane ($|z_0|$) is less than 200 cm.
- The magnitude of the impact parameter ($|d_0|$) is less than 5 cm.
- The χ^2 for the track fit is less than 100.

The quality criteria for the ECAL cluster are as follows.

- The raw energy of the cluster is larger than 50 MeV.
- The corrected energy of the cluster in EB is larger than 100 MeV.
- The corrected energy of the cluster in EE is larger than 200 MeV.

This axis is used to determine the axis along which $q\bar{q}$ are emitted. The polar angle of the axis is represented as θ_{thrust} . The range of the $|\cos\theta_{\text{thrust}}|$ is limited within 0.9, which corresponded to the angle covered by SI. The distribution of $|\cos\theta_{\text{thrust}}|$ is shown in Fig. 4.12.

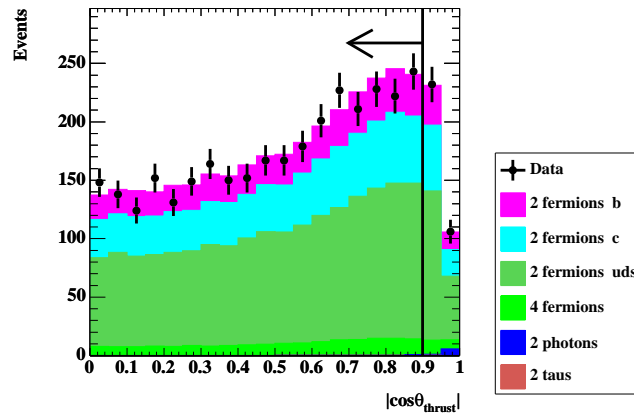


Figure 4.12: The $|\cos\theta_{\text{thrust}}|$ distribution at \sqrt{s} of 189 GeV. The arrow indicates the acceptance cut.

4.5.5 Effect of the Event Preselection

Fractions of the multi-hadronic, 4-fermion events after each event selection are shown in Table 4.3. The event-selection efficiencies of $b\bar{b}$ or $c\bar{c}$ event with $\sqrt{s'_{\text{true}}} > 0.85\sqrt{s}$ are also shown in Table 4.3. The L2MH selection keeps approximately 98% of multi-hadronic events. After all preselections are applied, about 78% of non-radiative $b\bar{b}$ events and 79% of non-radiative $c\bar{c}$ events are remained. The fraction of non-radiative multi-hadronic events is about 91% and the contamination of radiative multi-hadronic events is about 4%, that of 4-fermion events is about 6% and contributions from other sources are negligible. For example, the contribution from $\tau^+\tau^-$ process is approximately 0.2% after L2MH selection and less than 0.1% after all the preselections. The contribution from 2-photon process is approximately 2% after L2MH selections and approximately 0.1% after all the preselections.

Table 4.3: The event selection efficiencies and the fractions of selected events at \sqrt{s} of 189 GeV, which are estimated with Monte Carlo samples.

cut	Number	fraction[%]			efficiency[%]	
		q \bar{q}		4-fermion	b \bar{b}	c \bar{c}
	Data	non-radiative	radiative			non-radiative
L2MH	17744	19.4	61.0	17.6	98.1	98.2
$\sqrt{s'}$	5230	64.9	3.1	31.6	90.9	93.2
4f rejection	3491	89.8	4.1	5.7	84.9	87.1
$\cos\theta_{\text{thrust}}$	3153	90.6	3.6	5.7	77.6	79.4

4.6 Inclusive Analysis

The inclusive analysis is performed for the preselected events. The thrust axis is used to determine the axis along which the $q\bar{q}$ are emitted. The quark hemisphere, which the quark is emitted to, is determined with the hemisphere charge. In this section, the description about the quark-hemisphere determination is given at first. Then the inclusive b and c tagging is described. The description about the unbinned likelihood fit to obtain the $A_{\text{FB}}^{b,c}$ with the quark-hemisphere determination, and b and c tagging is followed. Finally, some corrections applied to the fitted values of A_{FB} are described.

4.6.1 Determination of the Quark-Hemisphere

The two hemispheres defined in section 4.3 are labeled as “hemisphere I” and “hemisphere II”, where one hemisphere arbitrarily selected is labeled as “hemisphere I” and the other

hemisphere is labeled as “hemisphere II”. The hemisphere charges for the “hemisphere I” and the “hemisphere II” are termed Q_I and Q_{II} respectively as shown in Fig 4.13(a).

If a quark or antiquark with positive charge is emitted to the “hemisphere I”, the “hemisphere I” is determined as the quark hemisphere for up-type quarks, whereas the “hemisphere II” is determined as the quark hemisphere for down-type quarks. Thus the charge identification of the hemisphere enables the quark-hemisphere determination.

The charge identification can be done with the hemisphere charge difference ($Q_I - Q_{II}$). If $Q_I - Q_{II} > 0$, the charge of a quark or antiquark emitted to the “hemisphere I” is identified as positive. The distribution of the hemisphere charge difference ($Q_I - Q_{II}$) is shown in Fig. 4.13(b), where the multi-hadronic events with an up-type quark emitting to “hemisphere I” or a down-type quark emitting to “hemisphere II” are labeled as “positive”. Those with an up-type quark emitting to “hemisphere II” or a down-type quark emitting to ‘hemisphere I’ are labeled as “negative”.

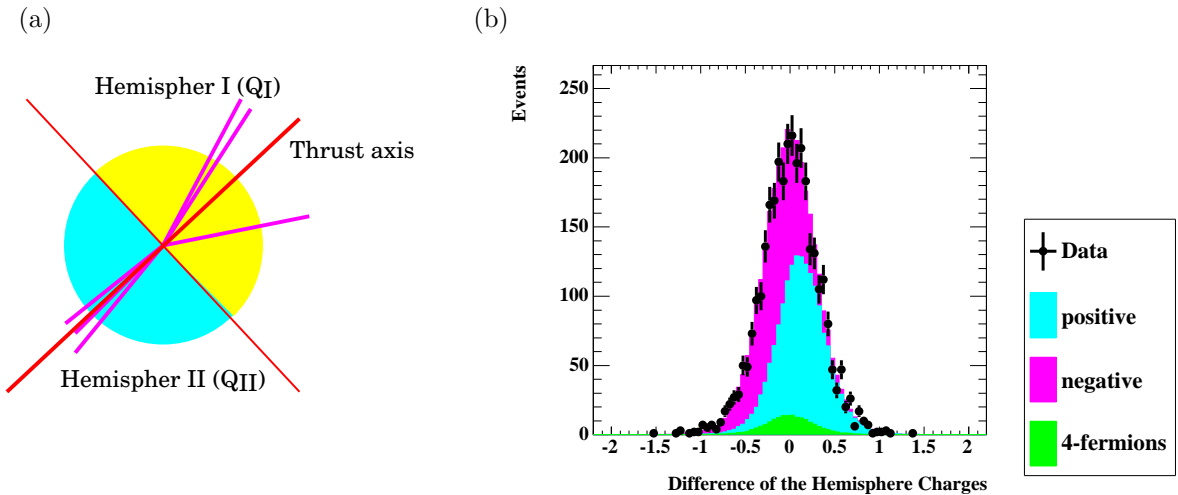


Figure 4.13: (a) Labeling of the hemispheres and (b) the distribution of the hemisphere charge difference ($Q_I - Q_{II}$). The multi-hadronic events with an up-type quark emitting to “hemisphere I” or a down-type quark emitting to “hemisphere II” are labeled as “positive”. The multi-hadronic events with an up-type quark emitting to “hemisphere II” or a down-type quark emitting to ‘hemisphere I’ are labeled as “negative”.

The performance of the charge identification is characterized by a probability that the quark charge in the “hemisphere I” is correctly determined (charge identification probability). The charge identification probabilities for all quarks for various values of κ are studied. The charge identification probabilities as a function of κ are shown in Fig. 4.14 and the best performance is obtained at a κ of 0.4 for bottom quarks.

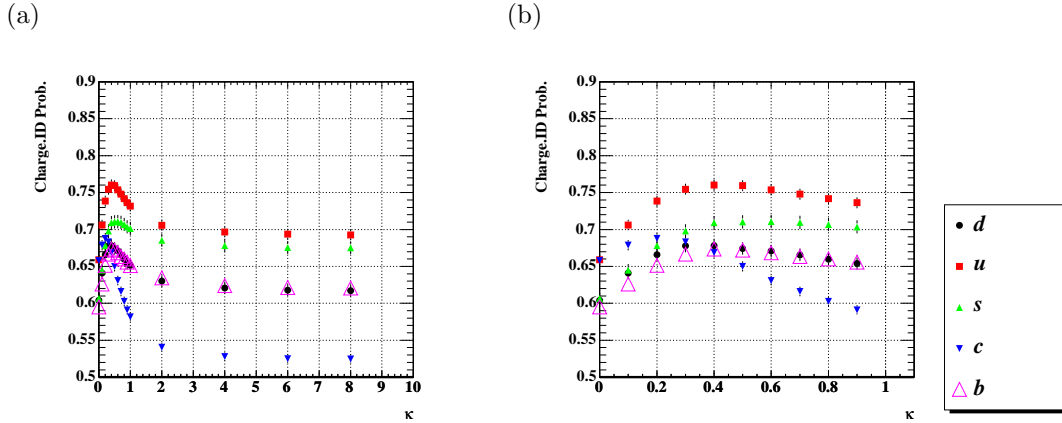


Figure 4.14: The charge identification probabilities as a function of κ .

If larger fraction of the momentum component of a quark along the quark direction is transferred to the corresponding hadron (, which means harder fragmentation), better performance of charge identification is expected since the charge of the hadron contributes more to the hemisphere charge. The contributions of harder or softer momentum component can be tuned by changing the κ .

A higher charge identification probability is potentially expected for up-type quarks due to their larger electric charge ($2/3$) compared to a charge of down-type quarks ($1/3$). It is also because up-type quarks have more chance to form charged hadrons, for they can couple anti-down or anti-strange quarks, while down-type quarks only have anti-up quarks to form charged hadrons. It is reflected in the higher charge identification probabilities for up-type quarks at a value of κ equal 0 in Fig. 4.14.

Charm quarks have lower charge identification probability in spite of their harder fragmentation function, since the decay products of the D^+ or D^0 mesons include significant fraction of K^- ($27.5 \pm 2.4\%$ for D^+ and $53 \pm 4\%$ for D^0). Such opposite charge dilutes the charge identification power.

Strange quarks have harder fragmentation function than that of down quarks and have higher charge identification probability. Both down and strange quarks form stabler hadrons and suffer smaller dilution due to their decays. Although bottom quarks have hardest fragmentation function than others, the charge identification power is as high as that of down quarks due to dilutions from both their decays and the $B^0 - \bar{B}^0$ mixing.

In the distribution of the hemisphere charge difference (Fig 4.13(b)), outer region presents higher charge identification performance than inner region. Therefore events are divided into 2 classes, “inner class” where $|Q_I - Q_{II}| < 0.15$ and “outer class” where $|Q_I - Q_{II}| \geq 0.15$. The threshold of 0.15 is selected, which is determined to minimize the

statistical error of the $A_{\text{FB}}^{\text{b,c}}$. The resulting charge identification probabilities are summarized in Table. 4.4.

Table 4.4: The charge identification probabilities for each quark and for each subclass at \sqrt{s} of 189 GeV. The errors assigned are statistical error from the MC statistics.

	d		u		s		c		b	
all	0.68	± 0.01	0.76	± 0.01	0.71	± 0.01	0.67	± 0.01	0.67	± 0.01
inner class	0.57	± 0.01	0.60	± 0.01	0.58	± 0.01	0.57	± 0.01	0.58	± 0.01
outer class	0.75	± 0.01	0.84	± 0.01	0.78	± 0.01	0.74	± 0.01	0.74	± 0.01

Practically, the quark hemisphere has to be determined with respect to the e^- beam direction. Accordingly, the hemisphere in the e^- beam direction is labeled as “forward hemisphere” and the other is labeled as “backward hemisphere”. The hemisphere charge corresponding to the forward hemisphere is represented as Q_F and that corresponding to the backward hemisphere is represented as Q_B as shown in Fig. 4.15.

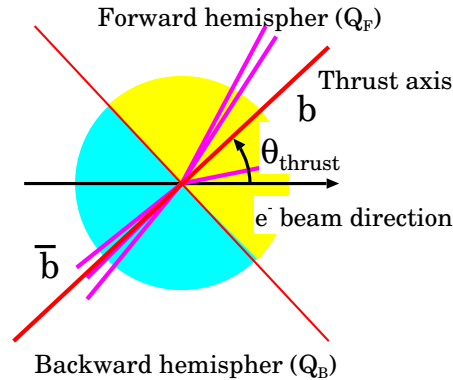


Figure 4.15: The forward and backward hemisphere. The hemisphere charge corresponding to the forward hemisphere is represented as Q_F and that corresponding to the backward hemisphere is represented as Q_B .

The quark direction for down-type quarks can be evaluated with the polar angle of the thrust axis (θ_{thrust}) as,

$$-\text{sign}(Q_F - Q_B) \cdot |\cos \theta_{\text{thrust}}|, \quad (4.7)$$

whereas that for up-type quarks can be evaluated as,

$$\text{sign}(Q_F - Q_B) \cdot |\cos \theta_{\text{thrust}}|. \quad (4.8)$$

The angular distribution evaluated with $-\text{sign}(Q_F - Q_B) \cdot |\cos \theta_{\text{thrust}}|$ for the events after the preselection is shown in Fig. 4.16(a), where the A_{FB}^{c} is observed to be negative sign,

and where the dilution of the A_{FB}^b and the A_{FB}^c due to the charge identification probability can be seen. Similar angular distributions corresponding to the inner charge identification class ($|Q_F - Q_B| < 0.15$) and the outer charge identification class ($|Q_F - Q_B| > 0.15$) are shown in Fig. 4.16(a) and (b), respectively, where the better charge identification performance for the outer charge identification class can be seen.

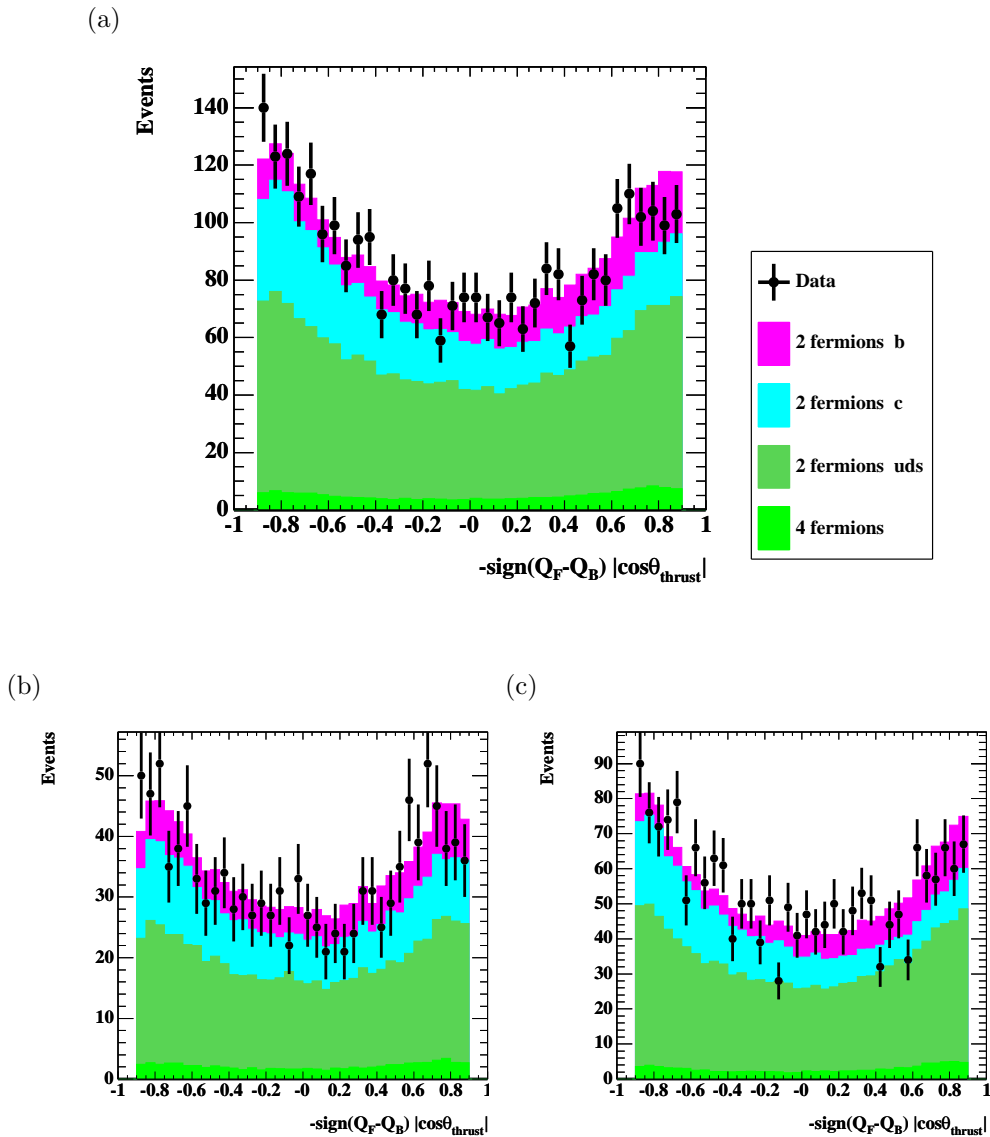


Figure 4.16: The angular distributions evaluated with $-\text{sign}(Q_F - Q_B) \cdot |\cos \theta_{\text{thrust}}|$ (a) after the preselection, (b) with the inner class and (c) with the outer class of the hemisphere charge.

4.6.2 Inclusive B and C Tagging

A high performance b-tagging algorithm termed “LB” [81] developed for the Higgs search at LEP2 is used to purify the $b\bar{b}$ and $c\bar{c}$ events.

Overview

The b-tagging algorithm is based on three nearly independent properties of the b-hadron and its decay products. The b-hadron has a long life and has a characteristic lepton in its semileptonic decay products. It has hard fragmentation and high multiplicity of its decay products, which makes difference in the jet kinematics from that of $u\bar{u}$, $d\bar{d}$ and $s\bar{s}$ events. The algorithm is composed of three tags, lifetime tag, lepton tag and kinematics tag, corresponding to the three properties. Finally, an unbinned likelihood is taken to combine the three roughly independent tag. The scheme is shown in Fig. 4.17.

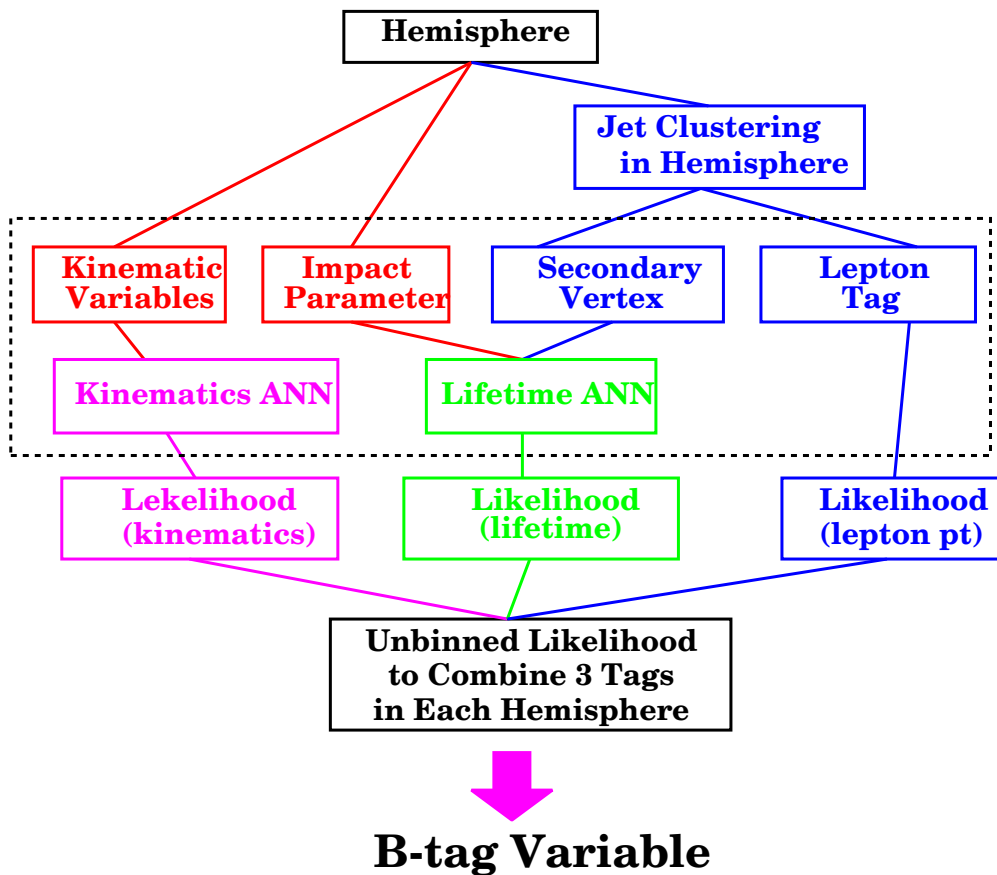


Figure 4.17: The scheme of b-tagging algorithm, LB.

Jet Clustering

The cone algorithm is used for the jet clustering since it is better to include the tracks from a b hadron forming a secondary vertex and exclude the tracks from the others, which makes the jet sensitive to the nature of the b hadron. Such characteristics of the cone algorithm is described in the appendix C. The jet clustering is performed for each hemisphere with the cone algorithm where the half angle of the cone is 0.5 radian and the minimum energy in forming the jet is 7 GeV.

Secondary Vertex Reconstruction

The secondary vertex reconstruction is one of the most important piece in the b-tagging. One secondary vertex is formed from each jet constructed as described in the subsection 4.6.2. In order to increase the purity of the tracks from the secondary vertex, tracks in the jet are ranked by an artificial neural net (ANN) termed “track-ANN” which tends to give a lower value for the track coming from the secondary vertex using the impact parameter of the tracks with respect to the primary vertex. The secondary vertex is reconstructed as follows.

- Tracks in a jet are sorted in a ascending order of the track-ANN discriminator.
- The first 6 tracks in the ordered tracks are selected as seed tracks which are used in the vertex search for the first time. If the number of tracks in the given jet is less than 6, all tracks are used as the seed tracks.
- If there are other tracks with the track-ANN outputs larger than 0.4, these tracks are additionally selected as the seed tracks.
- One vertex candidate is formed from the seed tracks as follows. A temporal vertex is formed by a fit using all tracks at first and then the track with the highest contribution to the χ^2 of the vertex fit is removed. This procedure is repeated until no track contributes more than 5 to the χ^2 and until at least two tracks are remained. Finally, one vertex is obtained, which is termed “seed vertex”.
- The remaining tracks not used for the seed vertex are sorted in the distance from the seed vertex.
- The tracks are added one by one from the nearest track into the seed vertex and vertex fit is performed again. If the contribution to the χ^2 in the fit is smaller than 5, the original seed vertex is replaced by the new vertex and the procedure is repeated. Then one final vertex is formed.

As regards each secondary vertex, a decay length significance is calculated with a distance from the primary vertex to the secondary vertex (l) and its error (σ_l), as l/σ_l . This will be used in the lifetime tag.

Lifetime Tag

The lifetime tag utilizes the information of the decay length significance, which is powerful b-tagging variable reflecting the long lifetime of b hadrons. It utilizes also the information of the impact parameter of the tracks which keeps the b-tagging efficiency in case no secondary vertex is formed. Four such variables are constructed as follows.

At first, the secondary-vertex likelihood, \mathcal{L}_{SV} , is calculated for each hemisphere with all the decay length significances in the hemisphere as follows. The probability density functions (PDF) of the decay length significance for $b\bar{b}$ events, $c\bar{c}$ events and uds events ($u\bar{u}$, $d\bar{d}$ and $s\bar{s}$ events) are constructed with Monte Carlo samples. The combined estimator F_q for each quark flavor q is computed by multiplying the PDF of the quark flavor for all tracks. The \mathcal{L}_{SV} is obtained as $F_b/(F_b + F_c + F_{uds})$.

Next, the impact-parameter likelihood, \mathcal{L}_{IP} , is calculated for each hemisphere with all the tracks in the hemisphere as follows. The impact parameter significances in the $r - \phi$ and $r - z$ projections are formed by dividing the track impact parameters in the $r - \phi$ plane³ and that in the $r - z$ plane⁴ by their errors, respectively. The PDFs for the two variables for each quark flavor are obtained from the Monte Carlo samples. The combined estimator F_q for each quark flavor q is computed by multiplying the PDFs of two variables for all tracks. The \mathcal{L}_{IP} is obtained as $F_b/(F_b + F_c + F_{uds})$.

Then, the reduced secondary-vertex likelihood, \mathcal{R}_{SV} , is calculated as follows. To reduce sensitivity to single mis-measured tracks, the track with the largest impact parameter significance is removed from the secondary vertex candidate and the remaining tracks are used to recompute the likelihood \mathcal{L}_{SV} , which is used as \mathcal{R}_{SV} . If the original vertex has only two tracks, the impact parameter significance of the remaining track after the removal of the track with the largest impact parameter significance is used as \mathcal{R}_{SV} .

Finally, the reduced vertex significance likelihood, \mathcal{R}_{IP} , is calculated as follows. The track having the largest impact parameter significance is removed in the calculation of \mathcal{L}_{IP} , which is used as \mathcal{R}_{IP} .

These highly correlating variables, \mathcal{L}_{SV} , \mathcal{R}_{SV} , \mathcal{L}_{IP} and \mathcal{R}_{IP} are combined with ANN and a corresponding likelihood, lifetime likelihood ($\mathcal{L}_{\text{lifetime}}$), is constructed. The distributions of the four inputs variables and $\mathcal{L}_{\text{lifetime}}$ for b are shown in Fig. 4.18(a)-(e).

³The distance between the point of closest approach to the beam axis and the the nominal interaction point in the $r - \phi$ plane.

⁴The z coordinate of the point of closest approach to the beam axis.

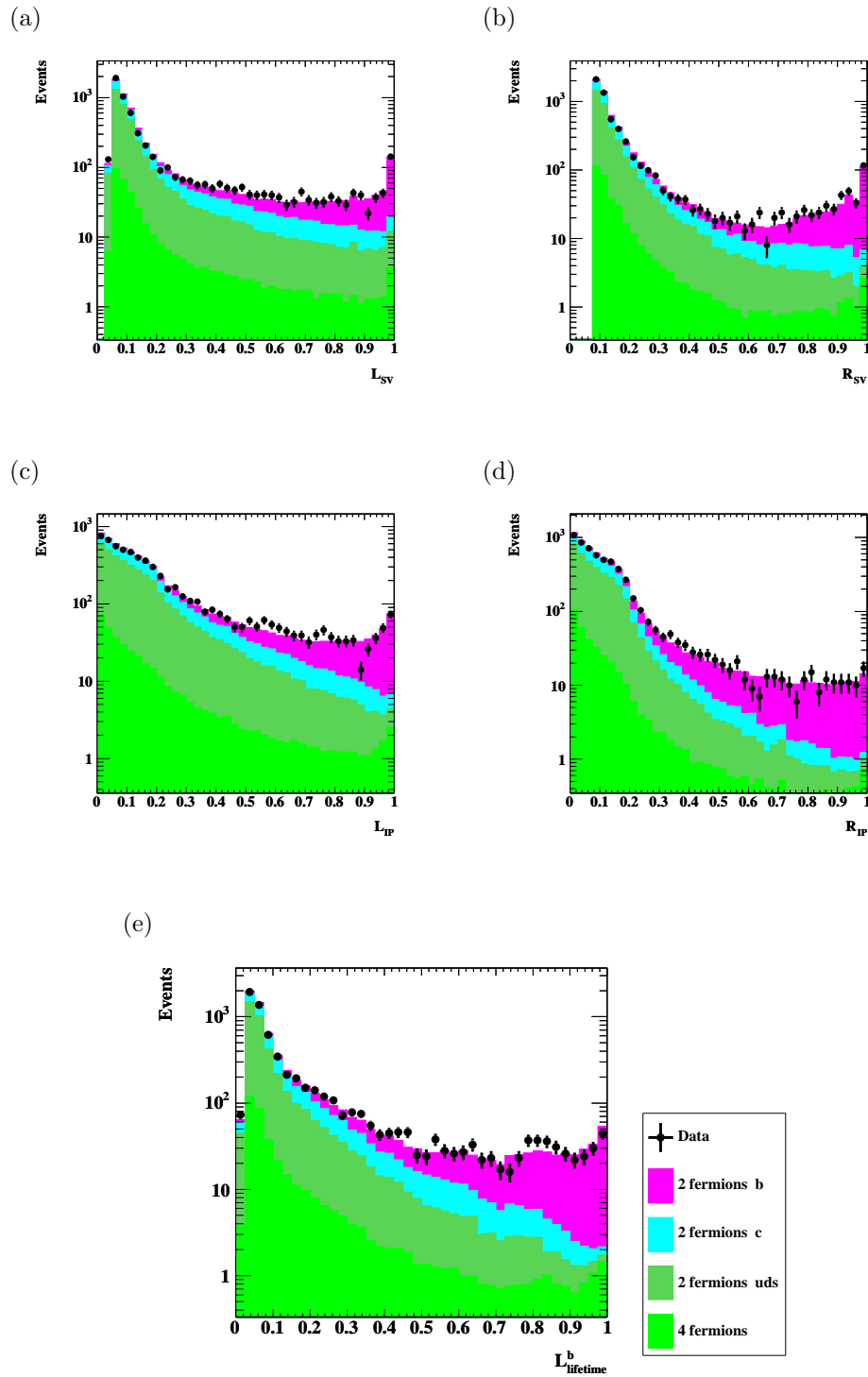


Figure 4.18: The input variables for the lifetime ANN and lifetime likelihood. (a) \mathcal{L}_{SV} , (b) \mathcal{R}_{SV} , (c) \mathcal{L}_{IP} , (d) \mathcal{R}_{IP} , (e) $\mathcal{L}_{lifetime}^b$ for b.

Lepton Tag

The lepton identification is performed in the jets constructed in the subsection 4.6.2. The transverse momentum (p_t) of the lepton is calculated with respect to the direction of the jet axis. The lepton likelihood ($\mathcal{L}_{\text{lepton}}$) is constructed by combining all the leptons found in the hemisphere. The distributions of p_t and $\mathcal{L}_{\text{lepton}}$ for b are shown in Fig. 4.19 (a) and (b), respectively.

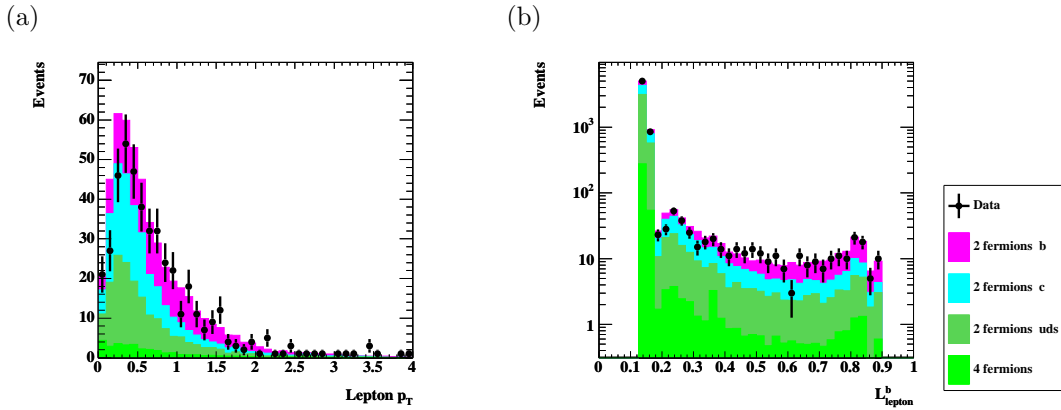


Figure 4.19: (a)The lepton p_t distribution. (b)The distribution of $\mathcal{L}_{\text{lepton}}$ for b.

Kinematics Tag

Two kinds of alternative jets are constructed for both hemisphere using the cone jet-clustering algorithm. One is constructed with relatively narrow cone size (0.4 radian) to enrich the tracks or clusters from b-hadrons, which is termed “narrow jet”. The other is constructed with wider cone size of 1.5 radian to keep the jet shape stable, which is termed “broad jet”. If two or more jets are formed, the most energetic jet is used. With the two kinds of the jets, three kinematic variables are introduced as follows.

- Number of tracks or clusters in the narrow jet, where the double counting of the associated clusters to tracks is corrected.
- Angle between the jet axis and sphericity axis for the narrow jet, which is calculated at the rest frame of the jet (boosted sphericity axis).
- C-parameter [82] for the broad jet, which is calculated at the rest frame of the jet (boosted C-parameter). The C-parameter is one of the jet shape variables ranging from 0 to 1. Events with $C = 0$ have a perfectly two-jet-like final state and events with $C = 1$ have an isotropic and coplanar distribution of final-state momenta.

These three variables are combined with ANN to form corresponding likelihood, kinematics likelihood ($\mathcal{L}_{kinematics}$). Such three input variables for the ANN and $\mathcal{L}_{kinematics}$ for b are shown in Fig. 4.20(a)-(d).

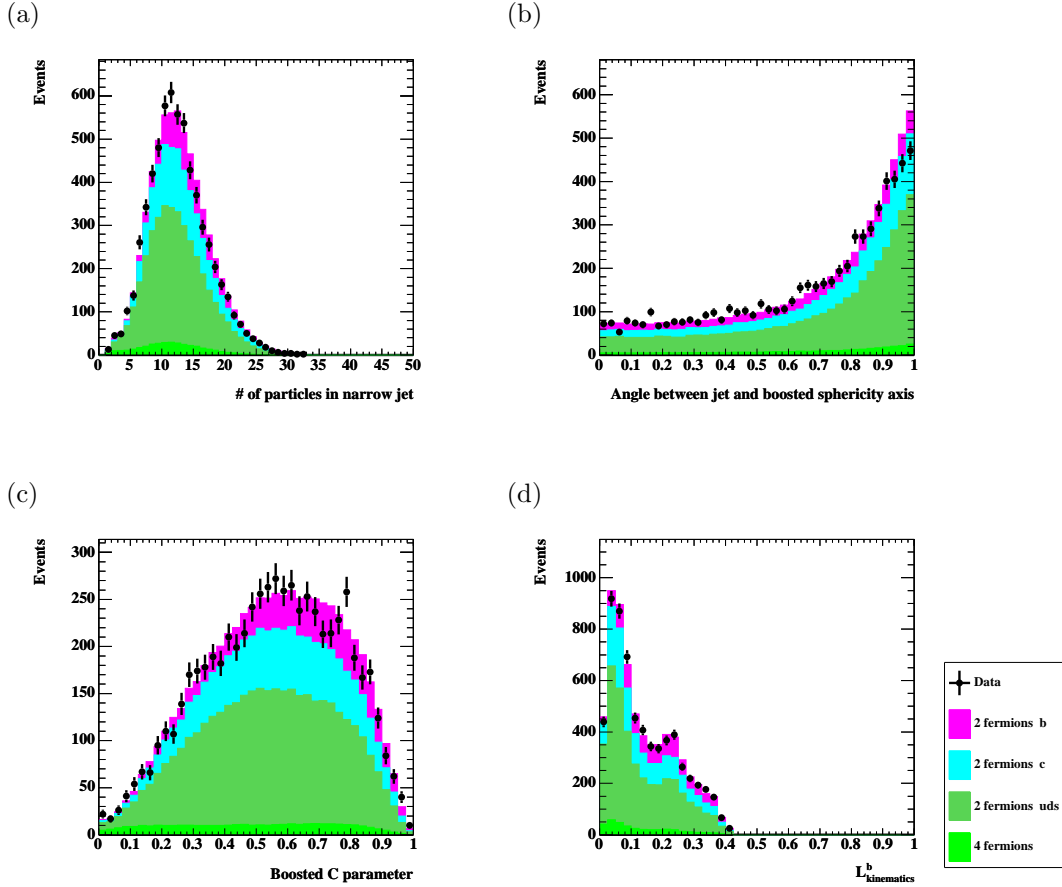


Figure 4.20: The input variables for the kinematics ANN and kinematics likelihood. (a) The number of tracks and clusters in the narrow jet. (b) The angle between the jet axis and the boosted supercity axis. (c) The boosted C parameter. (d) $\mathcal{L}_{kinematics}$ for b .

Combined Likelihood Tag

Three kinds of likelihood variables corresponding to three kinds of tags of the lifetime, lepton and kinematics tags for each hemisphere yield 6 likelihood variables. For each likelihood variable, probability densities for the $b\bar{b}$, $c\bar{c}$ and the remaining $u\bar{u}$, $d\bar{d}$, $s\bar{s}$ events are calculated as f_b , f_c and f_{uds} , respectively. Superscripts are used to indicate the kind of likelihood and hemisphere. For example, $f_b^{lifetime,1}$ means probability density for $b\bar{b}$ events in the hemisphere 1 corresponding to the lifetime tag. A combined probability is

defined as

$$f_{\text{b}}^{\text{comb}} = f_{\text{b}}^{\text{lifetime}} f_{\text{b}}^{\text{lepton}} f_{\text{b}}^{\text{kinematics}}. \quad (4.9)$$

The 6 variables mentioned above are combined to form event likelihood ($\mathcal{L}_{\text{event}}$) with unbinned likelihood as,

$$\mathcal{L}_{\text{event}}^{\text{b}} = \frac{R_{\text{b}} f_{\text{b}}^{\text{comb},1} f_{\text{b}}^{\text{comb},2}}{R_{\text{b}} f_{\text{b}}^{\text{comb},1} f_{\text{b}}^{\text{comb},2} + R_{\text{c}} f_{\text{c}}^{\text{comb},1} f_{\text{c}}^{\text{comb},2} + R_{\text{uds}} f_{\text{uds}}^{\text{comb},1} f_{\text{uds}}^{\text{comb},2}}, \quad (4.10)$$

$$\mathcal{L}_{\text{event}}^{\text{c}} = \frac{R_{\text{c}} f_{\text{c}}^{\text{comb},1} f_{\text{c}}^{\text{comb},2}}{R_{\text{b}} f_{\text{b}}^{\text{comb},1} f_{\text{b}}^{\text{comb},2} + R_{\text{c}} f_{\text{c}}^{\text{comb},1} f_{\text{c}}^{\text{comb},2} + R_{\text{uds}} f_{\text{uds}}^{\text{comb},1} f_{\text{uds}}^{\text{comb},2}}, \quad (4.11)$$

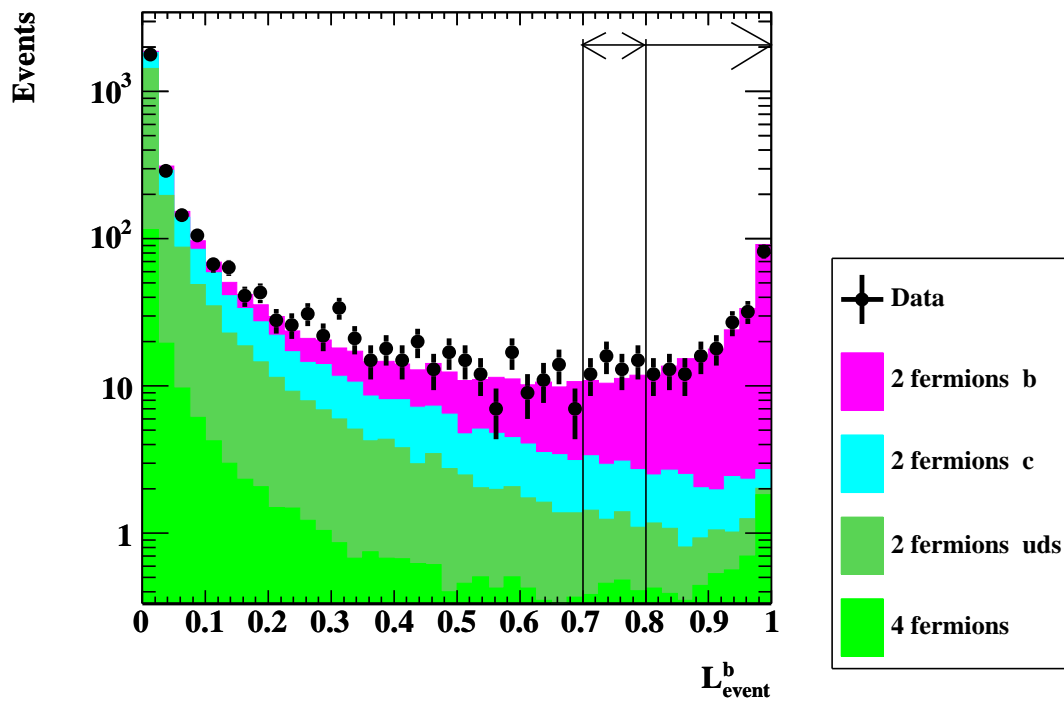
$$\mathcal{L}_{\text{event}}^{\text{uds}} = \frac{R_{\text{uds}} f_{\text{uds}}^{\text{comb},1} f_{\text{uds}}^{\text{comb},2}}{R_{\text{b}} f_{\text{b}}^{\text{comb},1} f_{\text{b}}^{\text{comb},2} + R_{\text{c}} f_{\text{c}}^{\text{comb},1} f_{\text{c}}^{\text{comb},2} + R_{\text{uds}} f_{\text{uds}}^{\text{comb},1} f_{\text{uds}}^{\text{comb},2}} \quad (4.12)$$

The distributions of event likelihood for b ($\mathcal{L}_{\text{event}}^{\text{b}}$), for c ($\mathcal{L}_{\text{event}}^{\text{c}}$) and for uds ($\mathcal{L}_{\text{event}}^{\text{uds}}$) are shown in Fig. 4.21(a), (b) and (c), respectively. The performance of each b-tagging variable is shown in Fig. 4.22(a). The c-tagging and uds-tagging performance for c and uds event likelihood are shown in Fig. 4.22(b), (c), respectively. A significance of inclusive analysis (inclusive significance) is defined as

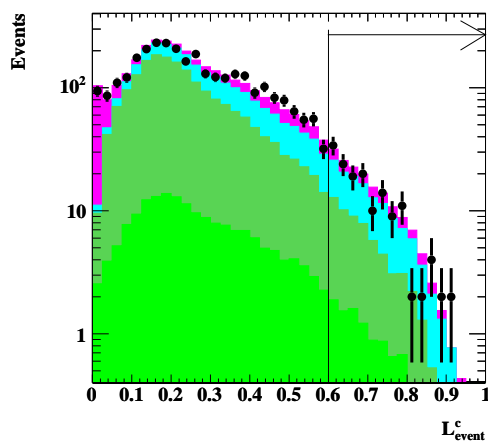
$$\mathcal{P}_{\text{sig}}^{(\text{inclusive})} \equiv (2P_{\text{b}} - 1) \mathcal{L}_{\text{event}}^{\text{b}}, \quad (4.13)$$

where P_{b} is the charge identification probability defined in subsection 4.6.1 for b quarks.

(a)



(b)



(c)

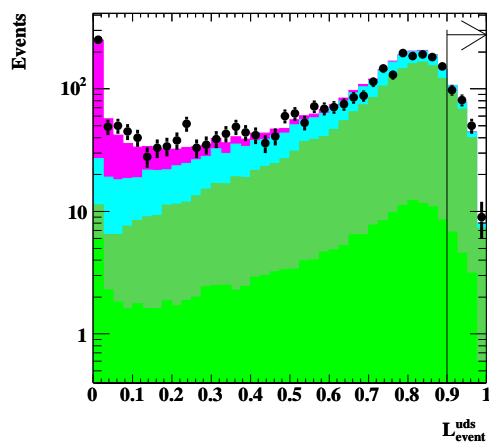
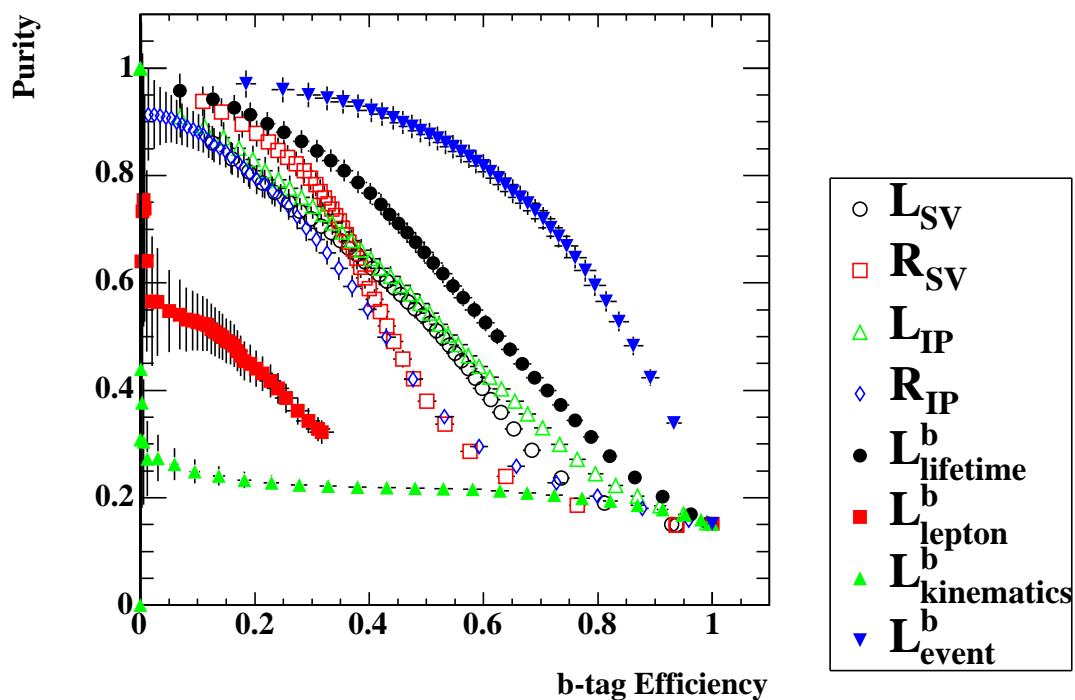
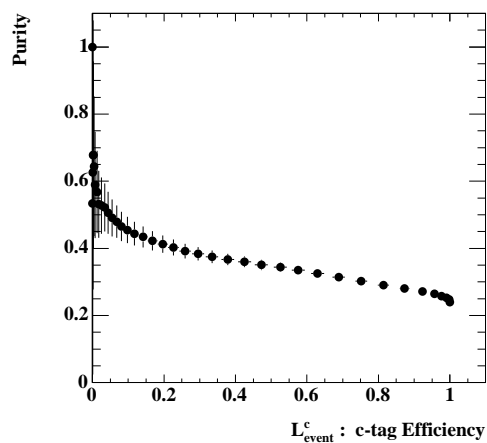


Figure 4.21: The event likelihood of (a) $\mathcal{L}_{\text{event}}^b$, (b) $\mathcal{L}_{\text{event}}^c$ and (c) $\mathcal{L}_{\text{event}}^{\text{uds}}$. The lines indicate cut position used in the event classification in the next section.

(a)



(b)



(c)

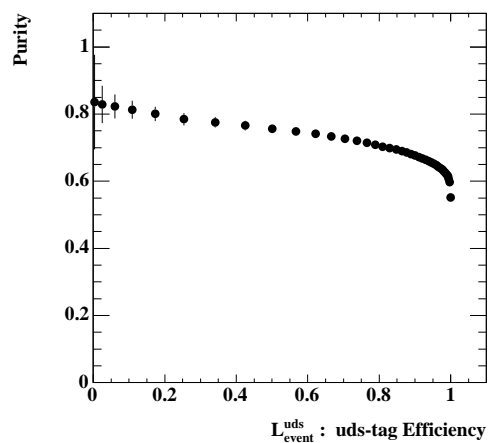


Figure 4.22: (a) The b-tag performance and (b) c-tag performance and (c) uds-tag performance of LB.

Event Classification with b-tagging variables

Event classification is performed with the $\mathcal{L}_{\text{event}}^b$, $\mathcal{L}_{\text{event}}^c$ and $\mathcal{L}_{\text{event}}^{uds}$ in order to obtain event sub-samples with high sensitivities to the $A_{\text{FB}}^{b,c}$. The two thresholds of 0.8 and 0.7 are assigned to $\mathcal{L}_{\text{event}}^b$ and a threshold of 0.6 is assigned to $\mathcal{L}_{\text{event}}^c$ and a threshold of 0.9 is assigned to $\mathcal{L}_{\text{event}}^{uds}$, which are indicated in Fig. 4.21. With these thresholds, event classification is performed as,

$$\text{classI} : 0.8 < \mathcal{L}_{\text{event}}^b, \quad (4.14)$$

$$\text{classII} : 0.7 < \mathcal{L}_{\text{event}}^b < 0.8, \quad (4.15)$$

$$\text{classIII} : \mathcal{L}_{\text{event}}^b < 0.7 \text{ and } 0.6 < \mathcal{L}_{\text{event}}^c, \quad (4.16)$$

$$\text{classIV} : \mathcal{L}_{\text{event}}^b < 0.7 \text{ and } \mathcal{L}_{\text{event}}^c < 0.6 \text{ and } 0.9 < \mathcal{L}_{\text{event}}^{uds}, \quad (4.17)$$

$$\text{classV} : \mathcal{L}_{\text{event}}^b < 0.7 \text{ and } \mathcal{L}_{\text{event}}^c < 0.6 \text{ and } \mathcal{L}_{\text{event}}^{uds} < 0.9. \quad (4.18)$$

These threshold values are optimized to get accurate values of A_{FB} . The angular distributions corresponding to each b, c-tagging subclass are shown in Fig. 4.23, where the quark direction is evaluated with

$$-\text{sign}(Q_{\text{F}} - Q_{\text{B}}) \cdot |\cos \theta_{\text{thrust}}|. \quad (4.19)$$

The sample of class I is most sensitive to the A_{FB}^b with less correlations to other A_{FB} . The class II still has high sensitivity to the A_{FB}^b with small correlations to other A_{FB} . The class III is sensitive to the A_{FB}^c but included large correlations to other A_{FB} . The class IV is sensitive to the $A_{\text{FB}}^{\text{uds}}$ which is defined as

$$A_{\text{FB}}^{\text{uds}} = -f_d A_{\text{FB}}^d + f_u A_{\text{FB}}^u - f_s A_{\text{FB}}^s. \quad (4.20)$$

where f_u is the $u\bar{u}$ event fraction to the sum of $u\bar{u}$, $d\bar{d}$ and $s\bar{s}$ events. The f_d and f_s are defined similarly. The variable $A_{\text{FB}}^{\text{uds}}$ is meaningful only when the f_u , f_d and f_s are stable against the b-tagging. The stabilities are natural because the b-tagging has little power to separate $u\bar{u}$, $d\bar{d}$ and $s\bar{s}$ events and it is checked with MC to find that the deviations are within the statistical fluctuations. The class V is less sensitive to A_{FB} due to the large contaminations of each flavor. It would also increase the correlations between A_{FB}^b , A_{FB}^c and $A_{\text{FB}}^{\text{uds}}$. Therefore A_{FB} fits are performed to the class I,II,III and IV. The events in the class V are rejected at the final event selection.

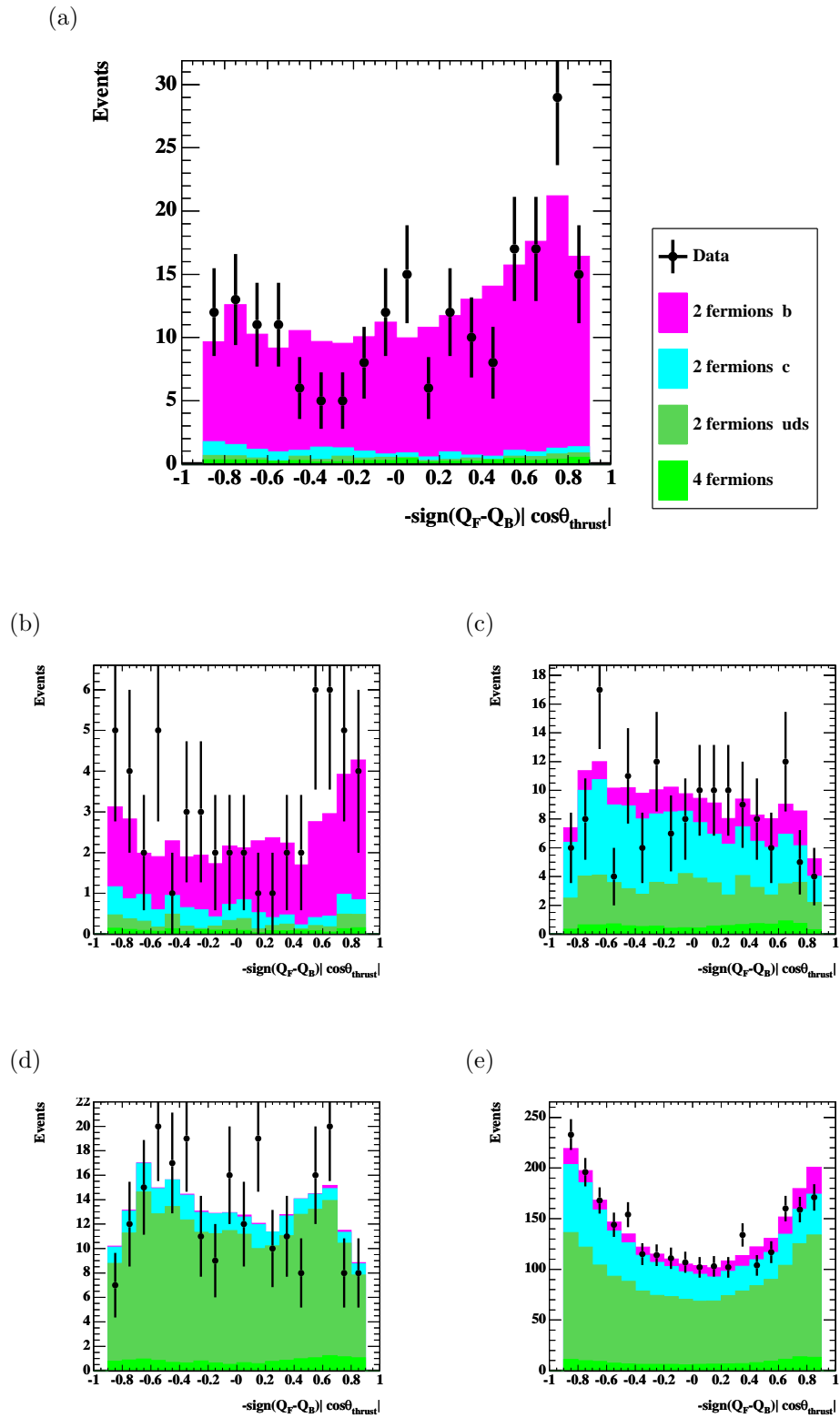


Figure 4.23: Angular distributions corresponding to each b-tag subclass, (a) class I, (b) class II, (c) class III, (d) class IV and (e) class V.

4.6.3 Unbinned Likelihood Fit

Finally, events in the b-tag event class V are rejected as described in the section 4.6.2. Consequently, two charge identification class (inner and outer class) for each b-tag event class yield 8 event subclasses. Angular distributions corresponding to the 8 subclasses are shown in Fig. 4.24 and the numbers of events are shown in Table. 4.5. A probability density function is constructed according as the A_{FB} and unbinned likelihood fit is performed to each subsample.

Table 4.5: The numbers of events in each subclass at \sqrt{s} of 189 GeV.

charge ID b-tag	inner class				outer class				sum
	I	II	III	IV	I	II	III	IV	
Data	252				407				659
	93	23	55	81	119	33	98	157	
MC	100	19	67	65	122	25	98	171	671
(b)	91	13	11	0	112	18	18	1	267
(c)	5	3	31	8	4	3	43	19	120
(s)	0	0	5	14	0	0	8	38	67
(u)	0	0	8	20	1	0	14	63	109
(d)	0	0	6	17	0	0	7	39	73
(4-fermion)	2	0	4	4	2	0	6	10	32

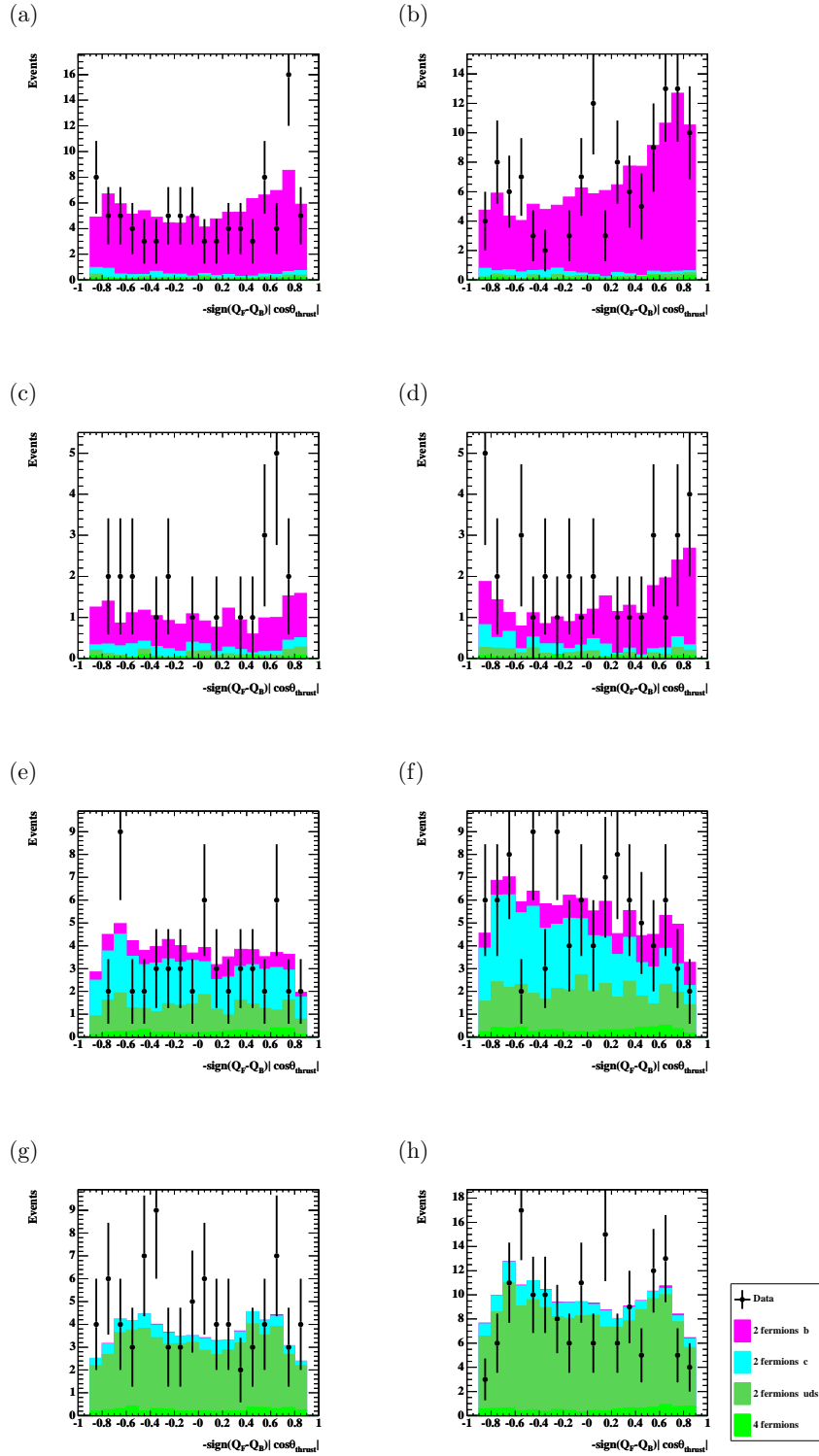


Figure 4.24: Angular distributions corresponding to each subclass constructed from event classifications concerning b-tag and charge identification. b-tag (a) b-tag class I, (c) b-tag class II, (e) b-tag class III, (g) b-tag class IV in the inner charge identification class and (b) b-tag class I, (d) b-tag class II, (f) b-tag class III, (h) b-tag class IV in the outer charge identification class.

Probability Density Function

The observed angular distribution can be written with A_{FB} for $\bar{b}\bar{b}$, $c\bar{c}$, $s\bar{s}$, $u\bar{u}$, $d\bar{d}$ and 4-fermion events as,

$$\frac{d\sigma^{obs}}{dx} = \mathcal{C}'(A_{\text{FB}}^{b,c,d,u,s,4f}) \sum_{q=b,c,d,u,s,4f} R_q \epsilon^q(x) \left[1 + x^2 + \frac{8}{3}(2P_q - 1)s_q A_{\text{FB}}^q x \right], \quad (4.21)$$

where

- $\mathcal{C}'(A_{\text{FB}}^{b,c,d,u,s,4f})$ is the normalization factor possibly depend on the A_{FB} ,
- R_q is the initial fraction of sample q ,
- x is the estimator of the emitting angle of primary quark:

$$x = -\text{sign}(Q_F - Q_B) |\cos \theta_{\text{thrust}}|, \quad (4.22)$$

- $\epsilon^q(x)$ is the event selection efficiency depend on x ,
- P_q is the charge identification probability
- s_q is 1 for both down-type quark and 4-fermion samples, -1 for up-type quark samples.

The event selections are performed so as to have dependence on θ_{thrust} only in the form of $|\cos \theta_{\text{thrust}}|$. If not, it would induce obvious bias on the A_{FB} . Hence $\epsilon^q(x)$ is naturally a symmetric function and it is checked with MC. Under such condition, the possible dependence to $A_{\text{FB}}^{b,c,d,u,s,4f}$ of normalization factor, \mathcal{C}' is vanished and it can be rewritten with a constant normalization factor, \mathcal{C} , as

$$\frac{d\sigma^{obs}}{dx} = \mathcal{C} \sum_{q=b,c,d,u,s,4f} R_q \epsilon^q(x) \left[1 + x^2 + \frac{8}{3}(2P_q - 1)s_q A_{\text{FB}}^q x \right] \quad (4.23)$$

If the function shapes of the $\epsilon^q(x)$ are the same for all q , the common function shape, $\epsilon(x)$ is extracted and the equation can be written as

$$\frac{d\sigma^{obs}}{dx} = \mathcal{C} \epsilon(x) \sum_{q=b,c,d,u,s,4f} \left[1 + x^2 + \frac{8}{3} F_q (2P_q - 1) s_q A_{\text{FB}}^q x \right], \quad (4.24)$$

$$\equiv \text{pdf}(x, A_{\text{FB}}^q), \quad (4.25)$$

where F_q is the event fraction of sample q after the final event selection. This function can be used as the probability density function ($\text{pdf}(x, A_{\text{FB}}^q)$) to fit the A_{FB} and the likelihood

\mathcal{L} can be written as,

$$\begin{aligned} \log \mathcal{L} &= \sum_{i \in \text{all data}} \log \text{pdf}(x_i, A_{\text{FB}}^q), & (4.26) \\ &= \sum_{i \in \text{all data}} \log \mathcal{C}\epsilon(x_i) \\ &+ \sum_{i \in \text{all data}} \log \left\{ \sum_{q=b,c,d,u,s,4f} \left[1 + x_i^2 + \frac{8}{3} F_q (2P_q - 1) s_q A_{\text{FB}}^q x_i \right] \right\} & (4.27) \end{aligned}$$

The first term is the constant term against the A_{FB} and can be removed from the likelihood function to fit the A_{FB} by maximizing the log likelihood. Accordingly simpler likelihood function is obtained as

$$\log \mathcal{L} = \sum_{i \in \text{all data}} \log \left\{ \sum_{b,c,d,u,s,4f} \left[1 + x_i^2 + \frac{8}{3} F_q (2P_q - 1) s_q A_{\text{FB}}^q x_i \right] \right\}. \quad (4.28)$$

If $A_{\text{FB}}^{\text{uds}}$ is introduced as

$$A_{\text{FB}}^{\text{uds}} \equiv \sum_{q=d,u,s} F_q s_q A_{\text{FB}}^q \quad (4.29)$$

and the equation can be written in terms of $A_{\text{FB}}^{\text{uds}}$ as,

$$\log \mathcal{L} = \sum_{i \in \text{all data}} \log \left\{ \sum_{b,c,uds,4f} \left[1 + x_i^2 + \frac{8}{3} F_q (2P_q - 1) s_q A_{\text{FB}}^q x_i \right] \right\}, \quad (4.30)$$

where P_{dus} is defined to keep the identity between the two equations and s_{dus} is set to 1.

Probability Density Function with Subsamples

The data have already been divided into 8 subsamples with different sensitivities to A_{FB}^b , A_{FB}^c and $A_{\text{FB}}^{\text{uds}}$. In order to realize the condition that the function shapes of $\epsilon_q(x)$ are the same among each $q\bar{q}$ and 4-fermion, the angular region is symmetrically divided into 3 regions as,

- Central Region : $|\cos \theta_{\text{thrust}}| < 0.65$,
- Transition Region : $0.65 < |\cos \theta_{\text{thrust}}| < 0.8$,
- Endcap Region : $0.8 < |\cos \theta_{\text{thrust}}|$.

In such a region, the requirement of the same function shapes of $\epsilon_q(x)$ is fulfilled well checked with MC and the division is altered to 2 or 4 to check the stability and to

evaluate corresponding systematic error. Consequently, the A_{FB} fitting is performed for 24 subsamples. The probability density function described in the previous section are adjusted to the condition as,

$$\log \mathcal{L} = \sum_{j \in \text{all subsamples}} \log \mathcal{L}_{\text{sub}}^j \quad (4.31)$$

where likelihood function in the subsample $\mathcal{L}_{\text{sub}}^j$ is defined as,

$$\log \mathcal{L}_{\text{sub}}^j = \sum_{i \in \text{subsample } j} \log \left\{ \sum_{b,c,uds,4f} \left[1 + x_i^2 + \frac{8}{3} F_q^j (2P_q^j - 1) s_q A_{\text{FB}}^q x_i \right] \right\}. \quad (4.32)$$

The definition of A_{FB}^{uds} is no longer valid since the event ratio among $u\bar{u}$, $d\bar{d}$ and $s\bar{s}$ samples are differ between the two charge identification classes although it is stable against the b-tag classes. The A_{FB}^{uds} is redefined separately in the two charge identification classes as,

$$A_{\text{FB}}^{dus,\text{in}} \equiv \sum_{q=d,u,s} F_q^{\text{in}} s_q A_{\text{FB}}^q \quad (4.33)$$

$$A_{\text{FB}}^{dus,\text{out}} \equiv \sum_{q=d,u,s} F_q^{\text{out}} s_q A_{\text{FB}}^q \quad (4.34)$$

, where F_q^{in} and F_q^{out} are the event fraction in the inner or outer charge identification class respectively.

Accordingly, the charge identification probabilities, flavor composition and 4-fermion contamination are evaluated in each subsample and the fitting of the 4 parameters, A_{FB}^b , A_{FB}^c , $A_{\text{FB}}^{uds,\text{in}}$ and $A_{\text{FB}}^{uds,\text{out}}$ is performed simultaneously. As regards the A_{FB} of the 4-fermion sample (A_{FB}^{4f}), an observed A_{FB} ($A_{\text{FB}}^{\text{obs},4f}$) is defined as

$$A_{\text{FB}}^{\text{obs},4f} \equiv (2P_{4f} - 1) s_{4f} A_{\text{FB}}^{4f}. \quad (4.35)$$

The $A_{\text{FB}}^{\text{obs},4f}$ is set to zero in the fitting. The possible contribution from the non-zero A_{FB}^{4f} is evaluated with Monte Carlo and is added to the systematic error.

Fitting

Fitting is performed to maximize the $\log \mathcal{L}$ and the following values are obtained at \sqrt{s} of 189 GeV as

$$\begin{aligned} A_{\text{FB}}^b &= 0.56 \quad {}^{+0.15}_{-0.16}, \\ A_{\text{FB}}^c &= 0.59 \quad {}^{+0.47}_{-0.48}, \\ A_{\text{FB}}^{uds,\text{in}} &= -0.63 \quad \pm 0.98, \\ A_{\text{FB}}^{uds,\text{out}} &= -0.058 \quad \pm 0.18, \end{aligned} \quad (4.36)$$

with a correlation matrix of

$$\begin{pmatrix} 1.00 & 0.29 & 0.03 & 0.09 \\ 0.29 & 1.00 & 0.16 & 0.51 \\ 0.03 & 0.16 & 1.00 & 0.08 \\ 0.09 & 0.51 & 0.08 & 1.00 \end{pmatrix}. \quad (4.37)$$

The contour plot corresponding to the 189 GeV result is shown in Fig. 4.25. The results for each energy point are shown in Table. 4.6. If $|A_{\text{FB}}|$ exceeds 0.75, the A_{FB} is unphysical. However the unphysical fitted value of the A_{FB} is possible, since the observed A_{FB} in the physical region as shown in Fig. 4.24 is converted according to the sample composition and the charge identification probabilities.

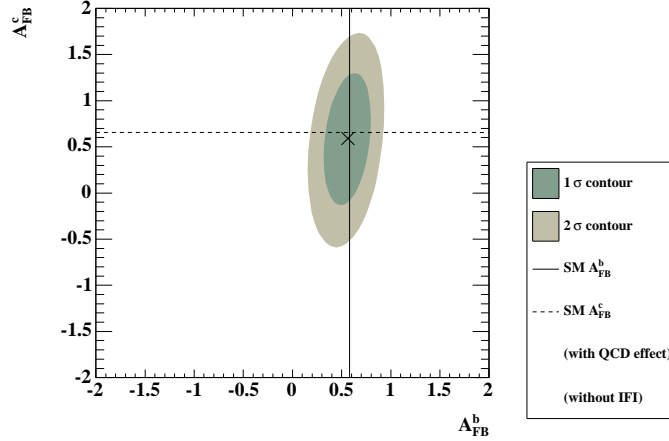


Figure 4.25: A one σ and two σ contours of the $A_{\text{FB}}^{\text{b,c}}$ result are shown.

Table 4.6: Results for the inclusive analysis with statistical errors.

E_{cm} [GeV]	A_{FB}^{b} (stat.)	$A_{\text{FB}}^{\text{b,SM}}$	A_{FB}^{c} (stat.)	$A_{\text{FB}}^{\text{c,SM}}$	Correlation
91	0.10 \pm 0.03	0.10	0.05 \pm 0.18	0.06	0.31
133	0.61 $^{+0.30}_{-0.32}$	0.48	2.50 $^{+0.93}_{-1.21}$	0.69	0.35
161	0.15 $^{+0.36}_{-0.37}$	0.55	-0.65 $^{+1.82}_{-2.10}$	0.67	0.33
172	1.53 $^{+0.37}_{-0.48}$	0.56	-0.29 $^{+1.33}_{-1.23}$	0.67	0.53
183	1.17 $^{+0.23}_{-0.26}$	0.58	2.30 $^{+0.63}_{-0.73}$	0.66	0.29
189	0.56 $^{+0.15}_{-0.16}$	0.58	0.59 $^{+0.47}_{-0.48}$	0.66	0.29
192	0.78 $^{+0.37}_{-0.42}$	0.58	-0.21 $^{+2.02}_{-1.81}$	0.65	0.42
196	0.46 $^{+0.30}_{-0.31}$	0.58	-0.63 $^{+0.92}_{-0.89}$	0.65	0.34
200	0.34 \pm 0.35	0.59	0.87 $^{+1.03}_{-1.07}$	0.65	0.26
202	0.07 $^{+0.46}_{-0.47}$	0.59	-0.37 $^{+1.30}_{-1.27}$	0.65	0.35
205	0.48 $^{+0.27}_{-0.28}$	0.59	0.60 $^{+0.78}_{-0.81}$	0.65	0.35
207	0.29 \pm 0.22	0.59	1.19 $^{+0.64}_{-0.66}$	0.64	0.31

4.6.4 Corrections Applied to the Fitted Values of A_{FB}

The fitted values of A_{FB} correspond to the distribution of initial-quark hemisphere $\times |\cos \theta_{\text{thrust}}|$ after the preselection. The shifts of the A_{FB} in the preselection should be corrected. The QCD effect should be recovered. The fitted values includes the effect of the ISR-FSR interference, which should be removed finally.

Biases in the Event Preselection The thrust axis is the good estimator of the initial quark direction, which is shown in Table. 4.7. The shifts of the A_{FB} at each stage of the event preselection are also shown.

Table 4.7: The A_{FB} shifts in the pre-selection for the initial-quark direction.

variable	cut	A_{FB}^{b}	$\Delta A_{\text{FB}}^{\text{b}}$	A_{FB}^{c}	$\Delta A_{\text{FB}}^{\text{c}}$
$\cos \theta_{\text{initialquark}}$	true s'	0.586 \pm 0.005		0.679 \pm 0.003	
(initial-quark hemisphere) $\times \cos \theta_{\text{thrust}} $	true s'	0.583 \pm 0.005	-0.003	0.674 \pm 0.003	-0.005
	measured s'	0.557 \pm 0.005	-0.026	0.657 \pm 0.003	-0.017
	+L2MH.	0.558 \pm 0.005	0.001	0.657 \pm 0.003	-0.000
	+4f rej.	0.562 \pm 0.005	0.004	0.660 \pm 0.003	0.003
	+ $ \cos \theta $ cut	0.569 \pm 0.006	0.008	0.667 \pm 0.004	0.007
Sum			-0.016		-0.012

QCD Correction The QCD effect is evaluated with the ZFITTER as shown in Table. 4.8.

Table 4.8: The QCD effect to the A_{FB} evaluated with the ZFITTER.

cut	A_{FB}^{b}	$\Delta A_{\text{FB}}^{\text{b}}$	A_{FB}^{c}	$\Delta A_{\text{FB}}^{\text{c}}$
with QCD, without IFI	0.580		0.656	
without QCD, without IFI	0.596	0.016	0.677	0.021

IFI effect The IFI effect included in the fitted value is evaluated with the ZFITTER as shown in Table. 4.9.

Table 4.9: The IFI effect evaluated with the ZFITTER..

cut	A_{FB}^{b}	$\Delta A_{\text{FB}}^{\text{b}}$	A_{FB}^{c}	$\Delta A_{\text{FB}}^{\text{c}}$
without QCD, without IFI	0.596		0.677	
without QCD, with IFI	0.601	0.005	0.668	-0.009

Total Correction The total corrections to be applied to the fitted A_{FB} are shown in Table. 4.10. These corrections are already included in the results on Table 4.6, since these corrections have been applied in the fitting procedure.

Table 4.10: The total correction to be added to the fitted A_{FB} . The error was due to the MC statistics used for evaluating the shift in the event preselection.

item	correction to the fitted A_{FB}^{b}	correction to the fitted A_{FB}^{c}
IFI	-0.005	0.009
QCD	-0.016	-0.021
pre-selection	0.028 \pm 0.007	0.022 \pm 0.004
sum	0.007 \pm 0.007	0.010 \pm 0.004

4.7 Lepton Analysis

The thrust axis is used to estimate the primary quark direction also in the lepton analysis. Leptons from semileptonic decay of bottom or charm hadrons (prompt leptons) are characteristics in their high momentum and high transverse momentum, which are used to identify the $b\bar{b}$ or $c\bar{c}$ events. Their charges are used to distinguish whether the leptons come from quarks or anti-quarks. In spite of the neutral B meson mixing, the quark-hemisphere identification with the lepton charge is still remarkable compared with that in the inclusive analysis, which makes the lepton analysis significant compensating the lower statistics due to the small branching ratio of the semileptonic decays.

In this section, the description about the prompt lepton is given at first. Then the description about the lepton analysis is followed. Lepton (electron or muon) tracks are selected with the OPAL electron [83] and muon [42] identification from the preselected events in the section 4.5. The conversion electrons are tagged with the OPAL conversion-electron finder [83] and are rejected. From the lepton tracks, the prompt-lepton tracks are selected and are classified by their flavors with an ANN constructed to discriminate the prompt leptons. Then events with the prompt leptons are selected with the information of the the prompt-lepton tracks and their angular distributions are evaluated with both the lepton charge and the thrust axis, which are fitted with unbinned likelihood fitting to obtain the A_{FB}^{b} and A_{FB}^{c} simultaneously.

4.7.1 Prompt Leptons

Leptons (electrons and muons) produced in semileptonic decays of bottom and charm hadrons usually are referred to as prompt leptons. Such leptons carry and hold the

information of the direction and the charge of the primary quark. In this analysis following prompt leptons are treated as signals, where ℓ represents an electron or a muon.

- $b \rightarrow \ell$

Leptons coming directly from the weak decays of b hadrons.

- $b \rightarrow \tau \rightarrow \ell$

Electrons and muons from leptonic τ decays where the τ lepton comes from a direct b decay.

- $b \rightarrow c \rightarrow \ell$

Leptons from semileptonic decays of c hadrons to which b hadrons decay.

- $b \rightarrow \bar{c} \rightarrow \ell$

Leptons from semileptonic decays of anti-c hadrons to which b hadrons decay.

- $c \rightarrow \ell$

Leptons coming directly from the weak decay of primary c hadrons.

Leptons from $c\bar{c}$ mesons, e.g. $b \rightarrow J/\psi \rightarrow \ell^+\ell^-$ decays, are included within the $b \rightarrow c \rightarrow \ell$ or $b \rightarrow \bar{c} \rightarrow \ell$ with the appropriate sign.

The relationships between the lepton charge and its parent primary quark or antiquark are important issues. The $b \rightarrow \ell$, $b \rightarrow \tau \rightarrow \ell$, $b \rightarrow \bar{c} \rightarrow \ell$ and $c \rightarrow \ell$ have the same sign of lepton charge as the primary quark's, while the $b \rightarrow c \rightarrow \ell$ have the opposite sign. From the point of such view, $b \rightarrow \ell$, $b \rightarrow \tau \rightarrow \ell$ and $b \rightarrow \bar{c} \rightarrow \ell$ are unified to $b\ell^-$ sample and $b \rightarrow c \rightarrow \ell$ and $c \rightarrow \ell$ were newly termed $b\ell^+$ and $c\ell^+$, respectively.

The opposite sign of the lepton charge to that of the primary quark in the $b\ell^+$ sample dilutes the charge identification performance. The existence of $B^0 - \bar{B}^0$ mixing also introduces another dilution. Leptons from these mixed B mesons are classified according to the decaying b quark. For example, $b \rightarrow \bar{b} \rightarrow \bar{c} \rightarrow \bar{\ell}$ is treated as $b \rightarrow c \rightarrow \ell$. The $B^0 - \bar{B}^0$ mixing at LEP is characterized by a mixing parameter ($\bar{\chi}$) which is the expectation value of mixing rate including the contribution of both B^0 and B_s^0 . The $\bar{\chi}$ was measured to be 0.1257 ± 0.0042 [51]. The observed A_{FB} is decreased by a factor of $(1 - 2\bar{\chi})$ effectively due to the mixing.

4.7.2 Lepton Identification

Electron Identification

The selection of electrons relies mainly on the dE/dx and the reconstructed energy in the ECAL. After the preselection described in section 4.5, electron candidates are preselected and then discriminated with an ANN.

Electron candidates are preselected with following criteria,

1. The momentum is larger than 2 GeV.
2. The number of hits used in the dE/dx measurements in the CJ is larger than or equal to 20.
3. The difference between the measured energy loss and that expected for an electron, divided by the measurement error, is required to be between -2 and 4 . Such quantity is termed normalized energy loss $((dE/dx)_{norm})$.

After the preselection, the electron identification ANN is performed separately in the barrel region ($|\cos\theta| < 0.8$) and in the endcap region ($|\cos\theta| > 0.8$). The ANN input variables in the barrel region are

- the track momentum,
- the absolute polar angle of the track,
- the normalized energy loss $((dE/dx)_{norm})$,
- the dE/dx measurement error,
- the energy deposited in the ECAL in a cone of half-angle 30 mrad around the track, divided by the track momentum, (Such energy in the cone is termed E_{cone} .)
- the number of lead glass blocks used to calculate E_{cone} .

In the endcap, two additional variables are used:

- the difference in the polar angle between the track position extrapolated to the ECAL and the center of the associated cluster,
- the corresponding difference in ϕ .

The $(dE/dx)_{norm}$ and the output of the electron identification ANN (\mathcal{N}_{el}) are shown in Fig. 4.26. In addition to the electron preselection, the \mathcal{N}_{el} is required to be larger than 0.9, with which the efficiency for selecting prompt electrons is approximately 25% at 189 GeV. The resulting sample is 75% pure in electrons.

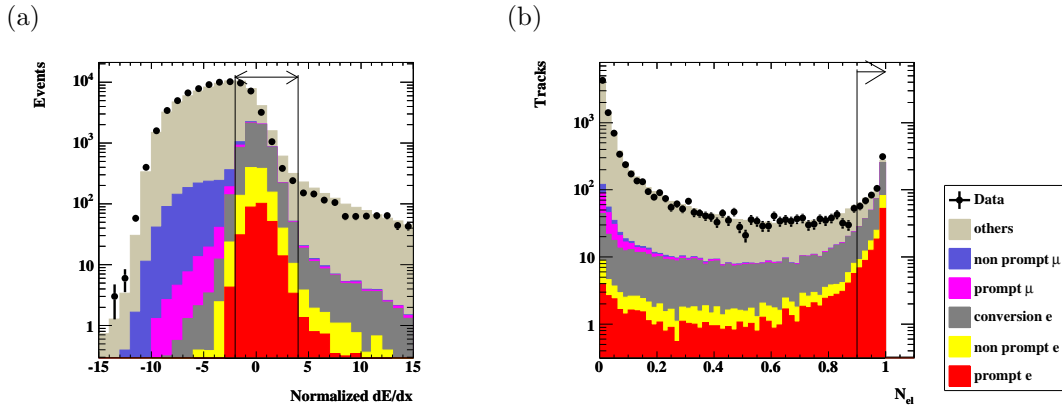


Figure 4.26: (a) The normalized dE/dx before electron preselection and (b) \mathcal{N}_{el} after the preselection of the electron identification.

After this selection, electrons from photon conversions (conversion electrons) are a dominant background to prompt electrons. A separate ANN is used to identify pairs of conversion electrons (conversion ANN), where track pairs are made by associating a track with all the other tracks. The nine inputs of the conversion ANN, related to whether a pair of tracks formed a vertex compatible with a photon conversion, are listed as follows.

- the distance in r - ϕ between the two tracks measured at points where the two tracks where parallel in r - ϕ plane.
- the radius of the first measured hit of both tracks, as well as the radius of their common vertex;
- the invariant mass of the pair assuming both tracks to be electrons and the impact parameter of the parent photon with respect to the primary vertex of the event;
- the two track momenta signed by their charge;
- the \mathcal{N}_{el} of the partner track.

The distribution of the ANN output (\mathcal{N}_{cv}) after the cut of $\mathcal{N}_{el} > 0.9$ is shown in Fig. 4.27. The contribution of the conversion electrons is reduced by requiring that the \mathcal{N}_{cv} is less than 0.4.

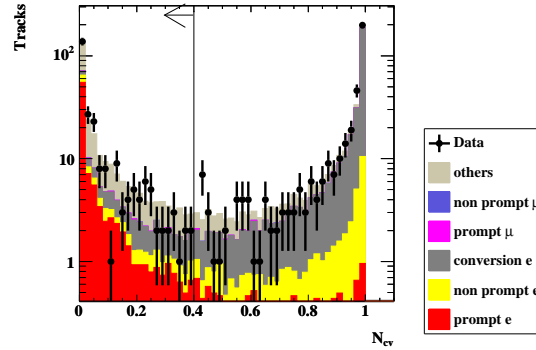


Figure 4.27: The \mathcal{N}_{cv} distribution after the cut of $\mathcal{N}_{el} > 0.9$.

Muon Identification

The identification of muons is based mainly on the matching of track segments reconstructed in the muon chamber with extrapolated tracks from the central detector. In addition, information both from the HCAL, where muons are expected to leave hits in all layers, and from the dE/dx in the CJ is used.

The muon track preselection is performed as follows.

- The momentum of the track is larger than 2 GeV.
- For each track segment in the muon chambers, only one track with “best matching” is selected, where the “best matching” means the track extrapolated to the muon detector has the smallest angular separation to the muon track segment.

Then further identification with an ANN (muon ANN) is performed. The ANN inputs are divided into 4 types as muon matching, HCAL, dE/dx and geometrical information. They are listed below.

- Information from the matching:
 - The square root of the χ^2 for the position match in θ and ϕ between the extrapolated track and the associated muon track segment in the muon chambers, as described in [84];
 - the ratio of distances of the best and second best matching track to the muon segment; this is a measure of how ambiguous the choice of the best matching track is in the preselection;
 - the χ^2 probability for the matching computed using both position and direction information for the track in the central detector and the associated muon track segment.

- Information from the hadron calorimeter:
 - The number of HCAL layers with hits in the cluster associated with the central track;
 - the layer number of the outermost HCAL layer with hits associated with the central track;
 - the χ^2 probability for the match in θ and ϕ between the track (extrapolated to the HCAL) and the associated cluster.
- Specific energy loss:
 - The muon dE/dx weight for the track, which is a measure of the probability that the track is compatible with a muon hypothesis;
 - $\sigma_{dE/dx}$, the error on the dE/dx measurement;
 - the momentum of the track.
- Geometrical information:
 - The position in $|\cos\theta|$ and ϕ where the extrapolated track enters the muon chambers.

The distribution of the muon best matching flag and the neural network output (\mathcal{N}_μ) is shown in Fig. 4.28. The \mathcal{N}_μ is required to be larger than 0.65, where the selection efficiency for the prompt muons are evaluated to be 43% and the muon purity is evaluated to be 73% with the MC at \sqrt{s} of 189 GeV.

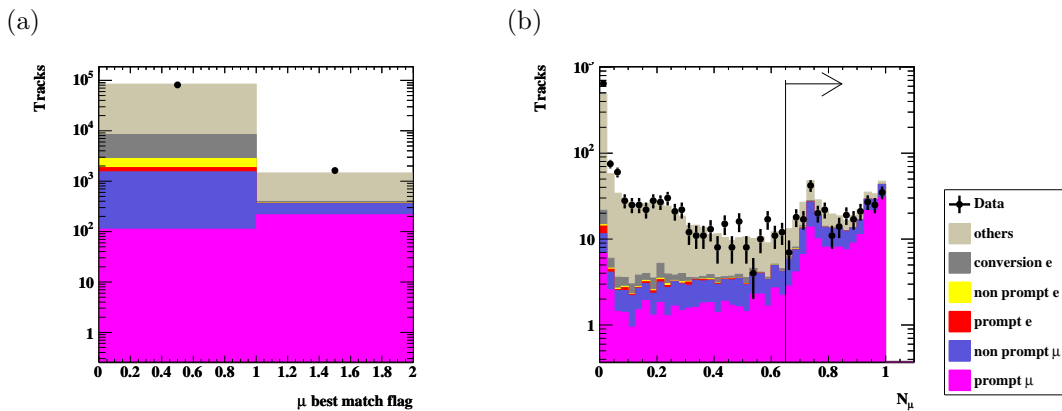


Figure 4.28: (a) The muon best match flag (1 means “best match”) for the tracks before the muon preselection and (b) \mathcal{N}_μ after the muon preselection.

4.7.3 b and c Tagging and Flavor Separation

Three types of prompt leptons, bl^- , bcl^+ and cl^+ , have different sensitivity to A_{FB}^b and A_{FB}^c . Hence it is important both to enhance them and also separate them. For the purpose, three ANNs are constructed separately for electrons and muons, \mathcal{N}_b to discriminate $b \rightarrow \ell$ tracks, \mathcal{N}_{bc} to discriminate $b \rightarrow c \rightarrow \ell$ tracks and \mathcal{N}_c to discriminate $c \rightarrow \ell$ tracks.

Construction of Artificial Neural Networks

All three ANNs giving track-by-track discrimination use the same input variables related to a track. As regards the track, three kinds of jets are used to construct some of the input variables. One is the jet containing the track, which is labeled as “associated jet”. The next is a jet with highest energy in the opposite hemisphere of the track, which is labeled as “other hemisphere jet”. The last is constructed with particles⁵ in the associated jet which are nearer to the track than the jet axis, which is labeled as “subset”. Each jet is formed with the cone algorithm (the half-angle of the cone is 0.55 radian and the minimum energy of 5 GeV). The ANN inputs are listed as follows.

- p , the track momentum;
- p_t , the transverse momentum of the track with respect to the jet axis of the associated jet, where the track is excluded in the calculation of the jet axis;
- E_{subset} , the energy of the subset;
- $E_{\text{jet}}^{\text{vis}}$, the sum of the energies of the particles within the associated jet;
- $\sum p_t$, scalar sum of the transverse momentum with respect to the ordinary jet axis in the associated jet;
- d/σ_d , the impact parameter significance in the three-dimensional space of the track with respect to the primary vertex, where the impact parameter is defined as the distance between the primary vertex and the track at the point of closest approach and its significance was defined as the impact parameter divided by its error;
- N_{fwd} , the number of tracks with d/σ_d larger than 2 (forward multiplicity) in the associated jet;
- L/σ_L , the decay length significances of the secondary vertexes (if existed) in the associated jet, where secondary vertexes’s are reconstructed in the three-dimensional spaces;

⁵tracks and unassociated clusters.

- L^o/σ_{L^o} , that corresponding to the other hemisphere jet;
- $Q_j \times Q_l$, the jet charges of the associated jet multiplied by the track charge, where the jet charge is defined as in Eq. 4.2 with $\kappa = 0.4$, but using only tracks associated to the jet;
- $Q_j^o \times Q_l$, that corresponding to the other hemisphere jet;
- \mathcal{N}_{el} and \mathcal{N}_{cv} , the outputs of the electron identification ANN and the photon conversion ANN respectively, used only in the case of tracks identified as electrons;
- \mathcal{N}_{μ} , the output of the muon identification ANN, used only in the case of tracks identified as muons;

The kinematic properties of the prompt leptons are best reflected to the two variables, p and p_t . In the direct decay ($b \rightarrow \ell$ or $c \rightarrow \ell$) the leptons tend to have large momentum due to the hard fragmentation of the b or c hadrons. The large mass of the b quark yields high lepton energies in the rest frame of the decaying b-hadrons. The transverse component is kept in the boost along the jet direction which resulted in the hard p_t spectrum of the $b \rightarrow \ell$, $b \rightarrow c \rightarrow \ell$ and $b \rightarrow \bar{c} \rightarrow \ell$ decays. The presence of a subjet is more characteristic of cascade decays ($b \rightarrow c \rightarrow \ell$ and $b \rightarrow \bar{c} \rightarrow \ell$), since the fragmentation of the secondary charm quarks is likely to form subjet near the lepton. The total jet energy, $E_{\text{jet}}^{\text{vis}}$, characterizes b-jets with semileptonic-decay leptons which are likely to have lower visible energy due to the emission of an energetic neutrino. The variable, $\sum p_t$, reflects the hard fragmentation and high multiplicity of the particles in b-jets. The variables d/σ_d , N_{fwd} , L/σ_L and L^o/σ_{L^o} reflect the long life time, hard fragmentation and high multiplicity in the decay of B mesons. The variables, $Q_j \times Q_l$ and $Q_j^o \times Q_l$ can separate the bl^+ leptons from bl^- and bcl^+ leptons. The bcl^+ leptons have the charge of opposite sign to that of their primary quarks, while bl^- and bcl^+ leptons have the charge of the same sign. Although the variables \mathcal{N}_{el} , \mathcal{N}_{cv} and \mathcal{N}_{μ} have already been used to remove non-prompt leptons, they are still used for the further separation of them.

With these input variables, 6 ANNs are constructed with JETNET [85]. These networks have only 1 hidden layer and the number of nodes in the hidden layer is optimized. More general description of the ANN is given in appendix D, where the structure of the \mathcal{N}_b is shown in Fig. D.4, for example. The training of the ANNs are done with events in the multi-hadronic MC at \sqrt{s} of 192 GeV after the lepton selection. For \mathcal{N}_b , only $b \rightarrow \ell$ leptons are used as signal and other tracks are used as background. The input variables for electrons are shown in Fig. 4.29 and those for muons are shown in Fig. 4.30. The outputs of the ANNs are shown in Fig. 4.31.

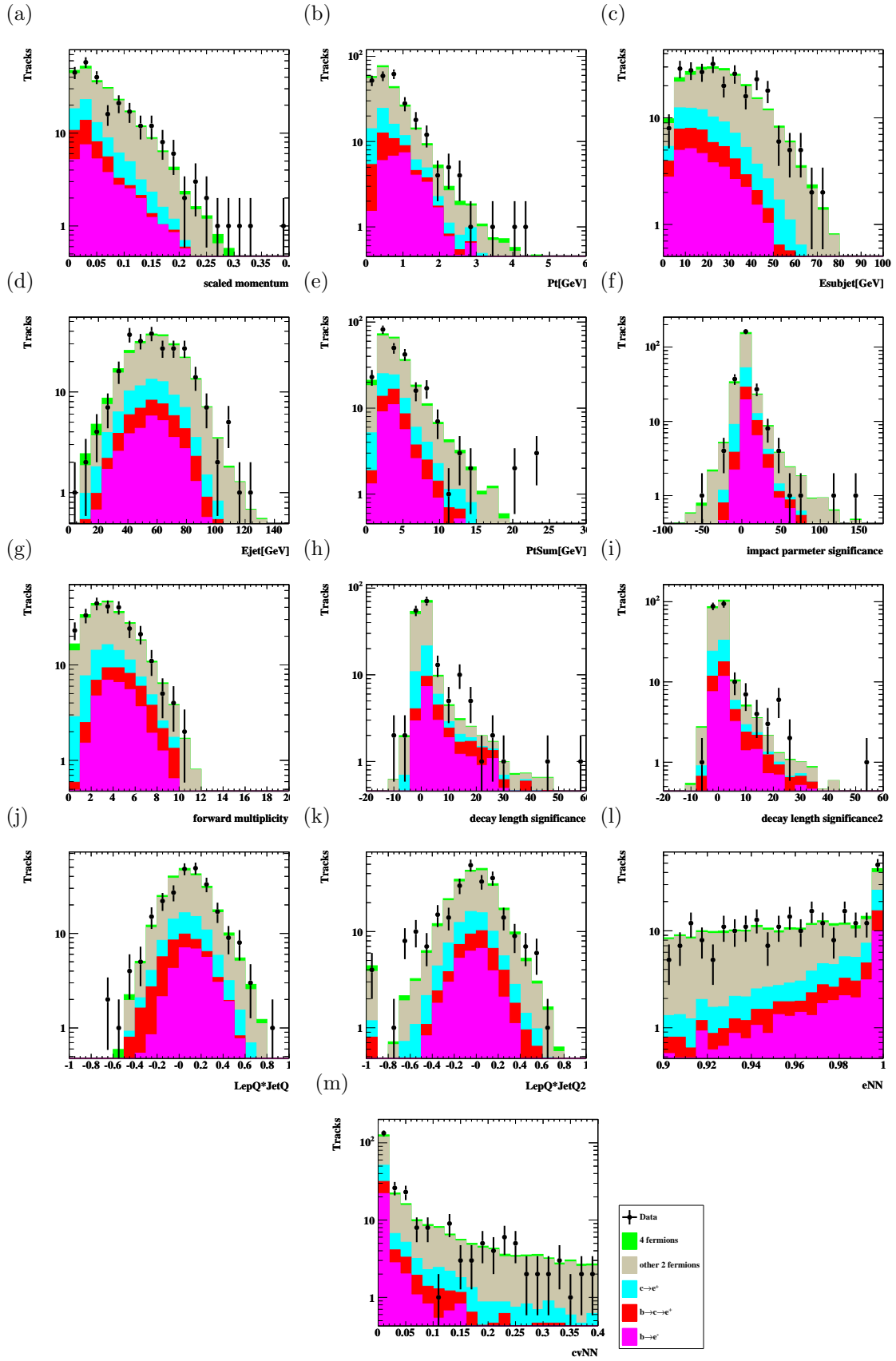


Figure 4.29: (a)-(m) The distributions of input variables for electron \mathcal{N}_b , \mathcal{N}_{bc} and \mathcal{N}_c after electron selection. The name of the variable are shown in the x-axis in each figure.

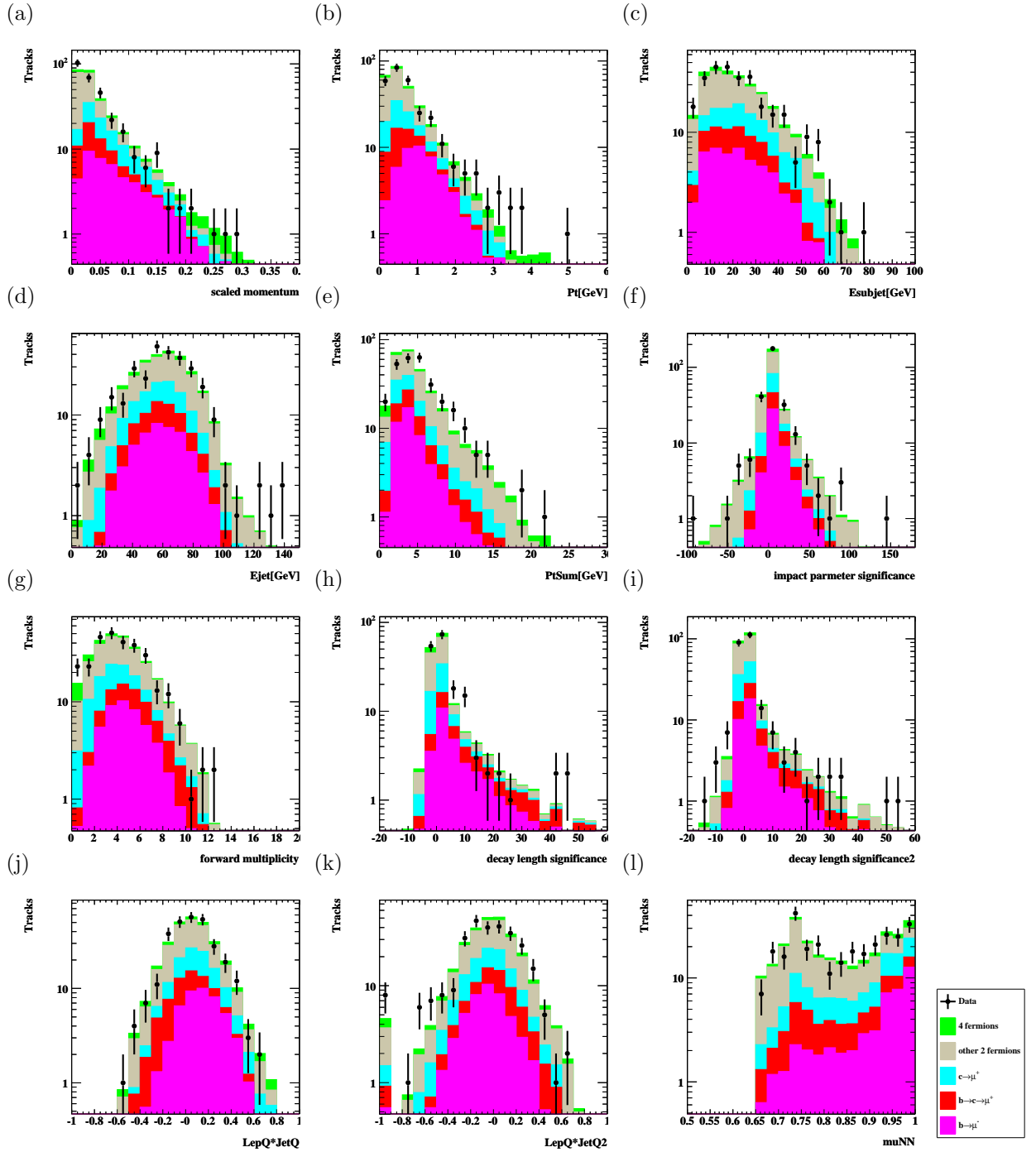


Figure 4.30: (a)-(l) The distributions of input variables for muon \mathcal{N}_b , \mathcal{N}_{bc} and \mathcal{N}_c after electron selection. The name of the variable are shown in the x-axis in each figure.

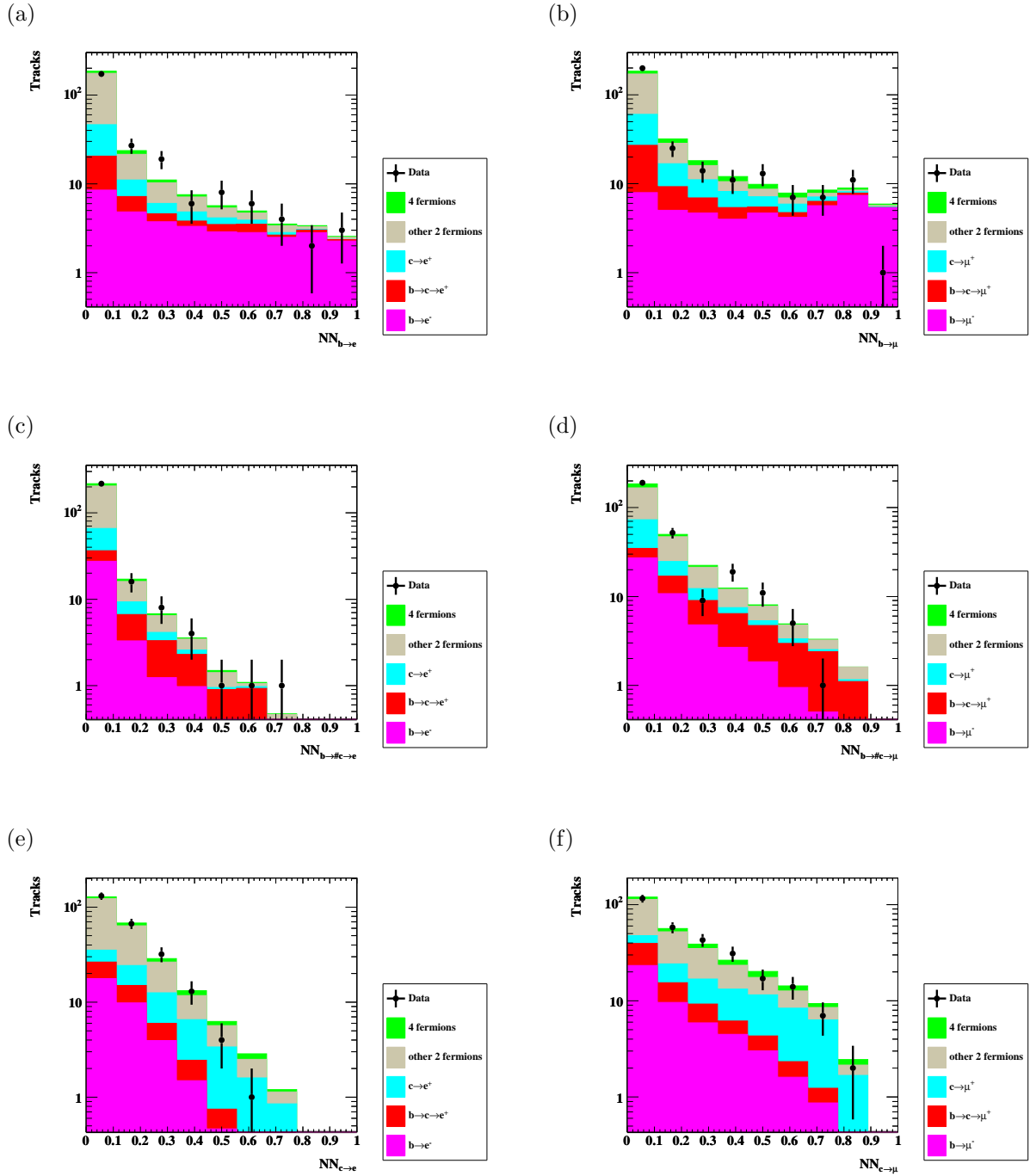


Figure 4.31: The distributions of ANN outputs, (a) electron \mathcal{N}_b , (b) muon \mathcal{N}_b , (c) electron \mathcal{N}_{bc} , (d) muon \mathcal{N}_{bc} , (e) electron \mathcal{N}_c (f) muon \mathcal{N}_c .

4.7.4 Event Selection

The output of the ANN is interpreted as the probability to discriminate the signal (as described in appendix D). Accordingly, significance of the prompt lepton, $\mathcal{P}_{\text{sig}}^{(\ell)}$, is defined with the three ANN outputs, \mathcal{N}_b , \mathcal{N}_{bc} and \mathcal{N}_c as,

$$\mathcal{P}_{\text{sig}}^{(\ell)} = \sqrt{(\mathcal{N}_b)^2 + (\mathcal{N}_{bc})^2 + (\mathcal{N}_c)^2}. \quad (4.38)$$

This prompt lepton significance is used to select one lepton candidate per events, with which the event-base analysis is performed. The largest value of $\mathcal{P}_{\text{sig}}^{(\ell)}$ in a event is selected to construct the event-base distribution and it is shown in Fig. 4.32. Finally, the prompt lepton significance, $\mathcal{P}_{\text{sig}}^{(\ell)}$, is required to be larger than 0.1 to enhance the prompt lepton.

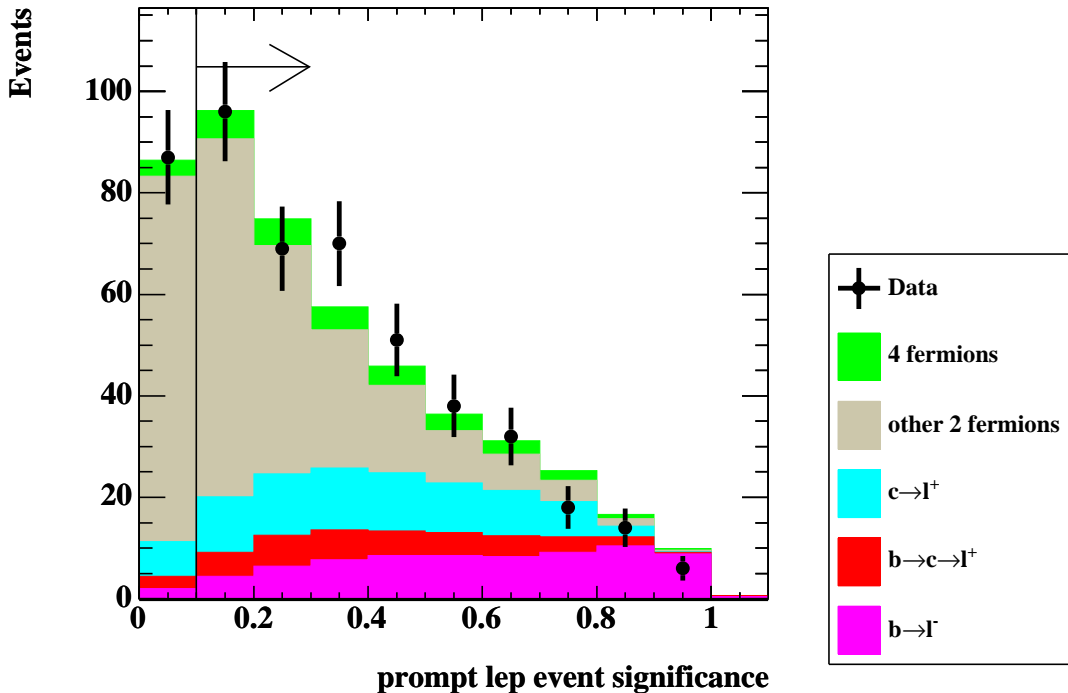


Figure 4.32: The distributions of the lepton significance which is most significant in the event.

4.7.5 Unbinned Likelihood Fit

Making Subsamples

The $A_{\text{FB}}^{b,c}$ fit is performed in a similar way as in the inclusive analysis. The event subsamples are constructed in order to enhance the sensitivity to A_{FB}^b or A_{FB}^c . The variables of \mathcal{N}_b , \mathcal{N}_{bc} and \mathcal{N}_c are used to divide the events into subsamples. The division is performed

with the values of each ANN output of $1/3$ and $1/6$ to make $3^3 = 27$ subsamples. Further divisions on $|\cos \theta_{\text{thrust}}|$ at 0.8 and 0.65 make 81 subsamples. The distributions of \mathcal{N}_b , \mathcal{N}_{bc} and \mathcal{N}_c for the most significant lepton are shown in Fig. 4.33(a), (b) and (c), respectively. Their angular distribution evaluated with the lepton charge, the hemisphere they belong, and $|\cos \theta_{\text{thrust}}|$ is shown in Fig. 4.33(d).

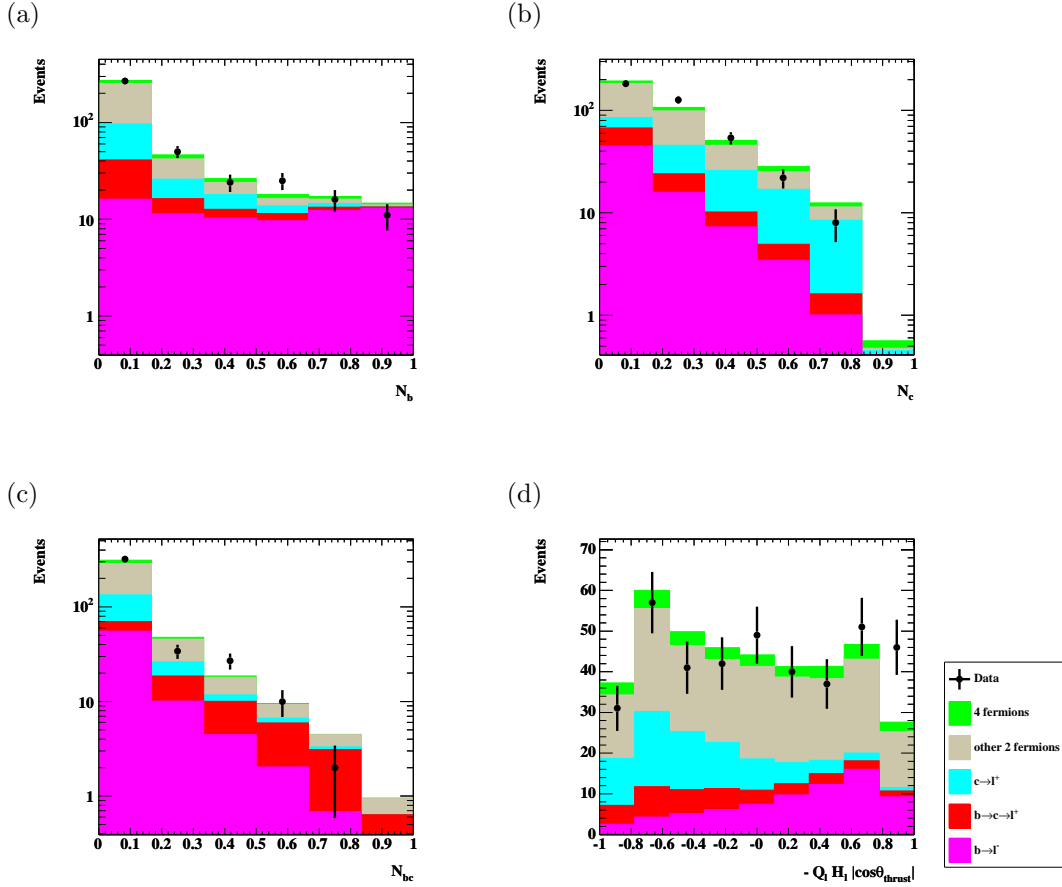


Figure 4.33: The distributions of ANN outputs, (a) \mathcal{N}_b , (b) \mathcal{N}_c , (c) \mathcal{N}_{bc} , (e) The angular distribution after the event selection with prompt lepton significance. The polar angle estimator is constructed from the lepton charge, lepton hemisphere and $|\cos \theta_{\text{thrust}}|$.

Probability Density Function

In a similar manner as in the inclusive analysis, the observed angular distribution can be represented with A_{FB} as

$$\frac{d\sigma_{\text{obs}}}{dy} \sim 1 + y^2 + \frac{8}{3} \left(\sum_{i=0, \dots, 3} f_i (1 - 2\bar{\chi}_i) A_{\text{FB}}^i \right) y, \quad (4.39)$$

where f_i is the fraction of each prompt lepton source. The subindex of 0, 1 and 2 means that the event has a track labeled as bl^- , bcl^+ and cl^+ respectively. The subindex of 3 means the event has no track with prompt-lepton label. The $\bar{\chi}_i$ is the mixing parameter corresponding to the prompt lepton sources. The $\bar{\chi}_2$ is set to 0 and $\bar{\chi}_3$ is set to 0.5. The y is the polar angle estimator defined as,

$$y = -q_l \cdot h_l \cdot \cos \theta_{\text{thrust}}. \quad (4.40)$$

The q_l is referred to as the track charge. The h_l is referred to as the hemisphere flag of the lepton which is 1 if the lepton is in the forward and -1 otherwise. The A_{FB}^i ($i=0,1,2,3$) can be written as

$$A_{\text{FB}}^0 = A_{\text{FB}}^b, A_{\text{FB}}^1 = -A_{\text{FB}}^b, A_{\text{FB}}^2 = -A_{\text{FB}}^c, A_{\text{FB}}^3 = 0. \quad (4.41)$$

The assumption of the 0 asymmetry on the non-prompt lepton source is almost true and effect of possible small non-zero asymmetry is evaluated with MC and added into the systematic errors. With the probability function, likelihood fit is performed and the result at the \sqrt{s} of 189 GeV is as follows.

$$\begin{aligned} A_{\text{FB}}^b &= 0.54 \quad {}^{+0.23}_{-0.24} \\ A_{\text{FB}}^c &= 0.25 \quad \pm 0.23, \end{aligned} \quad (4.42)$$

with a correlation matrix of

$$\begin{pmatrix} 1.00 & 0.26 \\ 0.26 & 1.00 \end{pmatrix}, \quad (4.43)$$

where the corrections discussed in the subsection 4.6.4 is already added in the result. The $1\text{-}\sigma$ and $2\text{-}\sigma$ contour plots corresponding to the 189 GeV analysis are shown in Fig. 4.34. The results corresponding to the each energy point are listed in Table. 4.11.

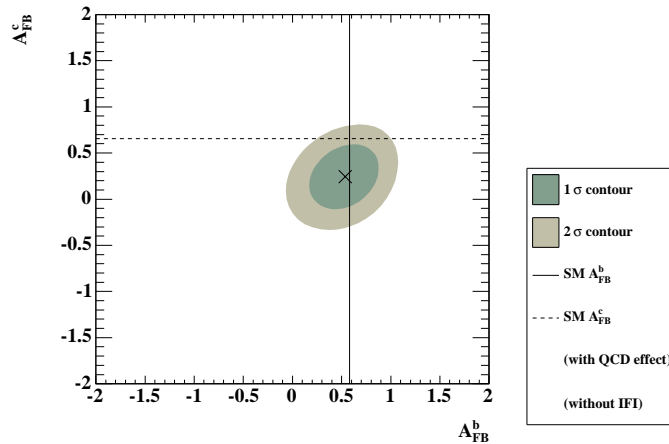


Figure 4.34: A one σ and two σ contours of the $A_{\text{FB}}^{b,c}$ result of 189 GeV lepton analysis.

Table 4.11: Results for the lepton analysis with statistical errors.

E_{cm} [GeV]	A_{FB}^{b} (stat.)	$A_{\text{FB}}^{\text{b,SM}}$	A_{FB}^{c} (stat.)	$A_{\text{FB}}^{\text{c,SM}}$	Correlation
91	0.05 \pm 0.05	0.10	-0.04 \pm 0.07	0.06	0.33
133	-0.24 $^{+0.35}_{-0.30}$	0.48	0.57 $^{+0.36}_{-0.39}$	0.69	0.13
161	0.29 $^{+0.38}_{-0.42}$	0.55	0.79 $^{+0.56}_{-0.64}$	0.67	0.13
172	0.45 $^{+0.36}_{-0.44}$	0.56	0.80 $^{+0.52}_{-0.62}$	0.67	0.10
183	0.67 $^{+0.35}_{-0.38}$	0.58	0.63 $^{+0.36}_{-0.38}$	0.66	0.23
189	0.54 $^{+0.23}_{-0.24}$	0.58	0.25 \pm 0.23	0.66	0.26
192	1.44 $^{+0.35}_{-0.53}$	0.58	0.65 $^{+0.72}_{-0.75}$	0.65	0.14
196	1.07 $^{+0.27}_{-0.32}$	0.59	0.78 $^{+0.35}_{-0.38}$	0.65	0.29
200	0.44 $^{+0.40}_{-0.42}$	0.59	0.36 $^{+0.41}_{-0.42}$	0.65	0.23
202	-0.16 $^{+0.63}_{-0.62}$	0.59	0.87 $^{+0.46}_{-0.53}$	0.65	0.14
205	0.26 $^{+0.32}_{-0.36}$	0.59	0.55 $^{+0.36}_{-0.38}$	0.65	0.23
207	0.35 \pm 0.27	0.59	0.84 $^{+0.26}_{-0.27}$	0.64	0.25

4.8 Combined Analysis

All events selected for the A_{FB} fits in the inclusive and lepton analyses are used in the combined analysis. These events are divided into two samples, where one is called as an inclusive sample and the other is called as a lepton sample. Basically, the events treated in the inclusive analysis is assigned to the inclusive sample and the events treated in the lepton analysis is assigned to the lepton sample. For the events shared between the inclusive and lepton analysis, events with $\mathcal{P}_{\text{sig}}^{(\text{inclusive})} > \mathcal{P}_{\text{sig}}^{(\ell)}$ (Eq. 4.13, Eq. 4.38) are assigned to the inclusive sample, whereas events with $\mathcal{P}_{\text{sig}}^{(\text{inclusive})} < \mathcal{P}_{\text{sig}}^{(\ell)}$ are assigned to the lepton sample.

For the inclusive sample, the same likelihood function as that used in the inclusive analysis is used and the corresponding likelihood is constructed as $\mathcal{L}^{\text{inclusive}}$, whereas for the lepton sample, the same likelihood function to that used in the lepton analysis is used to construct the corresponding likelihood ($\mathcal{L}^{\text{lepton}}$). The combined likelihood, $\mathcal{L}^{\text{combined}}$, is defined as

$$\mathcal{L}^{\text{combined}} = \mathcal{L}^{\text{inclusive}} \times \mathcal{L}^{\text{lepton}}. \quad (4.44)$$

With the combined likelihood, an unbinned maximum likelihood is performed to get the $A_{\text{FB}}^{\text{b,c}}$ simultaneously. The $1\text{-}\sigma$ and $2\text{-}\sigma$ contours are shown in Fig. 4.35.

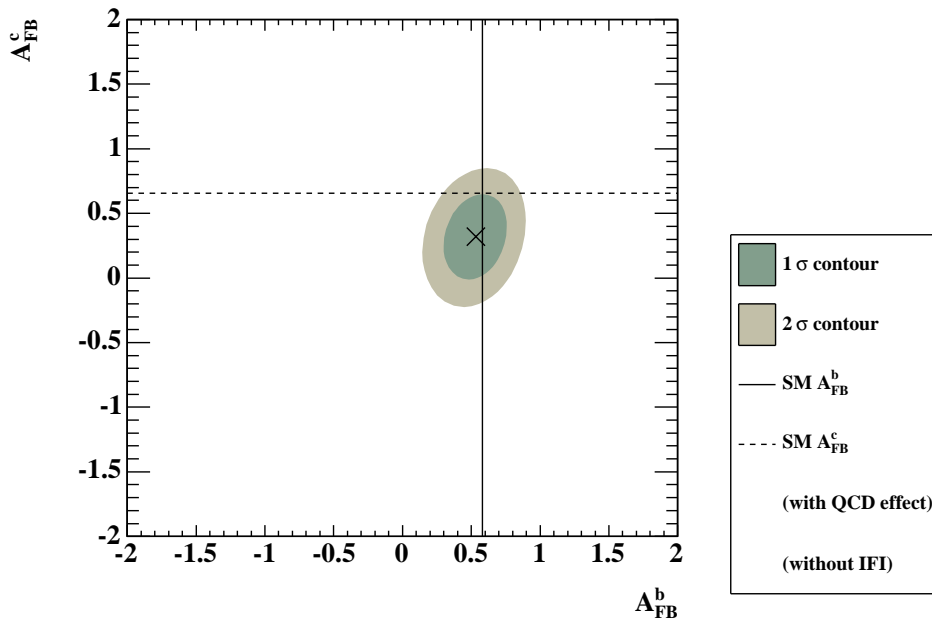


Figure 4.35: The results of the $A_{\text{FB}}^{\text{b,c}}$ measurement with $1\text{-}\sigma$ and $2\text{-}\sigma$ contours.

The values obtained for the 189 GeV data are as follows.

$$\begin{aligned}
A_{\text{FB}}^{\text{b}} &= 0.53 \quad {}^{+0.15}_{-0.16} \\
A_{\text{FB}}^{\text{c}} &= 0.32 \quad \pm 0.22, \\
A_{\text{FB}}^{\text{uds,in}} &= -0.63 \quad \pm 1.1, \\
A_{\text{FB}}^{\text{uds,out}} &= -0.08 \quad \pm 0.16,
\end{aligned}
\tag{4.45}$$

with a correlation matrix of

$$\begin{pmatrix}
1.00 & 0.22 & -0.01 & -0.001 \\
0.22 & 1.00 & 0.04 & 0.18 \\
-0.01 & 0.04 & 1.00 & 0.08 \\
-0.001 & 0.18 & 0.01 & 1.00
\end{pmatrix}.
\tag{4.46}$$

The result corresponding to each energy point is shown with the statistical error in Table. 4.12, where the values predicted by the standard model are also shown. The evaluation of the systematic errors is given in the next section.

Table 4.12: Results for the combined analysis with statistical errors.

E_{cm} [GeV]	A_{FB}^{b} (stat.)	$A_{\text{FB}}^{\text{b,SM}}$	A_{FB}^{c} (stat.)	$A_{\text{FB}}^{\text{c,SM}}$	Correlation
91	0.08 ± 0.03	0.10	-0.01 ± 0.07	0.06	0.27
133	0.21 ${}^{+0.28}_{-0.29}$	0.48	0.63 ${}^{+0.35}_{-0.38}$	0.69	0.15
161	0.06 ± 0.33	0.55	1.07 ${}^{+0.71}_{-0.74}$	0.67	0.15
172	0.70 ${}^{+0.39}_{-0.46}$	0.56	1.08 ${}^{+0.43}_{-0.54}$	0.67	0.19
183	0.90 ${}^{+0.25}_{-0.26}$	0.58	0.87 ${}^{+0.31}_{-0.34}$	0.66	0.22
189	0.53 ${}^{+0.15}_{-0.16}$	0.58	0.32 ± 0.22	0.66	0.22
192	1.14 ${}^{+0.31}_{-0.37}$	0.58	0.65 ${}^{+0.71}_{-0.74}$	0.65	0.18
196	0.83 ${}^{+0.26}_{-0.28}$	0.59	0.61 ${}^{+0.35}_{-0.37}$	0.65	0.26
200	0.31 ${}^{+0.30}_{-0.31}$	0.59	0.30 ${}^{+0.40}_{-0.41}$	0.65	0.20
202	0.11 ± 0.41	0.59	0.81 ${}^{+0.48}_{-0.55}$	0.65	0.12
205	0.26 ${}^{+0.24}_{-0.25}$	0.59	0.49 ${}^{+0.35}_{-0.36}$	0.65	0.23
207	0.26 ± 0.20	0.59	0.74 ${}^{+0.26}_{-0.27}$	0.64	0.24

4.9 Systematic Uncertainties

This analysis relies heavily on the correct modeling by the Monte Carlo simulation of the b-tagging and charge identification. Uncertainties which affect the charge identification probability and b-tagging variable are considered to be the important source of the systematic errors.

The hemisphere charge can be affected by the fragmentation, semileptonic model and decay multiplicity of b or c hadrons. The $B^0 - \bar{B}^0$ mixing can affect the hemisphere charge for b hadrons and it also affects the charge dilution factor in the lepton analysis.

As for the b-tagging variable, some change in the b-tagging variable affect the fractions of b, c and light-quark (u, d and s) events in the selected samples and change the values of the fitted $A_{\text{FB}}^{b,c}$. The b-tagging variables for the inclusive and lepton analysis are sensitive to the nature of b and c hadrons, such as the lifetime, fragmentation, decay multiplicity, and the momentum spectrum of the leptons from semileptonic decay. The b-tagging depends strongly on the secondary vertex reconstruction and the impact parameter where the resolution of the reconstructed tracks in the detector is essential. Accordingly, the uncertainties in the resolution for the track reconstruction should be considered as the systematic error. In this analysis, b-tagging variables are constructed with ANN, which is based on the validity of modeling of the Monte Carlo sample used in the ANN learning. The uncertainties in the modeling of the input variables for the ANN should be considered.

Furthermore, the rate of the gluon splitting to $b\bar{b}$ or $c\bar{c}$, the rate of long-lived light hadrons (K^0 and Λ), and the four-fermion rate can also affect the fractions. As regards the fitting procedure, the possible bias in the A_{FB} fitting should be taken into account. Uncertainties in some corrections to be added to the fitted values of A_{FB} should be considered too.

Most of the uncertainties mentioned above is evaluated by reweighting the concerning quantities in the Monte Carlo sample within the range of their uncertainties. Then the A_{FB} fit is repeated and deviation of the resulting value from the original one is treated as the systematic error. Since most of the systematic errors are common to all the energy points, such common systematic errors are evaluated using combined data and corresponding Monte Carlo samples with \sqrt{s} larger than 180 GeV. The evaluated systematic errors for the combined data are shown in Table. 4.13, where a systematic error due to the Monte Carlo statistics is that for the 189 GeV sample, which is not a common systematic error. The others are common to all the energy points. More detailed description is given as follows.

Uncertainty source	$\Delta A_{\text{FB}}^{\text{b}}$	$\Delta A_{\text{FB}}^{\text{c}}$
b fragmentation	0.010	0.012
b decay multiplicity	0.003	0.021
b hadron composition	0.012	0.005
b lifetime	0.001	0.001
$B^0 - \bar{B}^0$ mixing	0.018	0.002
c fragmentation	0.002	0.012
c decay multiplicity	0.010	0.015
c hadron composition	0.013	0.017
c lifetime	0.001	0.001
semileptonic branching ratio	0.007	0.029
semileptonic decay model	0.006	0.003
Total b,c physics modeling	0.031	0.046
ISR-FSR interference	0.005	0.009
Final state QCD effect	0.016	0.021
$g_{b\bar{b}}$ rate	0.004	0.001
$g_{c\bar{c}}$ rate	0.008	0.017
K^0, Λ rate	0.008	0.006
Four-fermion rate	0.001	0.001
Other physics modeling	0.021	0.029
Track reconstruction	0.076	0.029
Event pre-selection	0.001	0.001
Lepton ID	0.005	0.021
Modeling of ANN Inputs	0.011	0.017
Total detector modeling	0.077	0.040
Monte Carlo statistics	0.004	0.006
Background A_{FB}	0.002	0.047
Fitting Procedure	0.032	0.037
Total A_{FB} fit	0.032	0.060
Total systematic uncertainty	0.09	0.09

Table 4.13: Systematic uncertainty breakdown for the combined data with \sqrt{s} larger than 180 GeV. A systematic error due to the Monte Carlo statistics shown here is that for the 189 GeV sample, which is not a common systematic error. The others are common to all the energy points.

4.9.1 Bottom and Charm Physics Modeling

Uncertainties in bottom and charm fragmentation and decay properties are evaluated by reweighting the Monte Carlo samples in the ranges of their uncertainties as follows.

- **b fragmentation**

The Peterson fragmentation parameter (ϵ^{b}) which models the b-quark fragmentation process described in subsection 2.3.2 is considered not to vary with the \sqrt{s} , since the

energy scale of the hadronization phase where the fragmentation function is used is typically below 1 GeV. Therefore, the uncertainties from the study of the b-quark fragmentation at LEP1 [68] can be used in this thesis and the simulated $b\bar{b}$ events are reweighted within the range of $0.0030 < \epsilon^b < 0.0048$ [68].

In addition, other fragmentation functions are applied to the MC to evaluate the uncertainties from the fragmentation model. The b-quark fragmentation function is changed to that suggested by Collins and Spiller [86] and to that of Kartvelishvili [87]. The best-fit values of the fragmentation parameters of the two models in the study of the b-quark fragmentation at LEP1 [88] are used. The largest difference in the A_{FB} due to the above tests is taken as the systematic uncertainty.

- **b decay multiplicity**

The charged decay multiplicity of b hadrons is varied in the MC according to the combined results of the measurements at LEP [68] as 4.955 ± 0.062 . The largest difference in the A_{FB} is taken as the systematic uncertainty.

- **b hadron composition**

The tagging efficiency differs for the various b hadron species. The fractions of b hadrons and their errors have been calculated from the best values of mean lives, mixing parameters, and branching fractions measured at LEP and CDF [51]. The fractions of b baryon and B_s^0 are varied independently within their errors, as $9.9 \pm 1.7\%$ and $10.7 \pm 1.1\%$, respectively. Their variation is compensated by the fractions of B^0 and B^+ , where the fraction of B^0 and B^+ is the same.

- **b hadron lifetimes**

The lifetimes of the different b hadrons are varied in the Monte Carlo by their errors according to the results mainly from the measurements at LEP [68], as 1.576 ± 0.016 ps.

- **$B^0 - \bar{B}^0$ mixing**

The mixing parameter, $\bar{\chi}$, is varied in the Monte Carlo as 0.1257 ± 0.0042 from the measurements mainly at LEP as shown in [51].

- **c fragmentation**

The Peterson fragmentation parameter ϵ_P^c is varied in the Monte Carlo within the range of $0.022 < \epsilon_P^c < 0.039$, which is taken from the study of the c-quark fragmentation at LEP1 [68].

- **c decay multiplicity**

The average charged track multiplicities of D^+ , D^0 and D_s^+ decays are varied in the

Monte Carlo within the ranges of the experimental measurements [89], which are 2.38 ± 0.06 for D^+ , 2.56 ± 0.05 for D^0 , and 2.69 ± 0.33 for D_s^+ .

- **c hadron composition**

The D^0 fraction is written as $f(D^0) = 1 - f(D^+) - f(D_s^+) - f(c_{\text{baryon}})$. The last three parameters are varied independently by their uncertainties according to [68], which are obtained through fitting the electroweak observables as, 23.3 ± 2.7 % for D^+ , 10.3 ± 2.9 % for D_s^+ , and 6.3 ± 2.8 % for c baryons.

- **c hadron lifetimes**

Charmed hadron lifetimes are varied within their experimental uncertainties according to the several measurements [68], where the lifetime of D^+ is 1.057 ± 0.016 ps, that of D^0 is 0.415 ± 0.004 ps and that of D_s^+ is 0.467 ± 0.017 ps.

- **semileptonic decay modeling and branching ratios**

The semileptonic branching ratios of bottom- and charm-hadrons are varied within their experimental uncertainties shown in [68,90], where the uncertainties of branching ratio for $b \rightarrow \ell$ is 0.1056 ± 0.0021 , that for $b \rightarrow \tau \rightarrow \ell$ is 0.00419 ± 0.00055 , that for $b \rightarrow c \rightarrow \ell$ is 0.0801 ± 0.0026 , that for $b \rightarrow \bar{c} \rightarrow \ell$ is $0.0162_{-0.0036}^{+0.0044}$, and that for $c \rightarrow \ell$ is 0.098 ± 0.005 . The alternatives of semileptonic decay models shown in [68] are used to evaluate the systematic uncertainty, which makes the momentum spectrum of the lepton softer or harder.

4.9.2 Effect of the ISR-FSR Interference

The effect of the ISR-FSR interference to the A_{FB} is evaluated with ZFITTER, which is removed from the measured A_{FB} which is already described in Section 4.6.4. The full deviations of A_{FB} evaluated with or without the ISR-FSR interference with ZFITTER are added to the systematic errors.

4.9.3 Final State QCD Corrections

Since the thrust axis is the good estimator of the initial quark direction checked with MC as seen in Table 4.7, the A_{FB} for the initial quark direction is set to the value to be fitted. The charge identification with either the hemisphere or lepton charge technique is performed with respect to the initial quark direction. Hence the flip of the quark direction due to the hard gluon emission is treated as the dilution of the charge identification. The QCD effects are evaluated with ZFITTER, which are finally added to the fitted values as described in Section 4.6.4. The full corrections are assigned as systematic errors.

4.9.4 The Rates of Gluon Splitting to $b\bar{b}$ or $c\bar{c}$

The rates of gluon splitting to $b\bar{b}$ or $c\bar{c}$ ($g_{b\bar{b}}$, $g_{c\bar{c}}$) were measured at LEP1 [68, 90] as 0.00254 ± 0.00051 and 0.0296 ± 0.0038 respectively. The rates of $g_{b\bar{b}}$ and $g_{c\bar{c}}$ are increased as \sqrt{s} increase according to the theoretical calculation in the next-to-leading-logarithmic approximation shown in [91]. The measured values of $g_{b\bar{b}}$ and $g_{c\bar{c}}$ are extrapolated to the higher energies using the analytical formula in [91], where the uncertainties of α_s , m_b and m_c are added with in their errors in [51]. The rates of $g_{b\bar{b}}$ and $g_{c\bar{c}}$ in the Monte Carlo are varied with in the errors. At \sqrt{s} of 200 GeV, the rate of $g_{b\bar{b}}$ is evaluated as 0.0059 ± 0.0016 and that of $g_{c\bar{c}}$ as 0.051 ± 0.014 .

4.9.5 Total K^0 and Λ Rate

The rate of long lived light hadrons affects the background in a b-tagged samples. The total production rates of K^0 and Λ in the Monte Carlo are varied by 10% according to [68, 90].

4.9.6 Four-fermion Background

Above the WW production threshold, the four-fermion background is largely dominated by W pairs. The uncertainty in the W pair production cross-section is taken into account by changing the rate in the MC according to the results from the measurements of WW cross-section [35].

4.9.7 Track Reconstruction

The effect of the detector resolution on the track parameters is estimated by degrading or improving the resolution of all tracks in the Monte Carlo simulation. This is done by applying a single multiplicative scale factor to the difference between the reconstructed and true track parameters. A $\pm 5\%$ variation is applied independently to the $r\phi$ and rz track parameters, which fits the data distributions of the d_0 significance (d_0 divided by its error) and z_0 significance (z_0 divided by its error), respectively.

The number of SI hits along a track is compared between data and Monte Carlo samples and the difference is found to be small. To fit the small difference, the matching efficiency for assigning measurement points in the silicon microvertex detector to the tracks is varied by 1% in $r\phi$ and 3% in rz . The systematic errors resulting from the individual variations are summed in quadrature.

4.9.8 Event Pre-Selection

As for the uncertainty in the non-radiative event selection, the analysis is repeated using a different method for estimating s' , described in [72], which is a less sophisticated alternative of that used in the section 4.5.2. In the method, only single photon radiated either to the beam pipe direction or in the ECAL is considered. The difference of A_{FB} between the two methods is taken as the systematic error. The biases from other items of event selections are consistent to be zero within the statistics of the MC, where no systematic errors are assigned.

4.9.9 Lepton Identification

The fractions of misidentified electrons and muons are taken from Monte Carlo simulation. The systematic errors for the electron efficiency (15%) and fake rate (30%) described in [42] are used to reweight the Monte Carlo. The deviations of the A_{FB} due to the reweighting are treated as the systematic errors. The systematic errors in the muon identification is evaluated as in [42], where the scaling factors to reweight the Monte Carlo for the muon tracks is 0.953 ± 0.047 and that for the other background tracks is 0.971 ± 0.041 .

4.9.10 Modeling of Artificial Neural Network Inputs

The ANNs are used in the inclusive (the LB b-tagging method) and lepton analysis (\mathcal{N}_{b} , \mathcal{N}_{bc} and \mathcal{N}_{c}). Each of the input distributions used in those ANNs are compared between data and Monte Carlo. The simulated distributions are reweighted for each input variable in turn to agree with the corresponding data distributions, and the analysis is repeated with the weighted events. The observed differences from the original fit result are added in quadrature to yield the systematic uncertainty due to the modeling of the input variables.

4.9.11 Monte Carlo Statistics

The fractions of b, c-tagging events and charge identification probabilities are varied by the statistical error arising from the finite number of Monte Carlo simulated events.

4.9.12 Background Asymmetries

The A_{FB} of the backgrounds introduces the biases on the measured A_{FB} . In the inclusive analysis, the observed asymmetry of the 4-fermion events is assumed to be zero. In the lepton analysis, the observed asymmetry of the background events is assumed to be zero. The effects of the possible non-zero asymmetry evaluated with the Monte Carlo are added in the fitting and the deviations of the results are added as the systematic errors.

4.9.13 Fitting Procedure

The large Monte Carlo sample is used as the input data and the sample is fitted with the Monte Carlo to evaluate the fitting bias. The obtained values from the fitting is consistent with the input value of A_{FB} for the Monte Carlo within the statistical errors. The variation of the fitted values from the input values are treated as the systematic errors, where the contributions from the background asymmetries are removed which are already evaluated in the section 4.9.12. No local minimum is exist in the fitting, which is checked by scanning the value of the likelihood in the A_{FB}^b - A_{FB}^c plane as shown in Fig. 4.36.

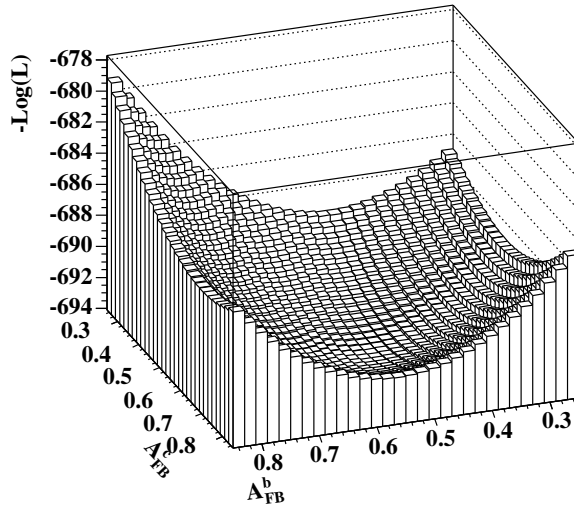


Figure 4.36: The distribution of $-\log \mathcal{L}$ in A_{FB}^b - A_{FB}^c plane for the combined data.

4.9.14 Cross-Checks

The data corrected at \sqrt{s} of Z mass in the LEP2 is used to check the fitting method. The same procedure is applied to the data and the consistent results to the standard model predictions are obtained. Since the measurements at LEP1 shows good agreements with the standard model predictions, it is a good cross-check of the methods of the measurement used in this thesis.

4.10 Result and Discussion

The result of the combined analysis is summarized here. The same analysis for combined data with \sqrt{s} larger than 180 GeV is performed. The both results are compared to the LEP results including previous OPAL result. They are also compared to the results for \sqrt{s} below LEP2 energy. The obtained results can be used to constrain some new physics. In a general framework, the existence of the contact interaction between electron and b or c quarks are investigated. It can be interpreted as the effective theory for the exchange of the heavy particle between electron and b or c quarks. In some specific cases, the limit on the mass of some leptoquarks or R-parity violating squarks are placed. Finally, new physics due to the effect of graviton exchange in large extra dimensions is also studied.

The result of the combined analysis is shown with the statistical and systematic errors in Table. 4.14 and Fig. 4.37, where the prediction of the standard model is also shown. For all measured points, good agreements with the standard model prediction are observed. The values of χ^2 for b and c with respect to the standard model prediction for the energy points from 130 to 207 GeV are calculated to be 14.6 and 4.68, respectively, where the number of degree of freedom is 11.

The data with \sqrt{s} larger than 180 GeV (the data samples of 183, 189, 192, 196, 200, 202, 205, and 207 GeV) are combined, where the expected variation of A_{FB} as a function of \sqrt{s} is less than 2% in the standard model prediction. With the combined data, the A_{FB}^{b} and A_{FB}^{c} are also measured with the same method, where the luminosity-weighted mean of \sqrt{s} is 197 GeV. The result is shown in Table. 4.15 and Fig. 4.37 with open markers. The result is consistent with the standard model prediction.

Table 4.14: Result for the combined analysis with statistical and systematic errors.

E_{cm} [GeV]	A_{FB}^b		$A_{FB}^{b,SM}$	A_{FB}^c		$A_{FB}^{c,SM}$	Correlation (stat.)		
	(stat.)	(syst.)		(stat.)	(syst.)				
91	0.08	± 0.03	± 0.09	0.10	-0.01	± 0.07	± 0.09	0.06	0.27
133	0.21	$^{+0.28}_{-0.29}$	± 0.09	0.48	0.63	$^{+0.35}_{-0.38}$	± 0.09	0.69	0.15
161	0.06	± 0.33	± 0.09	0.55	1.07	$^{+0.71}_{-0.74}$	± 0.10	0.67	0.15
172	0.70	$^{+0.39}_{-0.46}$	± 0.10	0.56	1.08	$^{+0.43}_{-0.54}$	± 0.10	0.67	0.19
183	0.90	$^{+0.25}_{-0.26}$	± 0.09	0.58	0.87	$^{+0.31}_{-0.34}$	± 0.09	0.66	0.22
189	0.53	$^{+0.15}_{-0.16}$	± 0.09	0.58	0.32	± 0.22	± 0.09	0.66	0.22
192	1.14	$^{+0.31}_{-0.37}$	± 0.09	0.58	0.65	$^{+0.71}_{-0.74}$	± 0.09	0.65	0.18
196	0.83	$^{+0.26}_{-0.28}$	± 0.09	0.59	0.61	$^{+0.35}_{-0.37}$	± 0.09	0.65	0.26
200	0.31	$^{+0.30}_{-0.31}$	± 0.09	0.59	0.30	$^{+0.40}_{-0.41}$	± 0.09	0.65	0.20
202	0.11	± 0.41	± 0.09	0.59	0.81	$^{+0.48}_{-0.55}$	± 0.09	0.65	0.12
205	0.26	$^{+0.24}_{-0.25}$	± 0.09	0.59	0.49	$^{+0.35}_{-0.36}$	± 0.09	0.65	0.23
207	0.26	± 0.20	± 0.09	0.59	0.74	$^{+0.26}_{-0.27}$	± 0.09	0.64	0.24

Table 4.15: Result for the combined data with \sqrt{s} larger than 180 GeV.

E_{cm} [GeV]	A_{FB}^b		$A_{FB}^{b,SM}$	A_{FB}^c		$A_{FB}^{c,SM}$	Correlation (stat.)		
	(stat.)	(syst.)		(stat.)	(syst.)				
197	0.52	± 0.09	± 0.09	0.59	0.59	± 0.12	± 0.09	0.65	0.23

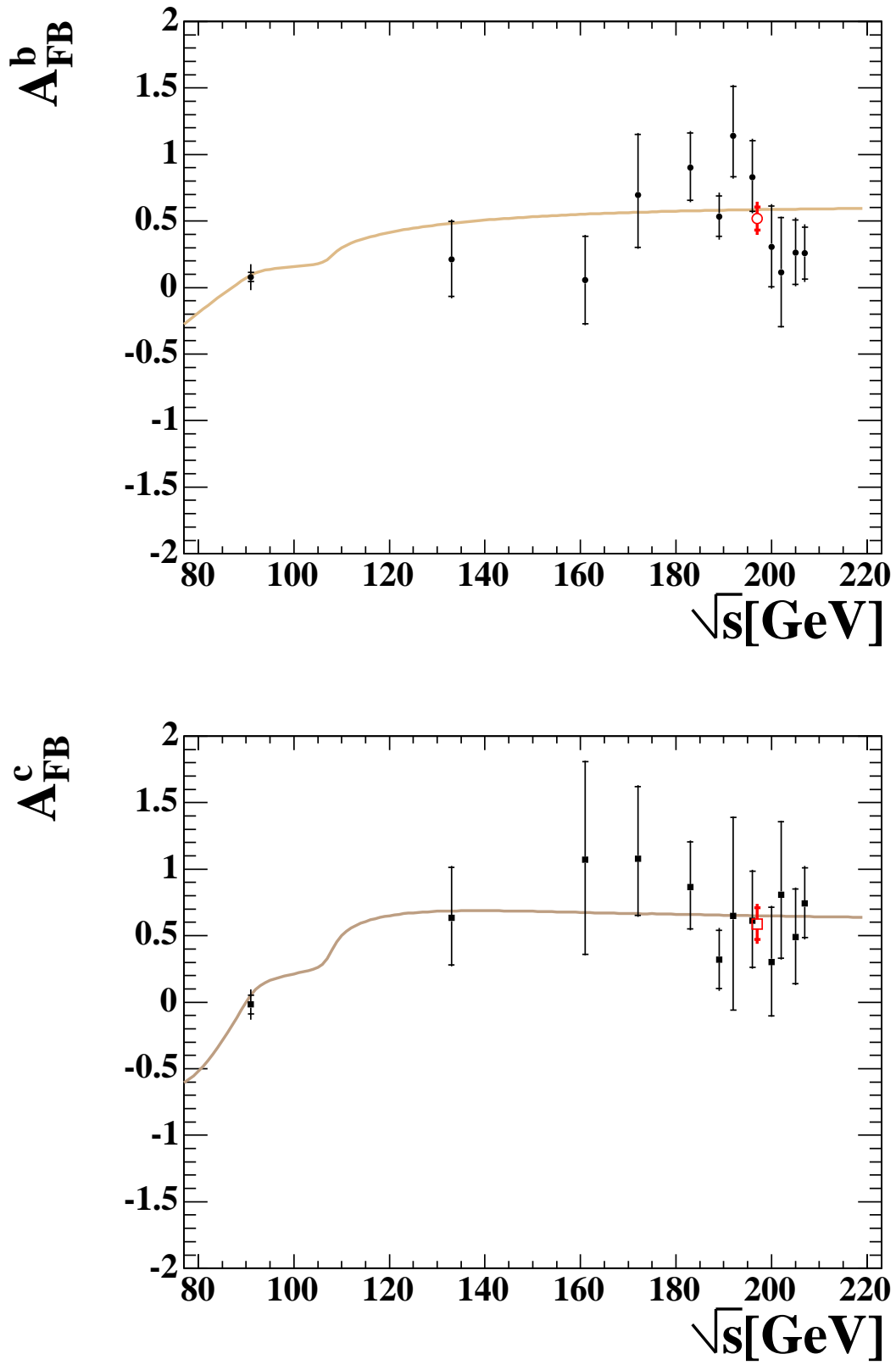


Figure 4.37: The measured A_{FB}^b and A_{FB}^c for each energy point where the values of the standard model expectation are indicated with lines. The measured A_{FB}^b and A_{FB}^c for the combined data with \sqrt{s} larger than 180 GeV are also plotted with open markers.

In addition to the results of the $A_{\text{FB}}^{\text{b,c}}$ measurements performed by OPAL (the previous results [42] and this measurement), results of $A_{\text{FB}}^{\text{b,c}}$ measurements at LEP2 performed by other experiments (ALEPH [92], DELPHI [93], L3 [94]) are also shown in Fig. 4.38. In the ALEPH analysis, multi-hadronic events with $\sqrt{s'}/s$ larger than 0.9 were used and they were clustered into two jets. The A_{FB}^{b} was measured for b-enriched sample based on the mean difference between the forward jet charge and backward jet charge, where the standard-model values of A_{FB} for u, d, s, and c were assumed. Delphi utilized the similar method to this inclusive analysis to measure the $A_{\text{FB}}^{\text{b,c}}$ by fitting the angular distributions of b, c, and light-quark (u, d, and s) enriched samples. The obtained values of this measurement are more accurate than all results reported by other experiments. The measurement of the A_{FB}^{c} is mainly performed by OPAL and is most precise. The result of this measurement at \sqrt{s} from 130 GeV to 189 GeV is consistent with and is comparable to the previous OPAL result. The result at \sqrt{s} larger than 189 GeV is unique to this measurement.

The results of the $A_{\text{FB}}^{\text{b,c}}$ performed at PEP, PETRA, TRISTAN, and LEP are summarized in Fig. 4.39, where the results at the \sqrt{s} of 133, 161 and 172 GeV, and the combined result for the energy points from 183 GeV to 207 GeV are shown for this measurement. The combined result for the energy points of 183 GeV and 189 GeV, and that for the energy points between 192 GeV to 209 GeV are also shown in the figure, where the latter is the combined result for the energy points newly measured in this thesis. The result of this measurement is important, since the measurement reported in this thesis is performed at the highest energy in e^+e^- collisions and gains the best accuracy at LEP2 with efficient analysis methods using all the data collected by OPAL during LEP2.

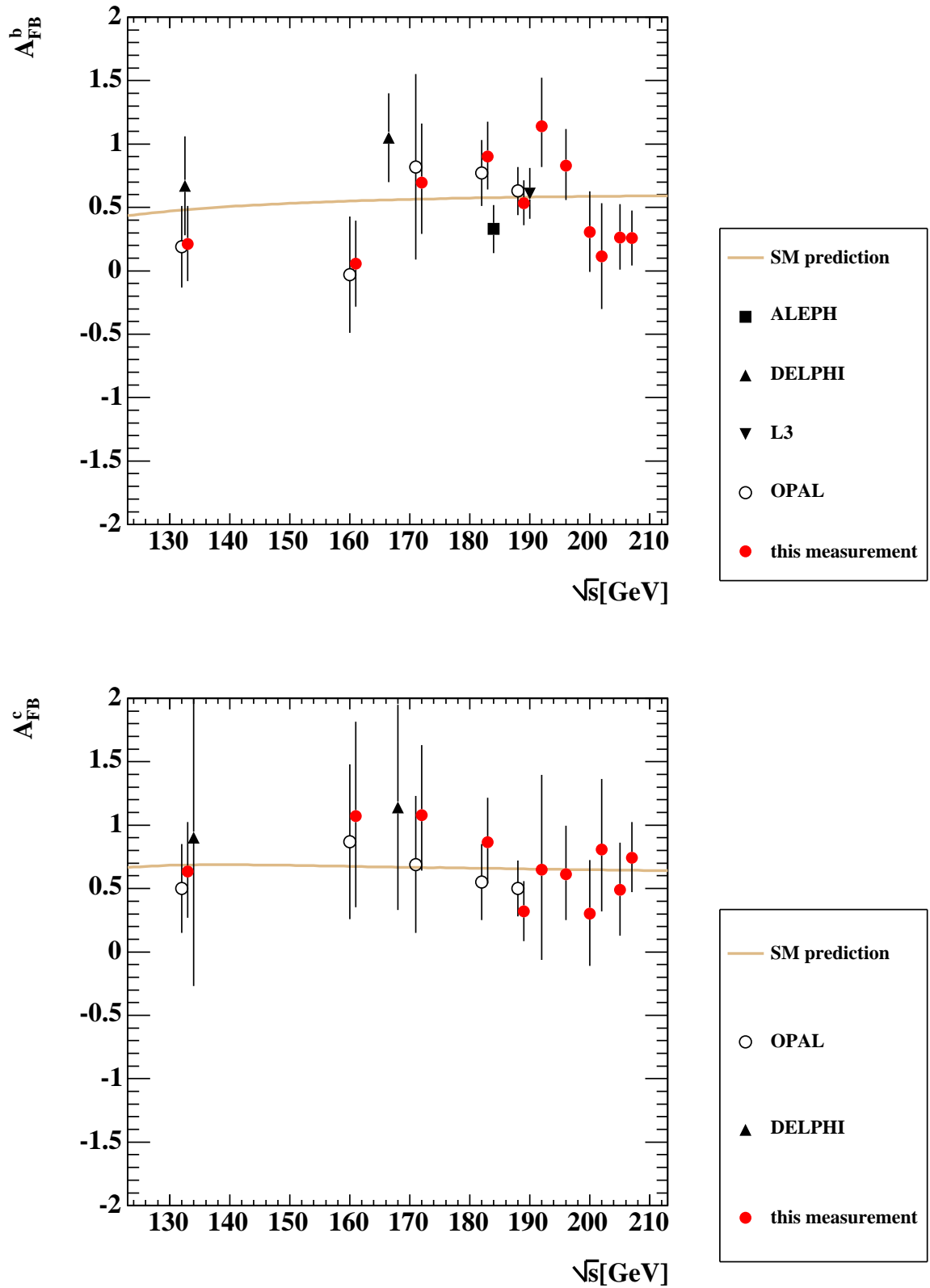


Figure 4.38: The measured A_{FB}^b and A_{FB}^c by ALEPH, DELPHI, L3, and OPAL at LEP2 where the values of the standard model expectation are indicated with lines. DELPHI obtained the result at \sqrt{s} of 167 GeV where data at \sqrt{s} of 161 GeV and 172 GeV were combined.

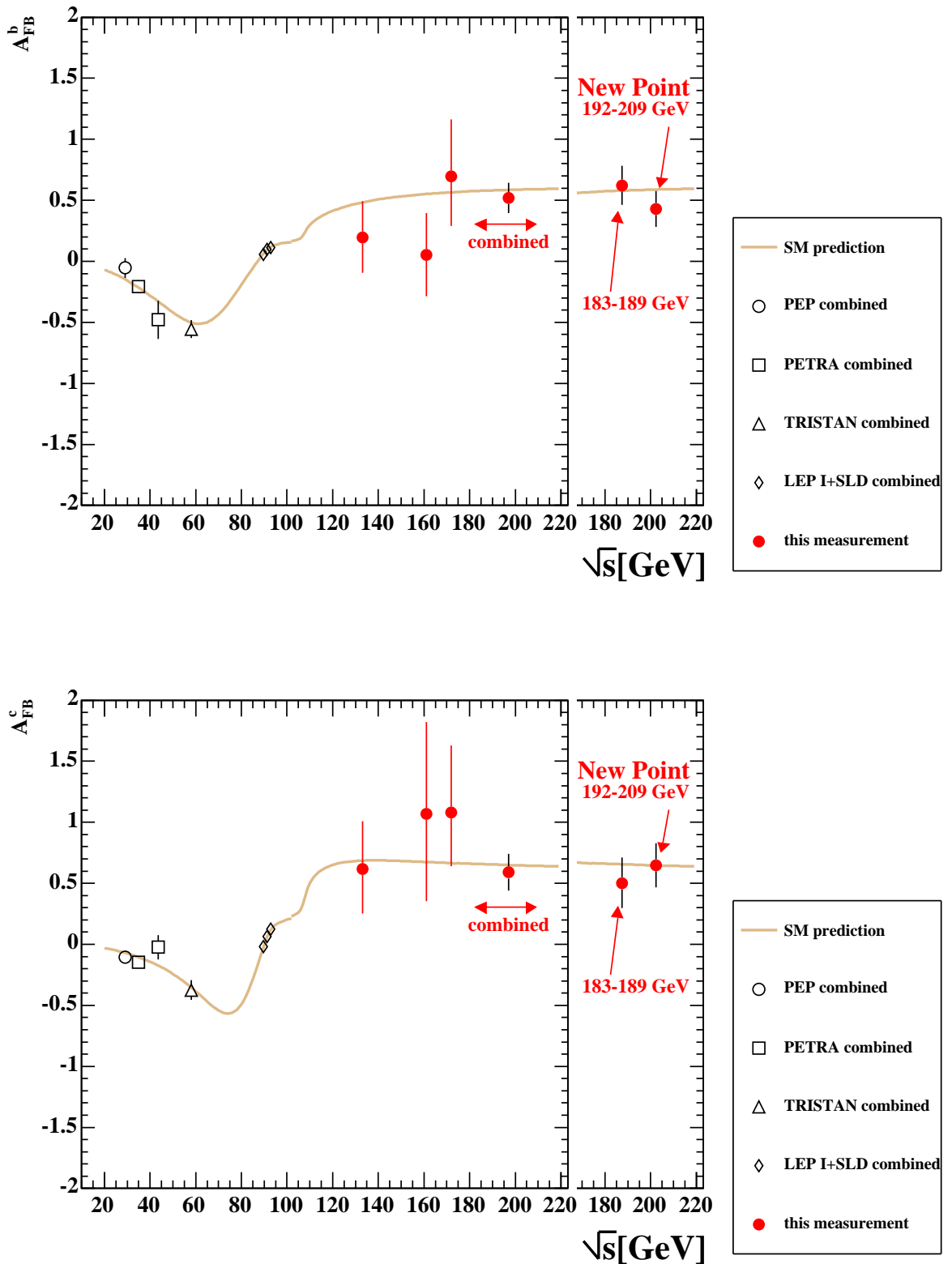


Figure 4.39: The results of the A_{FB}^b and A_{FB}^c measurements in e^+e^- collisions at the PEP, PETRA, TRISTAN, SLC and LEP are shown, where the combined result for the data with \sqrt{s} larger than 180 GeV is used for this measurement. The standard model predictions are given by lines. The combined result only for the energy points newly measured in this thesis is also indicated.

The result can be used to constrain some new physics beyond the standard model. For example, it can place a limit on contact interaction between electron and b or c quarks. It is a general framework of a new physics, since the contact interaction can be interpreted as the effective interaction of the exchange of a very heavy particle concerning to a new physics at a higher energy scale. In the context of the composite models of leptons and quarks, the contact interaction can also be interpreted as a remnant of the binding force between the substructures of fermions. The study of the contact interaction between electron and b or c quarks at e^+e^- colliders is particularly important since it is inaccessible to $p\bar{p}$ or ep colliders.

Following [95], the Lagrangian⁶ for the four-fermion contact interaction in the process $e^+e^- \rightarrow f\bar{f}$ ($f \neq e$) is defined by

$$\mathcal{L} = \frac{g_{CI}^2}{\Lambda^2} \sum_{i,j=L,R} \eta_{ij} [\bar{e}_i \gamma^\mu e_i] [\bar{f}_j \gamma_\mu f_j], \quad (4.47)$$

which is added to the standard model Lagrangian. Here e_L and e_R (f_L and f_R) are chirality projections of electron (fermion) spinors. The coefficients η_{ij} determine the type of chiral couplings of the four fermions, and the Λ is the energy scale of the contact interaction. By convention, the coupling constant, g_{CI} , is set to $g_{CI}^2/4\pi = 1$ and the η_{ij} is set to ± 1 or 0. The models of the contact interaction can be defined with sets of values of η_{ij} and some models used here are shown in Table 4.16 with the corresponding sets of values of η_{ij} . For example, LL^\pm means a model with left-handed couplings for both electrons and fermions. The $+$ ($-$) sign means constructive (destructive) interference between the standard model and the contact-interaction model.

Table 4.16: The models of the contact interaction and their corresponding values of η_{ij}

Model	η_{LL}	η_{RR}	η_{LR}	η_{RL}
LL^\pm	± 1	0	0	0
RR^\pm	0	± 1	0	0
VV^\pm	± 1	± 1	± 1	± 1
AA^\pm	± 1	± 1	∓ 1	∓ 1
LR^\pm	0	0	± 1	0
RL^\pm	0	0	0	± 1

According to [97], the helicity amplitude, $\mathcal{M}_{ij}(i, j = L, R)$, for $e^+e^- \rightarrow f\bar{f}$ including the contact interaction can be written as

$$\mathcal{M}_{ij}(s) = \frac{4\pi\alpha Q_e Q_f}{s} + \frac{4\pi\alpha}{\sin^2\theta_W \cos^2\theta_W} \cdot \frac{g_i^e g_j^f}{s - M_Z^2 + is\frac{\Gamma_Z}{M_Z}} + \eta_{ij} \frac{g_{CI}^2}{\Lambda^2}. \quad (4.48)$$

⁶Here only vector type contact interaction is considered, since other scalar and tensor type interactions are strongly limited [96].

The first and second terms in Eq. 4.48 correspond to γ and Z exchanges respectively, and the third one corresponds to the contact interaction, where Q_f is the electric charge of the fermion in units of the elementary charge. The subscripts i and j label the chiralities of the initial electron and final fermion, respectively ($i, j = L, R$), and g_i^f is the electroweak couplings of the fermion as follows.

$$\begin{aligned} g_L^f &= 2T_3^f - Q_f \sin^2 \theta_W, \\ g_R^f &= -Q_f \sin^2 \theta_W. \end{aligned} \quad (4.49)$$

The differential cross-section in the presence of the contact interaction can be written as

$$\frac{d\sigma}{d\cos\theta} = \text{SM}^0(s, t) + C_2^0(s, t) \frac{1}{\Lambda^2} + C_4^0(s, t) \frac{1}{\Lambda^4}. \quad (4.50)$$

where $\text{SM}^0(s, t)$ is the standard model cross-section and $t = -\frac{1}{2}s(1 - \cos\theta)$. The measured A_{FB} can be fitted with the A_{FB} calculated from Eq. 4.50, where the fitting parameter is the energy scale, Λ . In the calculation, the improved Born calculation of the contact-interaction part is corrected to take into account QED radiation as in [97]. The standard-model part is calculated with ZFITTER. Hereafter only the contact interaction between electron and b quark or that between electron and c quark is considered. For the model of RL^+ with Λ of 1 and 5 TeV, the σ' and A'_{FB} for b quarks with a cut of $\sqrt{s'/s} > 0.85$ as a function of \sqrt{s} are shown in Fig. 4.40, where the standard-model prediction is also shown. Deviations from the standard-model prediction due to the contact interaction can be seen in the figure.

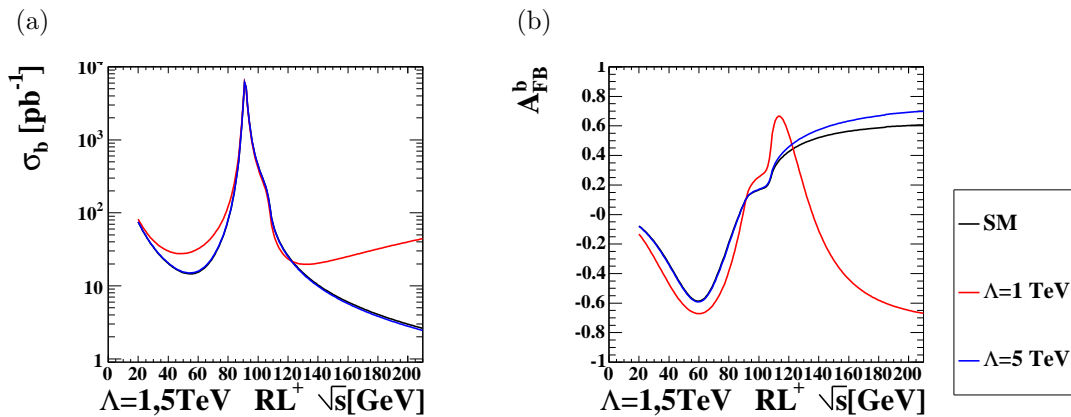


Figure 4.40: The calculation of the (a) cross-section and (b) forward-backward asymmetry of b quarks with a cut of $\sqrt{s'/s} > 0.85$ as a function of \sqrt{s} , where a contact interaction of RL^+ model with $\Lambda = 1$ or 5 TeV is added.

As regards the fitting, the parameter, $\epsilon \equiv 1/\Lambda^2$, is used practically instead of Λ . The ϵ is allowed to take both positive and negative values, which can treat the constructive and destructive models simultaneously since the η_{ij} always appears with $1/\Lambda^2$ according to Eq. 4.47. As regards the result of the combined data whose luminosity-weighted mean of \sqrt{s} is 197 GeV, the A_{FB}^{b} is shown as a function of ϵ for RL⁺ model in Fig. 4.41(a) and the χ^2 measured from its minimum ($\Delta\chi^2$) is shown in Fig. 4.41(b). The $\Delta\chi^2$ corresponding to the measured values of A_{FB}^{b} at 11 different \sqrt{s} points is also calculated as shown in Fig. 4.41(b), where the systematic correlations are taken into account. The latter non-combined case is more sensitive to ϵ due to the \sqrt{s} dependence of A_{FB}^{b} , which is used to set the limits on the contact interactions.

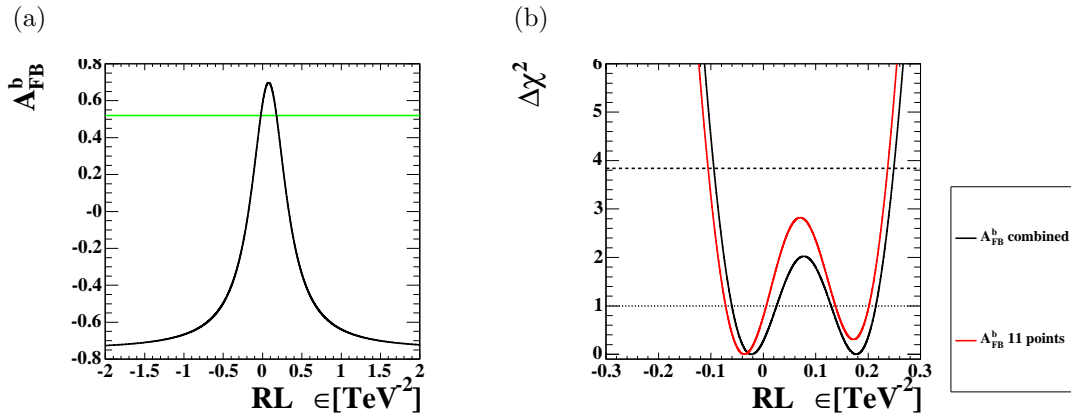


Figure 4.41: (a) The A_{FB}^{b} at \sqrt{s} of 197 GeV as a function of ϵ for RL model. The measured values of $A_{\text{FB}}^{\text{b,c}}$ for the combined data are indicated with horizontal lines. (b) The χ^2 measured from its minimum ($\Delta\chi^2$) for the A_{FB}^{b} corresponding to the combined data and 11 measured points.

The cross-sections of $e^+e^- \rightarrow b\bar{b}$ (σ_b) are calculated with the results of the R_b measurements [98] and total hadronic cross-section (σ_{had}) measurements at LEP2 [72, 99] at \sqrt{s} beyond 180 GeV, where correlations between R_b and σ_{had} measurements are neglected. The result of σ_b are also used to set the limit on the contact interaction. The $\Delta\chi^2$ corresponding to the A_{FB}^{b} and σ_b results as a function of ϵ are shown in Fig. 4.42. The χ^2 corresponding to the combination of A_{FB}^{b} and R_b results is calculated and is shown in Fig. 4.42, where R_b dependence of A_{FB}^{b} is treated but the systematic correlations are neglected.

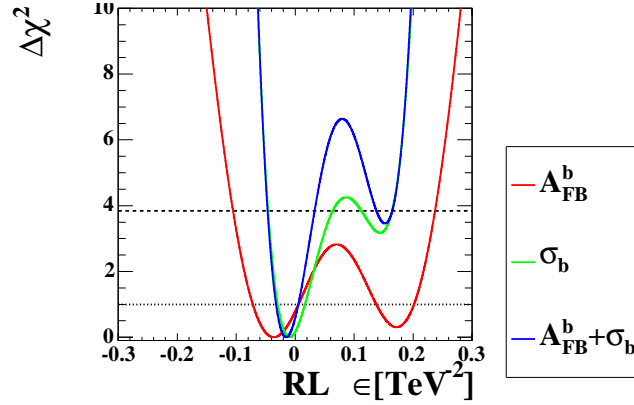


Figure 4.42: (a) The $\Delta\chi^2$ for A_{FB}^b , σ_b , and their combined results as a function of ϵ for RL model.

With the results of A_{FB}^b , σ_b , and their combination, χ^2 fits for ϵ are performed and the results are shown in Fig. 4.43 (a) with one standard deviation errors. Similar fits for A_{FB}^c are performed and the results are shown in Fig. 4.43(b). They shows that the ϵ is consistent to be zero, which means no contact interaction.

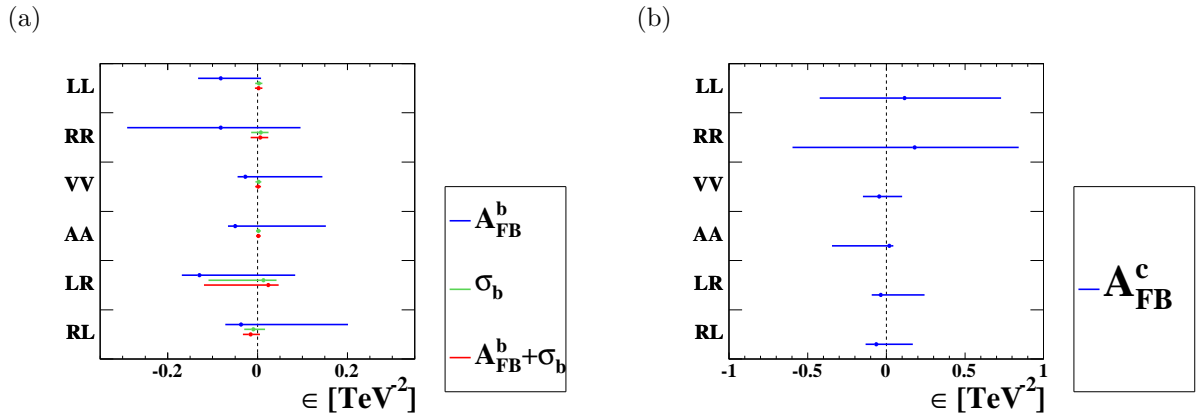
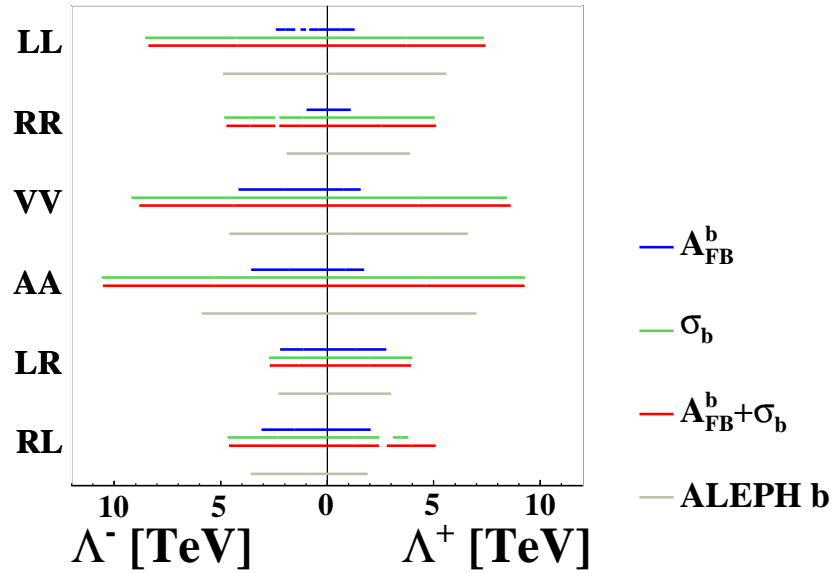


Figure 4.43: (a) The results of the χ^2 fits for A_{FB}^b , σ_b , and their combination. (b) The result of the χ^2 fits for A_{FB}^c .

For both positive and negative ϵ , the minimum of the χ^2 is calculated and 95% confidence level (95%CL) limits are set at ϵ where $\Delta\chi^2$ is 3.84. The Λ corresponding to the limit for positive (negative) ϵ is denoted as Λ^+ (Λ^-), which means the 95% CL limit for the energy scale of the constructive (destructive) model of the contact interaction. The evaluated limits are shown in Fig. 4.44 and Table. 4.17. In Fig. 4.44, the current limits

are also shown, which are evaluated by ALEPH [92] for b quarks, by DELPHI [93] and PETRA [20] for c quarks.

(a)



(b)

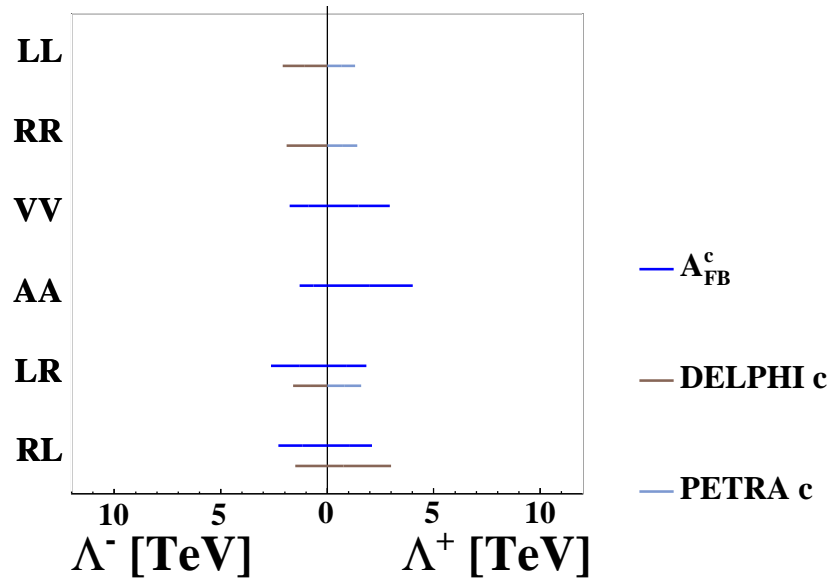


Figure 4.44: The excluded region of energy scale of the contact interactions in 95% confidence level (a) for b quark and (b) for c quarks.

For the limits with only A_{FB}^b result, the limit on LR^+ is better than the ALEPH's result. All limits with σ_b measurements and the combination of A_{FB}^b and σ_b measurements exceed the ALEPH's results and they are the highest limits for the contact interaction between electron and b quark. As regards the limits from A_{FB}^c , the limits on LL and RR models are not accessible. The limits on LR^\pm and RL^+ model exceed that for DELPHI or PETRA and they are the highest limits for the contact interaction between electron and c quark.

Table 4.17: The 95% confidence level limits on the energy scale of contact interaction.

model		95% CL limits on Λ [TeV]			
		b quark			c quark
		with A_{FB}^b	with σ_b	with $A_{\text{FB}}^b + \sigma_b$	with A_{FB}^c
LL	+	1.3	7.4	7.4	-
	-	2.4*	8.5	8.4	-
RR	+	1.1	5.1	5.1	-
	-	0.98	4.8*	4.7*	-
VV	+	1.6	8.5	8.6	2.9
	-	4.2	9.2	8.8	1.8
AA	+	1.7	9.3	9.3	4.0
	-	3.6	11	11	1.3
LR	+	2.8	4.0	3.9	1.8
	-	2.2	2.7	2.7	2.6
RL	+	2.0	3.8*	5.1*	2.1
	-	3.1	4.7	4.6	2.3

*) There are some regions not excluded at Λ smaller than the value listed in the table as shown in Fig. 4.44.

Next, leptoquarks are considered for examples of heavy particles exchanged between electron and b or c quark, which can be regarded as contact interaction effectively. The leptoquarks are motivated by the symmetry between leptons and quarks in the standard model and they appear in theories of grand unification [100] and in compositeness models [101]. The leptoquarks mediate quark-lepton transition carrying both color and fractional electric charge and a lepton number, which can be classified with Buchmüller-Rückl-Wyler (BRW) model [38] as shown in Table. 4.18. An S(V) denotes a scalar(vector) leptoquark and the subscript denotes the weak isospin. When the leptoquark can couple to both right- and left-handed leptons, an additional superscript indicates the lepton chirality. A tilde is introduced to differentiate between leptoquarks with different hypercharge. Some squarks in supersymmetric theories with broken R -parity couple to quark-lepton pair in the same way as leptoquarks. In the minimal supersymmetric extension of the standard model, the renormalizable gauge invariant operator that couples squarks

to quarks and leptons is given by $\lambda'_{ijk} L^i Q^j \overline{D^k}$, where i, j , or k denotes the generation, L is the left-handed lepton, Q is the left-handed quark, D is the right-handed singlet of down-type quark, and one of the three is the superparticle. The down-type squark (\widetilde{d}_R) mediates left-handed electron (e_L^-) and left-handed up-type quark (u_L) transition in the same way as S_0^L leptoquarks. The up-type squark (\widetilde{u}_L) mediates left-handed electron (e_L^-) and right-handed down-type quark (\overline{d}_R) transition in the same way as $\widetilde{S}_{1/2}$ leptoquarks. Such assignments of the squark to the leptoquarks are also shown in Table. 4.18. The leptoquark model used here is the same as the original BRW model but the leptoquark couplings between generations are allowed. For example, couplings between electron (1st generation) and b quark (3rd generation) is possible. Such leptoquarks can be exchanged in $e^+e^- \rightarrow q\bar{q}$ as shown in Fig. 4.45(b,c). The Feynman diagrams corresponding to the R -parity violating squarks are also shown in Fig. 4.45(d,e), where the cases with $b\bar{b}$ and $c\bar{c}$ final states are separately shown.

Model	Fermion number F	Charge Q	Coupling	Squark type
S_0^L	2	-1/3	$e_L u \quad \nu d$	\widetilde{d}_R
S_0^R	2	-1/3	$e_R u$	
\widetilde{S}_0	2	-4/3	$e_R d$	
$S_{1/2}^L$	0	-5/3	$e_L \bar{u}$	
$S_{1/2}^R$	0	-5/3 -2/3	$e_R \bar{u}$ $e_R \bar{d}$	
$\widetilde{S}_{1/2}$	0	-2/3	$e_L \bar{d}$	\widetilde{u}_L
S_1	2	-4/3 -1/3	$e_L d$ $e_L u \quad \nu d$	
V_0^L	0	-2/3	$e_L \bar{d} \quad \nu \bar{u}$	
V_0^R	0	-2/3	$e_R \bar{d}$	
\widetilde{V}_0	0	-5/3	$e_R \bar{u}$	
$V_{1/2}^L$	2	-4/3	$e_L d$	
$V_{1/2}^R$	2	-4/3 -1/3	$e_R d$ $e_R u$	
$\widetilde{V}_{1/2}$	2	-1/3	$e_L u$	
V_1	0	-5/3 -2/3	$e_L \bar{u}$ $e_L \bar{d} \quad \nu \bar{u}$	

Table 4.18: A general classification of leptoquark states in the Buchmüller-Rückl-Wyler model. Possible squark assignments to the leptoquark states in the minimal supersymmetric theories with broken R -parity are also also shown.

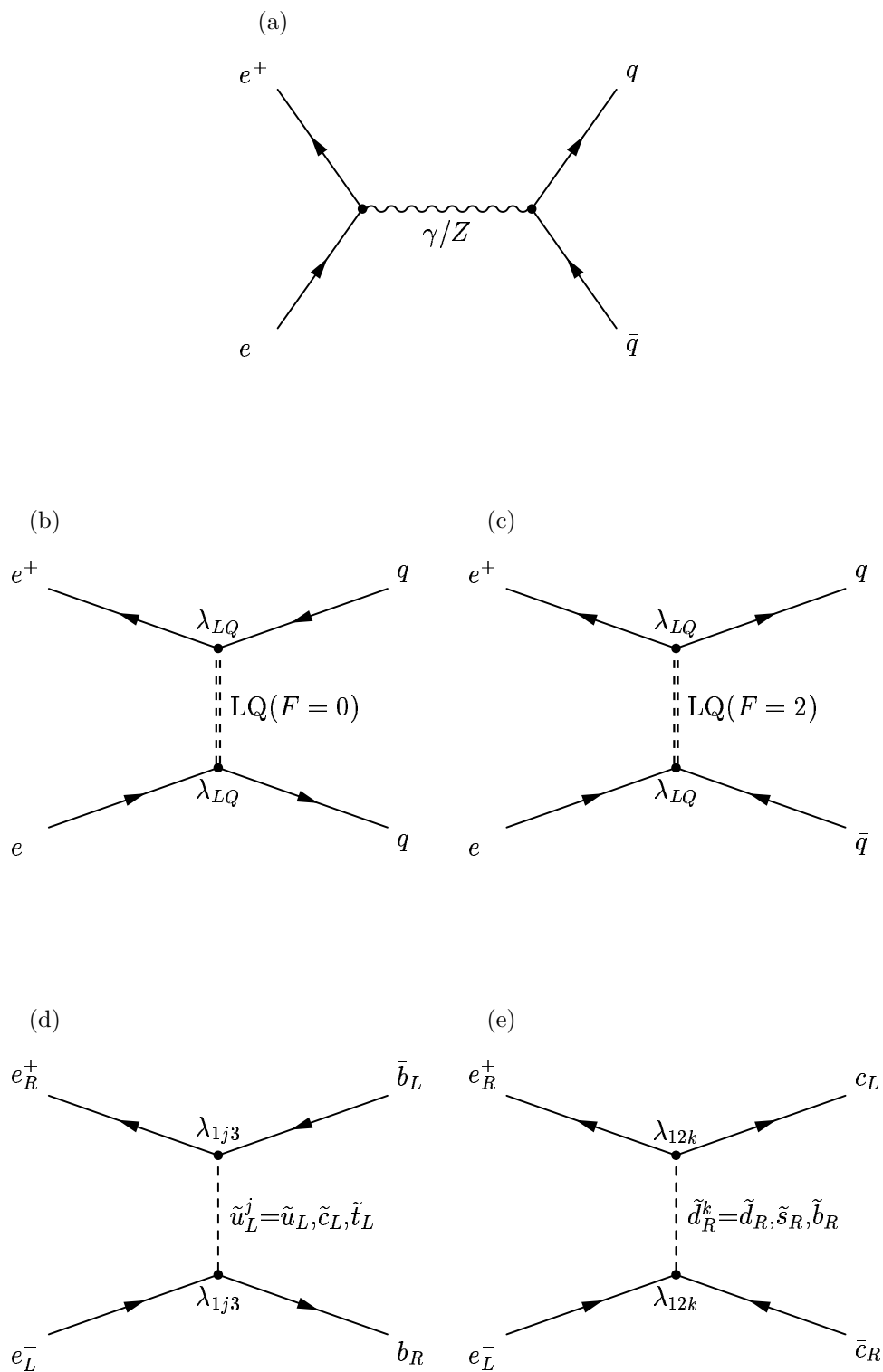


Figure 4.45: A Feynman diagram of $e^+e^- \rightarrow q\bar{q}$. (a) standard model. (b), (c) leptoquarks. (d), (e) R -parity violating squarks.

According to [96], the helicity amplitude of the $e^+e^- \rightarrow q\bar{q}$ with leptoquarks, $\mathcal{M}_{ij}(i, j = L, R)$ can be written as

$$\mathcal{M}_{ij}(s) = \frac{4\pi\alpha Q_e Q_f}{s} + \frac{4\pi\alpha}{\sin^2\theta_W \cos^2\theta_W} \cdot \frac{g_i^e g_j^f}{s - M_Z^2 + is\frac{\Gamma_Z}{M_Z}} + \eta_{ij}(t, u) \quad , \quad (4.51)$$

where $t = -\frac{1}{2}s(1 - \cos\theta)$, $u = -\frac{1}{2}s(1 + \cos\theta)$ and $\eta_{ij}(t, u)$ is defined as follows according to the fermion number, F , of the final state quark.

$$\eta_{ij}^{eq}(t, u) = \begin{cases} \frac{a_{ij} \cdot \lambda_{LQ}^2}{M_{LQ}^2 - t} & \text{for } F = 0 \quad ; \\ \frac{a_{ij} \cdot \lambda_{LQ}^2}{M_{LQ}^2 - u} & \text{for } |F| = 2 \quad . \end{cases} \quad ,$$

where the mass and coupling of the leptoquark are M_{LQ} and λ_{LQ} respectively. The type of the leptoquark is defined with a_{ij} as shown in Table. 4.19. In the limit of $M_{LQ}^2 \gg t, u$, the interaction is the same as the contact interaction, which can be seen by comparing Eq. 4.48 and Eq. 4.51. At such limit, corresponding energy scale of the contact interaction can be written as $\sqrt{4\pi|a_{ik}|\frac{M_{LQ}}{\lambda_{LQ}}}$. The corresponding contact-interaction model is seen in Table. 4.19. For example, $V_{1/2}^R$ corresponds to LR^+ model.

Table 4.19: The leptoquark types corresponding to the coefficients a_{ik} .

a_{ik}	up-type final state				down-type final state			
	LL	RR	LR	RL	LL	RR	LR	RL
S_0^L	1/2							
S_0^R		1/2						
\tilde{S}_0						1/2		
S_1	1/2				1			
$V_{1/2}^L$							1	
$V_{1/2}^R$				1				1
$\tilde{V}_{1/2}$			1					
$S_{1/2}^L$			-1/2					
$S_{1/2}^R$				-1/2				-1/2
$\tilde{S}_{1/2}$							-1/2	
V_0^L					-1			
V_0^R						-1		
\tilde{V}_0		-1						
V_1	-2				-1			

With the helicity amplitude, the theoretical cross-section and A_{FB} for $e^+e^- \rightarrow b\bar{b}$ or $c\bar{c}$ is calculated in a similar way to the case of the contact interaction. The λ_{LQ} is used as a fitting parameter and the fitting is performed at various M_{LQ} points for each leptoquark types. The 95% CL exclusion plots of λ_{LQ} as a function of M_{LQ} are shown in Fig. 4.46 (Fig. 4.46) for leptoquarks which couple electron and b (c) quark. In Fig. 4.46, exclusions with A_{FB}^b only, σ_b only and their combination are shown. For $V_{1/2}^R$, the information of A_{FB}^b is efficiently used in the exclusion with combination of A_{FB}^b and σ_b , which can be expected from the result of the contact interaction. In Fig. 4.47, figures corresponding to S_0^L , S_0^R and S_1 are not shown, for no space is excluded. The 95% CL limits on M_{LQ} at $\lambda = \sqrt{4\pi\alpha}$ are calculated and the results from $e^+e^- \rightarrow b\bar{b}$ and $c\bar{c}$ are shown in Table. 4.20 and Table. 4.21, respectively.

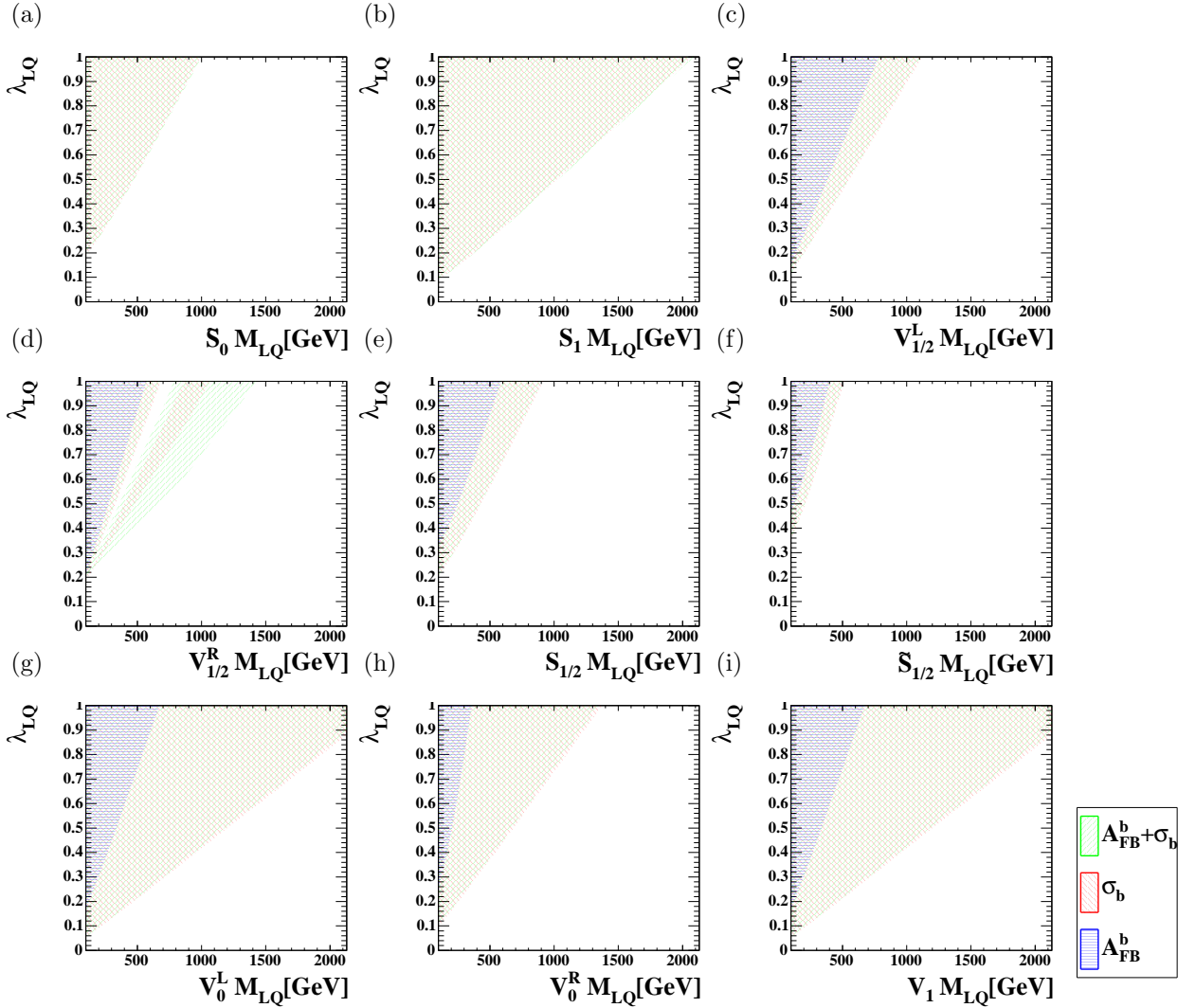


Figure 4.46: The 95% CL exclusion plots of λ_{LQ} as a function of M_{LQ} for leptoquarks which couple electron and b quark.

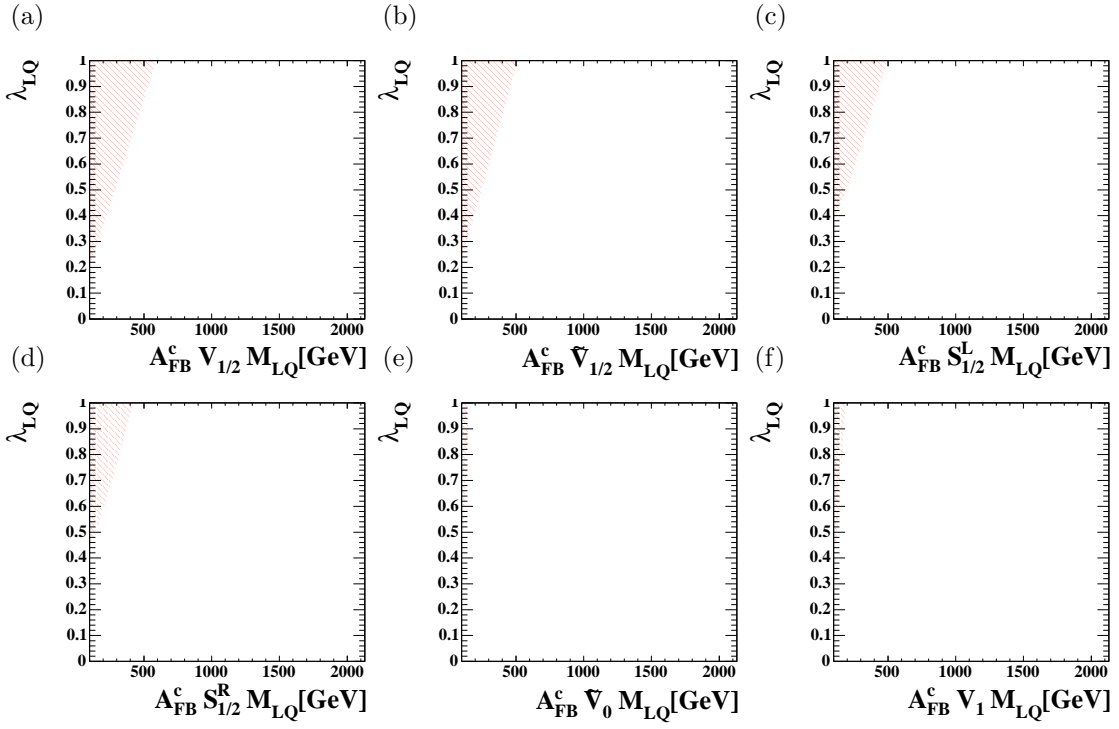


Figure 4.47: The 95% CL exclusion plots of λ_{LQ} as a function of M_{LQ} for leptoquarks which couple electron and c quark.

The results of leptoquarks which couple electron and b quark are compared to previously obtained ALEPH [92], DELPHI [93] and OPAL [99] results. This result for $V_{1/2}^R$ is better than them with only A_{FB}^b information. All results with σ_b and A_{FB}^b are better than the previous results. As regards the results of leptoquarks which couple electron and c quark are new for OPAL. The result of the $\tilde{S}_{1/2}$ is equivalent to that of R -parity violating squarks (\tilde{u}_L).

Table 4.20: 95%CL Limit on $M_{LQ}[\text{GeV}]$ at $\lambda_{LQ} = \sqrt{4\pi\alpha}$ from $e^+e^- \rightarrow b\bar{b}$

95%CL Limit on $M_{LQ}[\text{GeV}]$ at $\lambda_{LQ} = \sqrt{4\pi\alpha}$ from $e^+e^- \rightarrow b\bar{b}$			
LQ type	with A_{FB}^b	with σ_b	with $A_{FB}^b + \sigma_b$
\tilde{S}_0	—	253	256
S_1	—	603	612
$V_{1/2}^L$	233	333	330
$V_{1/2}^R$	171	308	422
$S_{1/2}$	—	230	227
$\tilde{S}_{1/2}$	—	—	—
V_0^L	201	720	707
V_0^R	131	401	393
V_1	201	720	707

Table 4.21: 95%CL Limits on $M_{LQ}[\text{GeV}]$ at $\lambda_{LQ} = \sqrt{4\pi\alpha}$ from $e^+e^- \rightarrow c\bar{c}$

95%CL Limits on $M_{LQ}[\text{GeV}]$ at $\lambda_{LQ} = \sqrt{4\pi\alpha}$ from $e^+e^- \rightarrow c\bar{c}$	
LQ type	with A_{FB}^c
S_0^L	—
S_0^R	—
S_1	—
$V_{1/2}$	174
$\tilde{V}_{1/2}$	146
$S_{1/2}^L$	—
$S_{1/2}^R$	—
\tilde{V}_0	—
V_1	109

Finally, new physics due to the effect of graviton exchange in large extra dimensions is studied. There are many orders of difference between the scale of the gravitational and electroweak interaction, which are the Planck scale ($M_{\text{pl}} \sim 10^{19}$ GeV) and the electroweak scale ($M_{\text{ew}} \sim 10^2$ GeV), respectively. The unexplained large difference is known as “hierarchy problem”. As a solution, it has been pointed out that the quantum-gravity scale could be as low as the electroweak scale with graviton propagating in the compactified higher dimensional space [102]. According to this theory, the Planck mass in $D = n + 4$ dimensions (M_D) is chosen to be the electroweak scale, where M_D is connected to the compactification radius (R) of the n extra dimension as $M_{\text{pl}}^2 = R^n M_D^{n+2}$. The gravitons can contribute to $e^+e^- \rightarrow f\bar{f}$ process via the process of virtual exchange of the possible excitation mode of the graviton (G^*) as $e^+e^- \rightarrow G^* \rightarrow f\bar{f}$. Although the contribution from single graviton mode is small, the large number of possible excitation modes can make the effect measurable [103]. According to [103], the differential cross-section with the virtual graviton exchange in the s -channel can be written as

$$\frac{d\sigma}{d\cos\theta} = A(s, t) + \frac{\lambda}{M_s^4} \cdot B(s, t) + \frac{\lambda^2}{M_s^8} \cdot C(s, t), \quad (4.52)$$

where $t = -\frac{1}{2}s(1 - \cos\theta)$, M_s is the mass scale of the order of M_D , and λ is of $\mathcal{O}(1)$ which depends on the details of the theory but weakly depends on the number of extra dimensions. With an assumption of $\lambda = \pm 1$, the $A_{\text{FB}}^{\text{b,c}}$ and σ_b are calculated according to [103], 95% CL limits on M_s are obtained as shown in Table. 4.22 in a similar way to the case of the contact interaction. Although this limits are not superior to limits from other measurements [104–109], this results can be used with them to improve the limits.

Table 4.22: The 95% CL limits on M_s .

95% CL limits on M_s [GeV]		
	$\lambda = -1$	$\lambda = 1$
with A_{FB}^{b}	300	420
with σ_b	490	490
with $A_{\text{FB}}^{\text{b}} + \sigma_b$	500	490
with A_{FB}^{c}	430	250
with $A_{\text{FB}}^{\text{b,c}} + \sigma_b$	510	490

Chapter 5

Conclusion

In this thesis, the forward-backward asymmetries for b and c quarks have been measured in e^+e^- collisions at center-of-mass energies between 130 GeV and 209 GeV, which is the measurement at the highest energy in e^+e^- collisions.

Two methods are used to evaluate the production angle of the primary quark and to identify the $b\bar{b}$ or $c\bar{c}$ events. One utilizes the hemisphere charge with a powerful b-tagging algorithm based on lifetime, lepton and event-shape information. The other uses the information of the leptons from semileptonic decays of heavy hadrons both to evaluate the primary-quark direction and to enhance events with primary b or c quarks. Finally, the two independent methods have been combined with a single likelihood function with which the A_{FB}^b and A_{FB}^c have been measured simultaneously by fitting the distribution of the evaluated primary-quark direction.

The forward-backward asymmetries for b and c quarks have been obtained at 11 different center-of-mass energies between 130 and 209 GeV, which are in good agreements with the standard model predictions. The corresponding χ^2 values are 14.6 and 4.68 for the A_{FB}^b and A_{FB}^c , respectively.

The same analysis has been performed for the combined data with \sqrt{s} larger than 180 GeV, where the expected variation of A_{FB} as a function of \sqrt{s} is less than 2% in the standard model prediction, and where the luminosity-weighted mean of \sqrt{s} is 197 GeV. The following results have been obtained.

$$\begin{aligned} A_{\text{FB}}^b &= 0.52 \pm 0.09(\text{stat.}) \pm 0.09(\text{syst.}), \\ A_{\text{FB}}^c &= 0.59 \pm 0.12(\text{stat.}) \pm 0.09(\text{syst.}). \end{aligned}$$

This analysis gains the best accuracy at LEP2 due to the development of the efficient methods and use of the full data collected by the OPAL detector during LEP2. This result is one of the verifications of the correctness of the standard model in the highest energy region currently available in e^+e^- collisions.

The result can be used to constrain some new physics beyond the standard model. Here, new physics due to contact interactions, leptoquarks, R -parity violating squarks,

and graviton in extra dimensions have been studied. New limit is obtained on the contact interaction between right-handed electron and left-handed b quark with constructive interference to the standard model (RL⁺ model). New limit on the RL⁺ contact interaction for c quark is also obtained. New limits on that between left-handed electron and right-handed c-quark with both constructive and destructive interference to the standard model (LR[±]) are also obtained. As regards the leptoquarks, new limit on the vector leptoquark with weak isospin of 1/2 which couples right-handed electron and left-handed b quark ($V_{1/2}^R$) is also obtained.

Appendix A

The Standard Model

The standard model is a theory to describe the constituents of matter and their interactions. There are two groups of particles, 'fermions' and 'bosons'. The fermions have odd-half-integer ($1/2, 3/2, \dots$) intrinsic angular momentum (spin)¹. The bosons have integer spin. The matter consists of two kinds of fermions, quarks and leptons. The interactions between fermions are described as exchanging of a boson between them. There are four kinds of such bosons, photon, W and Z bosons, and gluons. The electromagnetic and weak interactions are unified into the electroweak theory [4–6]. The strong interaction is described by quantum chromodynamics (QCD). The standard model is the union of the electroweak theory and QCD.

There are one more interaction known as gravity which is not included in the standard model. The gravitational interaction is too weak at the scale of the elementary particles and at the energy scale of this thesis, so it is negligible and ignored in subsequent consideration.

A.1 Elementary Particles in the Standard Model

A.1.1 Fermions

There are two groups of elementary fermions with spin $1/2$, quarks and leptons. Both are further divided into two classes with their electric charge. The quarks are divided in up-type quarks (electric charge² is $2/3$) and down-type quarks (electric charge is $-1/3$). The leptons are divided in charged leptons with -1 electric charge and neutrinos with neutral charge. Each of them is composed of three kinds of particles, manifesting three generations as shown in Table A.1. There are also anti-particles for each of them. The masses and the electric charges of the particles [51] are listed together.

¹The spin is always measured in the unit of reduced Plank constant ($\hbar = 1.054571596(82) \times 10^{-34}$ Js).

²The electric charge is always measured in the unit of the electron charge magnitude ($e = 1.602176462(63) \times 10^{-19}$ C).

Table A.1: Three generations of fermions in the standard model. The mass (in brackets) and the electric charge of the particles are listed together.

Fermion Generation						
1st	(mass)	2nd	(mass)	3rd	(mass)	Charge
Leptons						
ν_e	(0.5110 MeV/c ²)	ν_μ	(< 0.19 MeV/c ²)	ν_τ	(< 18.2 MeV/c ²)	0
e	(< 0.003 MeV/c ²)	μ	(105.7 MeV/c ²)	τ	(1777 MeV/c ²)	-1
Quarks						
u	(1.5 – 4.5 MeV/c ²)	c	(1.0 – 1.4 GeV/c ²)	t	(174 ± 5 GeV/c ²)	+ $\frac{2}{3}$
d	(5 – 8.5 MeV/c ²)	s	(80 – 155 MeV/c ²)	b	(4 – 4.5 GeV/c ²)	- $\frac{1}{3}$

A.1.2 Bosons

The interaction between fermions is described as exchanging of a spin-1 boson (vector boson) between them. Such bosons are photon (γ), W^\pm and Z bosons and eight kinds of gluons (g). The exchanging of photon corresponds to the electromagnetic interaction, that of W^\pm or Z bosons corresponds to the weak interactions and that of gluons corresponds to the strong interaction, as shown in Table A.2. Their masses and charges [51] are also listed together.

Table A.2: The vector bosons and their corresponding interactions are shown. Their masses and charges are also listed together.

Vector Boson	(mass)	charge	interaction
γ	< 2×10^{-16} eV	0	electromagnetic
W^\pm	80.42 ± 0.04 GeV	± 1	weak
Z	91.188 ± 0.002 GeV	0	weak
g	0 ^a	0	strong

^a Theoretical value.

A.1.3 Chirality and Quark Mixing

One of the characteristics of the weak interaction is left-right asymmetric nature, which violate parity conservation. The term ,left' or ,right' means the chirality, which correspond to the eigen value for the chirality operator, γ^5 . Left-handed state is the eigen state with eigen value of -1 . The relations of a fermion's field Ψ and its left(Ψ_L) or right(Ψ_R)

fields are as follows.

$$\Psi_L = \left(\frac{1 + \gamma^5}{2} \right) \Psi. \quad (\text{A.1})$$

$$\Psi_R = \left(\frac{1 - \gamma^5}{2} \right) \Psi. \quad (\text{A.2})$$

The chirality is invariant under the proper Lorentz transformation and it is equivalent to helicity for a massless particle.

For weak interaction, Left-handed and right-handed fermions have different quantum number and behave differently. For example, W^\pm boson couples only left-handed doublets,

$$\begin{pmatrix} \nu_e \\ e^- \end{pmatrix}_L, \begin{pmatrix} u \\ d' \end{pmatrix}_L, \quad (\text{A.3})$$

where the doublet of (u, d') is the eigen state of weak interaction. This is differ from the eigen state of mass. Such weak eigen state like d' is related to mass eigen state with 3×3 unitary matrix \mathbf{V} as,

$$\begin{pmatrix} d' \\ s' \\ b' \end{pmatrix} = \mathbf{V} \begin{pmatrix} d \\ s \\ b \end{pmatrix}. \quad (\text{A.4})$$

This matrix, \mathbf{V} , is called Cabbibo-Kobayashi-Masakawa matrix [110, 111] and is represented as,

$$\mathbf{V} \equiv \begin{pmatrix} V_{ud} & V_{us} & V_{ub} \\ V_{cd} & V_{cs} & V_{cb} \\ V_{td} & V_{ts} & V_{tb} \end{pmatrix}, \quad (\text{A.5})$$

and the 90% confidence limits on the magnitude of the elements are,

$$\begin{pmatrix} 0.9741 & \text{to} & 0.9756, & 0.219 & \text{to} & 0.226, & 0.0025 & \text{to} & 0.0048 \\ 0.219 & \text{to} & 0.226, & 0.9732 & \text{to} & 0.9748, & 0.038 & \text{to} & 0.044 \\ 0.004 & \text{to} & 0.014, & 0.037 & \text{to} & 0.044, & 0.9990 & \text{to} & 0.9993 \end{pmatrix}, \quad (\text{A.6})$$

Since \mathbf{V} is almost diagonal, weak interaction occurs within the single generation dominantly. The non-zero off-diagonal elements generate the couplings across quark generation. \mathbf{V} has 3 parameters corresponding to the rotation angles and one complex phase, which brakes the CP invariance³ for the weak interaction.

For lepton doublet such as $(\nu_e, e^-)_L$, there are no couplings across the generation in the framework of the standard model. The mass of the neutrinos is assumed to be zero⁴ and right-handed neutrino is not exist in the framework.

³the invariance under the series operation of the parity (P) transformation and the charge conjugation (C).

⁴The neutrino oscillation was observed at the Super-Kamiokande [112], therefore neutrinos have mass. Since its mass is very small, the standard model is still valid for almost all the subjects.

A.2 Interactions (Gauge Theory)

All interactions in the standard model can be understood in one theoretical framework, a gauge theory.

A.2.1 Gauge Theory

The gauge theory is a theory which require the invariance under certain symmetry transformations, called 'local gauge transformations'. (The term 'local' means the transformation is space-time dependent.)

The local gauge transformation transforms a fermion's field ψ as $\psi \rightarrow U\psi$, where U is parameterized in the form

$$U = \exp\left(i \sum_B \alpha^B(x) T^B\right). \quad (\text{A.7})$$

This is a presentation of a Lie group where T^B are the generators. Its lie algebra is the space yielded with the generators. The sum for the T^B is performed through the number of the group's dimension, which are decided from the kind of the group. For example, the natures of the $U(n)$, $SU(n)$ groups are shown in the following table.

Table A.3: Examples of lie groups.

lie group	representation	dimension	generator
$U(n)$	$n \times n$ complex Unitary matrix	n^2	$n \times n$ complex anti-Hermite matrix
$U(1)$	unit complex number	1	purely imaginary complex number
$SU(n)$	$n \times n$ complex Unitary matrix with determinant 1	$n^2 - 1$	$n \times n$ complex traceless anti-Hermite matrix
$SU(2)$		3	Pauli spin matrices
$SU(3)$		8	

In the framework of the gauge theory, interactions are naturally introduced to free fermions through following manner.

1. Select one symmetry group to reflect the symmetry related to the interaction.

2. Add an interaction term to the free Lagrangian in order that it is invariant under the local gauge transformation corresponding to the symmetry group.

This introduces massless vector bosons, gauge bosons, which mediate interactions among fermions. The invariance under the symmetry transformation is related to conserved quantity according to the Noether's theorem. Such conserved quantity corresponds to the 'charge', which is the measure of the strength of the coupling between a fermion and a gauge boson.

A.2.2 Quantum Electrodynamics(QED)

Quantum electrodynamics (QED) is the gauge theory for the electromagnetic interaction. It is based on the $U(1)$ symmetry group, which introduces invariance under complex phase transformation of the fermion's field. A free Lagrangian for a Dirac fermion field, Ψ , can be written as

$$\mathcal{L}_0 = i\bar{\Psi}(x)\gamma^\mu\partial_\mu\Psi(x) - m\bar{\Psi}(x)\Psi(x). \quad (\text{A.8})$$

The $U(1)$ local gauge transformation of the fermion's field, $\Psi(x)$, can be written as

$$\Psi(x) \rightarrow \Psi'(x) = U\Psi(x) \quad (\text{A.9})$$

$$= \exp(i\theta(x)Q)\Psi(x). \quad (\text{A.10})$$

The number of the generator is one because the dimension of the $U(1)$ gauge group is one. Therefore one new spin-1 gauge field, $A_\mu(x)$, is required from the gauge principle and it is transformed as

$$A_\mu(x) \rightarrow A'_\mu(x) = A_\mu(x) + \frac{1}{e}\partial_\mu\theta(x). \quad (\text{A.11})$$

Accordingly, the new Lagrangian is written as

$$\mathcal{L} = i\bar{\Psi}(x)\gamma^\mu D_\mu\Psi(x) - m\bar{\Psi}(x)\Psi(x) \quad (\text{A.12})$$

$$= \mathcal{L}_0 + eQA_\mu(x)\bar{\Psi}(x)\gamma^\mu\Psi(x), \quad (\text{A.13})$$

where D_μ is covariant derivative defined as

$$D_\mu \equiv [\partial_\mu - ieQA_\mu(x)]. \quad (\text{A.14})$$

This new Lagrangian is invariant under the local $U(1)$ transformation and the interaction term between the fermion and the gauge field is naturally introduced. The gauge boson corresponds to the photon and Q corresponds to the electric charge. Thus this $U(1)$ gauge symmetry related to the electromagnetic interaction is written as $U(1)_{\text{EM}}$. The electric charge is conserved quantity under the electromagnetic interaction, which is the 'Noether conserved quantity' for the $U(1)_{\text{EM}}$ gauge symmetry.

In addition, a gauge invariant kinetic term,

$$\mathcal{L}_{\text{kin}} \equiv -\frac{1}{4}F_{\mu\nu}F^{\mu\nu} \quad (\text{A.15})$$

is required for the gauge boson field to propagate, where $F_{\mu\nu} \equiv \partial_\mu A_\nu - \partial_\nu A_\mu$. The complete QED Lagrangian can be obtained adding the kinetic term. The gauge boson is massless because a possible mass term for the gauge field, $\frac{1}{2}m^2 A^\mu A_\mu$, would violate the gauge invariance.

A.2.3 Charge

The conserved quantity related to the gauge symmetry is the 'charge' for the interaction. This charge acts as the source of the force, deciding the coupling to the gauge boson corresponding to the interaction. There are three kinds of charge corresponding to the three kinds of interactions, electric charge, weak isospin and color charge.

Each quark has three kinds of color charge such as 'R', 'G' and 'B' which is the source of the strong interaction. This makes the quark a color triplet.

The left-handed fermions compose weak isospin doublets as shown in the section A.1.3. On the other hand, the right-handed fermions are singlets without weak isospin. Since W boson carrying the weak isospin has electric charge, electric charge contains weak isospin. In the electroweak theory, another charge, 'weak hypercharge' is used as more fundamental charge instead of the electric charge. The weak hypercharge (Y) is related to the third component of weak isospin (T_3) and electric charge (Q) as,

$$Y/2 \equiv Q - T_3. \quad (\text{A.16})$$

Then the fermions can be arranged with their charge as shown in Table A.4.

Table A.4: Fermion's charge, where Q is the electric charge, and T and T_3 denote the weak isospin and its third component Y is the hypercharge, C is the color charge. Y is related to Q with T_3 as $Q = T_3 + Y/2$. d', s', b' are the weak eigen states.

Fermion Generation			Quantum Numbers				
1	2	3	Q	T	T_3	Y	C
Leptons							
$\begin{pmatrix} \nu_e \\ e^- \end{pmatrix}_L$	$\begin{pmatrix} \nu_\mu \\ \mu^- \end{pmatrix}_L$	$\begin{pmatrix} \nu_\tau \\ \tau^- \end{pmatrix}_L$	0 -1	$\frac{1}{2}$	$+\frac{1}{2}$ $-\frac{1}{2}$	-1	0
e_R	μ_R	τ_R	-1	0	0	-2	0
Quarks							
$\begin{pmatrix} u \\ d' \end{pmatrix}_L$	$\begin{pmatrix} c \\ s' \end{pmatrix}_L$	$\begin{pmatrix} t \\ b' \end{pmatrix}_L$	$+\frac{2}{3}$ $-\frac{1}{3}$	$\frac{1}{2}$	$+\frac{1}{2}$ $-\frac{1}{2}$	$+\frac{1}{3}$	(R, G, B)
u_R	c_R	t_R	$+\frac{2}{3}$	0	0	$+\frac{4}{3}$	(R, G, B)
d_R	s_R	b_R	$-\frac{1}{3}$	0	0	$-\frac{2}{3}$	(R, G, B)

The quarks compose color triplet and the strong interaction is invariant under exchanging among the color triplet. Based on the symmetry, The strong interaction is introduced with the $SU(3)_C$ ⁵ gauge transformation. It requires 8 gluons, where the number of gluons is equal to the dimension of the $SU(3)$ group. The QCD Lagrangian \mathcal{L}_{QCD} can be written with a single parameter, a strong coupling constant (α_s) at certain energy scale. The α_s depends on the energy scale and tends to decrease at small distance or high energy scale. This nature is called ‘‘asymptotic freedom’’. Therefore, the quarks and gluons have the nature of ‘‘color confinement’’, which means quarks and gluons can not exist in states other than color singlet.

The left-handed fermions compose weak isospin doublet and related to $SU(2)_L$ ⁶ gauge symmetry. All of the fermions have weak hypercharge and related to $U(1)_Y$ ⁷ gauge symmetry. The electroweak interaction is introduced applying the invariance under the $SU(2)_L \otimes U(1)_Y$ gauge transformation.

⁵The subscript ‘C’ shows this $SU(3)$ group is related to the color charge.

⁶The subscript ‘L’ shows this $SU(2)$ group is related to the weak isospin doublet.

⁷The subscript ‘Y’ shows this $U(1)$ group is related to the weak hypercharge.

A.3 Electroweak Theory

A.3.1 Massless Electroweak Theory

The electroweak theory is based on the $SU(2)_L \otimes U(1)_Y$ gauge theory. The corresponding symmetry group is

$$G \equiv SU(2)_L \otimes U(1)_Y. \quad (\text{A.17})$$

A single family of quarks in the weak eigen state is considered for simplicity without loss of generality. The fermion field is represented as

$$\psi_1(x) = \begin{pmatrix} u \\ d' \end{pmatrix}_L, \quad \psi_2(x) = u_R, \quad \psi_3(x) = d'_R. \quad (\text{A.18})$$

The free Lagrangian of the fermion field is written as

$$\mathcal{L}_0 = \sum_{j=1}^3 i\bar{\psi}_j(x)\gamma^\mu\partial_\mu\psi_j(x), \quad (\text{A.19})$$

where no mass term exist. For fermion field Ψ , a possible mass term can be written as

$$m\bar{\Psi}\Psi = m(\bar{\Psi}_L + \bar{\Psi}_R)(\Psi_L + \Psi_R) = m(\bar{\Psi}_L\Psi_R + \bar{\Psi}_R\Psi_L), \quad (\text{A.20})$$

which mixes the left-handed and right-handed component of the fermion field. In the electroweak theory, left-handed and right-handed field are transformed differently (the symmetry is chiral). Hence no mass term is allowed in the electroweak theory because the mass term break the chiral symmetry.

According to the gauge principle, the Lagrangian is required to be invariant under the $SU(2)_L \otimes U(1)_Y$ local gauge transformation,

$$\psi_j(x) \xrightarrow{G} \psi'_j(x) \equiv \exp\left\{i\vec{\tau}\alpha(\vec{x})/2\right\} \exp\{iy_j\beta(x)\} \psi_j(x), \quad (\text{A.21})$$

where $\vec{\alpha}(x)$ is a three vector of real functions, $\vec{\tau}$ is the vector of the Pauli spin matrices, $\beta(x)$ is the real function and y_j is the weak hypercharge for ψ_j . The Pauli spin matrices are written as,

$$\tau_1 = \begin{pmatrix} 0 & 1 \\ 1 & 0 \end{pmatrix}, \quad \tau_2 = \begin{pmatrix} 0 & -i \\ i & 0 \end{pmatrix}, \quad \tau_3 = \begin{pmatrix} 1 & 0 \\ 0 & -1 \end{pmatrix}, \quad (\text{A.22})$$

and they only act on the doublet field ψ_1 as a $SU(2)$ generator.

It requires covariant derivatives with four new gauge bosons as,

$$D_\mu\psi_j(x) \equiv \left[\partial_\mu - ig\frac{\vec{\tau}}{2} \cdot \vec{W}_\mu - i\frac{g'}{2}y_jB_\mu \right] \psi_j(x), \quad (\text{A.23})$$

where g and g' are the coupling constants between fermions and gauge bosons for $SU(2)_L$ and $U(1)_Y$ respectively. The $\vec{W}_\mu = (W_\mu^1, W_\mu^2, W_\mu^3)$ are new vector bosons corresponding

to $SU(2)_L$ and B_μ is that for $U(1)_Y$, where the number of the new gauge bosons is as same as the dimension of the symmetry groups. To keep the gauge invariance, their transformation properties are fixed as,

$$B_\mu(x) \xrightarrow{G} B'_\mu(x) \equiv B_\mu(x) + \frac{2}{g'} \partial_\mu \beta(x), \quad (\text{A.24})$$

$$\vec{\tau} \cdot \vec{W}_\mu \xrightarrow{G} \vec{\tau} \cdot \vec{W}'_\mu \equiv U(x) \vec{\tau} \cdot \vec{W}_\mu U^\dagger(x) + \frac{2i}{g} U(x) \partial_\mu U^\dagger(x), \quad (\text{A.25})$$

where $U(x) \equiv \exp \{i\vec{\tau}\vec{\alpha}(x)/2\}$.

Then new Lagrangian

$$\mathcal{L} = \sum_{j=1}^3 i \bar{\psi}_j(x) \gamma^\mu D_\mu \psi_j(x) \quad (\text{A.26})$$

$$= \sum_{j=1}^3 i \bar{\psi}_j(x) \gamma^\mu \left[\partial_\mu - ig \frac{\vec{\tau}}{2} \cdot \vec{W}_\mu - i \frac{g'}{2} y_j B_\mu \right] \psi_j(x) \quad (\text{A.27})$$

$$= \mathcal{L}_0 + \frac{g}{2} \bar{\psi}_1(x) \gamma^\mu \left[\vec{\tau} \cdot \vec{W}_\mu \right] \psi_1(x) + \frac{g'}{2} \sum_{j=1}^3 \bar{\psi}_j(x) \gamma^\mu [y_j B_\mu] \psi_j(x) \quad (\text{A.28})$$

$$= \mathcal{L}_0 + \frac{g}{2} \bar{\psi}_1(x) \gamma^\mu \begin{pmatrix} W_\mu^3 & W_\mu^1 - iW_\mu^2 \\ W_\mu^1 + iW_\mu^2 & -W_\mu^3 \end{pmatrix} \psi_1(x) \\ + \frac{g'}{2} B_\mu \sum_{j=1}^3 y_j \bar{\psi}_j(x) \gamma^\mu \psi_j(x) \quad (\text{A.29})$$

$$\equiv \mathcal{L}_0 + \mathcal{L}_{\text{fermion}} \quad (\text{A.30})$$

is invariant under the $SU(2)_L \otimes U(1)_Y$ local gauge transformation G . The newly introduced term, $\mathcal{L}_{\text{fermion}}$ represents interactions between the gauge bosons and fermions.

The gauge boson fields, \vec{W}_μ and B_μ should be converted to the fields for existing bosons, W_μ^+ , W_μ^- , Z_μ , A_μ photon). The relations between them are defined as,

$$W_\mu^+ \equiv (W_\mu^1 - iW_\mu^2)/\sqrt{2}, \quad (\text{A.31})$$

$$W_\mu^- \equiv (W_\mu^1 + iW_\mu^2)/\sqrt{2}, \quad (\text{A.32})$$

$$\begin{pmatrix} W_\mu^3 \\ B_\mu \end{pmatrix} \equiv \begin{pmatrix} \cos \theta_W & \sin \theta_W \\ -\sin \theta_W & \cos \theta_W \end{pmatrix} \begin{pmatrix} Z_\mu \\ A_\mu \end{pmatrix}, \quad (\text{A.33})$$

where θ_W is called weak mixing angle ('Weinberg angle') to decide the mixing between W_μ^3 and B_μ . The θ_W will be fixed to realize the QED Lagrangian from A_μ piece. With these relations, the fermion part of the Lagrangian, $\mathcal{L}_{\text{fermion}}$ can be composed of three parts. The first One is \mathcal{L}_{CC} from W_μ^\pm piece representing the charged current. The second one is $\mathcal{L}_{\text{NC}}^Z$ from Z_μ piece representing the neutral current of Z . The third one is \mathcal{L}_{EM}

from A_μ piece representing the electromagnetic current. \mathcal{L}_{EM} can be written as

$$\begin{aligned}\mathcal{L}_{\text{EM}} &= \bar{\psi}_1 \gamma^\mu (g \sin \theta_W \tau^3 / 2 + g' \cos \theta_W y_1 / 2) \psi_1 \\ &\quad + \bar{\psi}_2 \gamma^\mu (g' \cos \theta_W y_2 / 2) \psi_2 \\ &\quad + \bar{\psi}_3 \gamma^\mu (g' \cos \theta_W y_3 / 2) \psi_3\end{aligned}\tag{A.34}$$

In order to match \mathcal{L}_{EM} to the QED Lagrangian, the θ_W is defined as

$$g \sin \theta_W = g' \cos \theta_W = e.\tag{A.35}$$

The electric charge operator $Q_j (j = 1, 2, 3)$ is defined as follows.

$$Q_1 = \begin{pmatrix} \frac{1}{2} + \frac{y_1}{2} & 0 \\ 0 & -\frac{1}{2} + \frac{y_1}{2} \end{pmatrix}, \quad Q_2 = \frac{y_2}{2}, \quad Q_3 = \frac{y_3}{2},\tag{A.36}$$

which corresponding to Eq. A.16. With these relations, the fermion part of the Lagrangian, $\mathcal{L}_{\text{fermion}}$ can be written as,

$$\mathcal{L}_{\text{fermion}} = \mathcal{L}_{\text{CC}} + \mathcal{L}_{\text{NC}}^Z + \mathcal{L}_{\text{EM}},\tag{A.37}$$

where,

$$\mathcal{L}_{\text{CC}} = \frac{e}{\sqrt{2} \sin \theta_W} (\bar{u}_L(x) \gamma^\mu d'_L(x) W_\mu^+ + h.c.),\tag{A.38}$$

$$\mathcal{L}_{\text{NC}}^Z = \frac{e}{\sin \theta_W \cos \theta_W} \sum_{j=1}^3 \bar{\psi}_j(x) \gamma^\mu \left(\frac{\tau_3}{2} - Q_j \sin^2 \theta_W \right) \psi_j(x) Z_\mu,\tag{A.39}$$

$$\mathcal{L}_{\text{EM}} = e \sum_{j=1}^3 \bar{\psi}_j(x) \gamma^\mu Q_j \psi_j(x) A_\mu.\tag{A.40}$$

The Lagrangian \mathcal{L}_{CC} is further converted with the fermion fields $u(x)$, $d'(x)$ as,

$$\mathcal{L}_{\text{CC}} = \frac{e}{2\sqrt{2} \sin \theta_W} (\bar{u}(x) \gamma^\mu (1 - \gamma^5) d'(x) W_\mu^+ + h.c.).\tag{A.41}$$

It can also be written with all quark fields in mass eigen stats ((d, s, b) and (u, c, t)) and the CKM matrix (\mathbf{V}) as,

$$\mathcal{L}_{\text{CC}} = \frac{e}{2\sqrt{2} \sin \theta_W} \left((\bar{u}, \bar{c}, \bar{t}) \gamma^\mu (1 - \gamma^5) \mathbf{V} \begin{pmatrix} d \\ s \\ b \end{pmatrix} W_\mu^+ + h.c. \right).\tag{A.42}$$

The Lagrangian \mathcal{L}_{EM} is further converted with the electric charge of u (Q_u) and that of d (Q_d) as,

$$\mathcal{L}_{\text{EM}} = e (\bar{u}(x) \gamma^\mu Q_u u(x) + \bar{d}'(x) \gamma^\mu Q_d d'(x)) A_\mu.\tag{A.43}$$

It also can be written with all the three generation and the CKM matrix \mathbf{V} ,

$$\mathcal{L}_{\text{EM}} = e \left[(\bar{u}, \bar{c}, \bar{t}) \gamma^\mu Q_u \begin{pmatrix} u \\ c \\ t \end{pmatrix} + (\bar{d}, \bar{s}, \bar{b}) \mathbf{V}^\dagger \gamma^\mu Q_d \mathbf{V} \begin{pmatrix} d \\ s \\ b \end{pmatrix} \right] A_\mu \quad (\text{A.44})$$

$$= e \sum_{f=d,u,s,c,b,t} [\bar{f} \gamma^\mu Q_f f] A_\mu. \quad (\text{A.45})$$

This reproduce the QED interaction. For the case of the leptons $(\nu_e, \nu_\mu, \nu_\tau)$ and (e, μ, τ) , their Lagrangian can be written in similar way.

For the case of the Lagrangian $\mathcal{L}_{\text{NC}}^Z$, the weak eigen states for the quarks d , s and b can be converted with the CKM matrix in the same way and it can be converted as

$$\mathcal{L}_{\text{NC}}^Z = \frac{e}{2 \sin \theta_W \cos \theta_W} \sum_{f=d,u,s,c,b,t} [\bar{f} \gamma^\mu \{v_f - a_f \gamma^5\} f Z_\mu], \quad (\text{A.46})$$

where v_f and a_f are the vector and axial vector couplings for the fermions f and can be written with its electric charge (Q_f) and the third component of the weak isospin for their left-handed part (T_3^f) as

$$v_f = T_3^f (1 - 4|Q_f| \sin^2 \theta_W), \quad (\text{A.47})$$

$$a_f = T_3^f, \quad (\text{A.48})$$

and their values are shown in Table A.5.

Table A.5: Fermion's vector and axial vector couplings (v and a respectively), where Q is the electric charge, and T_3 denote the third component of the weak isospin for the left-handed part.

Fermions		Q	T_3	v	a
neutrinos	$(\nu_e, \nu_\mu, \nu_\tau)$	0	$+\frac{1}{2}$	$+\frac{1}{2}$	$+\frac{1}{2}$
leptons	(e, μ, τ)	-1	$-\frac{1}{2}$	$-\frac{1}{2} + 2 \sin^2 \theta_W$	$-\frac{1}{2}$
up-type quarks	(u, c, t)	$+\frac{2}{3}$	$+\frac{1}{2}$	$+\frac{1}{2} - \frac{4}{3} \sin^2 \theta_W$	$+\frac{1}{2}$
down-type quarks	(d, s, b)	$-\frac{1}{3}$	$-\frac{1}{2}$	$-\frac{1}{2} + \frac{2}{3} \sin^2 \theta_W$	$-\frac{1}{2}$

In addition, gauge invariant kinetic terms \mathcal{L}_{kin} for the gauge bosons should be added to the Lagrangian. It is given by

$$\mathcal{L}_{\text{kin}} = -\frac{1}{4} B_{\mu\nu} B^{\mu\nu} - \frac{1}{4} \vec{W}_{\mu\nu} \vec{W}^{\mu\nu}, \quad (\text{A.49})$$

where $B_{\mu\nu}$ and $\vec{W}_{\mu\nu}$ are the field strengths:

$$B_{\mu\nu} \equiv \partial_\mu B_\nu - \partial_\nu B_\mu, \quad \vec{W}_{\mu\nu} \equiv \partial_\mu \vec{W}_\nu - \partial_\nu \vec{W}_\mu + g \vec{W}_\mu \times \vec{W}_\nu. \quad (\text{A.50})$$

With the existing bosons, W_μ^+ , W_μ^- , Z_μ , \mathcal{L}_{kin} represents the kinetic terms for the gauge bosons and the triple and quartic couplings between the gauge bosons.

A.3.2 Gauge Boson Masses and Higgs Mechanism

The gauge symmetry forbids the mass term of the gauge bosons. The fermion's mass term is also forbidden because of the chiral symmetry of the electroweak theory. They are introduced in gauge symmetric way through spontaneous electroweak symmetry breaking with a new $SU(2)_L$ doublet of complex scalar (spin-0) fields (Higgs fields),

$$\Phi \equiv \begin{pmatrix} \phi^+ \\ \phi^0 \end{pmatrix}. \quad (\text{A.51})$$

The weak hypercharge of the doublet is 1. With the covariant derivative,

$$D_\mu \equiv \partial_\mu + ig \frac{\vec{\tau}}{2} \cdot \vec{W}_\mu + ig' \frac{Y}{2} B_\mu \quad (\text{A.52})$$

the Lagrangian

$$\mathcal{L}_{\text{scalar}} = D_\mu \Phi^\dagger D^\mu \Phi - \mu^2 (\Phi^\dagger \Phi) - \lambda (\Phi^\dagger \Phi)^2 \quad (\lambda > 0, \mu^2 < 0), \quad (\text{A.53})$$

is invariant under local $SU(2)_L \otimes U(1)_Y$ transformations. There is an infinite set of degenerate vacuum states with the vacuum expectation value of

$$\langle \Phi \rangle_0 = \begin{pmatrix} \langle \phi^+ \rangle_0 \\ \langle \phi^0 \rangle_0 \end{pmatrix}, \quad (\text{A.54})$$

where

$$(\langle \phi^0 \rangle_0)^2 + (\langle \phi^+ \rangle_0)^2 = \frac{-\mu^2}{2\lambda}. \quad (\text{A.55})$$

If a vacuum expectation value is selected among them, the $SU(2)_L \otimes U(1)_Y$ symmetry of the vacuum is broken. The $U(1)$ symmetry for the electromagnetic force ($U(1)_{\text{EM}}$) should be kept in the vacuum after the symmetry breaking. In order to keep this $U(1)_{\text{EM}}$ symmetry, the invariance of the vacuum expectation value against the $U(1)_{\text{EM}}$ transformation is required as,

$$\langle e^{i\alpha(x)Q} \Phi \rangle_0 = \langle \Phi \rangle_0, \quad (\text{A.56})$$

where $\alpha(x)$ is real function and Q is the electric charge operator. This means the operator Q annihilates the vacuum as

$$Q \langle \Phi \rangle_0 = \begin{pmatrix} 1 & 0 \\ 0 & 0 \end{pmatrix} \begin{pmatrix} \langle \phi^+ \rangle_0 \\ \langle \phi^0 \rangle_0 \end{pmatrix} = \langle \phi^+ \rangle_0 = 0. \quad (\text{A.57})$$

Accordingly, in order to break the symmetry of the vacuum as $SU(2)_L \otimes U(1)_Y \rightarrow U(1)_{EM}$, the vacuum expectation value is selected as

$$\langle \Phi \rangle_0 = \begin{pmatrix} 0 \\ \frac{v}{\sqrt{2}} \end{pmatrix}, \quad (\text{A.58})$$

where

$$v = \sqrt{\frac{-\mu^2}{\lambda}}. \quad (\text{A.59})$$

The Higgs doublet can be represented with v as

$$\Phi = \exp\left(i\frac{\tau^i \chi_i}{2} \frac{\chi_i}{v}\right) \begin{pmatrix} 0 \\ (v+H)/\sqrt{2} \end{pmatrix}. \quad (\text{A.60})$$

The three fields, $\chi_i (i = 1, 2, 3)$, are related to massless Goldstone bosons. Due to the $SU(2)_L$ invariance of the Lagrangian, these Goldstone bosons disappear through fixing the gauge as,

$$\Psi' = \exp\left(-i\frac{\tau^i \chi_i}{2} \frac{\chi_i}{v}\right) \Psi = \begin{pmatrix} 0 \\ (v+H)/\sqrt{2} \end{pmatrix}. \quad (\text{A.61})$$

The fixed gauge is called as ‘‘unitary gauge’’ and the Lagrangian written with the new Higgs fields lose the freedom against $SU(2)_L$ transformation. The Lagrangian \mathcal{L}_{scalar} can be written in terms of the v and H as,

$$\begin{aligned} \mathcal{L}_{scalar} &= \left| \left(\partial_\mu + ig\frac{\tau^i}{2} W_\mu^i + i\frac{g'}{2} Y B_\mu \right) \frac{v+H}{\sqrt{2}} \begin{pmatrix} 0 \\ 1 \end{pmatrix} \right|^2 \\ &\quad - \mu^2 \frac{(v+H)^2}{2} - \lambda \frac{(v+H)^4}{4} \end{aligned} \quad (\text{A.62})$$

In terms of the physical fields W^\pm and Z , the \mathcal{L}_{scalar} can be written as,

$$\begin{aligned} \mathcal{L}_{scalar} &= \left| \begin{pmatrix} 0 \\ \partial_\mu H/\sqrt{2} \end{pmatrix} + i\frac{g}{2}(v+H) \begin{pmatrix} W_\mu^+ \\ (-1/\sqrt{2} \cos \theta_W) Z_\mu \end{pmatrix} \right|^2 \\ &\quad - \mu^2 \frac{(v+H)^2}{2} - \lambda \frac{(v+H)^4}{4} \end{aligned} \quad (\text{A.63})$$

$$\begin{aligned} &= \frac{1}{2} \partial_\mu H \partial^\mu H + \frac{g^2}{4} (v+H)^2 \left(W_\mu^+ W^{-\mu} + \frac{1}{2 \cos^2 \theta_W} Z_\mu Z^\mu \right) \\ &\quad - \mu^2 \frac{(v+H)^2}{2} - \lambda \frac{(v+H)^4}{4} \end{aligned} \quad (\text{A.64})$$

$$\begin{aligned} &= \frac{1}{2} \partial_\mu H \partial^\mu H \\ &\quad - \frac{1}{2} (-2\mu^2) H^2 + \frac{g^2 v^2}{4} W_\mu^+ W^{-\mu} + \frac{g^2 v^2}{8 \cos^2 \theta_W} Z_\mu Z^\mu \\ &\quad + \frac{g^2 v}{2} H W_\mu^+ W^{-\mu} + \frac{g^2 v}{4 \cos^2 \theta_W} H Z_\mu Z^\mu \\ &\quad + \frac{g^2}{4} H^2 W_\mu^+ W^{-\mu} + \frac{g^2}{8 \cos^2 \theta_W} H^2 Z_\mu Z^\mu \\ &\quad + \frac{\mu^2}{v} H^3 + \frac{\mu^2}{4v^2} H^4 - \frac{\mu^2}{4} v^2 \end{aligned} \quad (\text{A.65})$$

The first term is the kinetic term of the Higgs. The terms from fifth to tenth represent the triple and quartic couplings between the gauge bosons and the Higgs and the triple and quartic self coupling of the Higgs. The second to fourth terms can be interpreted as mass terms of the Higgs(M_H), $W^\pm(M_W)$ and $Z(M_Z)$ bosons respectively as,

$$\begin{aligned} & -\frac{1}{2}(-2\mu^2)H^2 + \frac{g^2v^2}{4}W_\mu^+W^{-\mu} + \frac{g^2v^2}{8\cos^2\theta_W}Z_\mu Z^\mu \\ = & -\frac{1}{2}M_H^2H^2 + M_W^2W_\mu^+W^{-\mu} + \frac{1}{2}M_Z^2Z_\mu Z^\mu. \end{aligned} \quad (\text{A.66})$$

Accordingly the Higgs, W and Z masses can be written as,

$$M_H = \sqrt{-2\mu^2} \quad (\text{A.67})$$

$$M_W = \frac{gv}{2} = \frac{ev}{2\sin\theta_W} \quad (\text{A.68})$$

$$M_Z = \frac{gv}{2\cos\theta_W} = \frac{ev}{2\sin\theta_W\cos\theta_W} \quad (\text{A.69})$$

From the low-energy phenomenology,

$$\frac{g}{2\sqrt{2}} = \left(\frac{M_W^2 G_F}{\sqrt{2}}\right)^{1/2}. \quad (\text{A.70})$$

From the measured value of G_F , v can be calculated as,

$$v = \left(\sqrt{2}G_F\right)^{1/2} \sim 246\text{GeV}. \quad (\text{A.71})$$

A.3.3 Fermion Masses

The masses of the fermions can be generated in a gauge symmetric way through Yukawa couplings with the Higgs boson. With the Higgs doublet, the following gauge-invariant Lagrangian, \mathcal{L}_Y , with fermion-scalar Yukawa couplings can be written as,

$$\begin{aligned} \mathcal{L}_Y = & c_1 (\bar{u}, \bar{d})_L \begin{pmatrix} \phi^+ \\ \phi^0 \end{pmatrix} d_R + c_2 (\bar{u}, \bar{d})_L \begin{pmatrix} \phi^{0\dagger} \\ -\phi^{+\dagger} \end{pmatrix} u_R \\ & + c_3 (\bar{\nu}_e, \bar{e})_L \begin{pmatrix} \phi^+ \\ \phi^0 \end{pmatrix} e_R + \text{h.c.} \end{aligned} \quad (\text{A.72})$$

In the unitary gauge after spontaneous symmetry breaking, the Yukawa-type Lagrangian takes the simple form as,

$$\mathcal{L}_Y = \frac{1}{\sqrt{2}}(v + H) \{c_1 \bar{d}d + c_2 \bar{u}u + c_3 \bar{e}e\}. \quad (\text{A.73})$$

Therefore, the mechanism of the spontaneous symmetry breaking also generates fermion masses as,

$$m_d = -c_1 v/\sqrt{2}; \quad m_u = -c_2 v/\sqrt{2}; \quad m_e = -c_3 v/\sqrt{2}. \quad (\text{A.74})$$

Since we do not know the parameters c_i , the values of the fermion masses are arbitrary.

A.4 The Standard Model Parameters

The standard model Lagrangian \mathcal{L}_{SM} can be written as

$$\mathcal{L}_{\text{SM}} = \mathcal{L}_{\text{QCD}} + \mathcal{L}_{\text{EW}} \quad (\text{A.75})$$

$$\mathcal{L}_{\text{EW}} = \mathcal{L}_0 + \mathcal{L}_{\text{CC}} + \mathcal{L}_{\text{NC}}^Z + \mathcal{L}_{\text{EM}} + \mathcal{L}_{\text{kin}} + \mathcal{L}_{\text{scalar}} + \mathcal{L}_Y. \quad (\text{A.76})$$

The parameters of the standard model (SM) are the couplings (α_s , g and g'), the vacuum expectation value (v), the Higgs mass (m_H), all fermion's masses (m_f) and the 4 parameters (3 rotation angles and 1 phase) of the CKM matrix (\mathbf{V}). The set of variables, g and g' can be replaced with θ_W and α_{EM} . The variable v can be replaced with the G_F . Once these parameters are set, the couplings between particles and their propagation in the space-time are known with the standard model Lagrangian and physics quantities related to the standard model process can be calculated. Particularly, a kind of diagram called ‘‘Feynman diagram’’ is used, which represents the couplings and the propagation of the particles in the SM Lagrangian.

Appendix B

Massless Tree-Level A_{FB} Calculation

The tree level Feynman diagram for the process $e^+e^- \rightarrow f\bar{f}$ is written in Fig. B.1.

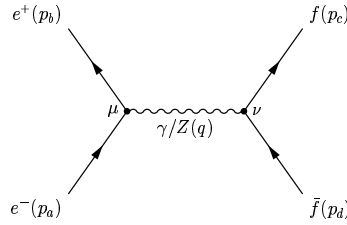


Figure B.1: The tree level diagram for $e^+e^- \rightarrow f\bar{f}$.

This is a superposition of the two diagrams below, where propagators and vertex coefficients are shown.

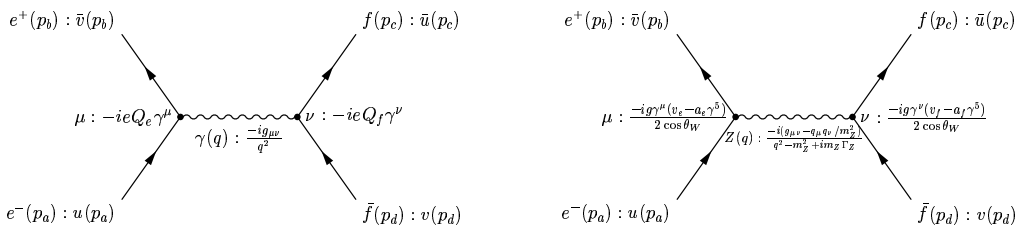


Figure B.2: The tree level diagrams for $e^+e^- \rightarrow f\bar{f}$.

The invariant amplitude for the diagram with γ propagator is defined as \mathcal{M}_γ and that for the diagram with Z propagator is defined as \mathcal{M}_Z . The invariant amplitude for the real process as shown in Fig. B.1 is defined as \mathcal{M} and is related with \mathcal{M}_Z and \mathcal{M}_γ as,

$$\mathcal{M} = \mathcal{M}_Z + \mathcal{M}_\gamma. \quad (\text{B.1})$$

The interaction rate Γ is given as,

$$\Gamma = (2\pi)^4 N_c \int \cdots \int \frac{d^3 \vec{p}_c}{(2\pi)^3 2E_c} \frac{d^3 \vec{p}_d}{(2\pi)^3 2E_d} \langle |\mathcal{M}|^2 \rangle \delta^4(p_a + p_b + p_c + p_d), \quad (\text{B.2})$$

where N_c is the degree of freedom due to the color charge of the final state fermion (1 for leptons, 3 for quarks), $p_i \equiv (E_i, \vec{p}_i)$ is 4-momentum of particle i , m_i is mass of particle i and $\langle |\mathcal{M}|^2 \rangle$ means that $|\mathcal{M}|^2$ is averaged over the initial number of the spin states and is summed over the final number of the spin states, which means that electron and positron are unpolarized and the polarization of the final fermion and anti-fermion are not measured. The $\langle |\mathcal{M}|^2 \rangle$ can be written as

$$\langle |\mathcal{M}|^2 \rangle = \langle |\mathcal{M}_Z|^2 \rangle + \langle |\mathcal{M}_\gamma|^2 \rangle + 2 \Re e \{ \langle \mathcal{M}_Z \mathcal{M}_\gamma^* \rangle \}. \quad (\text{B.3})$$

The third part means the contribution of the $Z - \gamma$ interference.

If the 4-momentums of initial electrons are given with the center-of-mass energy, \sqrt{s} , as

$$p_a = (\sqrt{s}/2, 0, 0, |\vec{p}_e|) \quad (\text{B.4})$$

$$p_b = (\sqrt{s}/2, 0, 0, -|\vec{p}_e|), \quad (\text{B.5})$$

the Γ can be written as

$$\Gamma = \frac{N_c |\vec{p}_f|}{16\pi^2 \sqrt{s}} \int \int \langle |\mathcal{M}|^2 \rangle d\Omega \quad (\text{B.6})$$

with constraints on the 4-momentums of the outgoing fermions as

$$\vec{p}_c = \vec{p}_f, \quad (\text{B.7})$$

$$\vec{p}_d = -\vec{p}_f, \quad (\text{B.8})$$

$$\sqrt{|\vec{p}_f|^2 + m_c^2} + \sqrt{|\vec{p}_f|^2 + m_d^2} = \sqrt{s}. \quad (\text{B.9})$$

With the incident flux

$$F = 2 E_a 2 E_b \left(\frac{|\vec{p}_a|}{E_a} + \frac{|\vec{p}_b|}{E_b} \right) = 4 |\vec{p}_e| \sqrt{s}, \quad (\text{B.10})$$

The differential cross-section of the $e^+ e^- \rightarrow f \bar{f}$ can be written as

$$\frac{d\sigma}{d\Omega} = \frac{1}{F} \frac{d\Gamma}{d\Omega} = \frac{N_c}{64\pi^2 s} \frac{|\vec{p}_f|}{|\vec{p}_e|} \langle |\mathcal{M}|^2 \rangle \quad (\text{B.11})$$

The invariant amplitudes can be written with the diagrams shown in Fig. B.2,

$$-i\mathcal{M}_\gamma = \bar{v}(p_b) (ie\gamma^\mu) u(p_a) \left(\frac{-ig_\mu\nu}{q^2} \right) \bar{u}(p_c) (-ieQ_f\gamma^\nu) v(p_d), \quad (\text{B.12})$$

$$\begin{aligned} -i\mathcal{M}_Z &= \bar{v}(p_b) \left(\frac{-ig\gamma^\mu(v_e - a_e\gamma^5)}{2\cos\theta_W} \right) u(p_a) \left(\frac{-i(g_\mu\nu - q_\mu q_\nu/m_Z^2)}{q^2 - m_Z^2 - im_Z\Gamma_Z} \right) \\ &\quad \bar{u}(p_c) \left(\frac{-ig\gamma^\nu(v_f - a_f\gamma^5)}{2\cos\theta_W} \right) v(p_d). \end{aligned} \quad (\text{B.13})$$

In the massless limit for the fermions and with θ which is defined as the polar angle of the fermion f , $\langle |\mathcal{M}_\gamma^2| \rangle$, $\langle |\mathcal{M}_Z^2| \rangle$ and $\langle \mathcal{M}_Z \mathcal{M}_\gamma^* \rangle$ can be written as

$$\langle |\mathcal{M}_\gamma^2| \rangle = Q_f^2 e^4 (1 + \cos^2 \theta) \quad (\text{B.14})$$

$$\langle |\mathcal{M}_Z^2| \rangle = |\chi(s)|^2 e^4 [(v_e^2 + a_e^2)(v_f^2 + a_f^2)(1 + \cos^2 \theta) + 8v_e a_e v_f a_f \cos \theta] \quad (\text{B.15})$$

$$\langle \mathcal{M}_Z \mathcal{M}_\gamma^* \rangle = -Q_f e^4 \chi(s) [v_e v_f (1 + \cos^2 \theta) + 2a_e a_f \cos \theta], \quad (\text{B.16})$$

where $\chi(s)$ is defined as

$$\chi(s) \equiv \left(\frac{s}{e^2} \right) \frac{g^2}{4 \cos^2 \theta_W} \frac{1}{s - m_Z^2 + im_Z \Gamma_Z} \quad (\text{B.17})$$

The differential cross-section also in the massless limit for the fermions can be written as

$$\frac{d\sigma}{d\Omega} = \frac{N_c \alpha^2}{4s} [G(s)(1 + \cos^2 \theta) + H(s) \cos \theta], \quad (\text{B.18})$$

where α is defined as $\frac{e^2}{4\pi}$, and where $G(s)$ and $H(s)$ are defined as

$$G(s) \equiv Q_f^2 + |\chi(s)|^2 (v_e^2 + a_e^2)(v_f^2 + a_f^2) - 2Q_f v_e v_f \Re\{\chi(s)\} \quad (\text{B.19})$$

$$H(s) \equiv \underbrace{}_{\gamma}, \quad \underbrace{+8|\chi(s)|^2 v_e a_e v_f a_f}_{Z \text{ exchange}}, \quad \underbrace{-4Q_f a_e a_f \Re\{\chi(s)\}}_{\gamma - Z \text{ interference}}. \quad (\text{B.20})$$

The total cross-section σ can be written as

$$\sigma = \frac{4N_c \pi \alpha^2}{3s} G(s), \quad (\text{B.21})$$

and the forward-backward asymmetry (A_{FB}) can be written as,

$$A_{\text{FB}} \equiv \frac{\sigma_F - \sigma_B}{\sigma_F + \sigma_B} = \frac{3H(s)}{8G(s)}, \quad (\text{B.22})$$

where σ_F and σ_B means the cross-section with $\cos \theta > 0$ and $\cos \theta < 0$, respectively. In Eq. B.20, B.21, contributions of γ exchange, Z exchange and $\gamma - Z$ interference are separately written. The A_{FB} for b and c quarks are shown as a function of \sqrt{s} in Fig. B.3.

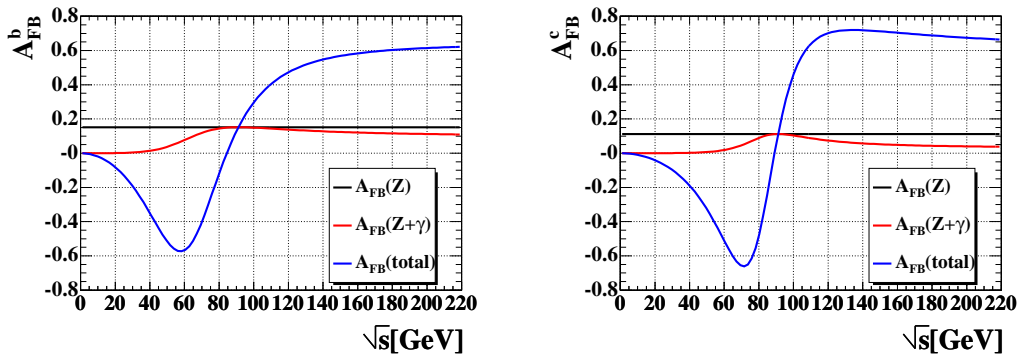


Figure B.3: The \sqrt{s} dependence of $A_{\text{FB}}^{\text{b,c}}$.

Appendix C

Jet Clustering

The emission of a parton (quarks or gluons) can form a jet at LEP. The jet can be used for many purposes, such as to determine the direction of a parton which initiates the jet, to evaluate the charge of such parton with the jet charge, and to construct secondary vertex from the tracks in the jet. The multiplicity of the jet is used to study the event topology. Some variables to characterize the shape of the jet are introduced, which are used to study the nature of the QCD. For those purposes, some jet-clustering algorithms are developed. In this thesis, the evaluations of the primary-quark direction and the identification of the primary-quark charge, and the secondary-vertex reconstruction with the jet are important. As regards the subjects, the performance is compared among some jet-clustering algorithms. The performance in the evaluation of the primary-quark direction with the jet is compared with the performance with the thrust axis. That in the identification of the primary-quark charge with the jet charge is compared with that with the hemisphere charge.

C.1 Jet-Clustering Algorithm

There are mainly two types of jet-clustering algorithms. One is based on successive recombinations of pairs of particles, such as the JADE algorithm [25, 113], the Durham algorithm [73]. The other is based on geometrical assembly, such as the cone algorithm, which is developed in the hadron-collider experiments [114–118] and imported to the OPAL experiment [119]. These jet-clustering algorithms are frequently used in LEP experiments and they are briefly described here.

C.1.1 JADE algorithm with the E0 recombination scheme

The jet clustering is started with a list of jets that are just the observed particles (tracks and unassociated clusters). Then an iterative process of successive recombinations of pairs of particles is followed as described below. At each stage of iteration, two jets, i and j ,

are considered as candidates for combination into a single jet according to the value of “jettiness” variable, x_{ij} or y_{ij} (x_{ij} scaled by the visible energy, E_{vis}), defined as,

$$x_{ij} = 2E_i E_j (1 - \cos \theta_{ij}), \quad (\text{C.1})$$

$$y_{ij} = x_{ij}/E_{vis}^2, \quad (\text{C.2})$$

where E_i and E_j are the energy of the jets i, j , and $\cos \theta_{ij}$ is the opening angle of the two jets. Among all the possible pairs, the pair with the smallest value of x_{ij} (or y_{ij}) is combined first, where the four-momentum of the combined jets is formed as the vector sum of the four-momentum of the original two jets. The jet list is updated by subtracting the original pair and adding the new jet. This process is iteratively continued until every remaining x_{ij} (or y_{ij}) is larger than a preset cut-off parameter x_{cut} (or y_{rmcut}), which is called as “jet resolution parameter”. This has been a very useful tool enabling the testing of many perturbative QCD calculations.

C.1.2 Durham algorithm

This algorithm is similar to the JADE algorithm, but the x_{ij} is defined differently as,

$$x_{ij} = 2 \min(E_i^2, E_j^2) (1 - \cos \theta_{ij}), \quad (\text{C.3})$$

which is interpreted as the relative transverse momentum of the pair. As regards the QCD study, this benefits from smaller hadronization corrections than the JADE schemes, and is calculable in resummed perturbation theory [73].

C.1.3 Cone algorithm

In the cone algorithm, a jet is formed with the particles (tracks and unassociated clusters) included in a cone with the interaction point as its apex, where the cone size is defined by its half-angle R . In addition to the R , the minimum jet energy to form the jet (ε) is used as the parameters to characterize the cone algorithm. The cone (jet) axis (\mathbf{p}_J) is defined as the sum of the momentum of the particles (\mathbf{p}_i) inside the cone. The condition to form a jet can be written as,

$$\mathbf{p}_J = \sum_{i \in \text{jet}} \mathbf{p}_i \quad ; \quad \frac{\mathbf{p}_i \cdot \mathbf{p}_J}{|\mathbf{p}_i| |\mathbf{p}_J|} \leq \cos(R) \quad \forall i \in \text{jet} \quad (\text{C.4})$$

The detail of the algorithm is described as follows. At first, for the given R , the algorithm seeks as many sets of particles to fulfill the condition as possible, where such set of particles is called as “proto-jet”. Then proto-jets with the energy less than ε is eliminated. If the two (or more) proto-jets share the same particles, the sharing is eliminated as follows. A proto-jet with its all particles included in another proto-jet is

eliminated. If the proto-jets share finite number of particles, If the sum of the energy for the shared particles is larger than 75% of the energy of the proto-jet which is the least energetic one among the proto-jet concerning the sharing, the shared particles are assigned to the proto-jet with the highest energy and the other proto-jets are eliminated. If the sum of the energy for the shared particles is less than 75% of the energy of the proto-jet with the smallest energy, the shared particles are assigned to the nearest proto-jet measured with the jet axis. Finally, proto-jets with the energy less than ε is again eliminated. The resulting proto-jets are the final jets.

The cone algorithm cluster the particle with definite opening angle, whereas the jade-like algorithm can cluster less energetic particle with large opening angle. It enables to study the kinematic information in a given jet with finer cone. For example, the tracks coming from the secondary vertex can be enriched with finer cone, the isolation for a given track can be studied with comparing the jets constructed with finer and broader cones.

C.2 Evaluation of Primary-Quark Direction

The performances in the evaluation of the primary-quark direction with the thrust axis and with the jet axes are compared. The jets are constructed with the above-mentioned three kinds of jet-clustering algorithms and they are labeled as follows.

Cone0.25/5 Cone algorithm with $R = 0.25$, $\varepsilon = 5[\text{GeV}]$.

Cone0.3/5 Cone algorithm with $R = 0.3$, $\varepsilon = 5[\text{GeV}]$.

Cone0.4/5 Cone algorithm with $R = 0.4$, $\varepsilon = 5[\text{GeV}]$.

Cone0.55/5 Cone algorithm with $R = 0.55$, $\varepsilon = 5[\text{GeV}]$.

Cone0.55/7 Cone algorithm with $R = 0.55$, $\varepsilon = 7[\text{GeV}]$.

Cone0.7/5 Cone algorithm with $R = 0.7$, $\varepsilon = 5[\text{GeV}]$.

Cone0.77/7 Cone algorithm with $R = 0.7$, $\varepsilon = 7[\text{GeV}]$.

Durham49 Durham algorithm with $x_{\text{cut}} = 49[\text{GeV}^2]$.

Durham0.001 Durham algorithm with $y_{\text{cut}} = 0.001$.

Durham0.01 Durham algorithm with $y_{\text{cut}} = 0.01$.

Durham0.02 Durham algorithm with $y_{\text{cut}} = 0.02$.

Durham0.03 Durham algorithm with $y_{\text{cut}} = 0.03$.

JadeE0/25 Jade algorithm(E0) with $x_{\text{cut}} = 25[\text{GeV}^2]$.

JadeE0/49 Jade algorithm(E0) with $x_{\text{cut}} = 49[\text{GeV}^2]$.

JadeE0/0.03 Jade algorithm(E0) with $y_{\text{cut}} = 0.03$.

By means of

$$\Delta \equiv |\cos \theta_{\text{thrust/jet}}| - |\cos \theta_{\text{primary quark}}|, \quad (\text{C.5})$$

where $\cos \theta_{\text{thrust/jet}}$ is the polar angle of the thrust or jet axis and $\cos \theta_{\text{primary quark}}$ is the polar angle of the primary quark direction, the resolution of the primary-quark direction is evaluated with the ratio of the events with $|\Delta| < 0.1$, which means the ratio of the entries in the colored histogram shown in Fig. C.1(a). The resolutions obtained with the thrust axis or the jet axes for each jet-clustering algorithm are shown in Fig. C.1(b). The use of the thrust axis marks the best performance, since it is not sensitive to the hard gluon emission.

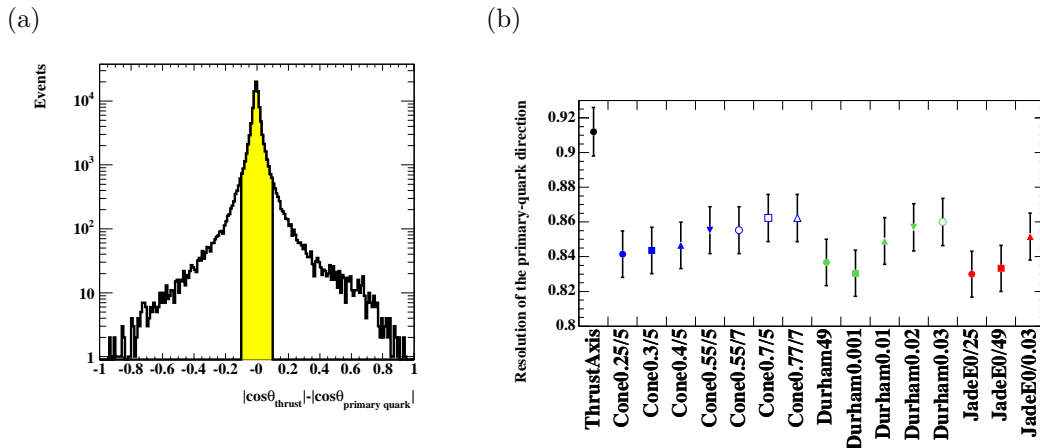


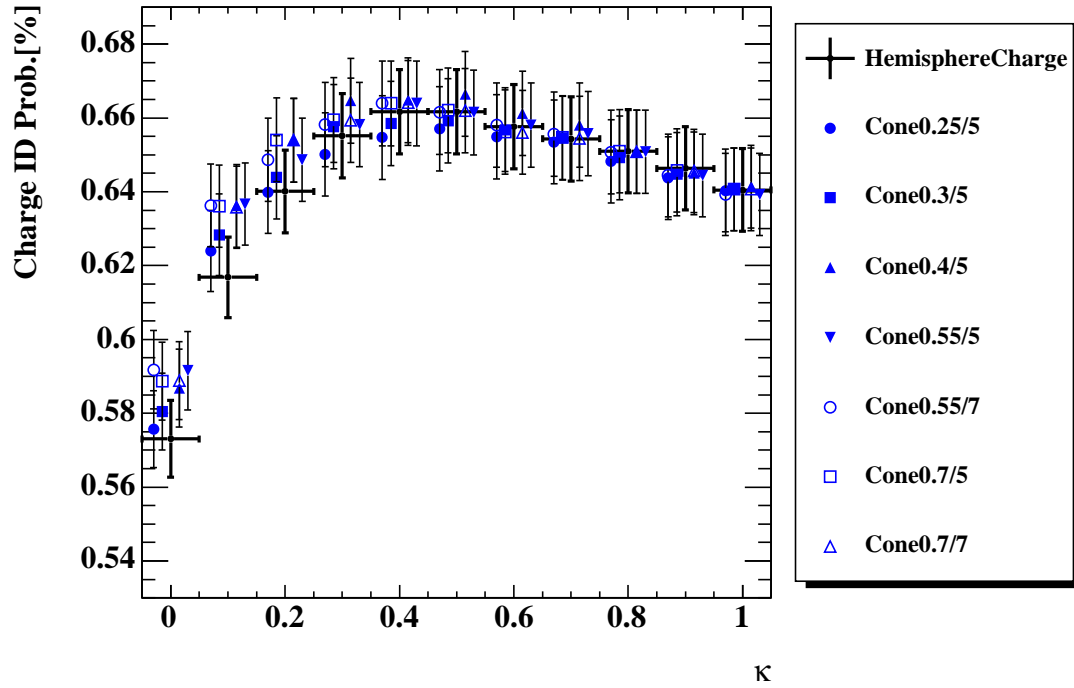
Figure C.1: (a) The distributions of $|\cos \theta_{\text{thrust/jet}}| - |\cos \theta_{\text{primary quark}}|$ and the resolutions of the primary-quark direction obtained with the thrust axis or the jet axes for each jet-clustering algorithm.

C.3 Evaluation of Primary-Quark Charge

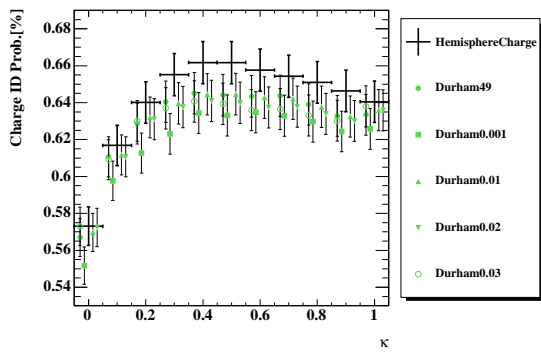
The performances in the identification of the primary-quark charge with the hemisphere charge and the jet charges constructed with the above-mentioned three kinds of jet-clustering algorithms are compared as follows, where the labeling of the jet-clustering algorithms in the section C.2 are used. The charge identification probabilities with the hemisphere charge and with the jet charges are shown in Fig. C.2, where the use of the

cone algorithm with broader cone marks best performance among the jet charges. The performance for the hemisphere charge is comparable to that for the jet charge with the cone algorithm. Furthermore, the performance with the hemisphere charge is close to optimal when only the track momentum and charge information is used [120].

(a)



(b)



(c)

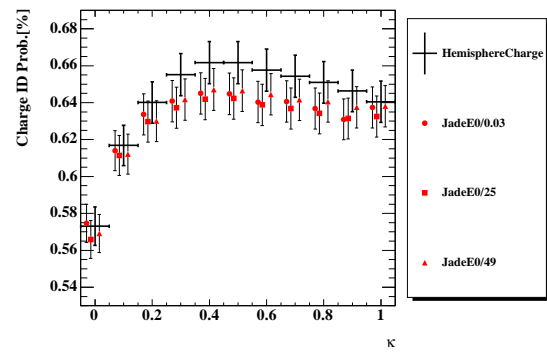


Figure C.2: The charge identification probabilities with jet charges constructed with (a) the cone algorithms, (b) the Durham algorithms, and (c) Jade (E0) algorithms, where that for the hemisphere charge is shown in each figure.

C.4 b-Tagging

Here the performances of jet-based b-tagging from the jets constructed with the above-mentioned three kinds of jet-clustering algorithms are compared. The jet-based b-tagging is done with two kinds of b-tagging methods as follows.

1. cut-based tag on the decay length significance.

The decay length significances (l/σ_l) are constructed from each secondary vertex which is reconstructed from each jet. The most significant l/σ_l is selected in a event and the b-tagging is done by applying a cut on the l/σ_l .

2. BT NN based tag. The ANN-based discriminant termed ‘‘BT NN’’ [40] is constructed from each jet with $|l/\sigma_l|$ larger than 4. In addition to the l/σ_l , the ANN have 4 more inputs derived from vertex multiplicity and invariant mass information. Then most significant value of the ANN outputs are selected and the b-tagging is performed by applying a cut on the ANN output.

The distributions of the decay length significance and the BT NN are shown in Fig. C.3(a) and (b), respectively.

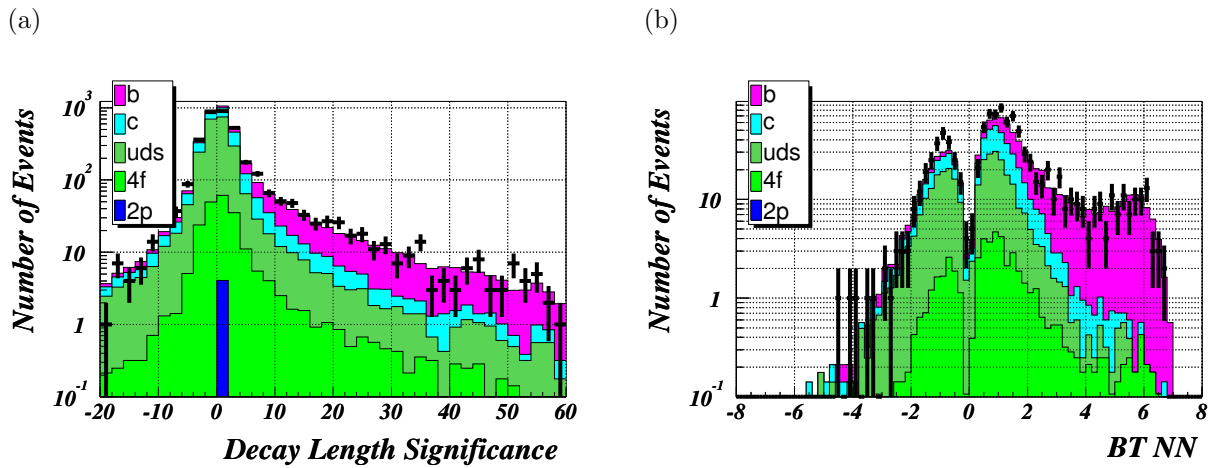


Figure C.3: The distributions of the decay length significance and the BT NN for the \sqrt{s} of 189 GeV.

With these discriminants, the b-tagging are preformed for each jet-clustering algorithm. The performances for each jet-clustering are shown in Fig. C.4(a) for the cut-based tag on the decay length significance. Those for the b-tagging with BT-NN are shown in Fig. C.4(b). For the both case, the cone algorithm marks the best performance. Among the cone algorithms, that with relatively finer cone marks better performance, which is

due to the higher efficiency and better purity of the tracks and clusters coming from the b hadrons in selecting them in the jet with the cone algorithms. It is shown in Fig. C.5, where a b-particle efficiency is defined as the ratio of the number of tracks or clusters originating from the b hadrons (b-particles) included in the jets to the total number of b-particles, and where a b-particle purity is defined as the ratio of the number of b-particles included in the jets to the total number of tracks or clusters included in the jets. A superior performance of the cone algorithms is observed.

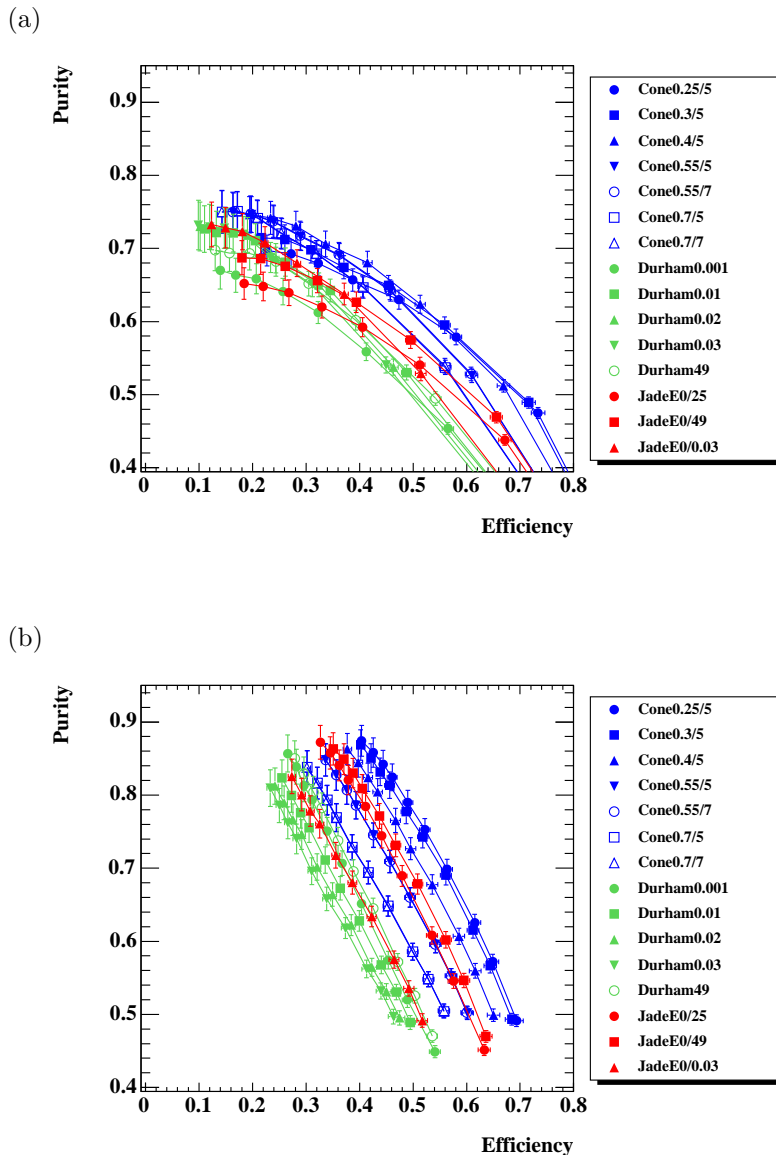


Figure C.4: (a) The purity vs. efficiency for the b-tagging with the cut-based b-tagging on the decay length significance for each jet-clustering algorithm. (b) That with the ANN-based b-tagging (BT NN)(b).

(a)

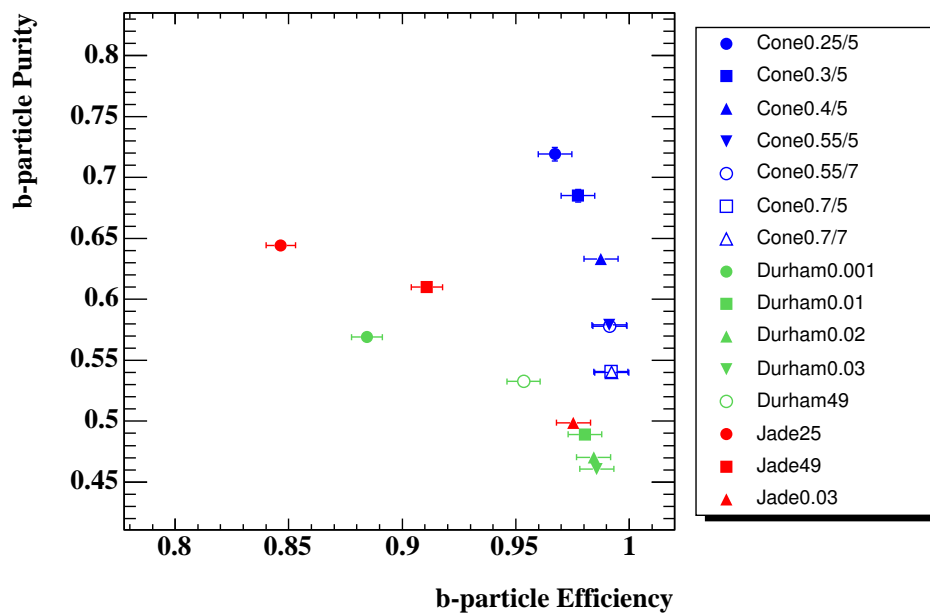


Figure C.5: The b-particle purity vs. efficiency for each jet-clustering algorithm.

Appendix D

Artificial Neural Network (ANN)

A measurement of a physical quantity of a particular class of events (signal) is performed generally under the existence of the background, where the discrimination of the signal from the background is important. For example, the b-tagging is important for the measurement of the A_{FB}^{b} .

The properties of the signal and background can be described by a set of variables (a input vector, \mathbf{x}), such as the momentum, the transverse momentum, number of hits, etc. For the case of n such variables, the discrimination can be done by constructing a intersecting hypersurface, which divide the n dimensional space of the variables into the signal and the background region. If the probability density function of the signal and background are known as $f^{\text{s}}(\mathbf{x})$ and $f^{\text{b}}(\mathbf{x})$, respectively, such intersecting hypersurface can be obtained as

$$\frac{f^{\text{s}}(\mathbf{x})}{f^{\text{b}}(\mathbf{x})} = r, \quad (\text{D.1})$$

where the r determines the signal-selection efficiency and the hypersurface gives the highest signal purity for the given signal-selection efficiency according to the Neyman-Pearson lemma [121]. In other words, the r is the optimal scalar test statistics on which a cut is applied giving maximum purity for the given efficiency.

Such scalar test statistics can be obtained with an Artificial Neural Networks (ANNs) [122], which is described as follows. The Artificial Neural Network is a term referring to numbers of mathematical models which have some distributed nodes connected with each other. Among them, one of the most important type of ANNs is a network termed “feedforward multilayer perceptron” which processes numbers of data inputs into some outputs through the layered network structure with nodes connected with each other as shown in Fig. D.1. Here the networks with only one output are described. Furthermore, the networks with only three layers (one input, one hidden, and one output layer) are described here, since it is proved by [123], [124] and [125] that one hidden layer is in principle sufficient for arbitrary recognition task which means, for example, any continuous function can be represented by the ANN with one hidden layer basically.

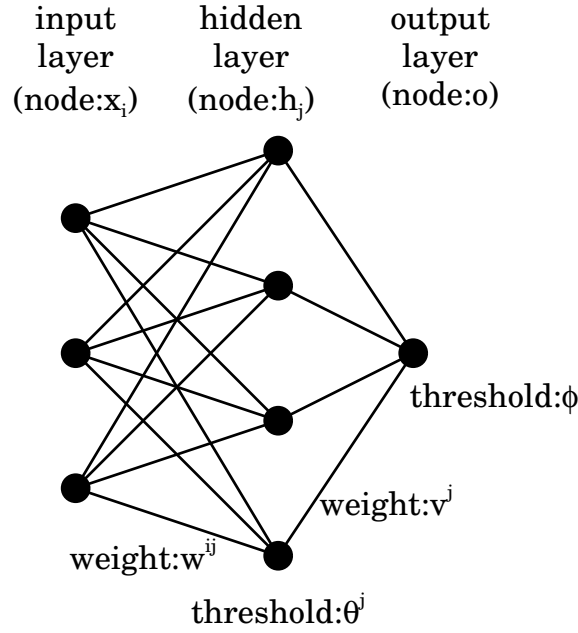


Figure D.1: The structure of the feedforward multilayer perceptron with one hidden layer.

The value of the output node of o is connected with the values of nodes in the hidden layer (h_j) and in the input layer (x_i) through the weights (w^{ij} , v^j), using a function ($g(z)$) and the thresholds (θ^j , ϕ), as,

$$o = g\left(\sum_j v^j h_j + \phi\right) \quad (\text{D.2})$$

$$= g\left(\sum_j v^j g\left(\sum_i w^{ij} x_i + \theta^j\right) + \phi\right), \quad (\text{D.3})$$

where the $g(z)$ is termed an activation function and can be written as

$$g(z) = \frac{1}{1 + \exp(-2z)}, \quad (\text{D.4})$$

which is called as a sigmoid function giving a value from 0 to 1 as shown in Fig. D.2.

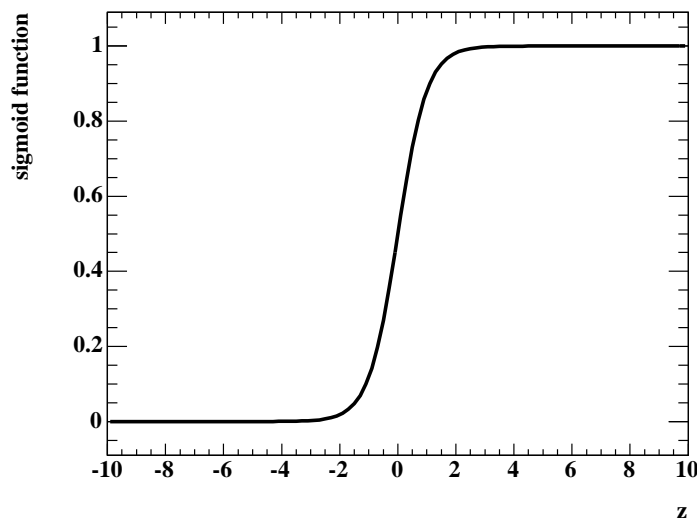


Figure D.2: The sigmoid function.

The feedforward multilayer perceptron can be used in the discrimination of the signal from the background by tuning the weights and thresholds to be fitted to the discrimination problem. Such tuning can be done through an iterative fitting with many sets of an input vector of signal or background and a desired feature value which is 1 for the signal or 0 for the background. The fitting is performed by minimizing an error measure of the fit, e.g. a mean square error

$$E = \frac{1}{N_p} \sum_{p=1}^{N_p} (o^{(p)} - t^{(p)})^2 \quad (\text{D.5})$$

between $o^{(p)}$ (o for the p^{th} input vector) and the desired feature value $t^{(p)}$ (1 for the signal or 0 for the background for the p^{th} input vector), where N_p is the number of samples (sets of an input vector and an output) used for the fitting. This process is called as a “supervised learning”. Among numbers of the supervised learning methods, a learning process termed “back propagation” learning [126, 127] is frequently used, which minimize the E updating the weight vector, $\boldsymbol{\omega}$ (vector of all weights and thresholds), with gradient descent as,

$$\boldsymbol{\omega}_{t+1} = \boldsymbol{\omega}_t + \Delta\boldsymbol{\omega}_t, \quad (\text{D.6})$$

where t represents the iteration number and $\Delta\boldsymbol{\omega}_t$ is represented as,

$$\Delta\boldsymbol{\omega}_t = -\eta \frac{\partial E_t}{\partial \boldsymbol{\omega}}. \quad (\text{D.7})$$

Practically, the back-propagation learning is performed with JETNET [85] using the MC sample containing the signal and background. The sample is divided into two independent samples termed “learning sample” and “validation sample”. The learning sample is used for the learning and the tuned networks is applied to the the validation sample to check the “overlearning” which means the ANN learns the characteristics specific to the learning sample which is not the global nature of the signal. The learning process has to be stopped before the overlearning starts. For example, the error (E) as a function of the number of the ANN updates (learning curve) for the prompt $b \rightarrow \mu$ discriminating ANN (\mathcal{N}_b for muon) described in subsection 4.7.3 is shown in Fig. D.3. After 114 updates, the error for the validation data starts to increase although the error for the learning data decrease, which shows the start of the overlearning and the learning is stopped there. The structure of the the \mathcal{N}_b for muon is shown in Fig. D.4, where the magnitudes of the weights are indicated with the line width.

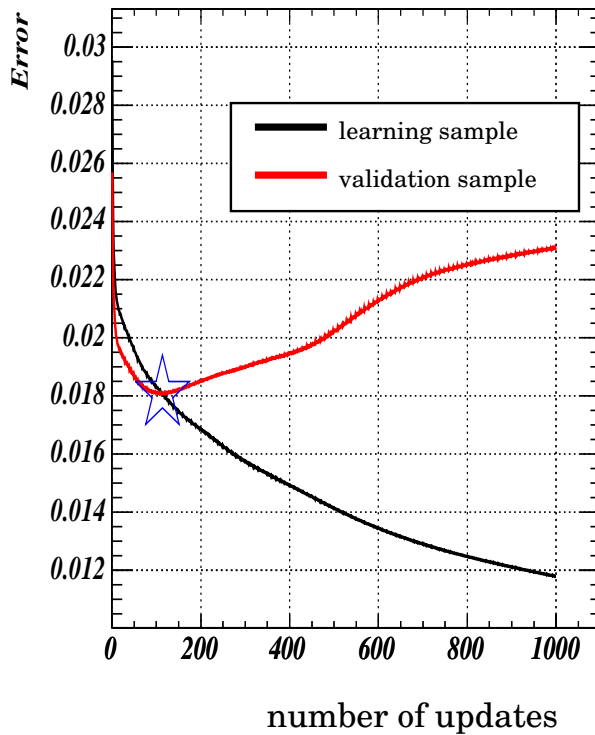


Figure D.3: The learning curve.

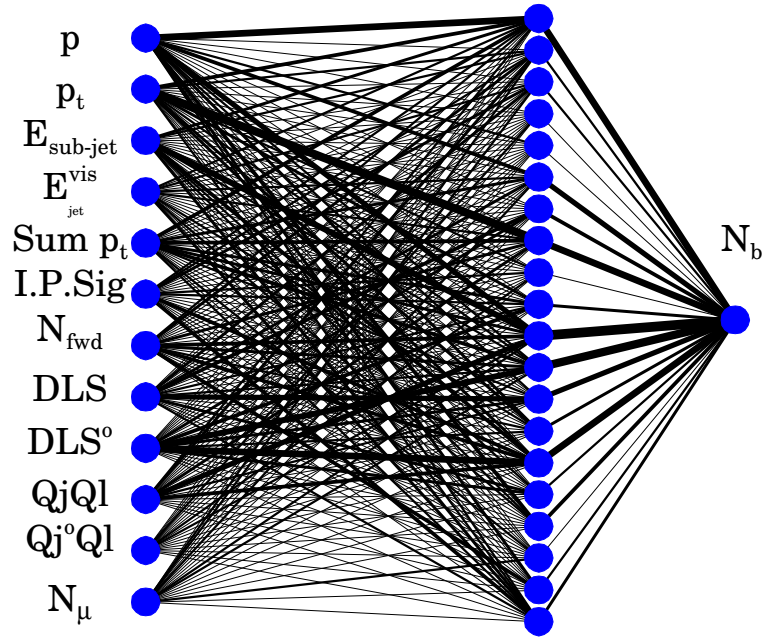


Figure D.4: An example of the constructed ANN (\mathcal{N}_b for muon). The width of the line indicated the strength of the coupling for the two nodes.

The output (o) of the feedforward multilayer perceptron after the learning can be used to discriminate the signal from the background for other samples. For example, the distribution of the output of the \mathcal{N}_b for muon is shown in Fig. D.5(a).

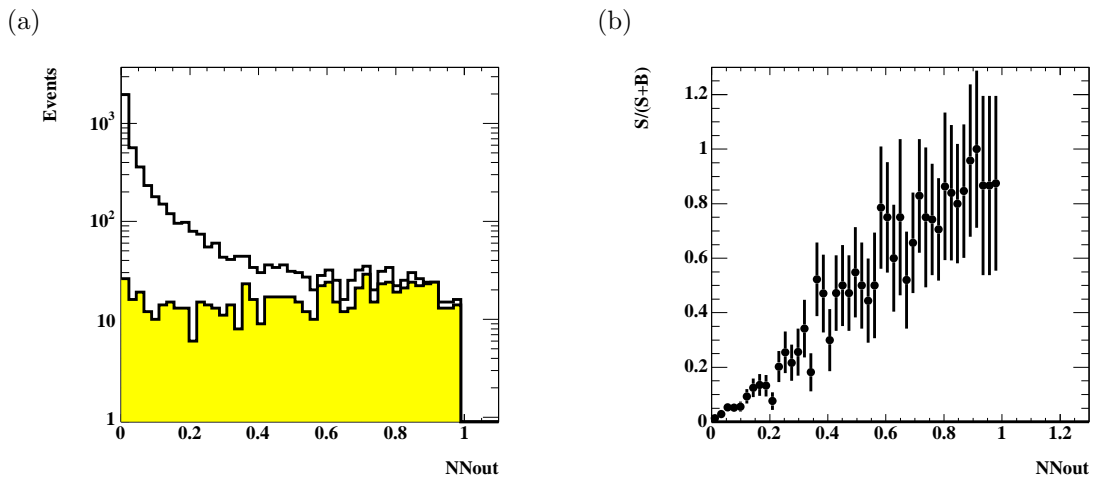


Figure D.5: The distribution of the output of the \mathcal{N}_b for muon and that of the signal ratio as a function of the ANN output.

The output of the such feedforward multilayer perceptron after the learning can be interpreted as the Bayesian *a posteriori* probability [128], which can be written with the probability density function of the signal and background used in Eq. D.1 as,

$$o = \frac{N_s f^s(\mathbf{x})}{N_s f^s(\mathbf{x}) + N_b f^b(\mathbf{x})}, \quad (\text{D.8})$$

where N_s and N_b are the numbers of signal and background, respectively. The relation can be seen in Fig. D.5(b), where the signal ratio is drawn at each bin for the histograms shown in Fig D.5(a). The Eq. D.8 can be written with the r (the ratio between the probability density functions of signal and background) defined in Eq. D.1 as,

$$o = \frac{1}{1 + \frac{1}{R \cdot r}}, \quad (\text{D.9})$$

where R is the signal to background ratio (N_s/N_b). Since the Eq. D.9 is the monotonic function of r , the output of the ANN can also be used as the optimal scalar test statistics. More proof about the fact can be found in [129] and [130]. Since the r can be obtained from the output of the ANN with the relation in Eq. D.9, it can be transformed to the output (o') corresponding to other sample with different signal to background ratio (R') as,

$$o' = \frac{R' o}{R' o + R(1 - o)}. \quad (\text{D.10})$$

For example, the output corresponding to the sample including the same numbers of signal and background is shown in Fig. D.6.

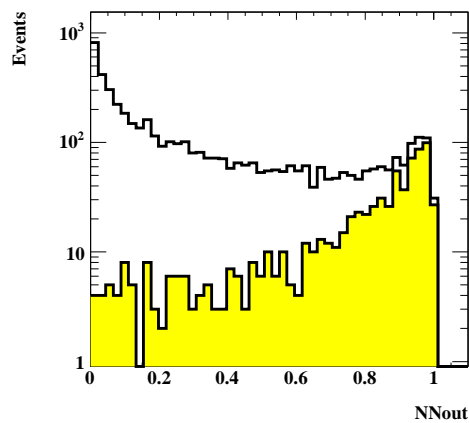


Figure D.6: The distribution of the output corresponding to the sample including the same numbers of signal and background, which is made from Fig. D.5(a).

Bibliography

- [1] C. S. Wu, E. Ambler, R. W. Hayward, D. D. Hoppes, and R. P. Hudson, *Phys. Rev.* **105** (1957) 1413–1414.
- [2] J. S. Schwinger, *Annals Phys.* **2** (1957) 407–434.
- [3] C.-N. Yang and R. L. Mills, *Phys. Rev.* **96** (1954) 191–195.
- [4] S. L. Glashow, J. Iliopoulos, and L. Maiani, *Phys. Rev.* **D2** (1970) 1285–1292.
- [5] S. Weinberg, *Phys. Rev. Lett.* **19** (1967) 1264–1266.
- [6] A. Salam, Originally printed in *Svartholm: Elementary Particle Theory, Proceedings Of The Nobel Symposium Held 1968 At Lerum, Sweden*, Stockholm 1968, 367-377.
- [7] F. J. Hasert *et al.*, *Phys. Lett.* **B46** (1973) 121–124.
- [8] A. C. Benvenuti and *e. al.*, *Phys. Rev. Lett.* **32** (1974) 800–803.
- [9] UA1 Collaboration, G. Arnison *et al.*, *Phys. Lett.* **B122** (1983) 103–116.
- [10] UA2 Collaboration, M. Banner *et al.*, *Phys. Lett.* **B122** (1983) 476–485.
- [11] UA1 Collaboration, G. Arnison *et al.*, *Phys. Lett.* **B126** (1983) 398–410.
- [12] UA2 Collaboration, P. Bagnaia *et al.*, *Phys. Lett.* **B129** (1983) 130–140.
- [13] HRS Collaboration, M. Derrick *et al.*, *Phys. Lett.* **B146** (1984) 261.
- [14] HRS Collaboration, P. Baringer *et al.*, *Phys. Lett.* **B206** (1988) 551–556.
- [15] HRS Collaboration, C. R. Ng *et al.*, *ANL-HEP-PR-88-11* (1988)
- [16] MAC Collaboration, H. Band *et al.*, *Phys. Lett.* **B218** (1989) 369.
- [17] TPC/Two Gamma Collaboration, H. Aihara *et al.*, *Phys. Rev.* **D34** (1986) 1945.
- [18] TPC/Two Gamma Collaboration, H. Aihara *et al.*, *Phys. Rev.* **D31** (1985) 2719.

- [19] TPC/Two Gamma Collaboration, H. Aihara *et al.*, *Z. Phys.* **C27** (1985) 39.
- [20] CELLO Collaboration, H. J. Behrend *et al.*, *Z. Phys.* **C47** (1990) 333–342.
- [21] CELLO Collaboration, H. Kroha, MPI-PAE/Exp-El-214/89.
- [22] JADE Collaboration, W. Bartel *et al.*, *Phys. Lett.* **B146** (1984) 121.
- [23] JADE Collaboration, F. Ould-Saada *et al.*, *Z. Phys.* **C44** (1989) 567.
- [24] JADE Collaboration, E. Elsen *et al.*, *Z. Phys.* **C46** (1990) 349–360.
- [25] JADE Collaboration, W. Bartel *et al.*, *Z. Phys.* **C33** (1986) 23.
- [26] Mark-J Collaboration, B. Adeva *et al.*, *Phys. Rept.* **109** (1984) 131.
- [27] S. L. Wu, *Nucl. Phys. Proc. Suppl.* **3** (1988) 39.
- [28] PLUTO Collaboration, C. Maxeiner, DESY PLUTO-85-03.
- [29] TASSO Collaboration, W. Braunschweig *et al.*, *Z. Phys.* **C44** (1989) 365.
- [30] TASSO Collaboration, M. Althoff *et al.*, *Phys. Lett.* **B146** (1984) 443–449.
- [31] TASSO Collaboration, W. Braunschweig *et al.*, *Z. Phys.* **C48** (1990) 433–444.
- [32] AMY Collaboration, K. Ueno *et al.*, *Phys. Lett.* **B381** (1996) 365–371.
- [33] TOPAZ Collaboration, Y. Inoue *et al.*, *Eur. Phys. J.* **C18** (2000) 273–282.
- [34] VENUS Collaboration, M. Shirakata *et al.*, *Phys. Lett.* **B278** (1992) 499–505.
- [35] The LEP Electroweak Working Group and the SLD Heavy Flavour Group, *A Combination of Preliminary LEP and SLD Electroweak Measurements and Constraints on the Standard Model*, Internal Note, LEPEWWG/2004-01, ALEPH 2004-010 PHYSIC 2004-002 DELPHI 2004-049 PHYS 943, L3 Note 2823, OPAL PR 406, hep-ex/0412015, 6 December 2004.
- [36] P. Langacker, R. W. Robinett, and J. L. Rosner, *Phys. Rev.* **D30** (1984) 1470.
- [37] D. London and J. L. Rosner, *Phys. Rev.* **D34** (1986) 1530.
- [38] W. Buchmuller, R. Ruckl, and D. Wyler, *Phys. Lett.* **B191** (1987) 442.
- [39] J. Kalinowski, R. Ruckl, H. Spiesberger, and P. M. Zerwas, *Z. Phys.* **C74** (1997) 595–603.
- [40] OPAL Collaboration, G. Abbiendi *et al.*, *Phys. Lett.* **B546** (2002) 29–47.

- [41] OPAL Collaboration, G. Abbiendi *et al.*, *Phys. Lett.* **B577** (2003) 18–36.
- [42] OPAL Collaboration, G. Abbiendi *et al.*, *Eur. Phys. J.* **C16** (2000) 41–60.
- [43] M. Consoli, W. Hollik, and F. Jegerlehner, CERN-TH-5527-89, Presented at Workshop on Z Physics at LEP.
- [44] D. Y. Bardin *et al.*, *Comput. Phys. Commun.* **133** (2001) 229–395.
- [45] S. Jadach, B. F. L. Ward, and Z. Was, *Comput. Phys. Commun.* **130** (2000) 260–325.
- [46] G. Altarelli and B. Lampe, *Nucl. Phys.* **B391** (1993) 3–22.
- [47] LEP Heavy Flavor Working Group Collaboration, D. Abbaneo *et al.*, *Eur. Phys. J.* **C4** (1998) 185–191.
- [48] T. Sjostrand *et al.*, *Comput. Phys. Commun.* **135** (2001) 238–259.
- [49] T. Sjostrand, *Int. J. Mod. Phys.* **A3** (1988) 751.
- [50] C. Peterson, D. Schlatter, I. Schmitt, and P. M. Zerwas, *Phys. Rev.* **D27** (1983) 105.
- [51] Particle Data Group Collaboration, S. Eidelman *et al.*, *Phys. Lett.* **B592** (2004) 1.
- [52] Lep Injector Study Group Collaboration. LEP DESIGN REPORT. VOL. 1. THE LEP INJECTOR CHAIN, CERN-LEP/TH/83-29.
- [53] LEP DESIGN REPORT: VOL. 2. THE LEP MAIN RING, CERN-LEP/84-01.
- [54] DELPHI Collaboration, P. A. Aarnio *et al.*, *Nucl. Instrum. Meth.* **A303** (1991) 233–276.
- [55] L3 Collaboration, *Nucl. Instrum. Meth.* **A289** (1990) 35–102.
- [56] OPAL Collaboration, K. Ahmet *et al.*, *Nucl. Instrum. Meth.* **A305** (1991) 275–319.
- [57] OPAL Collaboration, P. P. Allport *et al.*, *Nucl. Instrum. Meth.* **A324** (1993) 34–52.
OPAL Collaboration, P. P. Allport *et al.*, *Nucl. Instrum. Meth.* **A346** (1994) 476–495.
OPAL Collaboration, S. Anderson *et al.*, *Nucl. Instrum. Meth.* **A403** (1998) 326–350.

- [58] OPAL Collaboration, B. E. Anderson *et al.*, *IEEE Trans. Nucl. Sci.* **41** (1994) 845–852.
- [59] OPAL Collaboration, G. Abbiendi *et al.*, *Eur. Phys. J.* **C14** (2000) 373–425.
- [60] OPAL Collaboration, M. Arignon *et al.*, *Nucl. Instrum. Meth.* **A313** (1992) 103–125.
- [61] S. Jadach, W. Placzek, and B. F. L. Ward, *Phys. Lett.* **B390** (1997) 298–308.
- [62] S. Jadach, W. Placzek, M. Skrzypek, B. F. L. Ward, and Z. Was, *Comput. Phys. Commun.* **140** (2001) 432–474.
- [63] S. Jadach, W. Placzek, and B. F. L. Ward, *Phys. Rev.* **D56** (1997) 6939–6941.
- [64] R. Engel, *Z. Phys.* **C66** (1995) 203–214.
- [65] E. Farhi, *Phys. Rev. Lett.* **39** (1977) 1587–1588.
- [66] R. D. Field and R. P. Feynman, *Nucl. Phys.* **B136** (1978) 1.
- [67] T. Sjostrand, *Comput. Phys. Commun.* **82** (1994) 74–90.
- [68] ALEPH, DELPHI, L3, OPAL Collaboration, *Nucl. Instrum. Meth.* **A378** (1996) 101–115.
- The LEP Heavy Flavour Group, *Input Parameters for the LEP/SLD Electroweak Heavy Flavour Results for Summer 1998 Conferences*, LEPHF/98-01,
<http://www.cern.ch/LEPEWWG/heavy/>.
- The LEP Heavy Flavour Group, *Final Input Parameters for the LEP/SLD Electroweak Heavy Flavour Results*, LEPHF/2001-01,
<http://www.cern.ch/LEPEWWG/heavy/>.
- [69] J. Fujimoto *et al.*, *Comput. Phys. Commun.* **100** (1997) 128–156.
- [70] S. Jadach, W. Placzek, M. Skrzypek, B. F. L. Ward, and Z. Was, *Comput. Phys. Commun.* **119** (1999) 272–311.
- [71] S. Jadach, Z. Was, R. Decker, and J. H. Kuhn, *Comput. Phys. Commun.* **76** (1993) 361–380.
- [72] OPAL Collaboration, G. Abbiendi *et al.*, *Eur. Phys. J.* **C33** (2004) 173–212.
- [73] S. Bethke, Z. Kunszt, D. E. Soper, and W. J. Stirling, *Nucl. Phys.* **B370** (1992) 310–334.
- N. Brown and W. J. Stirling, *Z. Phys.* **C53** (1992) 629–636.

- [74] OPAL Collaboration, K. Ackerstaff *et al.*, *Eur. Phys. J.* **C1** (1998) 395–424.
- [75] OPAL Collaboration, G. Abbiendi *et al.*, *Eur. Phys. J.* **C8** (1999) 191–215.
- [76] OPAL Collaboration, G. Abbiendi *et al.*, *Phys. Lett.* **B493** (2000) 249–265.
- [77] S. Catani and M. H. Seymour, *Phys. Lett.* **B378** (1996) 287–301.
- [78] R. K. Ellis, D. A. Ross, and A. E. Terrano, *Nucl. Phys.* **B178** (1981) 421.
- [79] F. A. Berends, R. Pittau, and R. Kleiss, *Comput. Phys. Commun.* **85** (1995) 437–452.
- [80] J. D. Bjorken and S. J. Brodsky, *Phys. Rev.* **D1** (1970) 1416–1420.
- [81] OPAL Collaboration, G. Abbiendi *et al.*, *Eur. Phys. J.* **C26** (2003) 479–503.
- [82] G. Parisi, *Phys. Lett.* **B74** (1978) 65.
- [83] OPAL Collaboration, G. Abbiendi *et al.*, *Eur. Phys. J.* **C8** (1999) 217–239.
- [84] OPAL Collaboration, R. Akers *et al.*, *Z. Phys.* **C65** (1995) 17–30.
- [85] C. Peterson, T. Rognvaldsson, and L. Lonnblad, *Comput. Phys. Commun.* **81** (1994) 185–220.
- [86] P. D. B. Collins and T. P. Spiller, *J. Phys.* **G11** (1985) 1289.
- [87] V. G. Kartvelishvili, A. K. Likhoded, and V. A. Petrov, *Phys. Lett.* **B78** (1978) 615.
- [88] OPAL Collaboration, G. Abbiendi *et al.*, *Eur. Phys. J.* **C29** (2003) 463–478.
- [89] MARK-III Collaboration, D. Coffman *et al.*, *Phys. Lett.* **B263** (1991) 135–140.
- [90] ALEPH,CDF,DELPHI,L3,OPAL,SLD Collaboration, D. Abbaneo *et al.*, [hep-ex/0112028](https://arxiv.org/abs/hep-ex/0112028).
- [91] M. H. Seymour, *Nucl. Phys.* **B436** (1995) 163–183.
- [92] ALEPH Collaboration, R. Barate *et al.*, *Eur. Phys. J.* **C12** (2000) 183–207.
- [93] DELPHI Collaboration, P. Abreu *et al.*, *Eur. Phys. J.* **C11** (1999) 383–407.
- [94] L3 Collaboration, M. Acciarri *et al.*, *Phys. Lett.* **B485** (2000) 71–84.
- [95] E. Eichten, K. D. Lane, and M. E. Peskin, *Phys. Rev. Lett.* **50** (1983) 811–814.

- [96] A. F. Zarnecki, *Eur. Phys. J.* **C11** (1999) 539–557.
- [97] OPAL Collaboration, G. Alexander *et al.*, *Phys. Lett.* **B387** (1996) 432–442.
- [98] OPAL Collaboration, G. Abbiendi *et al.*, [hep-ex/0410034](#).
- [99] OPAL Collaboration, G. Abbiendi *et al.*, *Eur. Phys. J.* **C6** (1999) 1–18.
- [100] J. C. Pati and A. Salam, *Phys. Rev.* **D10** (1974) 275–289.
H. Georgi and S. L. Glashow, *Phys. Rev. Lett.* **32** (1974) 438–441.
J. L. Hewett and T. G. Rizzo, *Phys. Rept.* **183** (1989) 193.
- [101] L. F. Abbott and E. Farhi, *Phys. Lett.* **B101** (1981) 69.
L. F. Abbott and E. Farhi, *Nucl. Phys.* **B189** (1981) 547–556.
- [102] N. Arkani-Hamed, S. Dimopoulos, and G. R. Dvali, *Phys. Lett.* **B429** (1998) 263–272.
- [103] J. L. Hewett, *Phys. Rev. Lett.* **82** (1999) 4765–4768.
- [104] OPAL Collaboration, G. Abbiendi *et al.*, *Eur. Phys. J.* **C13** (2000) 553–572.
- [105] OPAL Collaboration, G. Abbiendi *et al.*, *Eur. Phys. J.* **C32** (2003) 303–322.
- [106] OPAL Collaboration, G. Abbiendi *et al.*, *Eur. Phys. J.* **C26** (2003) 331–344.
- [107] DELPHI Collaboration, P. Abreu *et al.*, *Phys. Lett.* **B491** (2000) 67–80.
- [108] DELPHI Collaboration, P. Abreu *et al.*, *Phys. Lett.* **B485** (2000) 45–61.
- [109] L3 Collaboration, M. Acciarri *et al.*, *Phys. Lett.* **B489** (2000) 81–92.
- [110] N. Cabibbo, *Phys. Rev. Lett.* **10** (1963) 531–532.
- [111] M. Kobayashi and T. Maskawa, *Prog. Theor. Phys.* **49** (1973) 652–657.
- [112] Super-Kamiokande Collaboration, Y. Fukuda *et al.*, *Phys. Rev. Lett.* **81** (1998) 1562–1567.
- [113] JADE Collaboration, S. Bethke *et al.*, *Phys. Lett.* **B213** (1988) 235.
- [114] CDF Collaboration, F. Abe *et al.*, *Phys. Rev.* **D45** (1992) 1448–1458.
- [115] UA1 Collaboration, G. Arnison *et al.*, *Phys. Lett.* **B132** (1983) 214.
- [116] UA1 Collaboration, G. Arnison *et al.*, *Phys. Lett.* **B123** (1983) 115.

- [117] UA2 Collaboration, J. Alitti *et al.*, *Phys. Lett.* **B257** (1991) 232–240.
- [118] J. E. Huth *et al.*, Presented at Summer Study on High Energy Physics, Reearch Directions for the Decade, Snowmass, CO, Jun 25 - Jul 13, 1990.
- [119] OPAL Collaboration, R. Akers *et al.*, *Z. Phys.* **C63** (1994) 197–212.
- [120] R. J. Barlow and O. Cooke, Prepared for 4th International Workshop on Software Engineering and Artificial Intelligence for High-energy and Nuclear Physics (AIHENP 95), Pisa, Italy, 3-8 April 1995.
- [121] S. Brandt, *Data analysis: statistical and computational methods for scientists and engineers*. Springer-Verlag New York Inc, 3 ed., 1998.
- [122] M. C. Bishop, *Neural Networks for Pattern Recognition*. Oxford University Press Inc, 1995.
- [123] K. Funahashi, *Proc,Int.Joint Conf. on Neural Networks* **1** (1988) 641, IEEE publications.
- [124] K. Cybenko, *Math. Control, Signals, and Systems* **2** (1989) 303.
- [125] K. M. Hornik, M. Stinchcombe, and H. White, *Neural Networks* **2** (1989) 359.
- [126] D. E. Rumelhart, G. E. Hinton, and R. J. Williams in *Parallel Distributed Processing:Explorations in the Microstructure of Cognition*, D. E. Rumelhart and J. L. McClelland, eds., vol. 1, p. 318. MIT Press: Boston, 1986.
- [127] D. E. Rumelhart, G. E. Hinton, and R. J. Williams, *Nature* **323** (1986) 533.
- [128] M. D. Richard and R. P. Lippmann, *Neural Computation* **3** (1991) 461.
- [129] J. B. Hampshire and B. Pearlmutter, Prepared for Proceedings of the 1990 Connectionist Models Summer School, San Mateo, CA, 1990.
- [130] L. Garrido, V. Gaitan, and M. Serra-Ricart, Prepared for 10th International Conference on Computing in High-energy Physics (CHEP 92), Annecy, France, 21-25 Sept 1992.

Acknowledgment

At first, I would like to thank Prof. Tomio Kobayashi, for his warm guidance and encouragement during over six years of my research. He guided me to the OPAL experiments for the theme of my doctor thesis. He allowed me to stay at CERN for the study, gave many suggestions about the analysis and read and corrected this draft many times. I learned much from his words, “Do exhaustively!” and “Be experimental physicist”.

I would like to thank Prof. Tatsuo Kawamoto, for his great help on this analysis. He gave many realistic and suggestive advices when I brooded over problems. He also corrected this draft many times patiently and gave me valuable suggestions in searching for new physics with the measurements. I learned much from him about the collider physics, analysis methods, the way of thinking in general, through many discussions. I really enjoyed discussions about many subjects (not only high-energy physics) with a cup of coffee or a glass of beer or wine.

I also appreciate Dr. Ikuo Ueda and Dr. Masaya Ishino for their daily maintenance and improvements of the computing environment at CERN. They accepted my annoying requests. I also thank Prof. Shoji Asai. They also gave me various suggestions about my analysis which made me think deeper on this analysis. I also thank them for their help on living at CERN for example, housing, French conversation and eating. I enjoyed conversation with them and learned there are many ways of thinking. I also thank Mrs. Terue Ishino for her help in obtaining the French visa and her inviting me to the dinner many times.

I would like to thank Dr. Daisuke Toya for his kind help about the OPAL analysis and about the life at CERN. I would like to thank Dr. Koichi Nagai, Dr. Keiichi Nagai, Dr. Kunihiro Nagano, Dr. Tadashi Maeno, and Dr. Naoko Kanaya. I enjoyed my life at CERN with them.

I am indebted to all the members of the OPAL Collaboration, for their construction of the detector and successful operation. They gave me the chance for the analysis and many suggestions at OPAL plenaries. I express my gratitude especially to Dr. David Plane, Dr. Pippa Wells, Dr. Patricia Ward, Dr. Richard Hawkins and Dr. Frank Fiedler. I also thank Ms Dawn Hudson who is the OPAL secretary. I couldn't get French visa without her help. I also thank Ms Mette Stuwe who is the previous OPAL secretary. She invited

us to the dinner many times.

I would like to express my gratitude to all members in ICEPP, especially to Prof. Sachio Komamiya, Prof. Toshinori Mori, Prof. Satoru Yamashita, Prof. Hiroshi Sakamoto, Prof. Tetsuro Mashimo, Dr. Junichi Tanaka, for useful comments at daily discussions, meetings and at the defense examination. I would like to thank secretaries in ICEPP: Ms. Emi Bandai, Ms. Chiyo Ito, Ms. Ryoko Ono, Ms. Ikue Tsukamoto, and Ms. Eiko Yuno, for supporting our researches. I would like to thank Dr. Kenji Ozone and Ms. Yasuko Hisamatsu for various discussions at night. I also enjoyed discussions with Dr. Toshio Namba, Dr. Toshiyuki Iwamoto, Dr. Shuei Yamada, Mr. Hajime Nishiguchi, Mr. Ryu Sawada, Mr. Yousuke Kataoka, Mr. Hiroshi Nomoto, Mr. Yusuke Fujii, Mr. Hiroaki Natori, Mr. Yusuke Uchiyama, Mr. Takayuki Sasaki and Mr. Yoshiki Yamaguchi.

Finally I thank my parents Osamu and Yoshi Nanjo for their continuous help, encouragement and understandings.

Hajime Nanjo